A REVISED TECHNIQUE FOR MEASURING VERTICAL VELOCITY USING DROPSONDES

by

Timothy Connor Nelson

A Dissertation

Submitted to the University at Albany, State University of New York

in Partial Fulfillment of

the Requirements for the Degree of

Doctor of Philosophy

College of Arts and Sciences

Department of Atmospheric and Environmental Sciences

2019

ABSTRACT

The earliest iterations of dropsondes in the 1960's obtained vertical velocity by measuring the geometric fall speed of the dropsonde and the true airspeed (TAS) of the dropsonde from a pitot-static. The vertical velocity errors from this methodology were claimed to be ± 1 m s^{-1}. Subsequent dropsonde iterations used various forms of the drag force equation to obtain vertical velocity. The accuracy of these drag force-based measurements, however, are also quite large at ± 1–2 m s^{-1}. In this dissertation, an attempt is made to improve vertical velocity errors by revisiting and revising the pitot-static-derived TAS methodology on the eXpendable Digital Dropsondes (XDDs). The primary goals were to decrease errors to ± 0.1 m s^{-1} and introduce a prototype for a highly accurate vertical velocity dropsonde for use in tropical cyclone (TC) research.

Three variations of the traditional pitot-static (the modified pitot-static, pitot-venturi, and venturi-static) were presented and evaluated. Computational fluid dynamics (CFD) model runs suggested that the pitot-venturi would be the most optimal configuration, and it would produce the smallest vertical velocity errors. A mean pitot-venturi calibration coefficient was found from a subset of eight XDDs using a large rotating arm device. Three fully calibrated pitot-venturi vertical velocity XDDs were launched operationally from a DC-8 aircraft off of the coast of the Baja California Peninsula. The results indicate that vertical velocity errors of 0.2–0.4 m s^{-1} are achievable using a pitot-venturi on the XDDs.

The vertical velocities using a modified version of the drag force method were also analyzed from the 2015 Tropical Cyclone Intensity (TCI) experiment. TCI sampled Erika, Marty, Joaquin, and Patricia with, an unprecedented, 784 XDDs. The results indicate

that: 1) high-spatial resolution vertical velocity measurements can be used to examine and document important convective features of TCs; 2) by improving the vertical velocity errors, it is possible to slightly improve dropsonde-derived horizontal wind speeds in the upper-levels of TCs; and, 3) the spatial resolution of XDDs should be less than 3 km in order to adequately “resolve” TC convection within transects of soundings.

PREFACE

This dissertation includes sections and chapters based upon research that was either previously published in a peer-reviewed journal by the author, or is currently in revision or preparation to a peer-reviewed journal, to adequately address the scientific concerns posed. Chapters 2 and 3 contain large excerpts, or slight rewordings, of the introductions, methods, data, results, figures, and some of the conclusions from Nelson et al. (2019a), Nelson and Harrison (2019), and Nelson et al. (2019b) (sections 2.2–3.1, 3.2, and 3.3, respectively). Nelson et al. (2019a) was published in *Monthly Weather Review*, and Nelson et al. (2019b) and Nelson and Harrison (2019) are in various stages of review or submission to the the *Journal of Atmospheric and Oceanic Technology.* The results, appendix, and supplementary material from Nelson et al. (2019a) are also used as motivation for this dissertation and is referenced throughout this work. Permission to use Nelson et al. (2019a) as part of this dissertation is granted by the American Meteorological Society and is copyrighted by the AMS, 2019 (see Appendix A for their signed permission).

References:

Nelson, T. C., L. Harrison, and K. L. Corbosiero, 2019a: Examination of the eXpendable Digital Dropsonde-derived vertical velocities from the Tropical Cyclone Intensity (TCI) experiment, *Mon. Wea. Rev.*, **147**, 2367-2386, doi: 10.1175/MWR-D-18-0414.1

Nelson, T. C., L. Harrison, and K. L. Corbosiero, 2019b: Temporal and spatial autocorrelations from eXpendable Digital Dropsondes (XDDs), 52 pp., *J. Atmos. Oceanic Technol.*, in

revision.

Nelson, T. C., L. Harrison, 2019: Revisiting the wind-finding equations for dropsondes, in preparation.

ACKNOWLEDGMENTS

I would like to thank my best friend and wife, Brianne M. Nelson, for standing beside me and supporting me through four years of challenges and triumphs in my Doctoral studies. I would also like to thank my son, Timothy Carter Nelson for giving me the strength to not only be a good scientist and husband, but also a good father.

I would like to thank my advisor, Dr. Lee Harrison. His advisement, guidance, and direction helped to make this work successful and complete. I would also like to sincerely thank Dr. Kristen Corbosiero for not only serving as a committee member, but for also re-reading my manuscripts many times over. I would also like to thank my other committee members, Drs. Brian Tang and Ryan Torn for their advice and comments on my dissertation.

I would like to thank all of the faculty and staff of the Department of Atmospheric and Environmental Sciences and all of the faculty and staff of the Atmospheric Sciences Research Center (ASRC) for their support and encouragement including Sandra George, Cathy Lott, and Joane MacMillan. I would like to extend a very sincere thank you to Mark Beaubien, Todd Allen, Will Jeffries, and all of the crew at Yankee Environmental Systems. Without their diligence and ingenuity, the eXpendable Digital Dropsondes would not be where they are today. I would also like to thank Ron Ferek at the Office of Naval Research, Dr. Jim Doyle at the Naval Research Laboratory, all of the principal investigators for the Tropical Cyclone Intensity (TCI) Experiment, all of the NASA WB-57 crew, and all others associated with TCI.

Last, I would like to thank my friends, family, and loved ones for their love, encouragement, and support. This group of individuals invested time and energy in me, pushed me to succeed and grow, especially when I did not believe in myself. I especially want to thank Sarah Ditchek, Jason Covert, Dr. Patrick Duran, Dr. Chip Helms, Josh Alland, Matt Ninneman, and Matthew Vaughan for all of their help, kindness, and friendship over the past four years. I want to thank my father for his endurance and steadfast care, my mother for her strength and supporting love, my sister for her dedication, and my grandparents for their belief in me. This research was supported by the Office of Naval Research (ONR) High Density Drop-Sonde Measurements grant 1141135-1-78783 and the ASRC Graduate Student Fellowship.

T. Connor Nelson

2019

CONTENTS

APPENDICES

LIST OF TABLES

LIST OF FIGURES

CHAPTER 1

Introduction

1.1 Motivation and purpose

In addition to the basic state variables (pressure, temperature, relative humidity, and horizontal wind), Global Positioning System (GPS) dropwindsondes (hereafter called "dropsondes") can measure vertical velocity. Dropsonde-derived vertical velocities have been obtained since the mid 1960's (Bushnell et al., 1973) through a variety of techniques, but the present state of the art for dropsonde-derived vertical velocity error is approximately $\pm 1-2$ m s^{-1} (Hock and Franklin, 1999; Stern et al., 2016; Nelson et al., 2019a). The vertical velocity errors need to be below ± 1 m s^{-1} to completely understand and defend the observations of both convection and weaker vertical motions in many atmospheric phenomena such as tropical cyclones (TCs). In some circumstances, vertical velocity errors of $\pm 1-2$ m s^{-1} could be the difference between diagnosing an updraft from a downdraft in the observed data (e.g., TC updrafts in Nelson et al., 2019a).

Accurate dropsonde-derived vertical velocities are also important to obtain information on atmospheric convection where Doppler radars do not perform well. Doppler radars have, historically, provided accurate measurements of vertical velocity within 1 m s^{-1}, but they can only measure vertical velocity if there is enough precipitation or particles large enough to be detected by the radar (e.g., Atlas et al., 1973; Jorgensen et al., 1985; Black et al., 1996; Jorgensen et al., 1996; Matejka and Bartels, 1998; Heymsfield et al., 2010). Doppler radars are also beam averaging, meaning that vertical velocity, or energy, is averaged over the beam volume and is not a true point measurement (Heymsfield et al., 2010; Ryzhkov, 2007). Dropsonde-derived vertical velocities fill this gap and complement radar data where there may not be precipitation or where point measurements are required. Dropsondes can also record vertical velocity profiles from their launched altitude to the surface in nearly all situations.

The need for more accurate dropsonde-derived vertical velocity measurements motivates this dissertation and serves as the basis for future dropsonde developments. This dissertation synthesizes 50–60 years of dropsonde-derived vertical velocity research and proposes to readdress the quality and accuracy of vertical velocity measurements by revisiting and revising older methods. Specifically, this work proposes to incorporate instrumentation on the eXpendable Digital Dropsondes (XDDs) manufactured by Yankee Environmental Systems to directly measure the true vertical air speed (TAS) from a differential pressure sensor in a pitot-static system, similar to what was originally done in the 1960's (e.g., sections 2.1 and 2.5; Bushnell et al., 1973). The goal of this research is to reduce the expected dropsonde-derived vertical velocity errors to ± 0.1 m s^{-1}. The corollary objectives of this dissertation are to: 1) provide a history of dropsondes and their developments (sections 1.2, 1.3); 2) document previous methods to obtain dropsonde-derived vertical velocities (chapter 2); 3) assess the strengths, weaknesses, and errors for the previous methods (section 2.4, 2.5); 4) analyze the vertical velocities from previous TC campaigns using the XDDs (chapter 3); 5) draw conclusions about performance requirements for XDDs and their launch spacing for future TC research missions (section 3.3); 6) compare design characteristics for pitot-static measurements on the XDDs (chapter 4); and, 7) demonstrate the capabilities of dropsonde-derived vertical velocities using a pitot-static system (chapters 5, 6).

1.2 Brief history of dropsondes

While the earliest balloon-borne observations of the atmosphere date back to the late 1800's and early 1900's (e.g., Rykatcheff, 1990), dropsonde technology is relatively young. Development of the National Center for Atmospheric Research (NCAR) dropsonde began in the early 1960's, with a principal goal of mapping the vertical velocity fields of deep convective thunderstorms (Bushnell et al., 1973). The early NCAR dropsonde (hereafter referred to as "ED") recorded atmospheric temperature (T), atmospheric pressure (p), dynamic pressure (p_d), and rate of change in pressure. The ED used a transponder method to calculate the dropsonde position by measuring the time delay of the pulse to estimate the distance from a set of two known fixed ground stations (Bushnell et al., 1973).

The initial NCAR ED design evolved into the Omega-based dropwindsonde (OD) in the early 1970's (Cole et al., 1973; Hock and Franklin, 1999; Wick et al., 2018). The OD operated at a very-low-frequency, used pulses of electromagnetic waves to obtain information on distance and location, and could be used in more remote locations than the ED (Cole et al., 1973; Govind, 1973). The OD also recorded data on T, p, and relative humidity (RH) (Govind, 1973). In 1987, the Office of Naval Research (ONR) conducted the Experiment on Rapid Intensification of Cyclones over the Atlantic using the NCAR developed Lightweight Long-Range (Loran) Digital Dropsonde (LDD; Hock and Franklin, 1999; Wick et al., 2018). The LDD was similar to the OD in that it also used phase shifts to obtain location information (Govind, 1973), but the LDD had improved horizontal wind measurements, was lighter than the OD, and had exchanged older analog circuitry for relatively modern digital circuitry (Hock and Franklin, 1999).

The modern NCAR GPS-based dropsonde began development in 1995 as part of the Airborne Vertical Atmospheric Profiling System (AVAPS; Hock and Franklin, 1999; Wang et al., 2015). Wang et al. (2015) documented the major developments of AVAPS and the NCAR/Vaisala RD-93 dropsondes, RD-94 dropsondes, and mini-sondes (called NRD94 in Wick et al., 2018). The mini-sonde is the most advanced research dropsonde available from NCAR at present, but future developments are expected regarding the T and RH sensors, as well as the GPS chipset (Vömel et al., 2018). Specifications of the variables recorded, accuracy, and data acquisition frequency of the NRD94 are provided in Table 1.1 (Wick et al., 2018). AVAPS can currently support the telemetry of eight dropsondes in the air simultaneously (Wang et al., 2015; Black et al., 2017; Wick et al., 2018).

1.3 Introduction of the XDDs

The XDD is a small, light-weight dropsonde used with the High-Definition Sounding System (HDSS) manufactured by Yankee Environmental Systems (Fig. 1.1). A comparison of the size of the XDD to the RD-94 and mini-sonde is shown in Figure 1.2. Specifications of the variables recorded by the XDDs, accuracy, and data acquisition frequency are provided in Table 1.2 (Black et al., 2017; Nelson et al., 2019a). The XDD was developed off of the eXpendable Digital Radiosonde (XDR) used in the 2008 Arctic Mechanisms of Interaction between the Surface and Atmosphere (AMISA) project (Black et al., 2017).

The XDD has a twisted, slotted foam body and a cardboard outer shell, with airflow cutaway windows (Fig. 1.1). This allows the XDD to spin during descent, obtain a ballistic trajectory, and promotes a stable fall mode. The XDD also features a quadrifilar antenna in the aft of the foam body and a loop nose antenna for transmitting and receiving data (Fig. 1.1).

At present, the HDSS consists of two, 48-dropsonde magazines, which allows for a total of 96 dropsondes to be used in a single flight. With two dispensers, the launch rate can be as quick as 5 s (Black et al., 2017). The HDSS can also uniquely identify and receive data from up to 40 dropsondes in the air, simultaneously, though the inclusion of forward error correction and time division multiplexing. The HDSS and the XDDs provide unprecedented temporal and spatial resolution of dropsondes from high altitudes (> 18 km).

Various test flights using the HDSS and XDD were conducted from 2011–2014, including drops into Hurricane Gonzalo (2014), and has been shown to compare well to the NCAR/Vaisala RD-94 dropsonde. The XDDs have comparable wind and temperature measurements and resolution to the Vaisala RD-94 dropsonde (Black et al., 2017). Black et al. (2017) note that the largest discrepancies between collocated XDD and the RD-94 data are for RH. The RH sensors on the XDDs have a coarser resolution and slower response rate, which leads to soundings being approximately 5% drier. Nonetheless, the XDDs allow for the collection of critical high-resolution observations of the thermodynamics, kinematics, and convection.

In 2015, the ONR conducted the Tropical Cyclone Intensity (TCI) experiment and launched an unprecedented 784 XDDs into four TCs: Erika (30 August), Marty (27–28 September), Joaquin (2–5 October), and Patricia (20–23 October) (Doyle et al., 2017). The XDDs were launched from a National Aeronautics and Space Administration (NASA) WB-57 aircraft at an altitude of approximately 19 km. The goal of TCI was to improve TC intensity prediction, especially in cases of rapid intensification and rapid weakening, and better understand TC structural change (Doyle et al., 2017). Specifically, TCI focused on the role of the outflow layer on intensity change in TCs.

Table 1.1: Variables recorded by the NRD94s and their range, resolution, repeatability, and data acquisition frequency. Adapted from Wick et al. (2018).

	Range	Resolution	Repeatability	τ
Pressure	3–1080 hPa	0.1 hPa	0.4 hPa	2-Hz
Temperature	−90°C to 60°C	0.2°C	0.2°C	2-Hz
Relative humidity	0–100%	1%	2%	2-Hz
Wind speed	——	0.1 m s^{-1}	0.2 m s^{-1}	4-Hz
Wind direction	0–360°	——	——	4-Hz
Fall speed	——	——	——	4-Hz

Table 1.2: Variables recorded by the XDDs and their range, resolution, accuracy, and data acquisition frequency. Adapted from Black et al. (2017).

	Range	Resolution	Accuracy	τ
Pressure	150–1150 hPa	2.5 hPa	1.5 hPa at 25°C	2-Hz
Temperature	−90°C to 60°C	0.016°C	0.14°C	2-Hz
Relative humidity	0–100%	0.1%	1.8% at 25°C	2-Hz
Wind speed	——	0.1 m s^{-1}	0.2 m s^{-1}	4-Hz
Wind direction	0–360°	——	——	4-Hz
Fall speed	——	0.1 m s^{-1}	0.2 m s^{-1}	4-Hz
Sea surface temp.	0°C to 50°C	0.016°C	0.2°C at 25°C	2-Hz

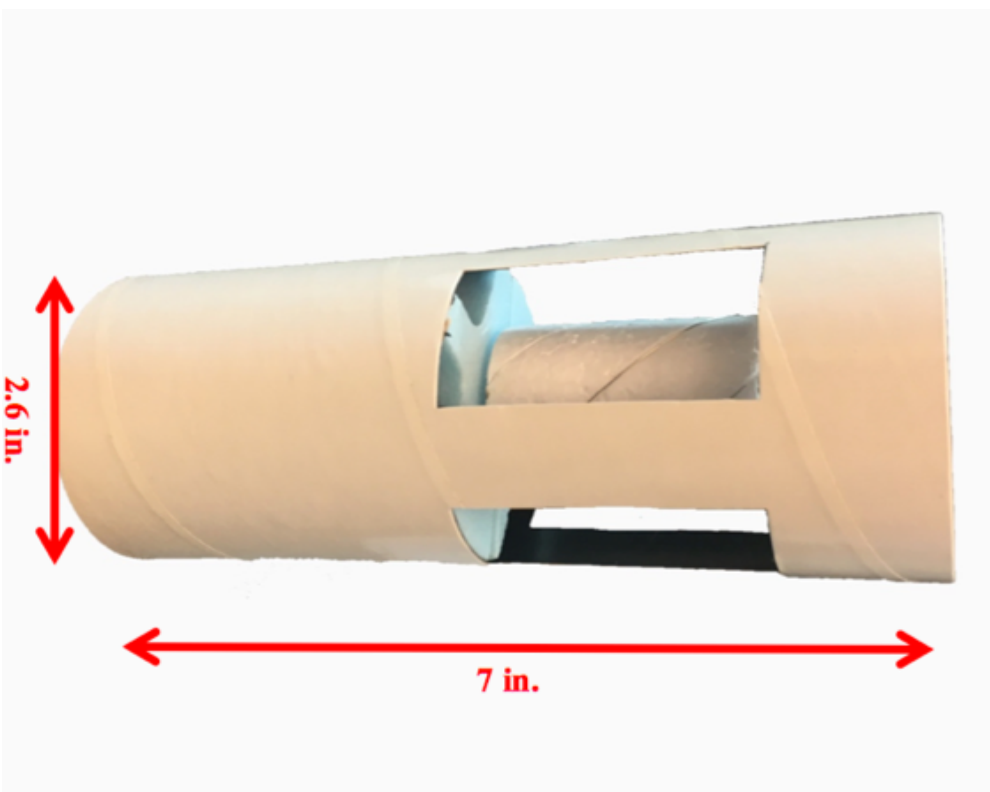

Figure 1.1: An example of an XDD manufactured in 2017.

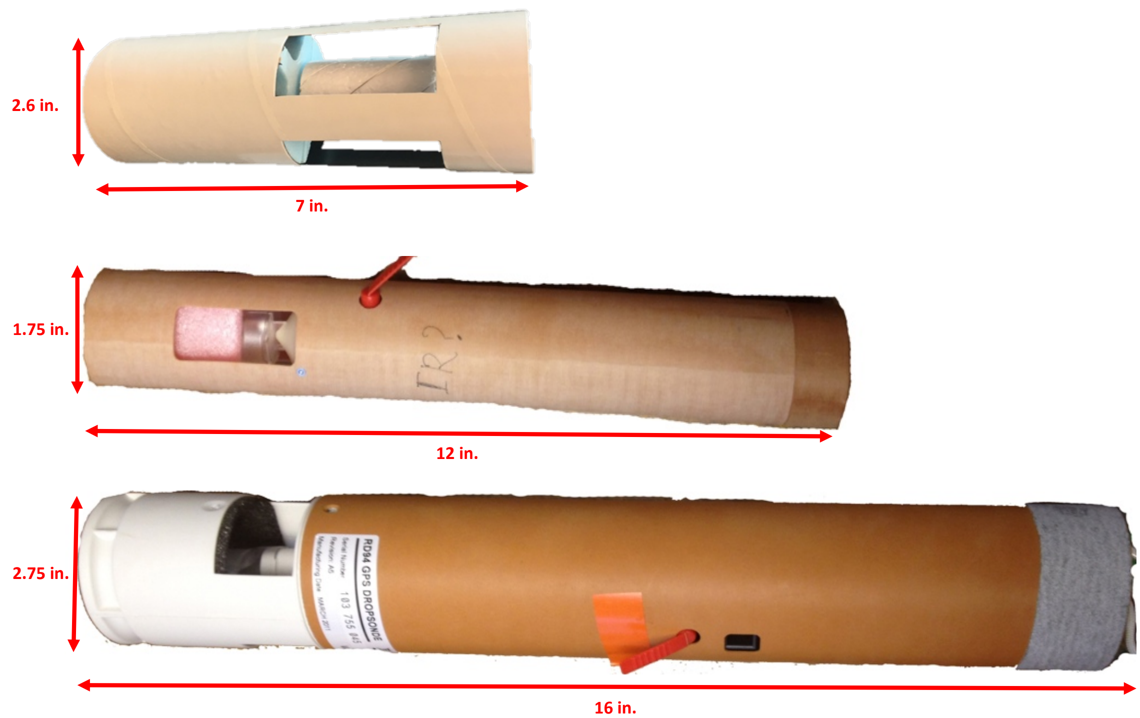

Figure 1.2: Size comparison of an XDD, mini-sonde, and RD-94 dropsonde. The dropsondes are approximately to scale.

CHAPTER 2

Previous dropsonde-derived velocity methods

There are three primary methods to obtain or calculate dropsonde-derived vertical velocities: 1) the pitot-static/differential pressure sensor method (e.g., Bushnell et al., 1973); 2) the drag force method (e.g., Hock and Franklin, 1999); and 3) the estimated drag force method. The pitot-static method was introduced by P. Squires at NCAR and was used in the original ED in the 1960's and 1970's (Bushnell et al., 1973). The pitot-static method was ultimately abandoned in the later NCAR dropsonde iterations for unknown reasons (T. Hock and P. Black, personal communication), but it is hypothesized that it was abandoned after the passing of Squires in lieu of GPS-based or digital methods that did not require multiple large, analog transducers. NCAR has since used the drag force method for all dropsonde-derived vertical velocities. It is also possible to use a modified version of the drag force method in situations where the required information for the drag force method are not known a priori; this is the estimated drag force method. The three methods are described in detail below and the typical errors, benefits, and limitations associated with each method are also discussed.

2.1 Pitot-static methods

The use of a pitot-static to obtain the velocity of air, or the TAS of a moving object, has been commonly done since the early 1700's with the invention of the pitot tube by Henri Pitot (Fig. 2.1; Pitot, 1732), eventually becoming the modern pitot-static design (Prandtl tube). The design was further improved upon in the 1850's by Henry Darcy (Darcy, 1858;

Brown, 2003).

The modern pitot-static system (Fig. 2.2) measures TAS by measuring the difference in pressure from the ambient air (static) and the total pressure or stagnation pressure (pitot). The total pressure measured by the pitot is the sum of the dynamic pressure caused by motion and the ambient pressure (Brousaides, 1983). Pitot-statics are routinely used to obtain the horizontal airspeed of aircraft (e.g., Brousaides, 1983; Haering Jr., 1995; Federal Aviation Administration, 2016) or determine the flow velocity in a wind tunnel (e.g., Beck et al., 2010; Mitchell, 2013). The physics and methodology of a pitot-static is demonstrated by a simplified form of the Bernoulli principle as shown in equations 2.1–2.3 (e.g., Brousaides, 1983; Federal Aviation Administration, 2016; Beck et al., 2010; Moum, 2015).

$$\frac{d}{dz}[\rho\frac{V^2}{2} + p + \rho g z] = 0 \tag{2.1}$$

$$\rho\frac{V^2}{2} + p + \rho g z = constant \tag{2.2}$$

$$V_2 = \sqrt{\frac{2(p_1 - p_2)}{\rho_2}} \approx V = \sqrt{\frac{2(dP)}{\rho}} \tag{2.3}$$

In order for equation 2.1 to be valid, then equation 2.2 must identically be true. If variations in height (z) are small, then the hydrostatic component of equation 2.2 is negligible and an equality between p, ρ, and velocity (V) at some arbitrary point 1 and point 2 is established. The left side of equation 2.3 solves for the velocity at point 2 and is simplified to the generic form on the right side of equation 2.3. TAS can, therefore, be directly calculated from the observed difference in pressure, if p_1 is assumed to be the total pressure and p_2

is the static pressure. The difference between p_1 and p_2 is known as the dynamic pressure (hereafter referred to as p_d). The indicated airspeed (IAS) traditionally used in avionics does not take into account the density of the ambient air (Federal Aviation Administration, 2016).

The ED, with a schematic of the pitot-static probe, is shown in Figure 2.3. The pitot-static probe extended 5.5 inches below the dropsonde and had one pitot port (0.25 in diameter tip) and six static ports (0.05 in diameter holes, 0.66 in from tip) large enough to ensure that blockage did not occur due to water (Bushnell et al., 1973). The tip had rounded edges and came to a 'point' at a 30° angle. The pitot-static tube was heated to 100°C to keep ice from building up on the probe (Bushnell et al., 1973).

Vertical velocity was obtained in two ways: 1) with a p_d transducer attached to the pitot port and a $\frac{\partial p}{\partial t}$ transducer (also known as a p-dot transducer) attached to the static ports; and, 2) with a p_d transducer attached to the pitot port and a standard pressure transducer attached to the static ports. The first method was filtered with a high-pass filter to remove low frequencies and the second method was filtered with a low-pass filter to remove high frequencies. The combination of both filtered signals yielded a final vertical velocity. The equations used to obtain the final vertical velocity are summarized below:

$$w_1 = \sqrt{\frac{2p_d}{\rho}} - \frac{1}{\rho g}\frac{dP}{dt} \tag{2.4}$$

$$w_2 = \sqrt{\frac{2p_d}{\rho}} - \frac{dz_p}{dt} \tag{2.5}$$

$$w = HP(w_1) + LP(w_2) \tag{2.6}$$

$$\rho = \frac{p}{R_d T_v}, \tag{2.7}$$

where w_1 is the vertical velocity obtained with the p_d and p-dot transducers, w_2 is the vertical velocity obtained with the p_d and pressure transducers, z_p is the hydrostatic height, t is time, ρ is density obtained by the ideal gas law using virtual temperature (equation 2.7), HP is a high-pass filter, and LP is a low-pass filter. Bushnell et al. (1973) used the combination of the two vertical velocities (w_1 and w_2), because of the better expected errors of w_1 for high-frequency data and of w_2 for low-frequency data. Modern sensors likely do not have as severe high- or low-frequency biases and, therefore, do not require the combination of the two vertical velocities. Equations 2.4 and 2.5 are used to calculate the difference between the pitot-static-indicated TAS and the geometric fall speed. For example, if a dropsonde was falling through the atmosphere and encountered an updraft strong enough to suspend it in the air, the geometric fall speed would be zero, but the (fully calibrated) pitot-static-indicated speed would be equal to the strength of the updraft.

2.2 Drag force methods

Since 1999, dropsonde-derived vertical velocities have been computed utilizing the dropsonde fall speed and the drag force equation, assuming that the drag coefficient is independent of the Reynolds number (Hock and Franklin, 1999). The Reynolds number is the ratio of the relative airspeed and length scale to the viscosity of air (equation 2.8):

$$R_e = \frac{UL}{\nu}. \tag{2.8}$$

Reynolds numbers below $5 \text{x} 10^5$ imply laminar flow plate object, and Reynolds numbers above 5x10^{5} imply turbulent flows (e.g., Happel and Brenner, 1965; Incropera et al., 2007). Dropsonde-derived vertical velocities are now routinely calculated in this manner (Wang et al., 2015). In more recent research, dropsonde-derived vertical velocities, calculated from the drag force method, have been used to examine the specifics of convection such as misovorticies and extremely strong updrafts in TCs (e.g., Aberson et al., 2006; Stern and Aberson, 2006; Stern et al., 2016).

The most common equation set used to calculate vertical velocity is as follows from Hock and Franklin (1999):

$$V = \left(\frac{2mg}{C_d A \rho}\right)^{\frac{1}{2}} = \sqrt{\frac{m}{C_d A}}\sqrt{\frac{2g}{\rho}} \tag{2.9}$$

$$w = V - V_f, \tag{2.10}$$

where w is the vertical velocity, V is a theoretical terminal fall speed, and V_f is the true fall speed of the dropsonde (note: V and V_f are positive pointing downward). On the right-hand side of equation 2.9, the $\sqrt{\frac{m}{C_d A}}$ term is referred to as the 'dropsonde parameter' (S_p). In equation 2.9, g is the gravitational acceleration (positive term), m is the mass of the dropsonde, C_d is the drag coefficient, A is the drag-affected area, and ρ is density. The area used for the RD-94 dropsondes is the open area of the parachute and it is presumed to be representative for all dropsondes. The C_d value used is typically 0.61, and the area is assumed to be fixed at 0.0676 m^2 or 0.09 m^2 (Wang et al., 2009; Stern et al., 2016).

Early studies, like Hock and Franklin (1999), used the GPS fall speed for V_f, but more recent studies such as Wang et al. (2015) and Stern et al. (2016) used a calculated hydrostatic differential pressure fall speed:

$$V_f = \frac{1}{\rho g} \frac{dP}{dt} \tag{2.11}$$

for V_f. A hydrostatic fall speed was used in these studies rather than the recorded GPS fall speed, because large, unrealistic and noisy GPS fall speeds occasionally occur (e.g., Fig. 2.4) and pressure is more accurate than GPS height (Stern et al., 2016). Figure 2.4 shows an example of erratic GPS fall speeds from an XDD sounding in Marty (2015) during TCI. The GPS fall speeds above 15 km and between 6–8 km have high variance and do not match the hydrostatic fall speeds (Fig. 2.4). The relatively weak GPS fall speeds aloft are not likely to be real, because they would indicate an unrealistically strong updraft of 15 m s^{-1} far away from the core of the TC (318 km from the eye). This is also suspicious, because the GPS fall speed decreases nearly linearly with decreasing altitude until 14 km, indicating a fall mode, stability, or GPS issue (Fig. 2.4). The large variance in the GPS fall speed, especially at high altitudes, is likely due to changing GPS constellations (L. Harrison, personal communication; Berg, 2003). Large variances in the lowest few kilometers above the surface are occasionally observed in both the XDD data (Fig. 2.4) and RD-94/NRD94 data (Vömel et al., 2018). If GPS fall speeds are used to derive vertical velocity, the fall speeds should be heavily screened based upon the calculated hydrostatic differential pressure fall speed or heavily filtered.

2.3 Estimated drag force methods

There are three variants of the estimated drag force method to use when the exact values for C_d and m, or the variance in those values, are unknown. These methods are proposed because the exact C_d of the XDDs used in TCI was not known a priori and the variances in the m and A of the XDDs used were not known. If it is assumed that S_p for any given dropsonde is constant as it falls from some arbitrary altitude (Z) to the surface (Z_o), then equation 2.12 must be true:

$$V(Z) = V(Z_o)\sqrt{\frac{\rho(Z_o)}{\rho(Z)}}. \tag{2.12}$$

The $V(Z_o)$ and $\rho(Z_o)$ terms represent the estimated surface fall speed and density of a dropsonde. The three methods to obtain $V(Z_o)$ and $\rho(Z_o)$ include: 1) an individualized last data point fall speed and density (M1), 2) a mean or median last data point fall speed and density from dropsondes launched outside of convective regions (M2), and 3) an estimated $V(Z_o)$ from a mean (or median) S_p from dropsondes outside of convective regions and the last data point density from dropsondes inside of convective regions (M3). The vertical velocities from M1–M3 were analyzed using the XDD soundings launched during TCI. It is assumed that the XDDs were launched outside of convective regions if the sounding profiles were unsaturated and infrared (IR) cloud top temperatures were above −30°C. The −30°C threshold was chosen, because it matches the warmest IR brightness temperatures for all deep convective regions observed by Jiang and Tao (2014).

The benefit to using an individualized fall speed (M1) is that it is self-calibrating and accounts for mass differences from dropsonde-to-dropsonde, including manufacturing differences, and any icing or riming that does not melt off of dropsondes launched into deep convection. The last data point fall speed, however, may not represent the still-air fall speed for an individual dropsonde, because low-level updrafts or downdrafts could be present or the dropsonde could be in a non-stable fall mode. This is still a problem even if a threshold is used for the height of the last data point (Fig. 2.5). The use of a mean or median last data point fall speed and ρ outside of convective regions (M2) is a non-self-calibrating estimation of $V(Z_o)$ and $\rho(Z_o)$ but is less prone to errors due to low-level updrafts or downdrafts affecting the value of $V(Z_o)$ in convective areas. The third method is a hybrid of the first two methods. Figure 2.6 shows that the variance in the estimated $V(Z_o)$ from $\rho(Z_o)$ in convective regions and the median S_p from data outside of convective regions is considerably smaller than the observed $V(Z_o)$ for the same dropsondes during TCI. The difference in the variance was 1.74 m^2 s^{-2}. The median S_p was 4.22 $kg^{\frac{1}{2}}$ $m^{\frac{3}{2}}$ (Fig. 2.6). The reduced variance using M3 compared to the others is a consequence of the high confidence in the measurements of pressure, and subsequently density, for the XDDs. The standard deviation of the last data point density was small at 0.02 kg m^{-3} (Fig. 2.6).

A comparison of the vertical velocities from TCI computed from the three methods, using notched boxplots, is provided in Figure 2.7. Also included in Figure 2.7 is M3 using the GPS fall speed for V_f rather than the hydrostatic fall speed (M3b). None of the notches of the box plots overlap, which indicates that the medians of all the methods are statistically different, but the differences are small enough to not be physically significant. M1 has the largest variance, with a standard deviation of 2.26 m s^{-1}. The relatively high variance is not likely physical, because it occurs simply by using different values of $\rho(Z_o)$ and $V(Z_o)$ and an individualized S_p. M2 and M3 have the lowest variance in vertical velocity from TCI, which suggests that M2 and M3 are more robust than M1. It should also be noted that variance of the vertical velocity is increased in the TCI dataset if the GPS fall speed was used (Fig. 2.7).

2.4 Benefits and limitations

Regardless of the method used to obtain vertical velocity, significant errors may still exist. In this section, the benefits and limitations of the previously discussed dropsonde-derived vertical velocity methods are detailed in depth. The typical errors associated with each of the three methods are also discussed.

One benefit of a pitot-static system on a dropsonde is that the pitot-static-derived TAS is a direct, physical measure of the dropsonde fall speed, relative to the air. The vertical velocity calculations for the pitot-static outlined by Bushnell et al. (1973) are also independent of m, C_d, and A, which are major sources of error in the two drag force methods. The drag force methods either use hydrostatic fall speeds calculated over fairly large distances (e.g., Stern et al., 2016) or GPS fall speeds that are prone to large amplitude noise (Fig. 2.4). The ED dropsonde directly recorded the hydrostatic height fall speed with a p-dot transducer (Bushnell et al., 1973).

Bushnell et al. (1973) also note that the ED had a Reynolds number of approximately 5x10^5, where transition from laminar to turbulent flow occurs. Bushnell et al. (1973) state that EDs falling at this 'critical' Reynolds number can lead to situations where C_d can change rapidly and irregularly. However, it is not clear if the fluctuations in C_d were due to parachute/drag device deformations. Regardless, it is plausible that C_d can vary for a dropsonde parachute as it falls, which causes vertical velocity errors when using the drag coefficient methods in convective regions.

High accuracy of IAS and, subsequently, TAS from a pitot-static on current operational aircraft is crucial for safe flights to be conducted (Haering Jr., 1995; Federal Aviation Administration, 2016; Carlson, 2012), so errors in IAS from any pitot-static need to be small. The accuracy of speed from pitot-static probes is usually between 0.5–2 m s^{-1} and are functions of small errors in the p_d (Bushnell, 1966; Bushnell et al., 1973; Brousaides, 1983; Pearson, 1983; SpaceAge Control, 1998; Barfield, 2013). The five primary sources for error are: 1) port blockage (Federal Aviation Administration, 2016); 2) port placement error (Haering Jr., 1995; Carlson, 2012); 3) angle of attack (Pearson, 1983; Haering Jr., 1995; Beck et al., 2010); 4) normal instrumentation error (Carlson, 2012); and, 5) low speed errors (SpaceAge Control, 1998). Over the past 160 years, many studies have been conducted to improve the design of the pitot-static system to decrease errors and offer more consistent calibration (e.g., Darcy, 1858; Salter et al., 1965; SpaceAge Control, 1998; Brown, 2003; Beck et al., 2010; Carlson, 2012; Reuder et al., 2013; Abdelrahman et al., 2015; Federal Aviation Administration, 2016).

Port blockage becomes a problem when water, ice, or other debris block the port holes and prohibit the pitot-static from working effectively (Federal Aviation Administration, 2016). If the pitot tube is blocked and a leak port is present, then the air inside the tube will eventually leak out and the pressure with match the static pressure, giving a zero-p_d. If the pitot tube is blocked and no leak port is present, or the leak port is also blocked, then the p_d will decrease with decreasing height to reflect the change in height. If the static port becomes blocked and the pitot port is clear, the p_d will be biased to positive values as the object descends. If the pitot and static ports are both blocked, the p_d will be zero.

Port placement errors, also known as position errors, occur as a result of the location of the pitot and static ports relative to the object body (Haering Jr., 1995; Carlson, 2012). Position errors primarily occur because any object within a stream of air disrupts the flow and can cause local pressure perturbations that affect the pitot-static measurement (Bushnell et al., 1973; Haering Jr., 1995). Compressibility and shock waves related to the disruption of flow by the object can also affect the measurement, but this is primarily at speeds greater than approximately 100 m s^{-1} or a Mach number of 0.3 (Haering Jr., 1995). Such high fall speeds are not observed with any current dropsonde. Position errors are also a function of the angle of attack.

The angle of attack of the pitot-static probe could have a significant effect on the indicated velocity (Pearson, 1983; Haering Jr., 1995; Beck et al., 2010; Carlson, 2012). The design, shape, and angle of the probe tip dictate the severity of the angle of attack error and the angles of attack that are suitable for the specific probe (Haering Jr., 1995). Beck et al. (2010) documented the change in the pitot-static measurements for a specific probe as a function of angle of incidence through wind tunnel tests (Fig. 2.8). The pressure coefficient (C_p), which is the ratio of the calibrated pitot-static p_d to the true wind tunnel p_d, reaches a minimum when the pitot-static probe is perpendicular to the incoming flow (Fig. 2.8). The maximum errors in this extreme situation were 7–8 m s^{-1} at wind tunnel speeds of 35–42 m s^{-1}. Given that modern dropsondes either fall with a parachute (e.g., RD-94s) or with a ballistic trajectory (e.g., XDDs), such extreme angles of incidence and large errors are not likely. At 35 m s^{-1}, C_p values of 0.95 or 1.05 correspond to errors of approximately 1 m s^{-1} (Fig. 2.8).

There are also inherent, normal, instrumentation errors associated with the p_d sensor upon leaving manufacturing. Instrumentation companies can calibrate the sensors before leaving and provide documentation on the expected error range of the sensor (e.g., All Sensors, 2019), but the errors still affect the confidence in the measurement. Bushnell et al. (1973) note that the typical instrumentation errors with the p_d and static pressure transducers ranged from 1x10^{-4}–0.8-hPa on the EDs.

At low air velocities, the ratio of the indicated air speed to the total error range decreases and tends toward unity (SpaceAge Control, 1998). At these low ratios, the total errors begin to saturate the signal and the percent errors become significant. This is an inherent problem for measuring any meteorological variable that can decrease to zero or below a detectable limit. SpaceAge Control (1998) note that at 12 m s^{-1}, the velocity errors for their wind tunnel pitot-statics were $\pm$2.5% (0.3 m s^{-1}). At higher velocities, error dropped below $\pm 0.7\%$.

The dropsonde-derived vertical velocities using the pitot-static method on the ED were compared to sailplane vertical velocity observations in quiescent conditions on two different days in northeastern Colorado (Bushnell et al., 1973). Figures 2.9 and 2.10 show the dropsonde-derived vertical velocities and the sailplane vertical velocities from 21 and 25 April 1972. The average true vertical velocity in each profile is assumed to be zero, but the average sailplane vertical velocity was -0.2 m s^{-1} and 0 m s^{-1}, respectively. The typical vertical velocity error bounds associated with this methodology were estimated by the difference between the average pitot-static indicated fall speed and geometric fall speed (Δw). The differences were on the order of ± 1 m s^{-1} and the standard error of the dropsonde-derived vertical velocities and the sailplane vertical velocities was 0.6 m s^{-1} (Bushnell et al., 1973).

Recent advancements in unmanned aerial vehicles (UAVs) have allowed for meteorological wind measurements using more modern pitot-static probes (Reuder et al., 2009, 2013; Niedzielski and Coauthors, 2017). Reuder et al. (2009) found that pitot-static UAV-derived horizontal wind speeds and Vaisala RS92 radiosonde data agreed within 0–2 m s^{-1}, with the largest discrepancies due to sampling differences and not systematic errors in the measurement or methods. Niedzielski and Coauthors (2017) also found that the differences between UAV-derived horizontal wind speeds and nearby tower data were at least 1–2 m s^{-1}. Vertical velocity UAV measurements taken at 100-Hz had low standard deviations of 0.31 m s^{-1} (Reuder et al., 2013).

Dropsonde-derived vertical velocities using drag force methods are attractive, because no additional specialized instrumentation is needed beyond what is currently on modern dropsondes, the calculations are straightforward and based upon Newtonian physics, the errors are easily characterized and estimated, and they have been the common-place, standard dropsonde-derived methods for almost 20 years. The potential errors associated with drag force-based calculations like Hock and Franklin (1999), Wang et al. (2015), and Stern et al. (2016) are: 1) added (subtracted) mass from icing (de-icing); 2) variations in the dropsonde drag area; 3) variations in drag coefficient; and, 4) presence of low-level updrafts or downdrafts. The first three affect the calculation of individual S_p values. While mass changes and dropsonde-to-dropsonde mass differences are more easily understood, variations in C_d and A are not. Li and Miller (2014a,b) assume that the drag coefficient and drag affected area of a dropsonde is constant, regardless of the angle of incidence. One can adjust the variables and parameters in equations 2.9 and 2.10 to estimate the sensitivity or potential errors in dropsonde-derived vertical velocity using the drag force methods.

The potential errors/sensitivities associated with the vertical velocity measurements using the Hock and Franklin (1999) methodology with RD-93 and RD-94 dropsondes and a hydrostatically derived V_f are outlined in the appendix of Stern et al. (2016). The sensitivities are shown in Figure 2.11, which was adapted from Stern et al. (2016). The true mass of the dropsonde used in the example sounding was 389 g, C_d was assumed to be 0.61, and A was assumed to be 0.09 m^2 (dashed blue lines in Fig. 2.11). Peak vertical velocity varied 2–5 m s^{-1} by changing the variables within the ranges examined by Stern et al. (2016). The author's state, however, that overall bias at low levels associated with uncertainty in m (60–80 g difference), A, and C_d is less than 1 m s^{-1}.

A similar analysis was conducted for the XDDs using the M3 estimated drag force method discussed previously. For the purposes of discussion, it is assumed that the mass of the XDD is 0.058 kg, the diameter is 0.066 m (Black et al., 2017), and C_d is 0.95. A drag coefficient of 0.95 was obtained by solving for C_d in equation 2.9, given the median

S_p from XDDs launched outside of convective regions during TCI and the m and A. For the four primary sources of error described previously, errors are largest aloft (Fig. 2.12). This is due to a larger ratio of $\rho(Z_o)$ to $\rho(Z)$ in equation 2.12. A ± 1 g change in mass (based upon weight measurements of eight XDDs) leads to errors of approximately ± 1 m s^{-1} aloft (Fig. 2.12a). If the diameter of the dropsonde varies by 0.0002 m (based upon caliper measurements of three XDDs), errors in vertical velocity of ± 0.14 m s^{-1} are possible aloft (Fig. 2.12b). Variance in the drag coefficient of ± 0.1 leads to errors of ± 2 m s^{-1} aloft (Fig. 2.12c). Lastly, the presence of low-level updrafts and downdrafts affecting the median by ± 0.5 m s^{-1} (close to standard deviation of the sea-level fall speed of 90 XDDs; Fig 2.6b) leads to errors of ± 1.36 m s^{-1} aloft (Fig. 2.12d).

The total standard deviation of the errors can be calculated by:

$$\sigma_t = \sqrt{\sigma_m^2 + \sigma_A^2 + \sigma_{C_d}^2 + \sigma_{w_L}^2} \tag{2.13}$$

The total standard deviation of the errors using the M3 methodology is approximately 0.86 m s^{-1} in the low-levels and 2.39 m s^{-1} in the upper-levels. The two major sources of error are the uncertainty in the value of C_d for each dropsonde and the presence of appreciable low-level vertical velocity. Even in completely quiescent or clear-air conditions where σ_{w_L} is zero, the standard deviation of errors is approximately 0.76 m s^{-1} in the low-levels and 2.11 m s^{-1} in the upper-levels. If the conditions were quiescent and C_d was obtained for individual dropsondes, which is operationally unrealistic, the standard deviation of the errors reduces to 0.24 m s^{-1} in the low-levels and 0.67 m s^{-1} in the upper-levels.

These error estimates agree well with the findings of Stern et al. (2016). A 1 g variation in the RD-94 calculation of vertical velocity leads to an error of approximately ± 0.25 m s^{-1}

at 12 km, which is similar to the XDDs at 12 km (Figs. 2.11, 2.12). The RD-94s and XDDs also have comparable errors in vertical velocity due to ± 0.05 variations in C_d (Figs. 2.11, 2.12). Stern et al. (2016) allow the RD-94 drag area to vary in size more what was done for the XDDs, but only small deviations in the XDDs are expected due to manufacturing differences and ice build-up (Fig. 2.12c). The area used with the RD-94 calculations is the area of the primary parachute, which can deform and change size during descent. Large deformations and pendulum motions of the RD-94s require extensive filtering of vertical velocity. Therefore, errors associated with A are expected to be smaller in the XDDs than the RD-94s using these drag force-based methodologies.

An additional source of error, GPS fall speed error, only matters if the GPS fall speed is used for V_f. The u-blox 6 GPS chip used on the XDDs during TCI is claimed to have a velocity accuracy of 0.1 m s^{-1} at a circular error probability of 50% (U-blox, 2019). However, GPS constellation errors, such as dropsondes switching to different GPS constellations, can cause large, unphysical outliers in the GPS fall speed and dropsonde-derived vertical velocity (e.g., Fig. 2.4). At the surface, the variances in GPS fall speed are small but not negligible (Fig. 2.6b). Figure 2.6b shows that the standard deviation of the last data point fall speed for dropsondes launched outside of convective regions during TCI was approximately 0.9 m s^{-1}. This agrees well with the standard deviation of the near-surface fall speed of XDDs launched in test flights in Black et al. (2017). While the variance and standard deviation of the last data point GPS fall speeds include errors and variances associated with atmospheric variances in each sounding, such as the presence of weak low-level updrafts or downdrafts and variations in dropsonde drag, it is the best estimation of the GPS fall speed variances and errors in the XDDs used during TCI.

Regardless of the dropsonde used, the typical errors for the two drag force methods range from ±1–2 m s^{-1}, which means that drag force-based methods do not work well for, and are not accurate for, weak vertical velocities. This is a major problem for atmospheric studies of weak convection such as orographic forcing (e.g., Wang et al., 2009) or analysis of vertical velocities in TCs (e.g., Black et al., 1996). However, these methods are sufficient in studies focusing on extremely strong convection, where the errors fall below 10% of the desired signal (e.g., Stern et al., 2016). In such situations, the estimated drag force methods like M3 are useful in that no knowledge of the drag coefficient, nor the mass, is required. The only required information for the M3 estimated drag force method is an accurate measure of surface fall speed outside of convective regions and profiles of p and T to altitudes relatively near the surface.

2.5 Proposal and hypothesis

The Reynolds number for the XDDs can be approximated by using equation 2.8 and by assuming that the length scale is the length of the dropsonde (7 in.; Black et al., 2017). This was done for 90 XDDs launched into clear air during TCI (Fig. 2.13). The Reynolds number is a function of fall speed, and thus a function of altitude, but maximizes at approximately 2.8×10^4 (Fig. 2.13). This implies laminar flow for the XDDs (Happel and Brenner, 1965; Incropera et al., 2007). Because of the laminar flow and lack of a parachute, the C_d is not expected to radically change during descent. This does not imply, however, that the C_d is uniform from dropsonde-to-dropsonde or that the C_d is independent of icing. This means that drag force-based methods to calculate vertical velocity for the XDDs are still problematic given the errors described previously.

Given the significant technological and mechanical advancements in the past 50–60 years since the introduction of the pitot-static TAS in dropsondes, the capabilities and accuracy of a dropsonde-derived vertical velocity with a pitot-static TAS should also, hypothetically, improve. It is proposed here to revisit and revise the older pitot-static dropsonde-derived vertical velocity methods by Bushnell et al. (1973) on the XDDs. In this dissertation, an attempt is made to decrease the error in vertical velocity measurements on the XDDs from ±1–2 m s^{-1} using the M3 estimated drag coefficient method to an average of ±0.1 m s^{-1} by using modern pitot-static methods in quiescent conditions. By directly measuring the TAS and using the hydrostatic fall speed as the geometric fall speed, GPS location and fall speed errors, such as in Figure 2.4, will not impact vertical velocity calculations. Further, the vertical velocity calculations will be independent from errors associated with variances in m, C_d, A, and low-level updrafts or downdrafts with the previous drag force methods.

Three variations of the classic pitot-static design were considered and tested: 1) a modified pitot-static (Fig. 2.14a, b); 2) a venturi-static (Fig. 2.15a, b); and, 3) a pitot-venturi (Fig. 2.16a, b). The three designs measure the pressure difference in three different ways across the XDDs as they fall. The modified pitot-static is similar to the traditional pitot-static in that it measures the total pressure through the leading-edge port near the center of the nose, but the static pressure is measured from the side of the dropsonde and is shielded from the ram air pressure caused by descent and updrafts or downdrafts (Fig. 2.14a, b). If the dropsonde is assumed to be a blunt cylinder with a length to diameter ratio of approximately three (Black et al., 2017), a fairly expansive wake is expected to form for flows with $R_e \approx 1\text{x}10^4$ (Fig. 2.17; Higuchi et al., 2006). In this situation, a low pressure is expected to form within the wake. A venturi-static would measure the difference between the static pressure at the side of the dropsonde and the low pressure in the aft of the dropsonde (Fig. 2.15a, b). The pitot-venturi measures the difference between the total pressure at the leading-edge of the dropsonde as it descends and the low pressure at the aft of the dropsonde

(Fig. 2.16a, b). The venturi ports are through the antenna or to one side of the antenna behind the foam body. The benefits and limitations of each design are summarized in Table 2.1. The optimum p_d measurement, however, would likely be from a venturi-static system (Fig. 2.15 a, b) as it would be the least likely to be affected by icing.

Because the typical fall speeds of the XDD range from 0–50 m s^{-1}, with an estimated sea-level fall speed of 18 m s^{-1}, small biases and errors are critical. A $1-2\%$ error, like those described by SpaceAge Control (1998), would lead to vertical velocity errors of 0.2–0.4 m s^{-1} at the surface and 0.5–1 m s^{-1} at 17.5 km for the XDDs. If a specialized small-range, low-differential pressure (low-p_d) sensor, like the DLHR-L05D-E1BD, was used, then relatively large errors associated with low fall speeds decrease (Fig. 2.18). The DLHR-L05D-E1BD sensor is an I2C/Serial Peripheral Interface with digital output (bits) and an overall accuracy of 0.2% (All Sensors, 2019). This would correspond to vertical velocity accuracies of approximately 0.2 m s^{-1} at the surface and 0.5 m s^{-1} aloft. With error compensation and improvement of techniques, it may be possible to further reduce these errors. The sensor is rated for temperatures of -20°C to 85°C (All Sensors, 2019). A table of the specifications for the sensor is provided in Table 2.2. It is expected that differential pressure measurements using the modern DLHR-L05D-E1BD sensor will provide lower clear air dropsonde-derived vertical velocity errors than the Bushnell et al. (1973) study.

The proposed error budget goal is partitioned into two components: 1) ± 0.05 m s^{-1} instrumentation error; and, 2) ± 0.05 m s^{-1} tube/port placement error. The first component comprises of the overall accuracy of the sensor, temperature dependent biases, instrument precision, and input voltage errors. The second component is the error associated with the sensitivity of the p_d measurement to the exact placement of the ports and tubes on the XDDs. The error budget of ± 0.1 m s^{-1} matches the velocity accuracy in the data sheet for the u-blox 6 GPS chip (U-blox, 2019). The proposed error budget does not take into account errors associated with port blockage or icing and is assumed to be at sea-level in relatively quiescent conditions. Vertical velocity errors in strong convection will likely exceed ±0.1 m s^{-1}.

Table 2.1: Analysis of the benefits and limitations of the three p_d configurations.

dP method	Benefits	Limitations
Pitot-static	1)Likely reproducible from drop-to-drop	1) Vulnerable to icing errors; 2) Pitot port blockage; 3) Static needs to bypass circuit board and penetrate side sleeve
Static-venturi	1) Least prone to icing errors	1) Venturi port may be hard to reproduce from drop-to-drop; 2) Venturi port placement harder; 3) Static needs to bypass circuit board and penetrate side sleeve
Pitot-venturi	1)No side port placement issues; 2) No competing issues with dropsonde rotation/angle of attack;	1) Vulnerable to icing errors; 2) Venturi port may be hard to reproduce from drop-to-drop; 3) Pitot port blockage; 4) Venturi port placement harder

Table 2.2: Sensor specifications for the DLHR-L05D-E1BD, adapted from All Sensors (2019). Full scale span (full range of the instrument) is abbreviated as FSS. FSS is the full range of the sensor.

Specification	Value (typical)	Maximum
Operating range	±12.44 hPa	———
Proof pressure	497.7 hPa	———
Burst pressure	746.5 hPa	———
Nominal span	$\pm 0.4 \times 2^{24}$ counts	———
Common mode pressure	———	689.5 hPa
Resolution	16 bit	———
Total Error Band	0.2% FSS	0.75% FSS

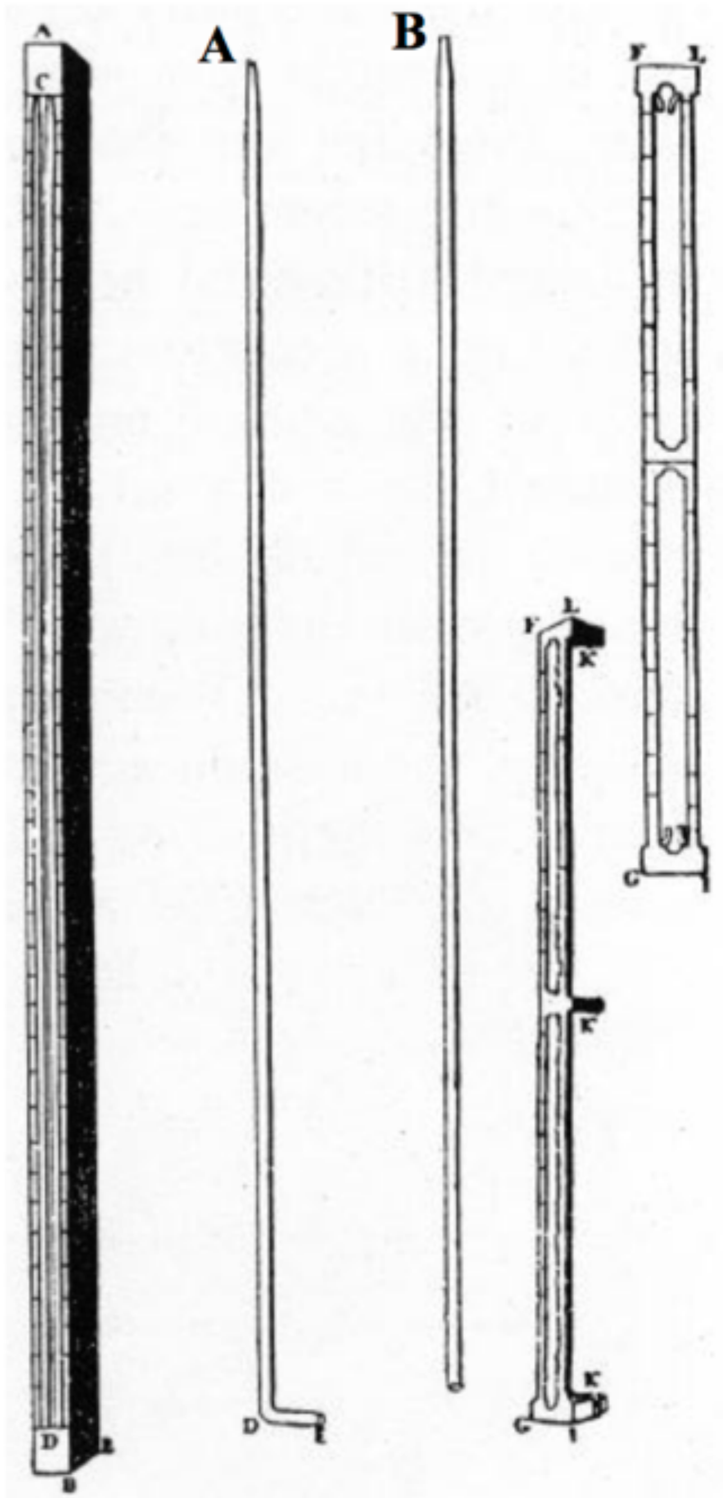

Figure 2.1: Henry Pitots original pitot tube design. The two tubes (labeled A and B) were lowered into the flow and the pressure was recorded as the difference in the water level between the two tubes (Brown, 2003). This figure is adapted from Brown (2003).

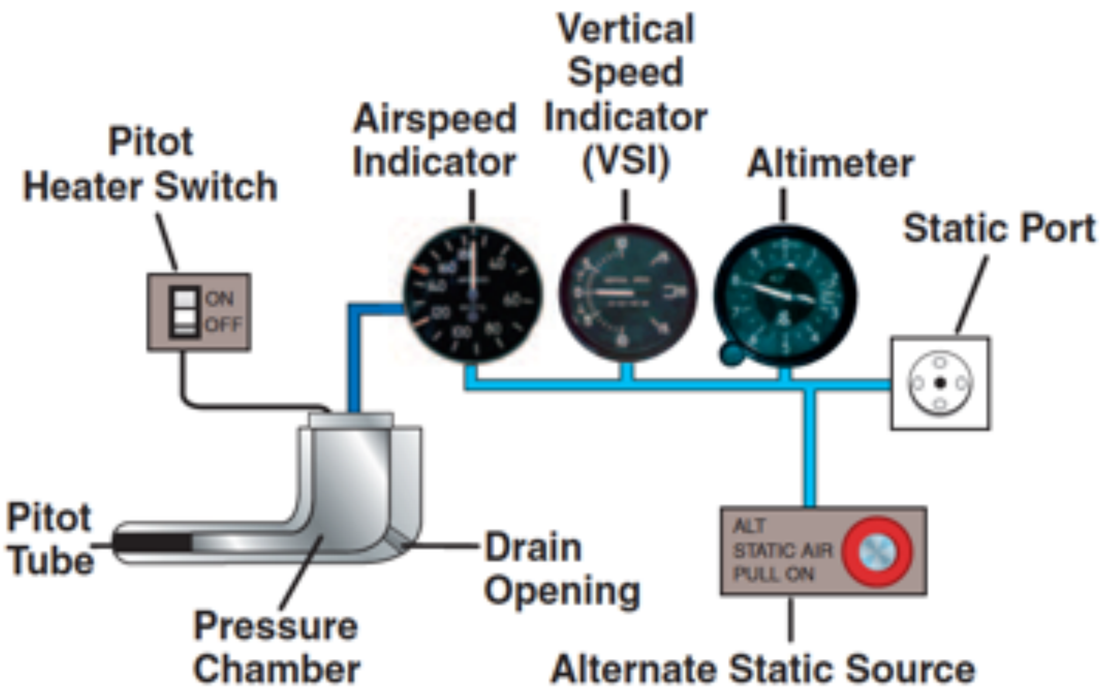

Figure 2.2: Modern pitot-static system and instruments for aircraft use. Figure adapted from Federal Aviation Administration (2016).

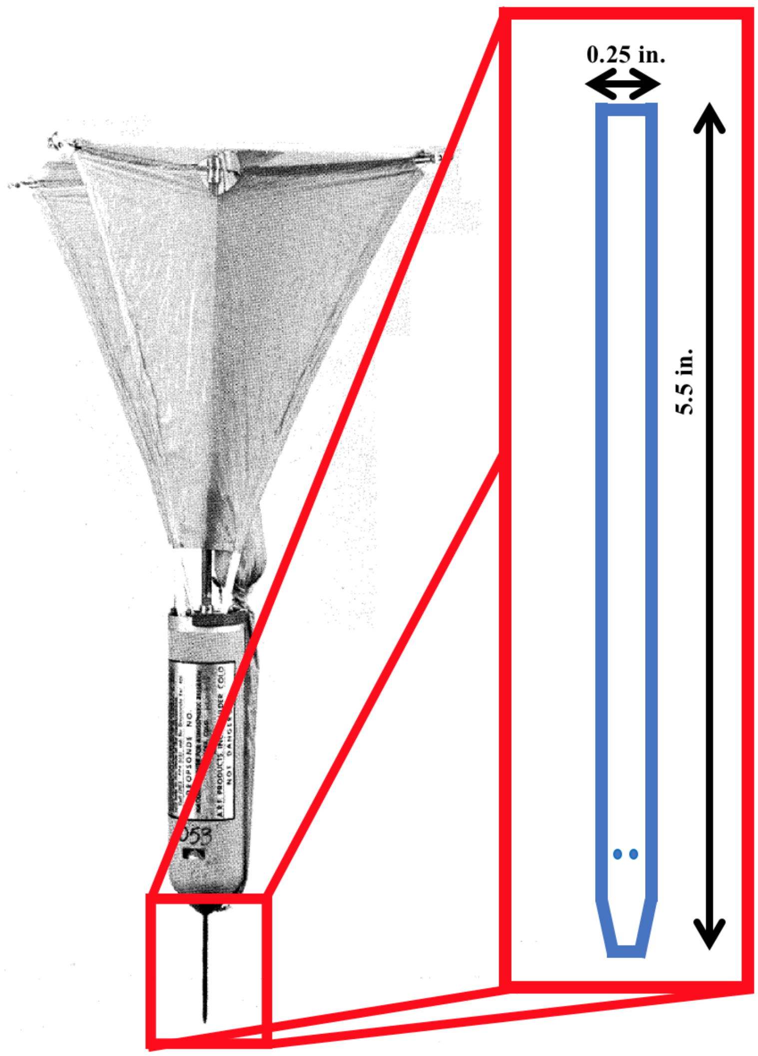

Figure 2.3: ED with a pitot-static probe. A schematic of the pitot-static probe is provided in the inset. Figure adapted from Bushnell et al. (1973).

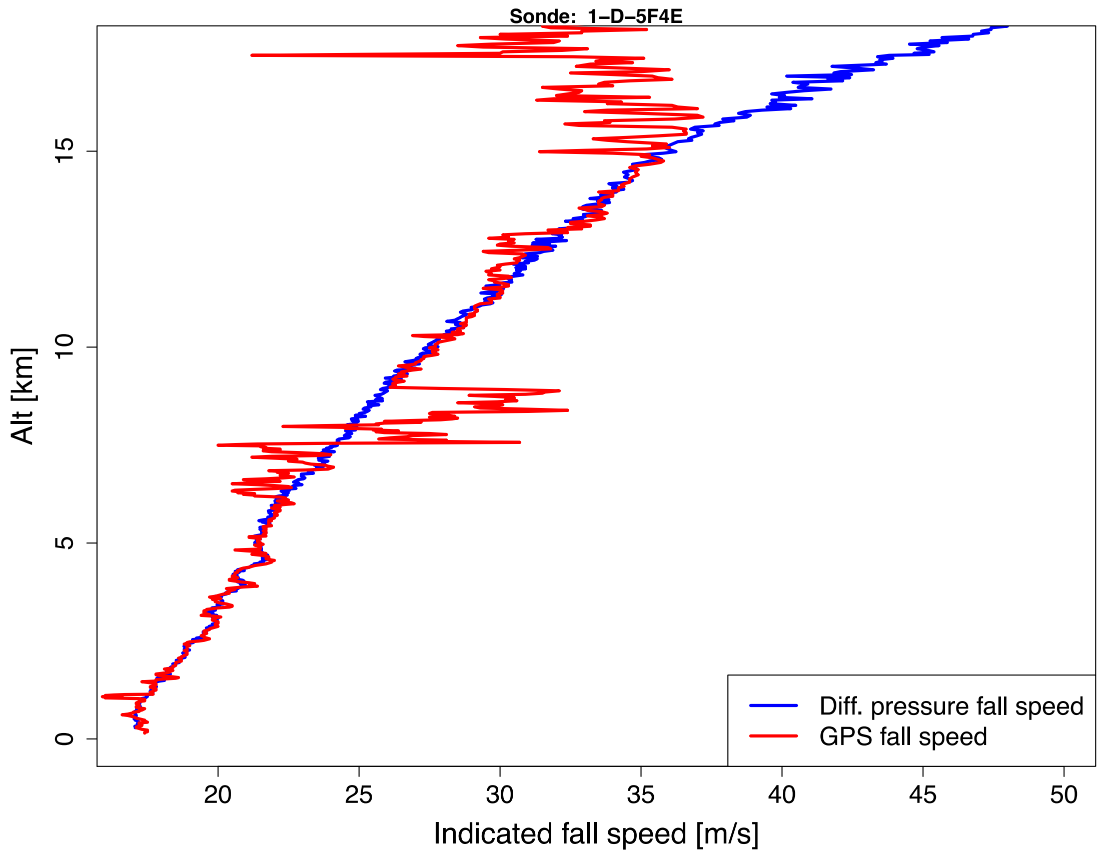

Figure 2.4: Atypical GPS fall speed (red) and hydrostatic or differential pressure indicated fall speed (blue) in m s^{-1} for one dropsonde (1-D-5F4E) launched in Marty on 27 September 2015. From Nelson et al. (2019a). ©American Meteorological Society. Used with permission.

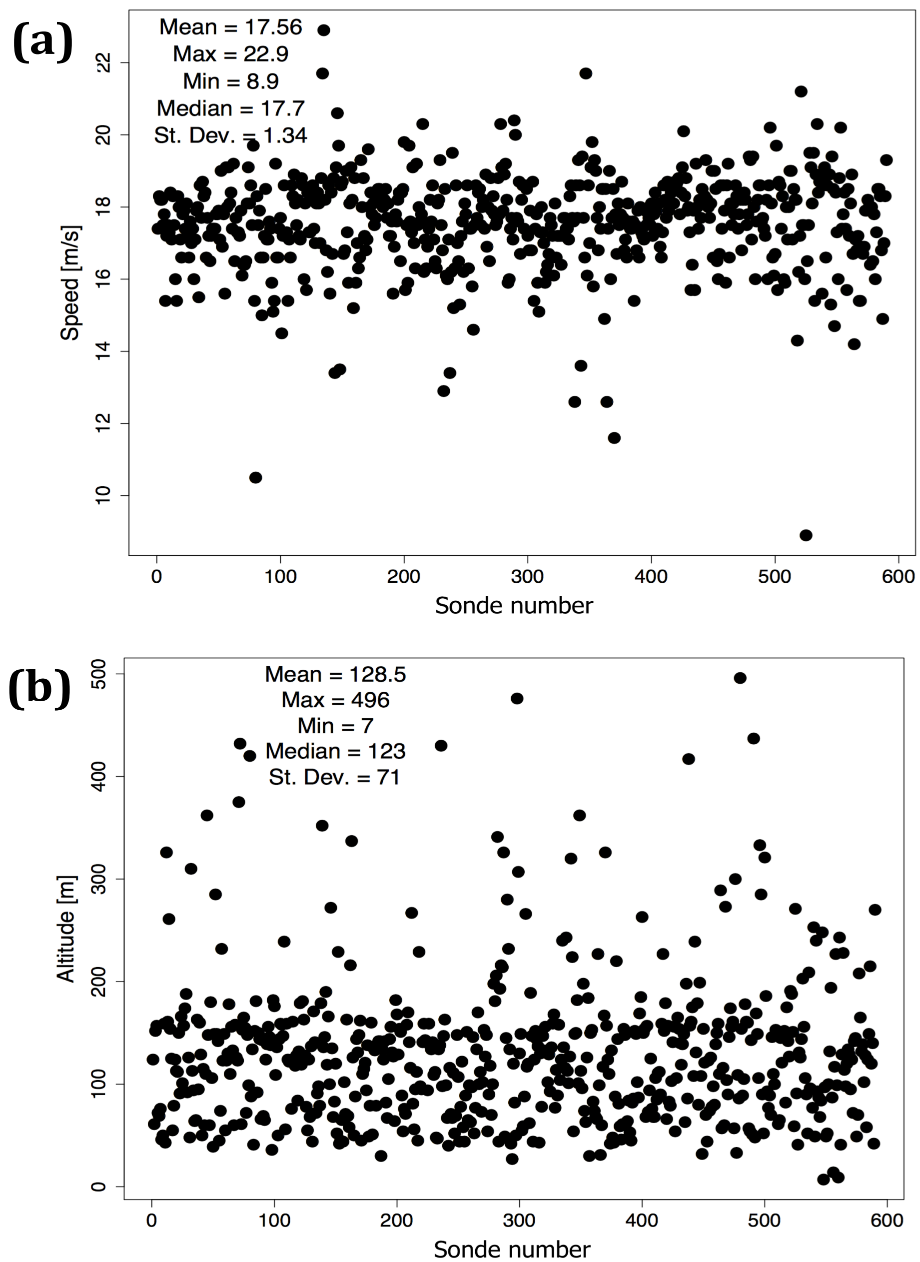

Figure 2.5: Individual last data point fall speeds and altitudes from the data using M1. Panel (a) is the last data point GPS fall speeds of the dropsondes. Panel (b) is the altitude of the last data point in each sounding that reached at least 500 m. Also included are mean, maximum, minimum, median, and standard deviation.

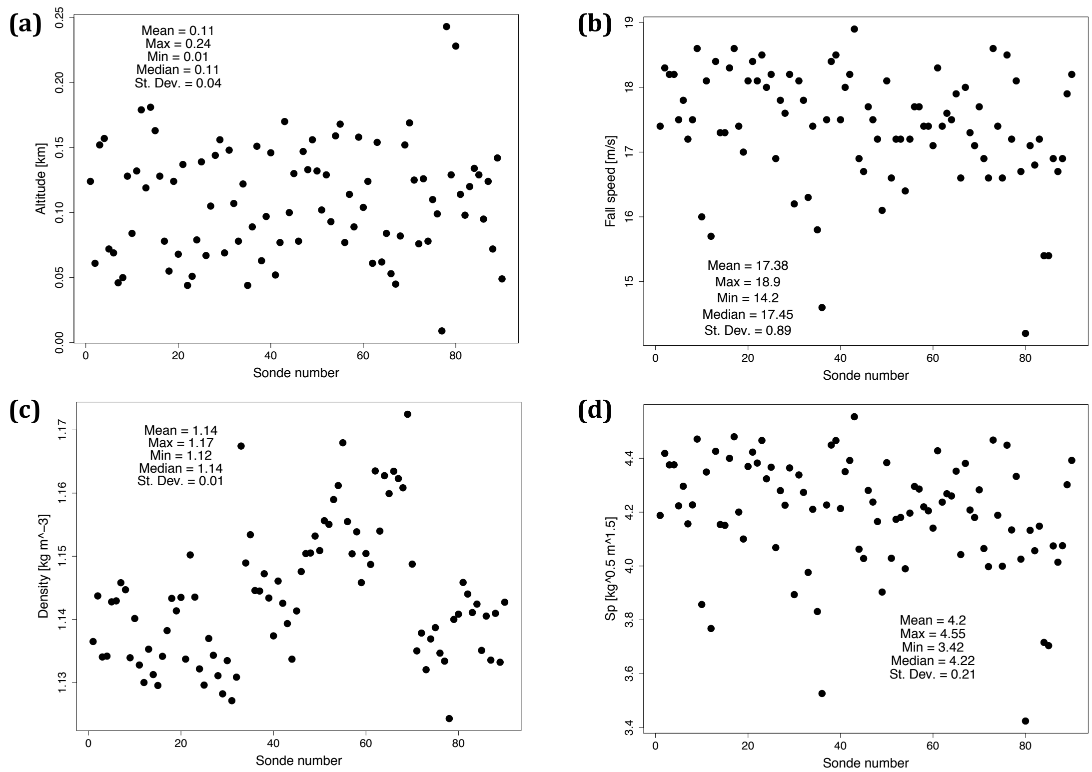

Figure 2.6: Data points outside of convective regions used to derive the median S_p. Panel (a) is the last data point altitude. Panel (b) is the last data point fall speed. Panel (c) is the last data point density. Panel (d) is the S_p for each dropsonde launched outside of convective regions. Also included are mean, maximum, minimum, median, and standard deviation.

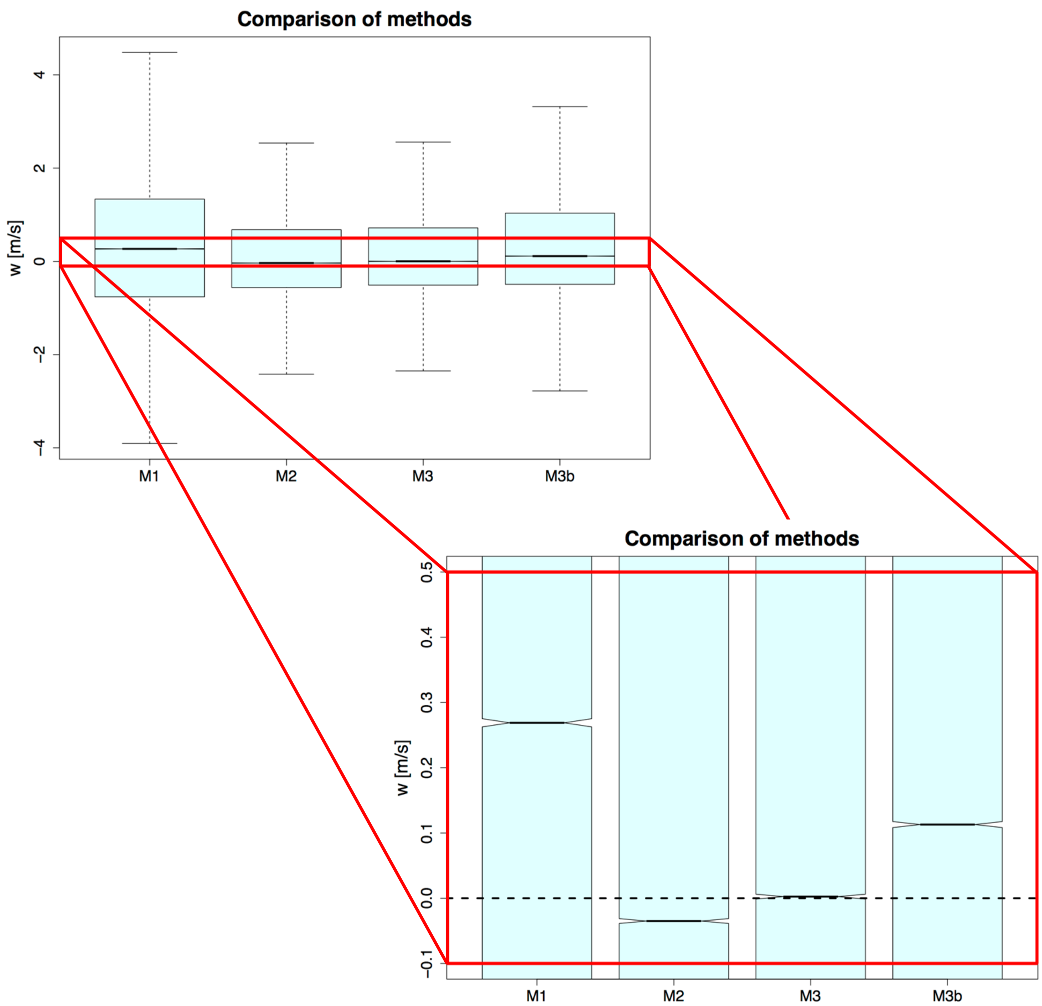

Figure 2.7: Box plot comparisons between M1, M2, M3, and M3b. The inset to the bottom right shows that the notches of the box plots do not overlap, which indicates that the medians are statistically different. From Nelson et al. (2019a). ©American Meteorological Society. Used with permission.

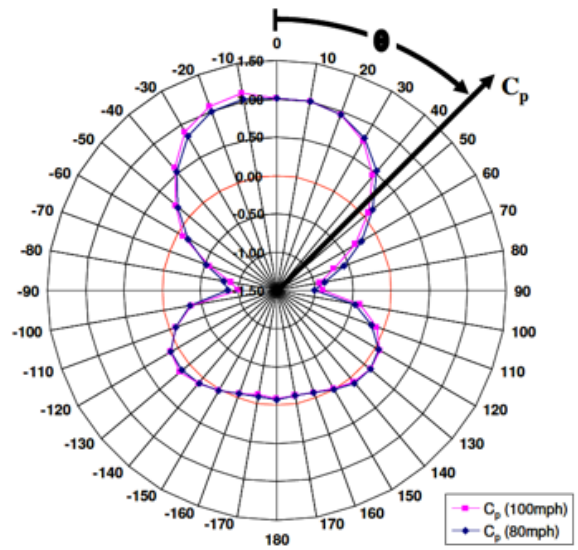

Figure 2.8: Polar plot of the pressure coefficient (C_p) at 10° angle of incidence intervals to the flow, 100 mph (pink) and 80 mph (purple). Figure adapted from Beck et al. (2010).

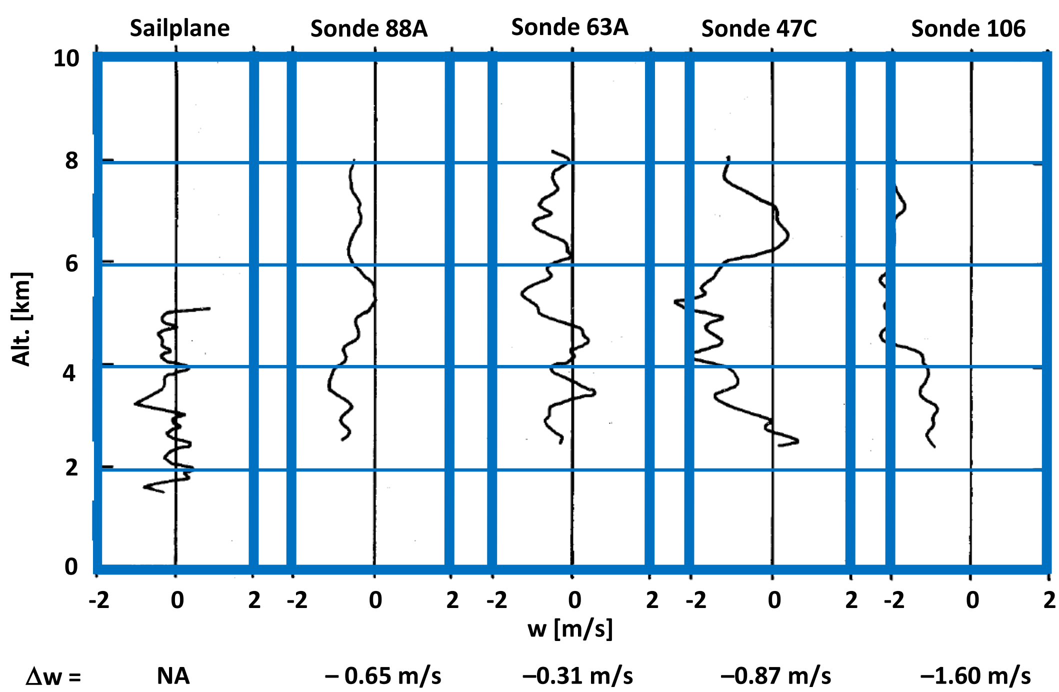

Figure 2.9: Vertical velocity soundings from sailplane and EDs with a pitot-static probe on 21 April 1972. Shown below each ED sounding is the mean difference in vertical velocity from the sailplane observations. Figure adapted from Bushnell et al. (1973).

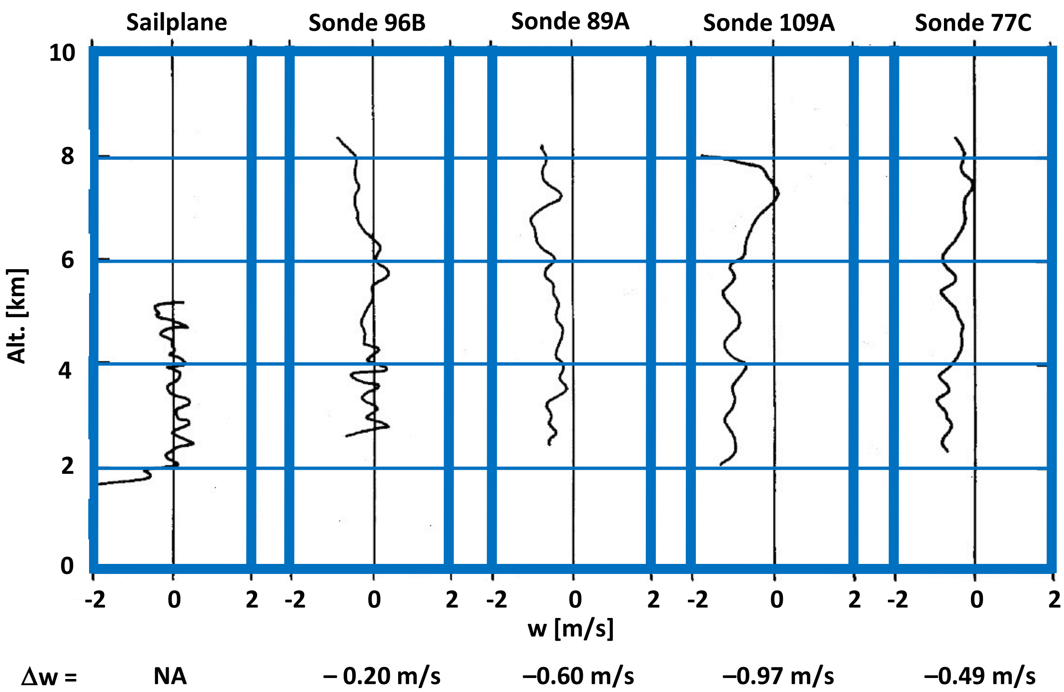

Figure 2.10: Same as Fig. 2.9, but for 25 April 1972.

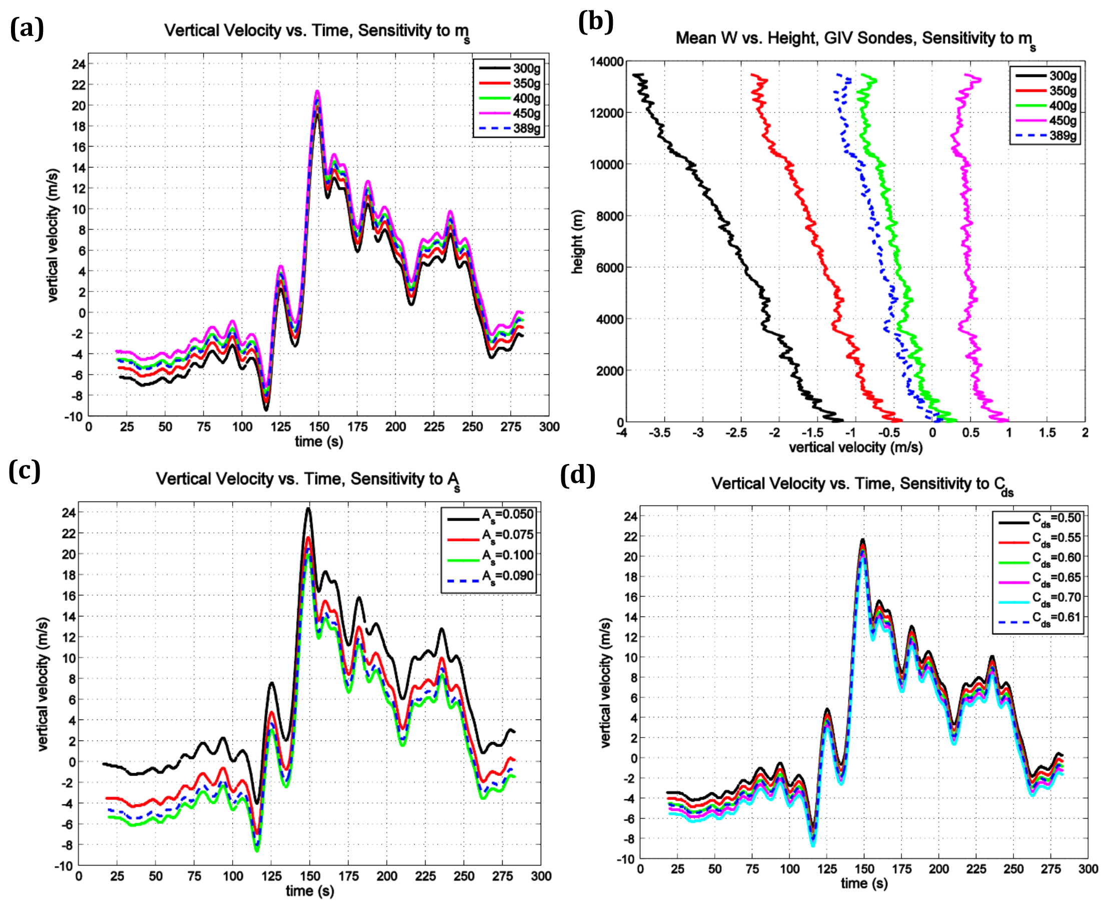

Figure 2.11: Sensitivity of vertical velocity of RD-94s due to changes in mass (m_s) (a, b), area (A_s) (c), and drag coefficient (C_{ds}) (d). Adapted from the appendix of Stern et al. (2016).

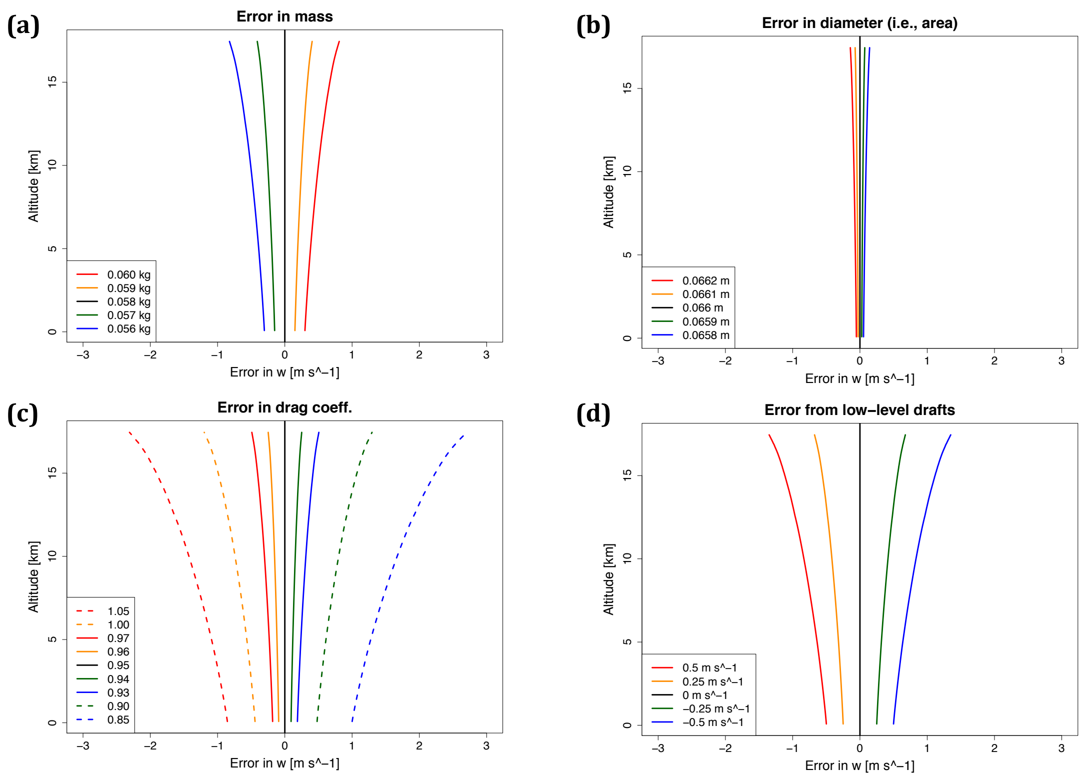

Figure 2.12: Errors in vertical velocity for XDDs given variations of mass (a), diameter/area (b), drag coefficient (c), and low-level updrafts (d), adapted from Nelson et al. (2019a). ©American Meteorological Society. Used with permission.

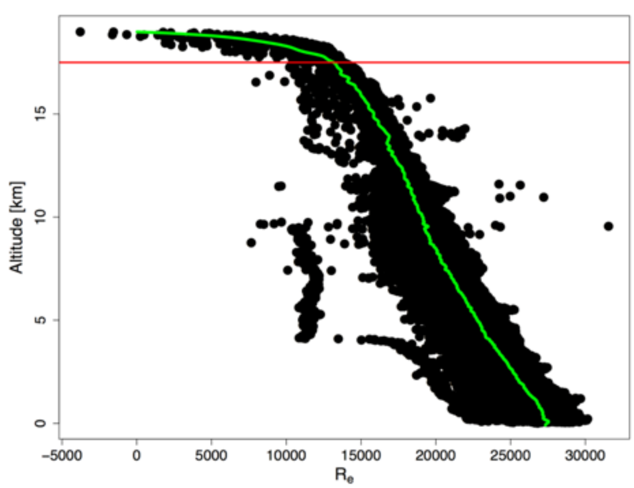

Figure 2.13: Reynolds number (R_e) as a function of altitude for all 90 TCI XDDs launched outside of convective regions. A smoothing spline (green) is used to illustrate the general trend. The 17.5 km altitude cutoff is shown in red.

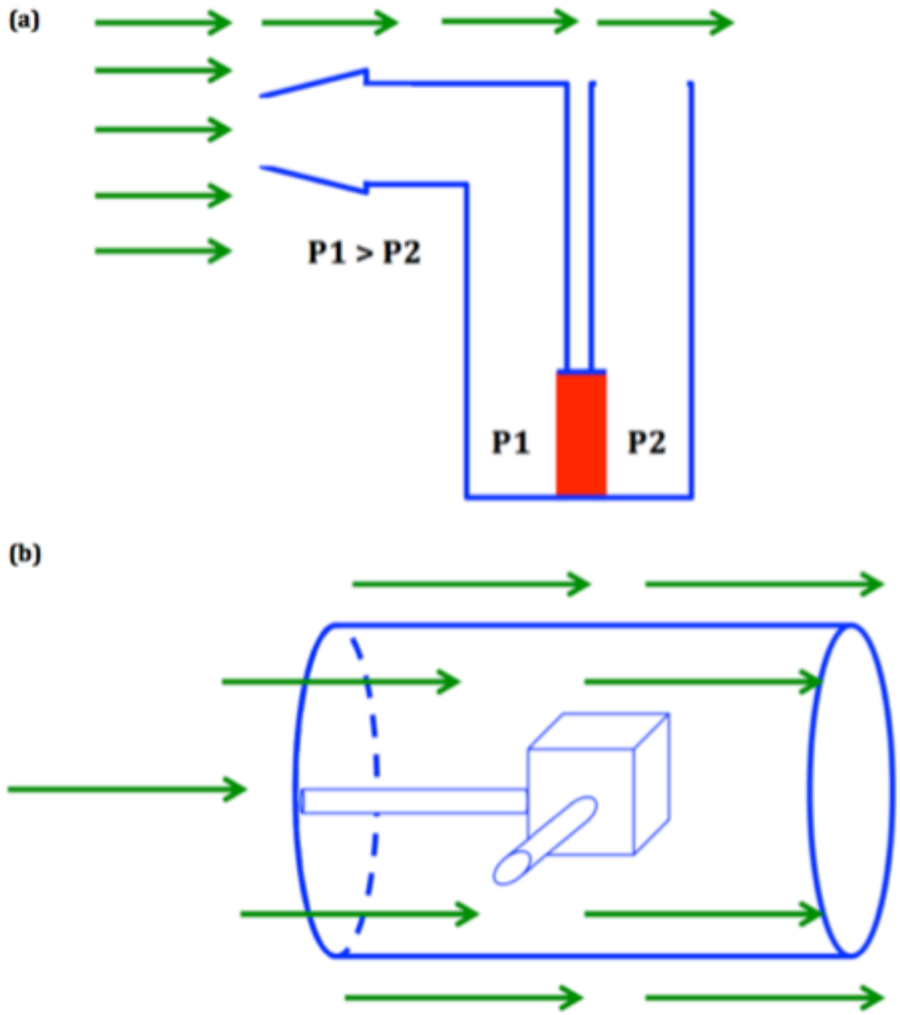

Figure 2.14: Design for a pitot-static system. Panel (a) is a generic schematic, where the pitot pressure (P1) is greater than the static pressure (P2), due to airflow (green arrows). The pressure transducer/membrane is the red square. Panel (b) illustrates a generic layout for a pitot-static system for the XDDs.

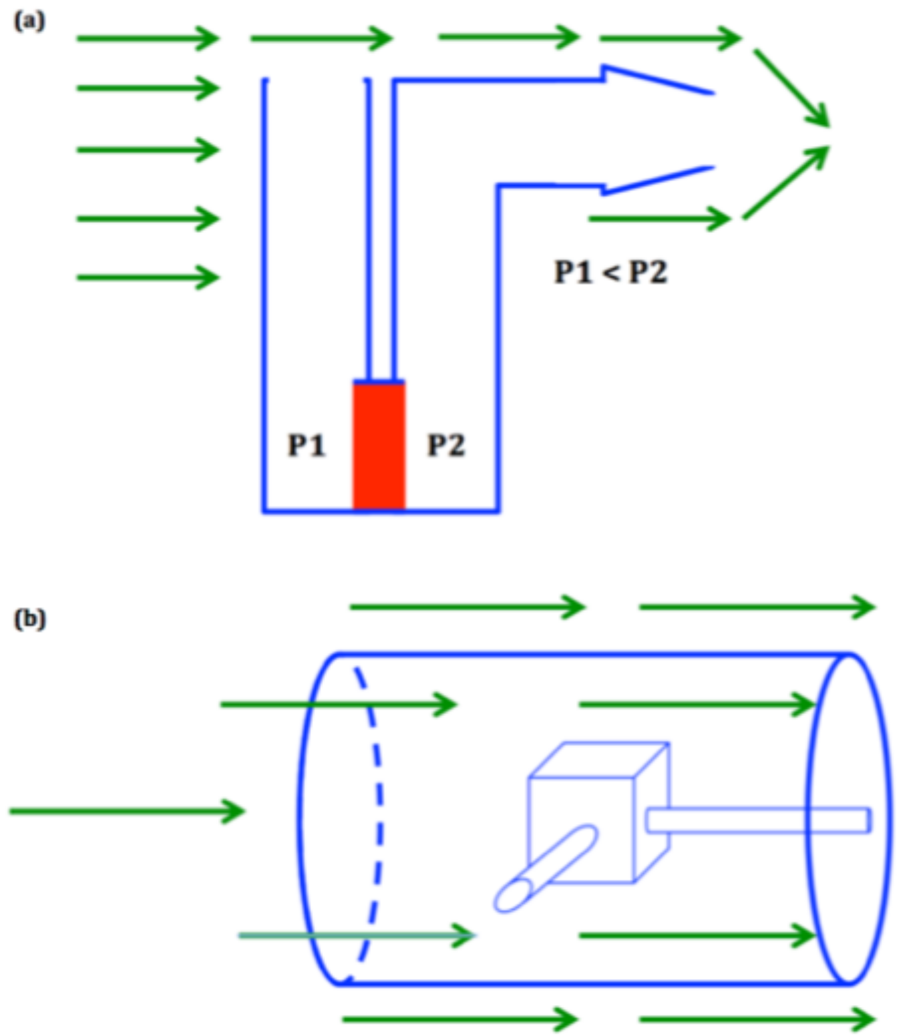

Figure 2.15: Design for a venturi-static system. Panel (a) is a generic schematic, where the static pressure (P1) is less than the venturi pressure (P2), due to airflow (green arrows). The pressure transducer/membrane is the red square. Panel (b) illustrates a generic layout for a venturi-static system for the XDDs.

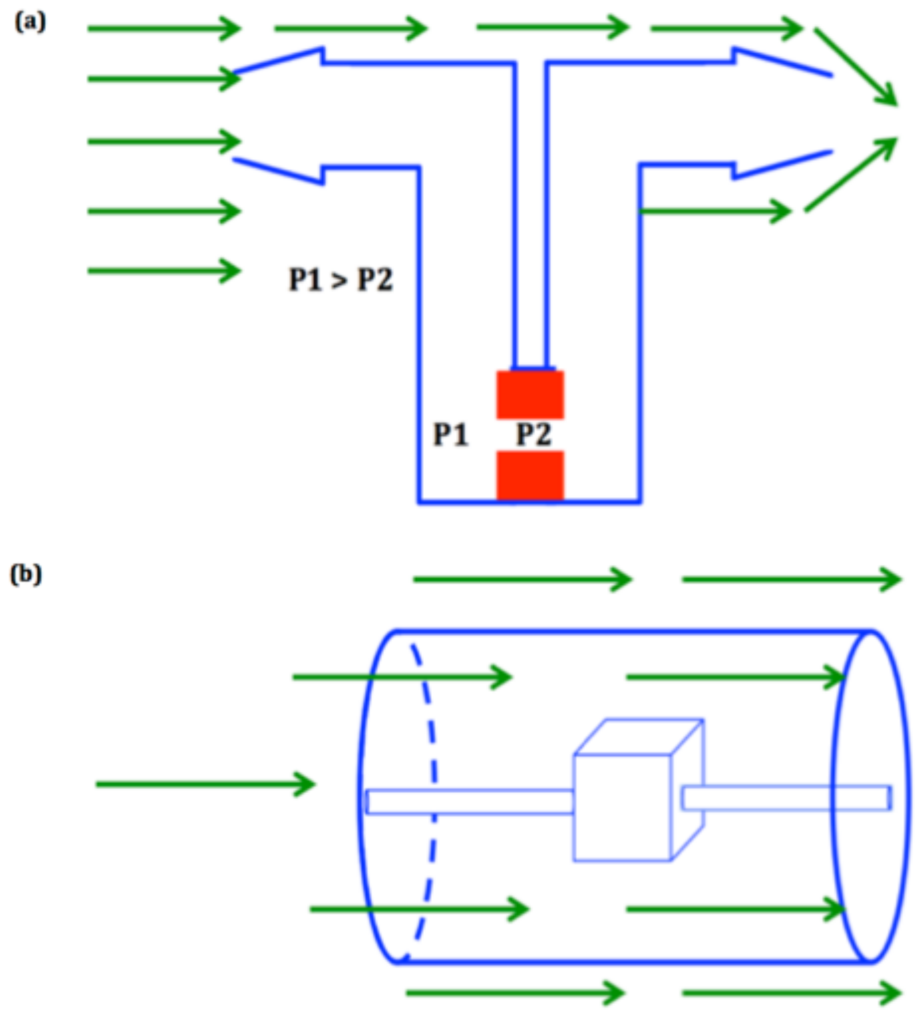

Figure 2.16: Design for a pitot-venturi system. Panel (a) is a generic schematic, where the pitot pressure (P1) is greater than the venturi pressure (P2), due to airflow and the venturi effect (green arrows). The pressure transducer constriction of airflow is the red squares. Panel (b) illustrates a generic layout for a pitot-venturi system for the XDDs.

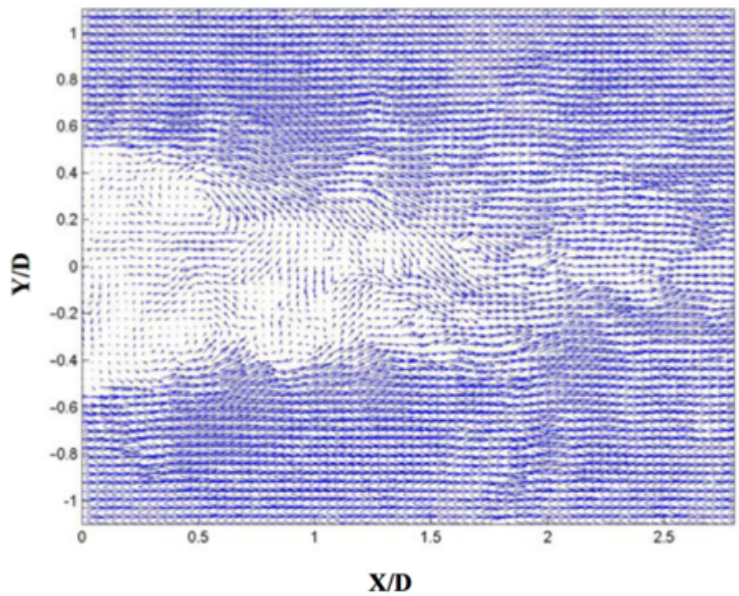

Figure 2.17: Visualization of wake flow behind a cylinder in axial flow with a length to diameter ratio of three. The x-axis and y-axis are normalized by the diameter of the cylinder. Figure is adapted from Higuchi et al. (2006).

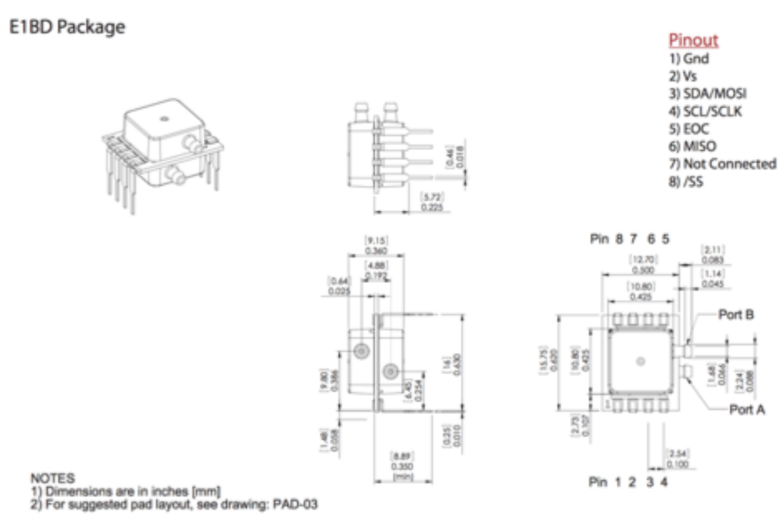

Figure 2.18: Schematic for the DLHR-L05D-E1BD sensor including output/input pins and dimensions. Adapted from All Sensors (2019).

CHAPTER 3

Results from TCI

Out of the 785 total XDDs used in the 2015 TCI experiment, 725 were launched into Marty, Joaquin, and Patricia. This corresponds to 140, 328, and 257 XDDs for each TC, respectively. Marty was sampled as a tropical storm (sustained winds of 26 m s^{-1}) and a Category 1 hurricane (36 m s^{-1}) (Berg, 2016b). Joaquin was sampled as a Category 3 (57 m s^{-1}), Category 4 (67 m s^{-1}), Category 2 (47 m s^{-1}), and Category 1 (39 m s^{-1}) hurricane (Berg, 2016a). Patricia, ultimately, reached a higher peak intensity but was sampled as a tropical depression (15 m s^{-1}), tropical storm (26 m s^{-1}), Category 4 hurricane (59 m s^{-1}), and during rapid weakening from a Category 5 hurricane (92 m s^{-1}) (Kimberlain et al., 2016). Figure 3.1 shows the intensity for each of the three TCs from the National Hurricane Center (NHC) Best Track dataset and the time periods that they were observed during TCI.

Because of the unprecedented sounding spacing, altitude, frequency and the relative dearth of in-situ observations in TCs, this analysis is crucial to the future of dropsonde-derived vertical velocity studies. This analysis also offers a unique opportunity to: 1) document the convective structure of individual TCs from dropsondes alone; 2) study updrafts and downdrafts in unprecedentedly strong TCs like Patricia; 3) evaluate locations where dropsonde-derived vertical velocities and their errors have appreciable impact; 4) evaluate the role of vertical velocity in the calculation of horizontal wind; and, 5) examine the impact of dropsonde spacing on the interpretation of the thermodynamic and kinematic structure and its impact on future dropsonde studies. Collectively, this chapter serves as documentation of the vertical velocities obtained using the M3 methodology discussed previously and further illustrates the importance of accurate vertical velocity measurements from dropsondes.

3.1 Summary of TCI XDD-derived vertical velocities

3.1.1 Introduction

Many studies concluded that deep, strong convection and updrafts are important in the intensification of TCs (e.g., Steranka et al., 1986; Vigh and Schubert, 2009; Rogers et al., 2016), but others argue that it is not (Jiang, 2012; Jiang and Ramirez, 2013). The discrepancies between these studies demonstrate the need for high-quality vertical velocity measurements and further study of TC convection, updrafts, and downdrafts. The examination of updrafts and downdrafts themselves, and their potential impacts on intensity change, in TCs is important. For example, deep-layer shear, and the subsequent asymmetric convection, can lead to short-term TC intensification with weakening thereafter (Kaplan and DeMaria, 2003; DeMaria et al., 2012). If there is sufficient energy provided to the TC from the ocean, the cyclone can resist the weakening effects of shear and maintain its strength or intensify (e.g., Black et al., 2002). As strong updrafts are often located near the radius of maximum wind (RMW; Black et al., 1994; Rogers et al., 2013; Stern et al., 2016) or just inside the RMW (Jorgensen et al., 1985; Marks et al., 2008), they can also be associated with intensification following RMW contraction (Stern et al., 2015).

Another unresolved TC intensification processes is the role of small-scale vorticity and collocated updrafts in the vicinity of the eyewall. As described by Persing and Montgomery (2003), TCs can reach intensities higher than their maximum potential intensity (MPI) by mixing high-entropy air from the eye into the eyewall through vorticity maxima at the eye–eyewall interface. This process has been dubbed “superintensity” and has been supported observationally by the analysis of Montgomery et al. (2006). Bryan and Rotunno (2009), however, have shown that this process is inconsequential for a TC to reach its MPI. Regardless, intensity changes below the MPI of a TC due to eye–eyewall mixing ("sub-MPI intensity changes"; Eastin et al., 2005c) remain plausible and are supported by the findings of Dolling and Barnes (2012).

Updrafts in excess of 10 m s^{-1} have been observed occasionally in TCs below a height of 6 km (Jorgensen et al., 1985; Aberson et al., 2006; Stern and Aberson, 2006; Stern et al., 2016). Stern et al. (2016) and Stern and Aberson (2006) found that extreme updrafts ($\geq$ 10 m s^{-1}) observed below 3 km were often collocated with low-level, extreme horizontal wind maxima ($\geq$ 90 m s^{-1}) in major hurricanes. Other low-altitude ($<$ 6 km) studies found that updraft strength increases with altitude (Jorgensen et al., 1985) and is strongest within the eyewall (Stern and Aberson, 2006; Aberson et al., 2006). In many cases, the updrafts are a part of the asymmetric component of eyewall convection on top of the symmetric component (Eastin et al., 2005a,c). Jorgensen et al. (1985) found that, between 1–6 km, the top 10% of eyewall updraft cores are larger and stronger than rainband updrafts. Stern et al. (2016) and Stern and Aberson (2006) also found that updrafts maximized in strength in the downshear-left quadrant in the core for soundings below 3 km.

Other high-altitude studies (0–16 km) using flight-level and Doppler radar data have also occasionally documented updrafts in excess of 10 m s^{-1} in TCs (Black et al., 1994, 1996, 2002; Marks et al., 2008; Heymsfield et al., 2010). These extremely strong vertical motions occur primarily in the upper-levels, above 10 km (Black et al., 1996; Guimond et al., 2010), which is not surprising as vertical velocity tends to maximize aloft between 10 and 15 km (Black et al., 2002; Heymsfield et al., 2010; Reasor et al., 2013; DeHart et al., 2014). Black et al. (1994) found strong updrafts widely scattered in the mid- and lower-levels (2–6 km) of

Hurricane Emily (1987), with small pockets of strong updrafts aloft (> 6 km). Black et al. (1996) observed a relative minimum at 5–6 km in mean vertical velocity profiles. DeHart et al. (2014) found that strong updrafts in the core tended to occur aloft and primarily in the downshear-left quadrant. Downdrafts tended to occur aloft and in the midlevels in the upshear-left quadrant.

The most accepted, and supported, theory for updraft azimuthal and altitudinal distributions is that updrafts tend to initiate at low levels in the downshear-right quadrant and rise helically to their maximum intensity aloft in the downshear-left quadrant, with downdrafts dominating the upshear quadrants, specifically the upshear-left quadrant (Franklin et al., 1993; Black et al., 2002; DeHart et al., 2014). Black et al. (2002), Zipser (2003), Guimond et al. (2010), Reasor et al. (2013), and DeHart et al. (2014) all show that updrafts maximize in strength in the downshear quadrants of the TC, especially the downshear-left quadrant in the core.

To date, radar, dropsonde, and flight-level data have found very few strong updrafts or downdrafts outside of 100 km from the storm center (e.g., Black et al., 1996), despite large amounts of lightning occurring in this region (Corbosiero and Molinari, 2002, 2003). This apparent discrepancy may be a result of limited samples at large radii, research and reconnaissance flights avoiding strong convection for safety, or relatively large radar volumes that cannot detect small scale convective features. While the eyewall embodies the primary ascending branch of the secondary circulation (Shapiro and Willoughby, 1982), convection outside of the eyewall can be excited by vortex Rossby waves (Black et al., 2002; Corbosiero et al., 2006) or consist of convective clouds stretched and deformed into intense banded structures (Moon and Nolan, 2015).

The most recent work on dropsonde-observed updrafts in TCs, Stern et al. (2016), had information for the radial, azimuthal, and altitudinal variances of updrafts in the lowest 2–3 km and examined updrafts that exceeded 10 m s^{-1}. The azimuthal, radial, and altitudinal XDD-derived vertical velocity distributions below 17.5 km from TCI flights into hurricanes Marty, Joaquin, and Patricia using the HDSS and XDDs (Doyle et al., 2017) were examined through the use of median vertical velocity profiles and contoured frequency diagrams. Bootstrap median significance tests were also conducted to examine statistical differences in the medians of positive and negative vertical velocities within specific sections of the TCs and are included in Appendix B. Basic characteristics of the observed updrafts and downdrafts from TCI were also examined.

3.1.2 Methods

The dropsonde-derived vertical velocities were calculated using the M3 methodology (equations 2.9, 2.10, 2.12), with the hydrostatic, or differential pressure, fall speed (equation 2.11) as V_f. The differential pressure fall speed was used in lieu of the GPS fall speed due to large, unrealistic discrepancies between the two fall speeds in the midlevels and aloft (e.g., Fig. 2.4) and because the accuracy of the pressure is better than GPS height derived fall speeds (Stern et al., 2016). This also matches the methodologies of Wang et al. (2015) and Stern et al. (2016). The differential pressure indicated fall speed was computed with a 15-point centered difference, after removing missing data, rather than from the Atmospheric Sounding Processing Environment (ASPEN) software (Bell et al., 2016), corresponding to a vertical depth of 750 m at 17.5 km and 270 m near sea-level, assuming there were no missing data points.

Dropsondes that were assumed to be launched outside of convective regions (see section 2.3) were removed from the dataset. An example of IR brightness temperatures on 23

October in Patricia, with dropsondes launched outside of convection indicated by red circles, is provided in Figure 3.2. Soundings were also removed from the dataset if their last observed data point was at a GPS altitude greater than 500 m. The rationale for such a restriction was to ensure that the dropsondes recorded data in the low levels of TCs, comparable to Stern et al. (2016). The data were also restricted to only include data points below an altitude of 17.5 km. While the WB-57 was flown at an altitude of approximately 19 km, most dropsondes launched outside of convective regions take approximately 25 s to reach a stable fall speed after launch, a distance of 0.5 km to 1 km. The altitude restriction of 17.5 km was chosen to prevent erroneous data and provide an approximate 500 m buffer. Data were also restricted to within an RMW normalized radius, R^*, of 10 to eliminate data points that were well removed from the TC. The distances that correspond to $10R^*$ for each day are provided in Table 3.1.

The XDD-derived vertical velocities were then filtered using a nine-point binomial smoother. This corresponds to altitudinal depths of 162–450 m assuming no missing data. Spurious data points outside of two standard deviations of the local mean in the nine-point filter were removed after smoothing was completed. The total dataset was reduced to 276,515 data points and 437 soundings after all of the data restriction and removal were conducted.

Individual data points are used to create and analyze the vertical velocity frequency distributions, but were not considered to be independent updrafts or downdrafts. Black et al. (1996) defined updrafts and downdrafts using Doppler radar data as consecutive, continuous vertical velocities exceeding $|1.5 \text{ m s}^{-1}|$ with at least one data point exceeding $|3 \text{ m s}^{-1}|$. The $|1.5 \text{ m s}^{-1}|$ threshold was chosen as it was outside the limits of uncertainty in the vertical incidence Doppler velocity and the $|3 \text{ m s}^{-1}|$ threshold was chosen as it was one standard deviation of hydrometeor fall speed above the limit of uncertainty (Black et al., 1996). Updrafts and downdrafts were similarly defined as consecutive, continuous vertical velocities exceeding |2 m s^{-1}| (limit of uncertainty, see section 2.4) with at least one data point exceeding |4 m s^{-1}| (one standard deviation of the vertical velocity above the limit of uncertainty).

3.1.2.1 Calculation of storm center and RMW

The storm center was calculated using an iterative method similar to the methodologies of Creasey and Elsberry (2017) and Willoughby and Chemlow (1982) to find an estimated XDD-derived zero-wind center (ZWC). The dropsonde horizontal winds were put into a storm-relative framework by subtracting the u and v components of TC motion from the horizontal wind components. The TC motion was calculated by taking six-hour centered differences about the closest (in time) Automated Tropical Cyclone Forecast (AFTC) Best Track center from NHC.

A single ZWC was found by constructing orthogonal lines to the storm-motion-relative horizontal wind vectors at all altitudes. Weighted means of the intersecting independent (x, y) coordinates from pairs of observations yield a single ZWC estimate and corresponding time for the depth of the troposphere. The weighting function was:

$$W = \frac{V_t}{(r^2)}, \tag{3.1}$$

where W is the weight for a given intersection, V_t is the mean storm-motion-relative horizontal wind speed for any observation pair, and r is the mean radial distance of the observation pairs to the previous TC center estimate at the time of the observations. The initial ZWC estimate was taken to be the NHC Best Track center, linearly interpolated to the minute. As a consequence of the weighting-function dependence on the ZWC estimate, equation 3.1

must be iterated to convergence. Iteration was done until the ZWC latitude and longitude converged on a single ZWC solution within 0.001° (approximately 100 m). All solutions converged within 18 iterations. The final ZWC is a single ZWC representative of the time of the observation with the highest weight. The final ZWC was also linearly interpolated to each minute of the observation period.

Rather than the traditional flight-level RMW, an estimated radius of maximum horizontal wind speed below an altitude of 2 km was calculated from the XDD horizontal wind data. The XDD-derived RMW was obtained by examining the strongest 99.98% of horizontal winds below 2 km and within a 100 km radius of the TC center. The RMW was approximated to be the mean radial distance of these relatively fast wind data points, rather than a single data point maximum. This averaging was done because a single data point may be unrepresentative of the true horizontal wind field of the TC, may be artificially strong due to turbulence or noise, or may not be appreciably different than other horizontal wind measurements at other radii. The 99.98% percentile was chosen iteratively to exclude secondary wind maxima within 100 km of the centers of the three TCs. The number of data points used to derive the RMW ranged from one to eight for each observation day, with most days having greater than five data points, corresponding to one to three soundings for each observation day with most days having only one RMW sounding.

An RMW was also calculated from overpasses of the Hurricane Imaging Radiometer (HIRAD; Cecil et al., 2016) as the radius with the strongest observed wind speed. For the HIRAD RMWs, the TC center was taken to be the ZWC linearly interpolated to match the approximate center crossing, except for Joaquin. The ZWCs for Joaquin in this section, and in Creasey and Elsberry (2017), differ from the HIRAD estimated center by approximately 5–7 km, potentially due to tilt of the TC. To alleviate this issue, the estimated HIRAD centers noted in Creasey and Elsberry (2017) were used to derive the HIRAD RMWs for Joaquin. Throughout the rest of this chapter, the RMWs used are the closest RMWs (derived from both the XDD data and the HIRAD data) to the Best Track dataset.

The well-documented, high-resolution, flight-level RMWs and Hurricane Research Division (HRD) centers were not used, because the flight-level data were rarely coincident with the TCI missions and HRD centers were not available for three of the ten observation days. Comparisons of the flight-level RMWs and HRD centers to the RMWs and ZWCs used in this chapter is provided in Appendix C, but the centers agree within a mean of approximately 17 km, the RMWs agree within a mean of 8–9 km, and the use of the flight-level RMWs and HRD centers do not produce statistically different results for the seven days of coverage.

3.1.2.2 Vertical wind shear

The 1800 UTC environmental shear was obtained from the Statistical Hurricane Intensity Prediction Scheme (SHIPS) dataset (DeMaria and Kaplan, 1994), as all flights were conducted near 1800 UTC. Data points were then analyzed in a shear-relative framework. Here, shear is defined conventionally (e.g., DeMaria and Kaplan, 1994) as the 850–200-hPa magnitude and direction with the vortex removed, and averaged from 0–500 km relative to the 850-hPa vortex center.

3.1.3 Results

Summarized in Table 3.1 is the number of viable dropsondes for each day in the full dataset. Also given are storm diagnostics including shear and intensity from the Best Track dataset. As can be seen in Table 3.1, the dataset contained a strongly-sheared case (Marty), a moderately-sheared case (Joaquin), and a weakly-sheared case (Patricia). Joaquin was an

Atlantic hurricane, while Marty and Patricia were in the eastern North Pacific. Most of the observation periods had a component of westerly shear and only Patricia on 21 October had easterly shear. It is also evident that the number of dropsondes after data exclusion was distributed evenly from day-to-day, except for 20 and 23 October.

Figure 3.3 shows the individual vertical velocity data points in a shear-relative framework within 10R* and 3R*. The downshear-right (DR) quadrant had the fewest observations: only 20% of the total vertical velocity data points. The upshear-right (UR) and upshear-left (UL) quadrants contained almost half of the data with 26% and 24% of the vertical velocity data points, respectively. The downshear-left (DL) contained 30%. Even though the majority of observations were outside of the RMW (approximately 80%), the area of the TC within the RMW had the highest number of data points per unit area, approximately 50 times more data points per unit area than outer radii (outside of 3R*). The area within 3R* is defined as the core following Rogers et al. (2013). Approximately 49% of the data was inside of the core.

3.1.3.1 Vertical profiles of vertical velocity

The mean vertical velocity values for the cores and outside of the cores of the three TCs agree well with the mean Doppler-derived vertical velocities for the eyewall and stratiform regions examined by Black et al. (1996) (Table 3.2). Mean, median, and standard deviation profiles of vertical velocity for all of the data, within the core, and outside of the core are provided in Figure 3.4. The mean profiles in vertical velocity for data inside and outside of the core also agree well with the Doppler vertical velocity profiles observed for the eyewall and stratiform regions in Black et al. (1996).

The median vertical velocity profiles were weaker than the mean vertical velocity profiles, but similar structures exist (Fig. 3.4a, b). The strongest vertical velocities were found aloft and within the core in both profiles (Fig. 3.4a, b), in agreement with the Doppler profiles observed by Black et al. (1996) despite XDD-derived vertical velocity errors increasing with altitude (section 2.4). Vertical velocities were positive for much of the depth of the troposphere, but some negative vertical velocities were found below 5 km in the mean profile for data outside of the core (Fig. 3.4a), below 10 km in the median profile for data outside of the core (Fig. 3.4b), and below 5 km in the median profile for data within the core (Fig. 3.4b).

There was a notable peak in mean vertical velocity strength and standard deviation within the core just above the approximate freezing level at 5–6 km (Fig. 3.4a, c). It is not known if this spike is physically significant (e.g., Black et al., 1996; Heymsfield et al., 2010) or instrumentation errors due to icing. Regardless, the standard deviation of the vertical velocity was largest within the core, but fairly constant for data outside the core below 10 km (Fig. 3.4c).

Figures 3.5–3.8 show median vertical velocity profiles both inside (red) and outside (blue) of the core and within each shear-relative quadrant for Marty, Joaquin, Patricia, and for the total dataset. The approximate number of soundings within the core and outside of the core in each quadrant are also provided. These numbers are approximate because some soundings crossed quadrant boundaries. In those situations, the sounding was classified in the quadrant where it had the most data points. Statistical differences or statistical significances of the vertical velocity strength cannot be inferred directly from the median profiles, but they do agree well with bootstrap analysis and significance tests of the median vertical velocities (see Appendix B). Mean profiles (not shown) show similar results as the median profiles.

Marty had large amplitude and noisy median vertical velocity profiles within the core in the DL quadrant and outside of the core in the DR quadrant (Fig. 3.5). This is likely a result of vertical variations in the vertical velocity data and a lack of samples (nine soundings and one sounding, respectively). The upshear profiles within the core and outside of the core are consistent and similar to each other, with the weakest median vertical velocity profiles in the UL quadrant (Fig. 3.5). Joaquin had stronger and more positive median vertical velocity profiles in the DL and UR quadrants within the core above 6 km, and strong low-level positive vertical velocities in the left-of-shear quadrants within the core, especially the UL quadrant (Fig. 3.6). Patricia had strong upper-level positive vertical velocities in the DR quadrant, while the median vertical velocity profiles in the UR and DL quadrants were primarily weak and negative (Fig. 3.7). Similar to Marty, Patricia had a noisy vertical velocity profile within the core in the UL quadrant (Fig. 3.7), caused by three soundings near the eye that had strong variations in vertical velocity about zero. The combined dataset features positive upper-level vertical velocities above 7.5 km in the DL quadrant and negative vertical velocities below; positive vertical velocities below 13 km within the core in the DR quadrant; negative vertical velocities below 13 km outside of the core in the DR quadrant; and, generally, weaker median vertical velocity profiles in the upshear quadrants (Fig. 3.8).

3.1.3.2 Contoured frequency diagrams

Contoured frequency diagrams with respect to radius (CFRD), shear-relative (SR) azimuth (CFAzD), and altitude (CFAD) are used to examine the XDD-derived vertical velocity distributions from TCI (Figs. 3.9–3.11). The contoured frequency plots were created for each TC as well as for the total dataset, with an altitudinal bin size of 250 m, a radial bin size of 0.5R*, and an azimuthal bin size of 10°. The bin sizes were chosen iteratively and subjectively. The vertical velocities were binned every 1 m s^{-1}. Due to the shear-relative and radial biases in sampling, the contoured frequency plots are displayed as contoured percent diagrams, with a logarithmic scale. All percentages within any given bin (radial, azimuth, or altitudinal) sum to 100%. For reference, black horizontal lines in the contoured frequency diagrams denote the vertical velocity thresholds used to define updrafts and downdrafts (|2 m s^{-1}| and |4 m s^{-1}|).

The peak vertical velocity strength generally decreased with increasing radius, and the radial distribution shows that positive vertical velocities more frequently exceeded the updraft thresholds than negative vertical velocities for the downdraft thresholds (Fig. 3.9d). The decrease in vertical velocity strength with increasing radius was not as prominent in Marty (Fig. 3.9a) as it was in Joaquin and Patricia (Fig. 3.9b, c). It should be noted, however, that negative vertical velocity magnitudes were much weaker than positive vertical velocity magnitudes, especially in Patricia (Fig. 3.9c) and exhibited less of a decrease in strength with increasing radius. Joaquin and Patricia had similar vertical velocity frequency distributions radially, especially for positive vertical velocities (Fig. 3.9b, c). Both TCs also had vertical velocity data points that exceeded 10 m s^{-1}, which occurred at the RMW in Patricia and at approximately 3.5R* in Joaquin (not shown in the CFRDs).

For all storms and all radii (Fig. 3.10d), there was little azimuthal variation in the observed vertical velocity distribution, but the strongest vertical velocities were primarily observed in the right-of-shear quadrants. The lack of azimuthal variation in the vertical velocity distribution could be attributed to the relatively small sample size of three TCs or the asymmetric sampling during TCI (Fig. 3.3). The CFAzD for Marty (Fig. 3.10a) shows little azimuthal variation in the strongest negative vertical velocities, with most of the variation in the distribution occurring within the vertical velocity uncertainty bounds. The strongest positive vertical velocities in the distribution, however, were observed in the left-of-shear quadrants, especially the DL quadrant (Fig. 3.10a). The vertical velocity distributions of Joaquin and Patricia also show little systematic azimuthal variation (Fig. 3.10b, c), with sporadic peaks in frequency at different vertical velocity values. There was a decrease in the vertical velocity strength, and frequency of vertical velocities above the updraft, and downdraft, thresholds in the upshear quadrants of Patricia (Fig. 3.10c).

The CFADs for all radii for each TC and the combined dataset are shown in Figure 3.11. Vertical velocity in the combined dataset was a weak function of altitude, with Figure 3.11d showing that the vertical velocity distribution broadens slightly aloft and becomes skewed towards larger, more positive values. There was little altitudinal variation in the CFAD for Marty, but the distribution was skewed towards positive vertical velocities, and there were higher frequencies of negative vertical velocity below 5 km (Fig. 3.11a). The altitudinal vertical velocity distribution in Joaquin was more centered around zero than in Marty, but high percentages of negative values of approximately -1.5 m s^{-1} were present in Joaquin (Fig. 3.11b). Positive vertical velocities in Joaquin weakly increased in strength aloft and negative vertical velocities were fairly uniform with altitude (Fig. 3.11b). Patricia had a different altitudinal vertical velocity distribution than Marty or Joaquin (Fig. 3.11c). The CFAD for Patricia shows that vertical velocity was skewed towards negative values, especially within the uncertainty bounds, but there was more spread in the positive values and little altitudinal signal (Fig. 3.11c).

CFRDs, CFAzDs, and CFADs for data within the core and outside of the core are provided in Appendix D, but the results are summarized here. The CFAzDs and CFADs for data within the core are not appreciably different from the total CFAzDs and CFADs. The similarities between the contoured frequency diagrams for all radii and the contoured frequency diagrams from the core reflect that the cores of the TCs have the most variation and spread in the strength of the observed vertical velocities. The azimuthal distributions for all three TCs outside of the core have higher frequencies of lower vertical velocity strength, but little azimuthal variability exists in vertical velocity strength. There were very few data points outside of the core in the DR or UR quadrants in Marty and in the DR quadrant in Joaquin due to sampling biases, which makes the distribution outside of the cores in Marty and Joaquin not robust. The CFADs for data outside of the core generally showed narrower vertical velocity distributions and more negative vertical velocities than the total CFADs, with differing altitudes of peak vertical velocity strength.

3.1.3.3 Updrafts and downdrafts

Table 3.3 shows the number of updrafts and downdrafts (defined using the $|2\ \mathrm{m\ s^{-1}}|$ and $|4\ \mathrm{m\ s^{-1}}|$ thresholds; section 3.1.2) observed in the subset of TCI soundings, as well as the means and medians of the maximum and minimum updraft and downdraft speeds. Given the small sample size of updrafts and downdrafts, robust conclusions about the convective asymmetries in the three TCs cannot be made, but the examination of the updrafts and downdrafts observed is useful in understanding the TCI vertical velocity dataset. Patricia had the strongest observed mean and median updraft speeds, the strongest peak updraft strength at 23.89 m $\mathrm{s^{-1}}$, and was the only TC to have a low-level updraft (below 2 km) with a maximum value exceeding 10 m $\mathrm{s^{-1}}$. Downdraft speeds were more comparable between the three TCs, with the strongest downdraft in Joaquin at -8.7 m $\mathrm{s^{-1}}$. Most updrafts and downdrafts observed during TCI had mean and median strengths of approximately |3–4 m $\mathrm{s^{-1}}$|, and maximum strengths of approximately |4–5 m $\mathrm{s^{-1}}$|. Updraft and downdraft depths were primarily less than 4 km with 50% of the updrafts and downdrafts smaller than 1.2–1.4

km.

Shown in Figures 3.12–3.14 are select “cross sections” of vertical velocity with updrafts and downdrafts contoured. It is important to note that the cross sections presented here are not true cross sections, because the dropsondes drift around the TC in a cyclonic trajectory. Each data point corresponds to a unique altitude and distance from the center to account for radial drift of the dropsondes during descent. The horizontal and radial winds reported in Figures 3.12–3.14 are storm-motion-relative.

The strongest vertical velocities and updrafts in Marty on 27 September were aloft, above 12 km in the eyewall (inner 30–40 km; Fig. 3.12). There were weaker bands of positive and negative vertical velocities outside of the eyewall to the northwest of the TC center (Fig. 3.12). Joaquin on 2 October was at a stronger intensity than Marty on 27 September and had considerably stronger and deeper eyewall updrafts than Marty at approximately 8 m s^{-1} (Fig. 3.13). Joaquin on 2 October also exhibited an asymmetric distribution in the eyewall convection (e.g., Fig. 3.13). The strongest eyewall convection was towards the southeast of the TC center, which is on the downshear side of the storm (Fig. 3.13).

The vertical velocity cross section on 23 October in Patricia shows deep, strong low-level and mid-level eyewall updrafts greater than 10 m s^{-1} (Fig. 3.14a, b). Patricia also had a low-level updraft that exceeded 10 m s^{-1} collocated with a localized azimuthal wind maximum (Fig. 3.14b) and apparent radial overturning circulation (Fig. 3.14c) in the vicinity of a secondary eyewall observed in HIRAD data (Fig. 3.15), which supports the numerical simulations by Hazelton et al. (2017). The low-level radial overturning circulation was sampled by six soundings spaced 5–11 km apart with small radial (approximately 18–300 m) and azimuthal (approximately 1–2 km) drifting below 2 km. The spacing of the last data points of the soundings also did not deviate drastically from their spacing at 2 km. The relatively small radial and azimuthal motions, and small spacing deviations of the soundings below 2 km, do not severely impact the interpretation of the low-level cross section in Figure 3.14c and indicates that the radial overturning circulation is real and not a manifestation of sounding issues. It cannot be concluded with absolute certainty, however, that the low-level radial circulation and the strong low-level updraft were directly associated with the secondary eyewall. The radial overturning circulation and low-level updraft were also collocated if the high-resolution HRD center was used instead of the XDD-derived ZWC, which had a mean difference of 6 km on 23 October. This suggests that the presence of the radial overturning circulation in Figure 3.14 is robust despite the differences between the two tracks.

Patricia also had a ± 2 m s^{-1} amplitude wave-like feature in the vertical velocity on 23 October near 17 km with a wavelength of approximately 20–30 km. This apparent wave-like feature is in the same approximate location to where Duran and Molinari (2018) found a potential gravity wave at a comparable wavelength (Fig. 3.14d, e). The potential gravity wave is visible in both pressure (Fig. 3.14d) and potential temperature (Fig. 3.14e) at a wavelength of 20–30 km. The agreement between both studies, and the agreement between the wave-like feature in the vertical velocity, pressure, and potential temperature, further supports that the XDDs sampled a gravity wave in Patricia on 23 October.

3.1.4 Discussion

Examining the altitudinal, azimuthal, and radial frequency distributions of vertical velocity, as well as the strength of the vertical velocity, serves a critical role in understanding the kinematic and convective environments of the TCs observed during TCI. The results presented here are a preliminary step at evaluating dropsonde-derived vertical velocities from the XDDs in TCs. The unprecedented high temporal and spatial resolution of these dropsondes during TCI allowed for analysis of the vertical velocities in Marty, Joaquin, and Patricia. These results serve as documentation of the strength and location of vertical velocities observed during TCI.

From the large datasets of RD-93 and RD-94 data, it has been shown that low-level (< 3 km) updrafts greater than 10 m s^{-1} occur exclusively in major hurricanes (Stern et al., 2016). Out of the 437 dropsondes (276,515 data points) considered, only 719 vertical data points had vertical velocities greater than 10 m s^{-1} (0.3% of the data), only 12 unique updrafts had maximum vertical velocities greater than 10 m s^{-1}, and only two of the positive vertical velocity data points below 3 km reached 10 m s^{-1}. The two data points were within a low-level updraft with collocated horizontal winds of 42 m s^{-1} and an overturning circulation in Patricia on 23 October as a major hurricane, but during rapid weakening (Figs. 3.14 and 3.15). At the same time, a potential upper-level gravity wave was observed in the vertical velocity, pressure, and potential temperature fields (Figs. 3.14). The strongest downdrafts, however, were not observed in Patricia, but in Joaquin.

The results show that vertical velocity strength, updraft strength, and downdraft strength are all strongest within the core (Figs. 3.4–3.9), which is also supported by comparisons of CFADs and CFAzDs for data within the core and outside of the core (see Appendix D). Evidence of stronger, positive mean and median vertical velocities were also found aloft for the entire dataset and within most shear quadrants in all three TCs (Figs. 3.4–3.8), which agrees with the findings of Black et al. (1996), Black et al. (2002), Heymsfield et al. (2010), Reasor et al. (2013), and DeHart et al. (2014) that utilized flight-level or Doppler-radar data for altitudes up to approximately 12–16 km. The CFADs either do not illustrate this characteristic or do not illustrate it as strongly as the CFADs in Black et al. (1996). For example, the 0.0625–8% frequency contours for positive vertical velocity in Joaquin broaden with height to varying degrees (Fig. 3.11b), but not as strongly as observed in Black et al. (1996).

The TCI XDD-derived vertical velocity CFADs and the CFADs shown by Black et al. (1996) may differ because: 1) vertical velocity errors are largest aloft (section 2.4); 2) dropsonde fall stability is likely a larger issue aloft; 3) there are three TCs in this dataset and seven TCs in Black et al. (1996); 4) the use of a differential pressure fall speed rather than the GPS fall speed produces weaker vertical velocities aloft (see Appendix E); 5) TC intensity, rate of intensity change, and time relative to peak intensity or rapid intensification can cause differences in CFADs (McFarquhar et al., 2012); 6) CFAD profiles can vary from storm-to-storm (Nguyen et al., 2017); 7) lack of radar data aloft and the use of a minimum reflectivity threshold drastically changes TC CFADs in the upper levels (McFarquhar et al., 2012; Nguyen et al., 2017); and, 8) if the true geometric center of an updraft or downdraft is not sampled, then vertical velocity may be underestimated for the updraft or downdraft (Jorgensen et al., 1985). The TCI XDD CFADs more resemble the rainband and stratiform CFADs from Black et al. (1996) than the eyewall CFAD (Fig. 3.11). The CFADs do resemble the CFAD from simulations of Dennis (2005) near rapid intensification, but without a minimum reflectivity threshold (McFarquhar et al., 2012). Further, the similarities between the mean and median values (Table 3.2), profiles (Figs. 3.4–3.8), and the results in Black et al. (1996) provide support and increase confidence in the quality of the XDD-derived TCI vertical velocity dataset.

The azimuthal vertical velocity distributions (Fig. 3.10) do not show robust patterns and do not agree well with the canonical wavenumber-one convective asymmetry within the core (e.g., Black et al., 2002; Corbosiero and Molinari, 2002, 2003; Stern and Aberson, 2006;

Guimond et al., 2010; Reasor et al., 2013; DeHart et al., 2014), which could be due to the relatively small sample size. Further, it is possible that the convection was organized by vortex tilt rather than the 850–200-hPa shear (e.g., Stevenson et al., 2014). It is important to note that the 850–200-hPa shear direction is a simple vector difference between two levels and assumes that the shear changes uniformly between the levels, whereas the tilt structure is a function of altitude through multiple layers and potentially exhibits more variability in space and time (e.g., Creasey and Elsberry, 2017). It is also plausible that the shear strength or direction changes non-linearly between the 850 and 200-hPa levels, which could account for these differences.

This discrepancy and lack of data, especially at outer radii, also suggests that more observations with an even distribution of samples in each shear-relative quadrant are likely required to analyze dropsonde-derived convective asymmetries in individual TCs using CFAzDs. Bootstrap analysis provided in Appendix B, however, suggests that Marty had the strongest median XDD-derived vertical velocities in the DL quadrant within the core, but the lack of data in each shear-relative quadrant make the finding unrobust. It is also important to remember that the CFAzDs are used to look at the azimuths with the highest frequency of vertical velocity, which can lead to discrepancies. For example, it is possible that a quadrant could have a relatively higher frequency of vertical velocities at an appreciable strength, but the mean or median strength within the quadrant may be considerably weaker.

In order to better understand dropsonde-derived vertical velocities, the errors associated with the calculation of vertical velocity need to be addressed. If GPS fall speeds are used in the calculation of vertical velocity, strict screening of the data must be conducted to remove large, unrealistic errors in the fall speed like in Figure 2.4. If a maximum difference of 1 m s^{-1} between the GPS fall speed and the hydrostatic differential pressure fall speed is allowed, then 40,168 data points from the subset TCI soundings used would need to be removed or quality controlled. Stern et al. (2016) note, however, that using the differential pressure fall speed alone may introduce errors when examining extreme non-hydrostatic updrafts. This serves as justification for the improvement of the measurement of dropsonde fall speed and the decrease in dropsonde fall speed errors. As shown in section 2.4, the dropsonde-derived vertical velocity errors from the XDDs are approximately ±1–2 m s^{-1}. Optimistically, dropsonde-derived vertical velocity errors an order of magnitude smaller would improve the confidence of the vertical velocities between ±2 m s^{-1}, which accounts for a large portion of the vertical velocity distributions in TCs (e.g., Black et al. (1996) and Figs. 3.9–3.11). Vertical velocity errors within the 1–2 m s^{-1} range also impact the ability to observe gravity wave features aloft in TCs like in Patricia on 23 October (Fig. 3.14).

3.2 Wind finding equations

3.2.1 Introduction

While this dissertation is focused on addressing dropsonde-derived vertical velocity methods, accuracies, and errors, accurate horizontal wind speeds are also important in depicting and documenting TC structure. While it is unlikely that dropsondes sample the most extreme horizontal wind speeds (e.g., Stern and Bryan, 2018), as they are difficult to use to identify the RMW (section 3.1; Cecil and Biswas, 2017), dropsondes are useful for depicting the general horizontal wind fields within the hurricane boundary layer (Franklin et al., 2003). These horizontal wind observations are also important in analyzing features associated with deep, strong convection within TCs (Aberson et al., 2006; Stern et al., 2016; Stern and Bryan, 2018), documenting TC outflow and the strength of the warm core (e.g., Komaromi and Doyle, 2017), analyzing turbulence (Li and Miller, 2014a,b), and creating composite radial and azimuthal wind profiles (Giammanco et al., 2013). For example, Figure 3.14 depicts a strong updraft that was associated with the radial overturning circulation of a secondary eyewall that occurred in Patricia on 23 October.

As GPS chip sets improve, so do the reported horizontal position and velocity accuracies. Past dropsonde studies using the RD-93s, RD-94s, or XDDs have noted horizontal wind accuracies or error estimates between 0.1 m s^{-1} and 0.5 m s^{-1} (Hock and Franklin, 1999; Wang et al., 2015; Black et al., 2017). The u-blox 6 GPS chip used on the XDDs during TCI is claimed to have a velocity accuracy of 0.1 m s^{-1} at a circular error probability of 50% (U-blox, 2019). Accuracies of 0.05 m s^{-1}, however, may be possible if the GPS chip was upgraded to the new u-blox 8 (U-blox, 2019).

Despite the increased position and velocity accuracies in dropsonde GPS chip sets, inaccuracies exist in the methods used to calculate the horizontal wind speed. One of the most rudimentary methods for calculating the horizontal wind is to assume that the horizontal wind components (u, v) are equal to the horizontal motion components ($\dot{x}$, $\dot{y}$) of the dropsonde (Hock and Franklin, 1999; Houchi et al., 2015). This incorrectly assumes that: 1) the dropsonde can be considered as a spherical point; 2) the dropsonde acclimates immediately to the horizontal wind; 3) the dropsonde acclimates immediately to the local wind shear; and, 4) there are no appreciable vertical or horizontal accelerations of the dropsonde motion speed. This method will, hereafter, be referred to as the xy-methodology.

Hock and Franklin (1999), referred to as HF99 in this chapter, derived a set of equations, commonly referred to as the 'wind-finding equations' (WFEs), to calculate the horizontal wind components from the position information of a falling object in the presence of wind shear. In their calculations, they assume that: 1) the dropsonde can be considered as a spherical point; 2) the dropsonde acclimates immediately to the wind shear; 3) the magnitude of the difference between the true horizontal wind and the dropsonde motion is small compared to the difference between the true vertical wind and the dropsonde fall speed; 4) the vertical velocity is negligible; 5) the Coriolis parameter can be neglected; and, 6) the vertical acceleration of the dropsonde motion is small compared to the gravitational force. The HF99 methodology is an improvement upon the rudimentary xy-methodology, because it accounts for the dropsonde fall speed and the ratio of the horizontal accelerations to the downward gravitational acceleration.

Li and Miller (2014a), referred to as LM14a in this chapter, note that vertical velocity cannot be ignored or cancelled when dropsondes are launched operationally into convection. In some cases, the dropsonde may stall or ascend and the horizontal motion of the dropsonde more closely matches the true horizontal wind (LM14a). LM14a still assumes, however, that the magnitude of the difference between the true horizontal wind and the dropsonde motion is small compared to the difference between the true vertical wind and the dropsonde fall speed. This assumption may not hold in the situations they cite, where the dropsonde fall speed is approximately equal to the vertical wind speed. In that case the magnitude of the difference between the true horizontal wind and the dropsonde motion may be comparable to the difference between the true vertical wind and the dropsonde fall speed. LM14a use their version of the WFEs to find analytical solutions to depict dropsonde-observed turbulence.

The HF99 and LM14a WFE methodologies were derived, analyzed, and optimized for simple calculations of u and v for the RD-93 and RD-94 dropsondes, which have parachutes. Unlike these dropsondes, the XDDs do not have parachutes and fall at much faster rates (Black et al., 2017). Because of their fast, ballistic fall trajectories, the standard xy-methodology is likely not the optimum or most accurate method to compute horizontal winds for the XDDs. The HF99 and LM14a methodologies both contain major assumptions that do not hold in convective environments, like the inner core of a TC, and, therefore, may not be true for the XDDs. The xy-, HF99, and LM14a methodologies were used to compute horizontal winds using data from the TCI dataset. An alternative method to compute the horizontal wind using a more complete equation set was also analyzed.

3.2.2 Methods

3.2.2.1 Governing equations

From the governing equations for a falling object, derived below, there are four methods for calculating the horizontal winds using dropsondes: 1) the xy-method (equations 3.18, 3.19); 2) the HF99 WFEs (equations 3.16, 3.17); 3) the LM14a WFEs (equations 2.9, 3.14, 3.15); and, 4) the full WFEs (equations 2.9, 3.12, 3.13). This section summarizes the derivation of the four equation sets starting from Newton's second law:

$$\vec{F} = m\vec{a} \tag{3.2}$$

$$\vec{F} = m\vec{a_x}\hat{\imath} + m\vec{a_y}\hat{\jmath} + m\vec{a_z}\hat{k} \tag{3.3}$$

$$\vec{a} = \vec{g} + \frac{C_d \rho A \vec{V}|\vec{V}|}{2m} \tag{3.4}$$

$$a_x = \frac{C_d \rho A V_x |\vec{V}|}{2m} \tag{3.5}$$

$$a_y = \frac{C_d \rho A V_y |\vec{V}|}{2m} \tag{3.6}$$

$$a_z = g + \frac{C_d \rho A V_z |\vec{V}|}{2m} \tag{3.7}$$

where $\vec{V}$ is the three-dimensional motion-relative wind vector. It should be noted that the true C_d for any dropsonde is not likely to be uniform. The dropsonde horizontal C_d may be larger than the vertical (nose into the flow) C_d. Computational fluid dynamics simulations of the XDDs in axial and radial flow using the *simFlow* software (see chapter 4) suggest that C_d varies from 0.93 (axial) to 1.28 (radial), respectively. The relative uniformity of C_d for the XDDs with respect to angle of incidence to the flow is due to the similar ratios of drag force to area in the model. The assumption of a uniform C_d, however, would lead to weaker horizontal accelerations of the XDDs than what is observed in reality (equations 3.5, 3.6). Given that the XDDs do not have a parachute and fall faster than other dropsondes, the horizontal accelerations are not likely to be appreciably large, except for in areas of strong gradients in wind speed (e.g., the core of Patricia; Fig. 3.14). This implies that the uniform C_d assumption is not likely to introduce large errors when using the XDDs outside of the eyewall or other high-gradient regions in the wind speed. For simplicity, it is hereafter assumed that the XDDs have a uniform C_d to derive the WFEs.

If equations 3.5, 3.6, and 3.7, are expanded, the following equations are obtained:

$$m\ddot{x} = 0.5\rho C_d A(u - \dot{x})\sqrt{(u - \dot{x})^2 + (v - \dot{y})^2 + (w - \dot{z})^2} \tag{3.8}$$

$$m\ddot{y} = 0.5\rho C_d A(v - \dot{y})\sqrt{(u - \dot{x})^2 + (v - \dot{y})^2 + (w - \dot{z})^2} \tag{3.9}$$

$$m\ddot{z} = mg + 0.5\rho C_d A(w - \dot{z})\sqrt{(u - \dot{x})^2 + (v - \dot{y})^2 + (w - \dot{z})^2} \tag{3.10}$$

where $\ddot{x}$, $\ddot{y}$, and $\ddot{z}$ are the dropsonde acceleration components. Equation 3.10 can be re-arranged as:

$$\frac{0.5\rho C_d A}{m} = \frac{(\ddot{z} - g)}{(w - \dot{z})\sqrt{(u - \dot{x})^2 + (v - \dot{y})^2 + (w - \dot{z})^2}} \tag{3.11}$$

If equation 3.11 is plugged into equations 3.8 and 3.9, and re-arranged to solve for u and v, an equation set is obtained to compute the horizontal wind components.

$$u = \frac{\ddot{x}(w - \dot{z})}{(\ddot{z} - g)} + \dot{x} \tag{3.12}$$

$$v = \frac{\ddot{y}(w - \dot{z})}{(\ddot{z} - g)} + \dot{y} \tag{3.13}$$

Using the assumptions of LM14a, equations 3.12 and 3.13 can be simplified to be:

$$u = \left|\frac{w}{g}\ddot{x} - \frac{\dot{x}}{g}\ddot{z}\right| + \dot{x} \tag{3.14}$$

$$v = \left|\frac{w}{g}\ddot{y} - \frac{\dot{z}}{g}\ddot{x}\right| + \dot{y} \tag{3.15}$$

If it is assumed that $\ddot{x}$ and w are zero, however, the equations reduce to the HF99 WFEs.

$$u = -\frac{\dot{z}}{g}\ddot{x} + \dot{x} \tag{3.16}$$

$$v = -\frac{\dot{z}}{g}\ddot{y} + \dot{y} \tag{3.17}$$

A form of the HF99 WFEs is commonly used in the Atmospheric Sounding Processing Environment (ASPEN) software for quality controlling dropsonde data (Bell et al., 2016).

If it is further assumed that there are no horizontal accelerations of the dropsonde, equations 3.16 and 3.17 reduce to the xy-method equations.

$$u = \dot{x} \tag{3.18}$$

$$v = \dot{y} \tag{3.19}$$

Equations 3.12 and 3.13 indicate that by increasing the accuracy of the dropsonde GPS position and dropsonde horizontal velocity, the accuracy of u and v should increase. Another consequence of equations 3.12 and 3.13 is that by increasing the accuracy of vertical velocity and dropsonde fall speed, the accuracy of u and v should increase, which further motivates this dissertation. It also supports further analysis of dropsonde-derived vertical velocity errors and the addressing ways to improve the measurements.

HF99 calculated vertical velocity using equations 2.9 and 2.10. If it is assumed that w is zero and the dropsonde is falling at terminal speed ($\ddot{z}$ equals zero), then the u and v wind components equal the horizontal motion of the dropsonde. In this situation, equation 3.11 is reduced to equation 2.9 (chapter 2). HF99 note that the differences between the full WFE horizontal winds and their WFE horizontal winds are small and on the order of 0.5 m s^{-1}. It is unknown if these small differences are comparable for the XDDs or if they are larger/smaller in the convective environments of a TC.

3.2.2.2 Data

A total of 725 XDDs were launched into Marty, Joaquin, and Patricia, but the horizontal wind was calculated using the four equation sets for only 631 XDD of the soundings from the TCI experiment, because they terminated below an altitude of 500 m. This 500 m restriction was used to ensure that soundings contained data within the low levels of the TCs comparable to Stern et al. (2016). Note that the R^* restriction used in section 3.1 was not used in this section in order to compare the four WFE methods both within the TCs and within the environments outside of the TCs. Data were also restricted to be below 17.5 km due to dropsonde kinematic adjustments upon launching from the aircraft at 19 km. The TC centers and RMWs were the same as in section 3.1 and vertical velocity was computed from using the M3 methodology.

The latitude, longitude, altitude, vertical velocity, dropsonde velocity, and dropsonde acceleration were smoothed using a nine-point binomial smoother, and anomalous data points outside of two standard deviations of the local mean in the nine-point filter were removed. After all data removal and data restriction, a total of 376,717 horizontal wind data points were compared. In an effort to estimate the utility of using any version of the higher-order WFEs, the HF99, LM14a, and full WFE methodology horizontal winds are compared to the xy-method horizontal winds. In addition, the full WFE methodology horizontal winds are compared to the others to demonstrate the utility of using the full,"un-approximated," equation sets to obtain the horizontal wind. For the sake of brevity, the xy-, HF99, LM14a, and full WFE methods are abbreviated as V1–V4, respectively, in all plots.

3.2.3 Results

Figure 3.16 shows two sample soundings of horizontal wind from a non-convective (NC) region of Marty on 28 September and a highly convective region (C) of Patricia during rapid decay on 23 October. The designation of NC versus C is qualitative, but is supported by the strength of vertical velocity in the profile (Fig. 3.17), the infrared brightness temperatures (Fig. 3.18), and the distance from the eye. The sounding from Marty on 28 September had a mean R^* of approximately nine and a mean distance of approximately 340 km from the eye, which is well outside of convection of the TC core. The sounding from Patricia on 23 October had a mean R^* of approximately one and a mean distance of approximately 11 km from the eye, which is well within eyewall convection.

The horizontal winds from the four equation sets agree well in both the NC and C soundings and show the same qualitative structure, with only slight differences between them (Fig. 3.16a, b). Figures 3.16c and 3.16d show the differences between the horizontal winds from the three higher-order WFE methods (HF99, LM14a, and full WFE methodologies) and the xy-method. Both the NC and C soundings show that the largest differences are aloft, and the smallest differences occur in the low-levels. The C sounding, however, has the largest absolute differences (Fig. 3.16d). The direction of the difference (positive or negative) depends upon the method used, but the methods agree more within the NC sounding than the C sounding (Fig. 3.16c, d). This could be due to, in part, by the high amplitude noise in the differences in the C sounding (Fig. 3.16d).

Figure 3.19 shows notched box plots of the horizontal winds from each of the four methods. The edges of the notches denote the 95% confidence interval of the median. If the notches of any box plots overlap, then the medians are statistically similar (Chambers et al., 1983). The horizontal winds from the xy- and HF99 methods have medians that are statistically similar (Fig. 3.19). Only the full WFE and LM14a horizontal winds have statistically different medians (Fig. 3.19), but the differences in the medians are not physically large for any of the methods. Mean and median profiles of the horizontal wind speed at all radii illustrate that the largest variance between the four methods is above 12 km (Fig. 3.20). This agrees with the sample soundings in Figure 3.16. All four methods agree that the wind speed maximizes at 22 m s^{-1} at an altitude of 0.88 km.

3.2.3.1 Comparing to the xy-method

The mean, median, and standard deviation of the absolute difference between the three higher-order WFE horizontal winds and the xy-method horizontal winds is provided in Table 3.4. All three higher-order WFE methods have similar mean, median, and standard deviation absolute differences in the horizontal winds of approximately 0.6, 0.3, and 0.9 m s^{-1}, respectively. Student's t-tests show that the HF99, LM14a, full WFE methods have statistically different horizontal winds compared to the xy-method at the 95% level. Only the horizontal winds from the LM14a and full WFE methods are statistically different at the 99% level using Student's t-tests. The results from Table 3.4 suggest that any of the higher-order WFE methods offer statistically significant changes to the horizontal wind compared to the xy-method.

Figure 3.21 shows histograms for the horizontal wind differences for all of the data. While all three higher-order WFEs have similar absolute horizontal wind differences and percent of difference to the xy-method horizontal wind, the HF99 method had a slightly negative skew, and the full and LM14a methods had similar weak negative skews (Fig. 3.21a, b). All three methods have similar interquartile ranges (IQRs), with spans of approximately 0.65 m s^{-1}. Figure 3.21c indicates that using any of the three higher-order WFE equation sets produces approximately 4–8% change in the horizontal wind over the xy-method, which corresponds to approximately 0.5–1 m s^{-1} (Fig. 3.21d).

The horizontal wind differences between the full WFE methodology and the xy-method horizontal winds are largest aloft and near the surface (Fig. 3.22a), which agrees well with the C sounding from Patricia (Fig. 3.16d). The differences also generally decrease in magnitude with increasing radius away from the TC cores. This indicates that the horizontal wind from soundings within the environments of the TCs are not as strongly affected by the method used as within the TC itself (Fig. 3.22b, c). It is also evident that the strength of the vertical velocity impacts the strength of the difference, which is not surprising considering that vertical velocity is used in the full WFE method to obtain the horizontal wind (Fig. 3.22d). In areas where vertical velocity is weak or negative, larger differences between the xy-methodology and the full WFE methodology horizontal winds exist (Fig. 3.22d).

Figure 3.23 shows profiles of mean and median differences between the three higher-order methods and the xy-method, as well as the standard deviations in the differences. Negative values indicate that the xy-method horizontal winds are weaker. The largest impact of the choice of method, and the overall variance in the wind speed differences, is largest aloft (Fig. 3.23). The differences are only statistically significant, however, above 12 km (Fig. 3.23a, b), which agrees with the findings in Figure 3.22a.

The general locations and conditions where the two methods differ (Figs. 3.22, 3.23) suggests that using the full WFE method may impact the horizontal wind in key areas of the TCs and impact the interpretation of the strength of the horizontal wind physically. To test this hypothesis, the horizontal winds from the xy-methodology and the full WFE methodology were compared directly for transects of soundings across the TC centers. Figures 3.24a, b, 3.25a, b and 3.26a, b show the horizontal wind using the xy-method for select cross sections in Marty (27 September), Joaquin (2 October), and Patricia (23 October). These are the same cross sections analyzed in section 3.1 (Figs. 3.12–3.14). The cross sections also show the change (Figs. 3.24b, 3.25b, 3.26b) or absolute change (Figs. 3.24a, 3.25a, 3.26a) in the horizontal wind by using the full WFE methodology in lieu of the xy-methodology.

The strongest location for absolute change in Marty occurs in sporadic pockets above 13 km (Fig. 3.24a). The largest absolute difference was approximately 6 m s^{-1} at 315 km from the eye and an altitude of 16.4 km (Fig. 3.24a), which is adjacent to a region of weak, positive vertical velocity (Fig. 3.12). The low-level ($<$ 2 km) eyewall horizontal wind maximum is relatively unaffected by the use of the full WFE methodology (Fig. 3.24a, b). Most of the upper-level horizontal winds of Marty on 27 September were strengthened by 2–4 m s^{-1} by using the full WFE method, but there are areas aloft where the horizontal wind is weakened by -2 m s^{-1} (Fig. 3.24b).

Like in Marty, the largest absolute differences between the horizontal winds using the xy-methodology and the full WFE methodology were aloft (Fig. 3.25a). However, absolute differences greater than 2–4 m s^{-1} were observed at lower altitudes than in Marty, above 10 km (Fig. 3.25a). The largest absolute differences in Joaquin on 2 October were above 15 km in the downshear (southeast) side of the eyewall (Fig. 3.25a) above a strong updraft that was stronger than 10 m s^{-1} (Fig. 3.13). The horizontal winds using the full WFE methodology were generally faster aloft by 2–5 m s^{-1}, but one area aloft and adjacent to a weak updraft to the southeast (downshear) at 200 km was approximately 5 m s^{-1} slower using the full WFE methodology (Fig. 3.25b).

The location for the strongest absolute change occurs within the uppermost section of Patricia from 15–17.5 km (Fig. 3.26a). In some locations, the differences are large at 6 m s^{-1} (Fig. 3.26a). Weaker, but notable 0.5–2 m s^{-1} changes occur within the eyewall (inner

20–40 km) and below the freezing level outside of the eyewall (below 6 km) (Fig. 3.26a). The midlevel, 5–6 km, horizontal wind speed maxima to the southeast side of the eye is strengthened by approximately 3 m s^{-1} and broadened by using the full WFE methodology (Fig. 3.26a, b). Using the full WFEs increases the speed of the horizontal wind at the base of the TC outflow layer and increases the speed of the horizontal wind within the eyewall (Fig. 3.26b). Sporadic increases and decreases exist within the eye, and outside of the eyewall (Fig. 3.26b).

3.2.3.2 Comparing to the full WFEs

As all three higher-order methods produce statistically different horizontal winds to the xy-method, the full WFE method horizontal winds are compared directly to the HF99 and LM14a horizontal wind speeds to examine the impact of using it over any of the other methods. The mean, median, and standard deviation of the absolute difference between the horizontal winds from the three other methods and the full WFE method is provided in Table 3.5. The LM14a method and the xy-method have similar mean, median, and standard deviation absolute differences in horizontal wind to the full WFE method, but the HF99 methodology has larger mean, median, and standard deviation absolute differences by approximately a factor of two (Table 3.5). Student's t-tests at the 99% level also indicate that the full WFE method produces statistically different horizontal wind speeds compared to any of the other methods.

The results in Table 3.5 are also supported by the histograms in Figure 3.27. The HF99 methodology had the largest spread in wind speed difference (Fig. 3.27a), largest absolute difference (Fig. 3.27b), largest percent difference (Fig. 3.27c), and smallest percentiles of absolute differences (Fig. 3.27d). The results in Figure 3.27 indicate that by using the full

WFEs for the XDDs in TCI rather than the HF99 methodology, a 5–10% change or 1–3 m s^{-1} difference in the horizontal wind can be achieved. The IQRs for the differences between the full WFE methodology and the xy-methodology or LM14a methodology horizontal winds are similar with spans of 0.5–0.6 m s^{-1}, but the IQR for the differences between the full WFE methodology and the HF99 methodology horizontal winds was statistically significantly larger at approximately 1.3 m s^{-1}.

Figure 3.28 shows profiles of mean and median horizontal wind speed differences between the full WFE method and the other methods. Negative values indicate that the full WFE methodology produces weaker horizontal wind speeds. Like in Figure 3.23, the largest, statistically significant differences are above 12 km (Fig. 3.28). The HF99 and xy-methodologies have similar horizontal wind speed difference profiles (Fig. 3.28a, b), but the standard deviation in the horizontal wind speed differences between the HF99 and full WFE methodologies are considerably larger than for the xy- and LM14a methodologies (Fig. 3.28c). The LM14a methodology has a median difference of zero to the full WFE methodology horizontal winds below 13 km (Fig. 3.28a). The LM14a methodology also overestimates the horizontal wind speed aloft compared to the full WFE methodology (e.g., Fig. 3.28b).

Transect figures similar to Figures 3.24a, b, 3.25a, b, and 3.26a, b were produced comparing the HF99 methodology horizontal wind to the full WFE methodology horizontal wind (Figs. 3.24c, d, 3.25c, d, and 3.26c, d). Similar qualitative results can be obtained when comparing the two methodologies. One of the ubiquitous findings is that the absolute differences between the HF99 methodology and the full WFE methodology horizontal winds are larger than the absolute differences between the xy-method and the full WFE methodology horizontal winds, especially in the upper levels of all three cross sections (Figs. 3.24c, 3.25c, and 3.26c). This is similar to the findings in Table 3.5, implying that incorporating dropsonde accelerations without taking into account vertical velocity in the WFEs likely increases the dropsonde-derived horizontal wind errors. In many cases, the absolute differences exceed 5 m s^{-1}, with pockets of greater than 6 m s^{-1} differences (e.g., Fig 3.26c). Given that the horizontal winds using the HF99 method are approximately 10 m s^{-1} in these areas aloft, percent differences can approach approximately 50%, which is both statistically and physically significant.

The largest differences occur: 1) in the upper levels of Marty (15–17.5 km), with radial bands below (Fig. 3.24c); 2) above 10 km on the downshear (southeast) side of Joaquin (Fig. 3.25c); 3) above 10 km and outside of the inner 200 km on the upshear (northwest) side of Joaquin (Fig. 3.25c); 4) in the upper levels of Patricia (15–17.5 km; Fig. 3.26c); 5) in the eyewall of Patricia, especially the upper and middle portions of the eyewall (Fig. 3.26c); and, 6) areas below the freezing level outside of the eyewall in Joaquin and Patricia (Figs. 3.25c, 3.26c).

This means that the upper levels of all three TCs, especially for Patricia on 23 October, and the upper eyewalls, have horizontal winds that are stronger using the full WFEs rather than the HF99 methodology (Figs. 3.24d, 3.25d, 3.26d). The full WFE method does produce weaker horizontal winds in some locations of the core, near the eye (e.g., Patricia; Fig. 3.26d), and upper levels at outer radii (e.g., Joaquin at 180 km southeast of the eye; Fig. 3.25d), but the overall impact of using the full WFEs is an increase of the horizontal wind in the upper levels of the cross sections by a mean of 0.75 m s^{-1} and a median of 0.5 m s^{-1}.

3.2.4 Conclusions

The use of one of the three higher-order WFE sets (HF99, LM14a, or full) does change the horizontal wind in the TCI dataset using the XDDs. The difference is on the order of approximately 5% of the xy-methodology winds, or approximately 0.5–1 m s^{-1}, over the entire dataset (Fig. 3.21). This is close to the 0.5 m s^{-1} estimate by HF99, but specific areas of the TCs have larger changes of > 5 m s^{-1} (e.g., Fig. 3.25a).

The HF99, LM14a, and full WFE methodologies produced horizontal winds that were statistically different from the simplistic xy-methodology. Student's t-tests show that all methods were statistically different from one-another, despite the medians being statistically similar for the xy- and HF99 methodology horizontal wind speeds (Fig. 3.19). The largest mean or median absolute difference in horizontal wind speeds, however, was between the HF99 methodology and the full WFE methodology (e.g., Tables 3.4, 3.5). The full WFE methodology is also the only methodology to include information on XDD accelerations and the vertical velocity. This suggests that the full WFE methodology is the most robust, physically correct, and complete methodology for the XDDs.

The full WFE method produces a 5–10% difference in horizontal wind, or approximately a 1–3 m s^{-1} difference compared to the HF99 methodology (Fig. 3.27). There are differences, however, of more than 5 m s^{-1} in key areas of the TCs such as the bottom of the outflow layer, the eyewall, and, potentially, the rainband regions (Figs. 3.24, 3.25, 3.26). The HF99 method also underestimated the horizontal wind speed aloft to the full WFE method the most, with a mean and median of approximately -0.75 and -0.54 m s^{-1}, respectively.

The HF99 method horizontal winds also have the most spread and largest IQR for the differences from the full WFE method horizontal winds, whereas the LM14a method horizontal winds have the least spread and smallest IQR. Interestingly, the horizontal wind speed differences between the xy-method and the full WFE method horizontal wind speed are similar to the differences between the LM14a method and the full WFE method (Fig. 3.27). This collectively suggests that incorporating dropsonde fall speed and horizontal acceleration without accounting for vertical velocity or vertical acceleration like in the HF99 method erroneously increases the variance in the horizontal wind speed.

The largest impact of using the full WFEs is within the TCs themselves, rather than the environment, where weaker horizontal winds occur, and in areas of weak or negative vertical velocity (Fig. 3.22). This is a result of equations 3.12 and 3.13, where only when w equals z does the horizontal wind equal the same as the xy-method. If $w \leq 0$, substantial differences in the horizontal winds speeds occur. This agrees well with the finding that the largest impacts occur within the upper levels of Marty and Patricia and below the freezing level outside of the eyewall region in Patricia. These situations, however, are in contrast to the large differences in the eyewall, especially in the upper portions, where w can be strongly positive and compete with $\dot{z}$, which would cause the horizontal winds from the full WFE method and the xy-method to be comparable. The large differences in the upper levels, especially the upper levels of the eyewall, likely occur due to the deceleration of the XDDs as they encounter strong updrafts. Strong deceleration would cause the denominators of equations 3.12 and 3.13 to be small, resulting in a larger difference.

The large, ±3–5 m s^{-1} differences aloft are not likely to be completely caused by the expected 2 m s^{-1} vertical velocity errors described in section 2.4. By perturbing the observed vertical velocity by ±2 m s^{-1}, horizontal wind errors associated with vertical velocity errors can be estimated. The horizontal wind errors caused by potential vertical velocity errors have an absolute mean and median between 0.25–0.57 m s^{-1} for the entire dataset. The absolute mean and median errors increase to approximately 0.57–1.54 m s^{-1} for data above 15 km, which does not fully account for the ±3–5 m s^{-1} differences aloft between the HF99 and full WFE methodologies.

The relatively small impact of the vertical velocity errors is because $(\ddot{z} - g) >> (\dot{x})$ or

($\dot{y}$) in equations 3.12 and 3.13 for most of the XDDs launched into TCI. For example, the median horizontal errors aloft due to potential vertical velocity errors is only ± 0.1 m s^{-1} in Patricia on 23 October, because the vertical deceleration of the XDDs as they encounter the convective eyewall and statically stable upper levels is exceedingly stronger than the horizontal acceleration of the dropsondes.

It is not shown here that the use of the full WFE method produces more accurate horizontal winds. There were no independent, collocated horizontal wind data in time and space to the TCI soundings to validate upon. Other flights either did not coincide with TCI soundings or they sampled other regions of the TCs. The results do show, however, that the use of a more complete, less approximated equation set yields statistically different horizontal winds, with a mean absolute change of at most 0.5–2 m s^{-1} over the entire dataset. This difference may be small and physically insignificant, but larger differences (> 5 m s^{-1}) were possible aloft are physically significant and warrant further examination of the equations used to derive horizontal wind from dropsondes.

3.3 Temporal and spatial autocorrelations: Implications for future dropsonde-based missions

3.3.1 Introduction

Due to the high sampling rate of the XDDs, it is possible that successive data points in a sounding, or data points from adjacent soundings, were appreciably correlated (i.e., correlation values greater than 0.5; Brooks and Carruthers, 1978), and likely represented the same atmospheric phenomena, such as an updraft or small-scale vorticity maximum. At present, no study has considered the temporal and spatial autocorrelations (Brett and

Tuller, 1991; Griffith, 2003; Khalili et al., 2007) of dropsondes in TCs. Only one study, Black et al. (1996), has directly examined the spatial autocorrelations of radar data in TCs. Analysis of the temporal and spatial autocorrelations of the TCI soundings are important to: 1) aid targeted dropsonde or dropsonde deniability studies (studies examining the impact of removing observational data to be assimilated into a model; Mu et al., 2009; Torn and Hakim, 2009; Wu et al., 2009; Romine et al., 2016); 2) evaluate what coherent features are resolvable by the dropsondes; 3) perform accurate spatial interpolation of any recorded variable; and, 4) provide guidance as to what horizontal spacing is required to resolve various aspects of TC structure within transects of soundings. This dissertation only focuses on the latter three points. In this section, an analysis is conducted to evaluate the temporal and spatial autocorrelations of the XDDs used in TCI with the kriging spatial interpolation framework. The autocorrelation of data points in individual soundings as well as the spatial correlation between adjacent soundings are considered. The variables considered were vertical velocity, relative humidity, horizontal wind speed, temperature, and equivalent potential temperature (abbreviated as w, RH, $|V_h|$, T, and θ_e in this section).

Knowledge of the temporal and spatial autocorrelations of dropsondes is also required in order to accurately depict TC structure from transects of dropsondes or aircraft. Some studies indicate that to resolve features on the scale of the RMW, grid spacing of approximately 14 km or less is required (Gentry and Lackmann, 2010). The results of Gentry and Lackmann (2010), however, show that increased model resolution down to 2-km grid spacing or less is required to understand TC eyewall kinematics and physics. These results suggest that observations should also be taken at high resolutions. The likelihood of highly correlated data points increases, however, with the increase in horizontal or vertical resolution and should approach unity (Brett and Tuller, 1991; Khalili et al., 2007). Conversely, if dropsondes are launched too far apart then the thermodynamic and kinematic structure of a TC will not be well resolved or represented. Similarly, if data in a single sounding is recorded at low frequency, the thermodynamic and kinematic structure of a TC will not be well resolved or represented.

Examination of the temporal and spatial autocorrelations in the XDDs is critical to accurately perform any objective spatial interpolation. One interpolation scheme, called kriging, is a geostatistical interpolation method that uses covariance information to interpolate data fields (e.g., Biau et al., 1999). If adjacent data points in space or time are appreciably correlated, well modeled, or vary slowly in time and space, interpolation can easily be conducted between the data points (Gorman, 2009). If adjacent data points are not appreciably correlated, however, then interpolation cannot be as easily conducted and could create unrealistic and uncharacteristic TCs by smoothing or smearing small-scale phenomena or sharp gradients in time and space (Privé and Errico, 2016). One of the important distinctions between statistical interpolation methods like kriging and observational data assimilation methods (discussed previously) is that kriging is based completely on observations (Biau et al., 1999). Data assimilation is based upon observations, model physics, resolution, and domain size (e.g., Aberson, 2008).

Temporal and spatial (both horizontal and vertical) variability of observations in various atmospheric phenomena suggest a complex relationship between the autocorrelation, observational density, observation method, and location of the observations. Tables 3.6 and 3.7 summarize the findings of studies that examined the temporal or spatial autocorrelations for $|V_h|$, T, water vapor, precipitation, and w. It is important to note that most of the studies presented in Tables 3.6 and 3.7 did not analyze observations from TCs, evaluated various physical parameters and observations, used different instrumentation, studied a range of length scales, and used a range of critical correlation coefficients to determine autocorrelation scales. Nevertheless, they are included because of the lack of studies that have examined autocorrelations in dropsonde data in TCs and they provide some context to the autocorrelations observed from the TCI dataset.

There are large variations in the autocorrelation horizontal distances for the non-TC variables considered in Tables 3.6 and 3.7, with lengths ranging from 200 m (w; Lothon et al., 2006) to 1000 km (T; Gunst, 1995). The vertical autocorrelation length scales for w and water vapor given in Tables 3.6 and 3.7 are comparable and less than 1 km (Fisher et al., 2013; Lothon et al., 2006). The 0.5-autocorrelation temporal scales for T and horizontal wind speed (Tables 3.6 and 3.7) are comparable, between 4–12 h, and are a function of altitude (Brett and Tuller, 1991; Raymond et al., 2003; Pérez et al., 2004). Horizontal autocorrelation spatial scales for T are greater than, or are comparable to, the horizontal autocorrelation spatial scales for horizontal wind (Tables 3.6 and 3.7). Convection, and variables related to convection (e.g., precipitation rates), should have smaller correlation length scales horizontally due to higher small-scale variance (Fisher et al., 2013). Spatial autocorrelations in precipitation and rain rate drop below 0.5, from 1.5 to 10 km, with convective precipitation primarily at 4 km and stratiform precipitation primarily at larger distances (Tables 3.6 and 3.7). Lothon et al. (2006) examined the autocorrelation of w in the daytime, convective, planetary boundary layer (PBL) using Doppler Lidar data and found small, 0.5, autocorrelation distances between 200–300 m both horizontally and vertically (Tables 3.6 and 3.7).

Black et al. (1996) examined the spatial autocorrelations of w in TCs from flight-level and Doppler radar data. Black et al. (1996) found that w autocorrelations of approximately 0.2 were statistically significant, horizontal and vertical autocorrelation distances were between 1–6 km, and updrafts were more spatially correlated than downdrafts, especially within the eyewall. The 0.2-autocorrelation threshold noted in Black et al. (1996) indicates statistically significant relationships, but does not indicate that the autocorrelation is strong. The use of a higher autocorrelation threshold, like 0.5, would indicate a stronger relationship and decrease the horizontal, and vertical, autocorrelation distances in Black et al. (1996) by approximately 50%.

The definition of convection, updrafts, and downdrafts is also important in discerning the autocorrelation scales within those updrafts and downdrafts. Jorgensen et al. (1985) defined convective vertical motions in TC flight-level data as continuous positive or negative vertical velocities for at least 500 m, with at least one data point achieving a magnitude of 0.5 m s^{-1}. Convective cores were defined as continuous w magnitudes of at least 1 m s^{-1} for 500 m or greater. These distances and values were determined iteratively and subjectively in LeMone and Zipser (1980) to more easily differentiate turbulent motions from coherent vertical velocities without needing a complex statistical analysis. This definition was also adopted by studies such as Black et al. (1994); however, the spatial correlations of the w data were not presented. Black et al. (1996) defined an updraft or downdraft as continuous, X-band radar, vertical velocities exceeding $|1.5 \text{ m s}^{-1}|$ with at least one data point exceeding $|3 \text{ m s}^{-1}|$.

Eastin et al. (2002a,b, 2005b) examined the spatiotemporal characteristics and statistics of instrument wetting events (IWEs) in TCs, which are periods where flight-level, probe-derived T measurements were significantly (using the 3σ level; or ΔT =0.5°C) colder than radiometer-derived temperatures. These IWEs were primarily correlated with the presence of updrafts and appreciable cloud water. The results from Eastin et al. (2002a,b, 2005b) were not included in Tables 3.6 and 3.7, because they did not directly report upon the autocorrelation of the data nor present correlograms of the data. Eastin et al. (2002a) showed that 90% of the IWEs were less than 10 km in scale. Magnitudes of moisture, w, and ΔT decrease and, therefore, decorrelate rapidly within 3–6 km of the peak of the IWEs (Eastin et al., 2002a). θ_e and moisture values decreased rapidly (decorrelated) within 8 km radially outward of updraft maxima (Eastin et al., 2002b). The mean IWE diameters were also a function of altitude, where IWE diameters were 7 km below the freezing level and 14 km above (Eastin et al., 2002a).

3.3.2 Data and methods

In order to compute the temporal and spatial autocorrelation scales, the data within any sounding need to be detrended (Janert, 2011). If a trend or mean state is present in the data, then correlograms show smoothed and high-amplitude periodic curves or large, negative correlations at long lags (see Appendix F). Rather than using a linear detrend, median atmospheric profiles of w, T, $|V_h|$, RH, and θ_e were used to detrend the data. Six detrend methods were explored: 1) no detrend; 2) detrend using median profiles from a specific date (date detrend); 3) detrend using median profiles from a specific TC (storm detrend); 4) detrend using median profiles from the entire dataset (total detrend); 5) detrend using median profiles within four radial sections from the entire dataset (radial detrend); and, 6) detrend using median profiles within four radial sections from a specific date (D+R detrend). The sixth method (D+R detrend) was ultimately used, because it exhibited the largest autocorrelations among the most parameters, while accounting for the variance in the mean state radially, from date-to-date, and from storm-to-storm. The four radial sections were: 1) $\leq 1.25\mathrm{R}^*$; 2) 1.25–3R^*; 3) 3–5R^*; and, 4) 5–10R^*. It should be noted that by combining all soundings within 1.25R^*, data from the high-gradient region near the eyewall are used and the median state can be influenced by the soundings within the eye itself. Further details about the six detrending methods, their results, and comparisons can be found in Appendix F.

The D+R detrend median profiles for each variable and each date are provided in Figures 3.29–3.31 and the total number of soundings in each radial section are provided in Table 3.9. The mean and median number of soundings in each radial section was 11–12, with a maximum of 24 (Joaquin on 5 October) and a minimum of zero (Patricia on 20 October). Many of the median w profiles resemble profiles observed by Black et al. (1996) and primarily show weak, near zero vertical motions below the average freezing level ($5-6$ km) and stronger vertical velocities aloft (Figs. 3.29a–d, 3.30a–d, 3.31a–d), but it is unknown if this increase is real or due to errors aloft (section 3.1). The median w profiles were especially noisy in Patricia on 20 and 23 October likely due to the low number of soundings in the radial section (Table 3.9) or strong vertical motions in the eyewall (e.g, Fig. 3.14). The $|V_h|$ median profiles differ from day-to-day and show the evolution of the TC wind fields, but also show that peak $|V_h|$ strengths generally occurred between 0.5 and 1 km (Figs. 3.29e–h, 3.30e–h, 3.31e–h). The $|V_h|$ median profile for Patricia on 23 October had a noisy double jet structure, with strong median $|V_h|$ from 5–7 km similar to the double jet structure in the eyewall of Patricia shown by Rogers et al. (2017) (Fig. 3.31e). Median RH profiles show that the lowest 6 km were fairly moist and varied slightly from day-to-day, but the upper levels were dry (Figs. 3.29i–l, 3.30i–l, 3.31i–l). The zero percent RH values above 12.5 km are a manifestation of the sensor performance below $-40°$C (e.g., Bell et al., 2016). RH values at temperatures below $-40°$C are telemetered as “NaN”, because the sensor is not rated for extremely cold temperatures. Further, no “thermodynamic” smoothing or adjustments are made to the measurements. T and θ_e varied slightly from day-to-day, and had smooth decreases aloft for

T and increases aloft for θ_e (Figs. 3.29m–t, 3.30m–t, 3.31m–t).

To calculate horizontal dropsonde-to-dropsonde autocorrelations, median profiles similar to those in Figures 3.29–3.31 were created using 0.25 km bins from 0 to 17 km to account for small altitudinal variations among the observations and differences in the number of data points in each sounding. The bin size was chosen to match the altitudinal binning scheme in section 3.1.

Spatial dropsonde-to-dropsonde autocorrelations and corresponding distances were computed using the following equations:

$$\bar{r}_t(k) = \frac{\sum_{i=1}^{n}(X_i' - \overline{X_i'})(X_{i+k}' - \overline{X_{i+k}'})}{\sqrt{\sum_{i=1}^{n}(X_i' - \overline{X_i'})^2(x_{i+k}' - \overline{X_{i+k}'})^2}} \tag{3.20}$$

$$d = \sqrt{(x_i - x_{i+k})^2 + (y_i - y_{i+k})^2} \tag{3.21}$$

where the autocorrelation ($\bar{r}_t$) is calculated for the binned median D+R detrended data (X') at a distance d in the x-y plane. The autocorrelation of each sounding is calculated from pairs of all soundings and not just those immediately adjacent to a given sounding. n is the total number of soundings for each date or TC, and k is an index that runs from 0 to $n-1$ that accounts for each sounding in the calculation. If it is assumed that the D+R detrend process accurately removed the mean state in each sounding, then the mean of X' should be zero in all of the equations presented here. The d used is the mean distance between the two soundings. Given the uneven spacing of soundings and the finer resolution of observations within the core, the spatial autocorrelation distances presented here may be biased towards lower values. In contrast, the use of a median profile creates smoother soundings than what was actually observed in TCI and may bias autocorrelation distances toward larger values.

These assumptions in the methodology, however, do not severely impact the results, because it is not expected to have statistically significant high autocorrelations at large (> 100 km) distance scales within a TC, even in areas outside of the core.

To calculate the autocorrelations within an individual sounding, data were ordered with respect to time and the "acf" function in the R software package was used for each individual sounding. This was done for each observation day and for each storm. The acf function computes autocorrelation using the following equations:

$$r_t = \frac{c_t}{c_o} \tag{3.22}$$

$$c_t = \frac{1}{n} \sum_{min(n-t,n)}^{max(1,-t)} [X'_{s+t} - \bar{X}'][X_s - \bar{X}'] \tag{3.23}$$

$$c_o = \frac{1}{n} \sum [X' - \bar{X}']^2 \tag{3.24}$$

where r_t is the autocorrelation, c_t is the autocovariance, c_o is the variance of the series, n is the length of the series, s is time, and t is some lag forward in time (Venables and Ripley, 2002). For the temporal autocorrelations within any given sounding, the X' data were not binned like in the dropsonde-to-dropsonde data. The soundings, therefore, have differences in the total number of data points, which is a function of the fall speed, horizontal wind speed, dropsonde fall behavior, icing, and missing data. The autocorrelations were computed assuming that no missing data was present and the temporal resolution was 1 Hz. If there was missing data in the sounding, the data were not replaced with an interpolated mean value or padded with a fill value, because that would, potentially, increase the autocorrelations artificially depending on how many missing data points were present. It is hypothesized that missing data would affect the results by biasing the autocorrelations to smaller temporal scales. Due to the highly-accurate data telemetry and data screening process used, however, large regions of missing data are rarely present in soundings. The autocorrelation scales and correlograms presented here are interpolated splines over all of the soundings for an individual date or TC, which would decrease the impact of missing data in a relatively small number of soundings within the dataset.

3.3.3 Results

The autocorrelations for each TC and in total were plotted as correlograms. Individual correlograms for each of the ten days in the dataset are not provided, but the results from those figures are summarized in Tables 3.10 and 3.11, and Figure 3.32. Correlograms for each TC are provided in Figures 3.33 and 3.34. The correlograms are smoothed splines fitted to scatter plots of the correlograms for each sounding or altitude level. Table 3.10 documents the autocorrelation spatial scales where correlation drops below 0.5 for adjacent data points at a fixed altitude (dropsonde-to-dropsonde). Table 3.11 documents the autocorrelation time scales where correlation drops below 0.5 for data within a given individual sounding. The means, medians, and standard deviations for the spatial and temporal autocorrelation scales computed from all ten observation days are included in Tables 3.10 and 3.11.

3.3.3.1 Correlations from dropsonde-to-dropsonde

w, RH, and θ_e had the smallest mean and median spatial autocorrelation length scales at 4–6 km (Table 3.10). w, however, generally had the smallest spatial autocorrelation length scales. All variables had comparable standard deviations in the 0.5-autocorrelation length scales between 4–5 km, but $|V_h|$ and T had the smallest spreads in 0.5-autocorrelation distances (Table 3.10). Mean and median $|V_h|$ and T spatial autocorrelation length scales were 10–11 km and 7–9 km, respectively (Table 3.10). Most of the autocorrelation length scales were comparable in magnitude or less than the minimum sounding spacing on each day (Table 3.8).

The autocorrelation length scales for all variables increased with increasing RMW (Fig. 3.32a). The length scales for w, RH, and θ_e had the strongest positive correlations with RMW size. While the correlations do not indicate a robust, conclusive relationship between the RMW size and the spatial 0.5-autocorrelation scales because of the relatively small sample size, it is plausible that the spatial autocorrelation scales could be influenced by the storm-scale structure of the TCs. $|V_h|$ and T do show appreciably strong (> 0.5) correlations with the RMW, but not as strong as the other three variables. This result is interesting, because $|V_h|$ and T would be expected to have the strongest correlations with the RMW based upon the well-recognized idea that gradient or thermal wind balance dominates the storm-scale structure of TCs (e.g., Willoughby, 1990; Molinari et al., 1993). Rather, variables more associated with convective features (w, RH, and θ_e) are more correlated with the RMW. Figure 3.32a also illustrates that most of the autocorrelation length scales are smaller than the RMW by a factor of 4–8, with $|V_h|$ mostly on the low-end and w on the high-end of the range. Despite the relationship between the RMW and the autocorrelation length scales, data are still grouped by each TC to examine the differences in the temporal and spatial autocorrelations present from storm-to-storm.

Figure 3.33 shows the spatial correlograms for all five variables in Marty, Joaquin, and Patricia. w, RH, and θ_e decorrelate rapidly within 10–20 km, reaching zero at approximately 20 km (Fig. 3.33a, c, e). T and $|V_h|$ decorrelate slower, reaching zero between 40–60 km

(Fig. 3.33b, d). All of the variables have autocorrelations that fluctuate around zero outside of 50 km (Fig. 3.33).

Marty had the largest 0.5-autocorrelation length scales out of the three TCs for w, RH, T, and θ_e at 3.2–4.2 km, likely attributed to the weaker convection and temperature gradients in Marty. Joaquin and Patricia had comparable 0.5-autocorrelation length scales for w, RH, and θ_e at 2.8 km. The 0.5-autocorrelation length scales for T in Joaquin and Patricia were also comparable, but larger at 3.6 km. Patricia had the largest 0.5-autocorrelation length scale for $|V_h|$, which is not surprising as the horizontal wind field associated with the primary TC circulation was strong and expansive in Patricia (e.g., Fig. 3.14). The 0.5-autocorrelation length scales for $|V_h|$ in Marty and Joaquin were comparable at approximately 4.2 km. The 0.5-autocorrelations were examined as a function of altitude, but the corresponding distances were often non-linear or non-monotonic and no robust conclusions could be made.

To put the autocorrelation length scales into context, the values are compared to the correlation length scales in Tables 3.6 and 3.7. The correlation distances observed in non-TC studies, except for w, are considerably larger compared to what was observed in the TCI data. For example, the 0.5-autocorrelation lengths for T observed on an individual day and in an individual TC are much smaller than the horizontal autocorrelation distances observed by Gunst (1995) and Nichol and Wong (2008). The autocorrelation length scales for w were primarily between 1 and 5 km from day-to-day (excluding 20 October), and 2 and 4 km from storm-to-storm (Table 3.10 and Fig. 3.33a). The w length scales are most comparable to the rainfall and convective rain rate autocorrelation distances over land with rain gauge, and radar, data in Habib et al. (2001), Bringi et al. (2015), and Jameson (2017). The values are also slightly smaller than the w 0.2-autocorrelation length scales adjacent to updrafts and downdrafts in TCs as shown by Black et al. (1996), but are comparable if Black et al. (1996)

used a 0.5-autocorrelation threshold. Most of the w autocorrelation length scales observed in the TCI data are a factor of ten larger than the 0.5-autocorrelation horizontal length scale observed with Lidar data over land by Lothon et al. (2006).

3.3.3.2 Correlations within a sounding

The temporal 0.5-autocorrelation scales were above 8 s for all variables and for each observation day, with most above 15 s (Table 3.11). Mean and median temporal autocorrelation scales ranged from 20–31 s for all variables (Table 3.11). The smallest mean and median temporal scales were for w and T. The smaller temporal autocorrelation thresholds in T and w could be due to smaller thermal perturbations away from the median profiles in each radial section (e.g., Fig. 3.30) and weaker vertical motions dominating the vertical velocity distribution (Fig. 3.11). The mean and median temporal autocorrelation scales for θ_e were slightly larger than for w and T at 26.5 s. $|V_h|$ and RH had the largest temporal autocorrelation scales within individual soundings at approximately 30 s. The estimated still air dropsonde fall speed ranges from approximately 52 m s^{-1} at 17.5 km to 18 m s^{-1} at sea-level. It is estimated from the typical fall speeds that vertical autocorrelation length scales would likely range from 0.1–2 km.

Figure 3.32b shows that as the horizontal autocorrelation length scale increases, the temporal autocorrelation scale generally decreases for all variables, except RH and θ_e. The RH temporal scales have a weak, positive correlation with the horizontal autocorrelation length scales (Fig. 3.32b). The θ_e temporal scales have a weak, negative correlation with the horizontal autocorrelation length scales, but this is primarily due to one outlier data point. If this data point was removed, the correlation would be positive at 0.32. This single data point outlier is not present in the other four variables, but did occur in Patricia on 20

October, where few dropsondes were launched (Table 3.9). The strongest correlation was for the w temporal and spatial autocorrelation scales at -0.91. The general negative correlation, especially for w, is not surprising. As a hypothetical situation, if an XDD sampled a coherent tropospheric depth feature, like an eyewall updraft, that sounding will likely not correlate well with other dropsonde data launched outside of the convective region of the eyewall, leading to smaller spatial correlation scales. Conversely, if an XDD sampled an area with weak radial gradients, but incoherent vertical structure, then the dropsonde-to-dropsonde spatial scale will be larger and the temporal scale will be smaller. Similar to the relationship between the RMW and spatial 0.5-autocorrelation scale (Fig. 3.32a), these correlations do not provide robust conclusions because of the relatively small sample size, but they can be used to develop a hypothesis as to the relationships between the two scales.

Figure 3.34 shows the temporal correlograms for all five variables in Marty, Joaquin, and Patricia. All variables decorrelate rapidly within 80 s, reaching zero at approximately 100–150 s (Fig. 3.34). Weak, negative autocorrelation values were observed at longer time lags for all variables (Fig. 3.34). w decorrelated the fastest, but the difference in the rate of decorrelation is negligible.

Joaquin consistently had the largest 0.5-autocorrelation temporal scales out of the three TCs for all variables, but both Marty and Joaquin had the same temporal 0.5-autocorrelation scales for θ_e (Fig. 3.34e). There was little variation in the temporal 0.5-autocorrelation scales for w from storm-to-storm, with temporal scales of 19–21.5 s (Fig. 3.34a). Marty and Patricia had comparable 0.5-autocorrelation temporal scales for $|V_h|$ (27–28.5 s) and RH (26–27.5 s). In comparison, the 0.5-autocorrelation temporal scales for $|V_h|$ and RH in Joaquin were approximately 33 s. Patricia had considerably smaller temporal autocorrelation scales for T and θ_e than compared to Marty or Joaquin. The 0.5-autocorrelations were also examined as a function of radius, but the corresponding temporal scales were often non-linear or non-monotonic and no robust conclusions could be made.

3.3.3.3 Correlations within updrafts and downdrafts

Given that the typical structure of a TC features strong kinematic and thermal perturbations within the convective eyewall and rainbands, it is possible that the 0.5-autocorrelation temporal scales differ in soundings that observed updrafts or downdrafts from soundings in less convective areas. It is also possible that the temporal scales in these updraft and downdraft soundings differ from the findings in Figure 3.34 and Table 3.11, which include all soundings in the dataset. Updrafts and downdrafts are defined here, following section 3.1, as consecutive w above ± 2 m s^{-1} with at least one data point above ± 4 m s^{-1}. There was not a requirement for the minimum depth for the updrafts or downdrafts. Updraft and downdraft soundings are the subset of soundings with at least one updraft or downdraft, respectively, in the sounding. In the rare situation where both an updraft and a downdraft is observed in a given sounding, it is classified as both an updraft and downdraft sounding. P-values of below 0.05 are used to define statistically significant differences.

As an example, shown in Figures 3.35 and 3.36 are sounding profiles from the eyewall of Patricia on 23 October. The red lines denote the start and end of the updraft. The updraft occurred in the midlevels, was 7.45 km deep, and was sampled for over 400 s (Figs. 3.35, 3.36). The updraft was also collocated with the midlevel jet shown by Rogers et al. (2017), high-RH values, a relatively warm θ_e bubble, and small variations in the T profile. The perturbation profile of T, however, shows strong, negative 5–10-K perturbations, and the perturbation profile of θ_e shows weak, near zero perturbations in the middle of the updraft and strong, negative perturbations at the base of the downdraft (Fig. 3.37d, e). These perturbation profiles are not congruent with what is expected for an updraft sounding and may be due to the median profiles reflecting the relatively warmer low- and mid-level eye. In contrast, the w, $|V_h|$, and RH perturbation profiles exhibited strong, positive perturbations within the defined updraft as expected for an eyewall updraft (Fig. 3.37a, b, c). The temporal autocorrelations within this sounding were significantly larger than for the entire date, with a p-value of 0.009 (Fig. 3.38). The autocorrelations for the Patricia eyewall sounding ranged from 43 s (RH) to 113 s (θ_e).

Temporal autocorrelations were computed for all 78 updraft and 37 downdraft soundings on each day and are provided in Tables 3.13 and 3.14. The number of updraft and downdraft soundings for each day is provided in Table 3.12. The mean and median 0.5-autocorrelation temporal scales in updraft soundings were larger than, or comparable to, the temporal scales in all soundings, except for RH, which was statistically significantly smaller by a Student's t-test (Tables 3.11, 3.13). Similarly, mean and median 0.5-autocorrelation temporal scales in downdraft soundings were larger than, or comparable to, the temporal scales in all soundings, except for RH (Tables 3.11, 3.14). None of the differences, however, were statistically significant.

Figures 3.39 and 3.40 show the temporal autocorrelations for individual soundings computed similarly to the single sounding in Figure 3.38. The temporal scales for w, $|V_h|$, T, and θ_e in updraft soundings have positive correlations with the maximum updraft depth in the soundings (Fig. 3.39). The correlation for w was strong at 0.76, with a p-value of $6\text{x}10^{-16}$ (Fig. 3.39a). Correlations were also statistically significant at a p-value below 0.05 for $|V_h|$ (0.04) and θ_e (0.008), but the correlations themselves are relatively weak compared to w. The positive, statistically significant correlations between w and θ_e to the mean updraft depth agrees well with the parcel buoyancy arguments and correlations between draft core diameters and mean w strength, and thermal buoyancy, in Eastin et al. (2005b). RH was uncorrelated with draft depth in updraft soundings (Fig. 3.39c). In contrast to the updraft soundings, the downdraft soundings had near-zero or weakly negative correlations between the maximum downdraft depth and temporal autocorrelation scale, with no statistically significant relationships (Fig. 3.40). The positive correlations for updraft soundings indicate that there are, potentially, statistically significant relationships between the temporal autocorrelation scales and the depth of the updrafts, even though the mean and median temporal autocorrelation scales do not differ appreciably from the total dataset.

3.3.4 Discussion

From the large dataset of 437 XDDs in three TCs, it was evident that mean temporal autocorrelations were approximately 20–30 s for w, T, $|V_h|$, RH and θ_e in the entire dataset. This corresponds to an approximate altitudinal depth of 0.3–1.5 km, given the typical XDD fall speeds. The temporal autocorrelation scales suggest that interpolating sounding data to matching altitudes is justifiable within small 0.5-km intervals. The binning scheme used here is finer than this estimate. These results also imply that the XDD sampling frequency adeptly oversampled the TCs in TCI.

From dropsonde-to-dropsonde, one of the conclusions that can be drawn is the minimum spatial distribution of dropsondes needed to accurately depict a TC with transects of dropsondes from the observed atmospheric variables. Another way to phrase the previous statement is: "How close together can the XDDs be in TCs before adjacent data points become appreciably correlated?". The horizontal autocorrelation length scales for all variables, except for w (Black et al., 1996; Lothon et al., 2006), are smaller than what was observed in previous studies (Tables 3.6, 3.7). Specifically, $|V_h|$ (Wylie et al., 1985) and T (Gunst, 1995; Nichol and Wong, 2008) autocorrelation length scales are smaller for all observation days in the dataset. It is important to note that one cannot truly know the spatial correlation limit without testing observations (like the XDDs) at a much higher launch rate/finer horizontal resolution. The autocorrelations below the minimum horizontal sounding spacing (e.g., Patricia on 23 October; Tables 3.8, 3.10) are estimates that are limited by the spacing of the original dataset. The relatively high resolution of the original dataset could be why some of the autocorrelation length scales for the TCI data are smaller relative to past studies (Tables 3.6, 3.7). It is also plausible that the features measured by the non-TC studies were synoptic-scale features rather than mesoscale features, like in the three TCs observed during TCI, which would lead to smaller autocorrelation length scales (Tables 3.6, 3.7). Regardless, the agreement between the spatial autocorrelations for w in this section and the spatial autocorrelations for w radar data adjacent to updrafts and downdrafts in Black et al. (1996) is encouraging, and provides support for the findings herein.

The medians for all of the individual days illustrate that w, RH, and θ_e all had low spatial autocorrelations between 4–6 km (Table 3.10). This agrees well with the model grid spacing required to resolve TC eyewall kinematics and physics (Gentry and Lackmann, 2010). The spatial autocorrelation scales for w, RH, and θ_e also agree well with the mean diameter of strong, buoyant updrafts documented in flight-level observations (e.g., Black et al., 1996; Eastin et al., 2005b), which indicate that the spatial scales for these variables are governed at the convective scale and not the storm-scale. $|V_h|$ and T had slightly larger dropsonde-to-dropsonde spatial autocorrelation scales, with means/medians of approximately 7–11 km, which agrees well with the model grid spacing required to resolve features on the scale of the average RMW (approximately 55 km; Kimball and Mulekar, 2004; Gentry and Lackmann, 2010). When data were combined for each TC, w or θ_e always had the smallest autocorrelation length scale, with the mean and median below 2.9 km. RH had comparable, but slightly larger autocorrelation spatial scales in the combined three TCs. $|V_h|$ or T always had the largest autocorrelation length scales for each TC between 3–6 km. The results, not surprisingly, imply that the spatial resolution of dropsondes needed to adequately depict the thermal or horizontal wind fields in transects of TCs is larger than what is needed to adequately depict convection and convection-related variables by approximately a factor of two.

The spatial requirements of the XDDs for each atmospheric variable present an operational challenge for future TC dropsonde campaigns. The spatial autocorrelations presented suggest that the finest spatial resolution (approximately 3–4 km) and quickest launch frequency was at the limit of the required spatial resolution needed to accurately, and adequately, depict TC structure in transects of dropsondes. In situations where the spatial resolution was larger than 3–4 km, spatial interpolation cannot be accurately conducted and does not completely depict the thermal or kinematic structure in the transects of these three TCs. The same conclusion can be made if dropsondes are launched at a resolution of 3–4 km, but one dropsonde fails. The latter situation suggests that a finer horizontal spatial resolution of soundings than what was achieved during TCI should be used in future dropsonde-based TC campaigns. If it is assumed that the 0.5-autocorrelation spatial distances observed in the TCI data indicate the approximate scales of the observable features in the three TCs, then the spacing of observations required to accurately resolve those features can be estimated from the "$4\Delta x$ rule" (Grasso, 2000). The results imply that the launch rate needs to be increased by approximately a factor of four to adequately resolve convection and thermal perturbations in transects of TCs, except for possible small-scale (smaller than 3 km) eyewall vortices (Grasso, 2000; Gentry and Lackmann, 2010). This assumes that the

XDDs can adequately measure both weak and strong convection, since the expected vertical velocity errors are ±1–2 m s^{-1} (section 2.4).

Table 3.1: Number of dropsondes from each day in the dataset (N_t). S is the deep-layer shear (850–200 hPa) in m s^{-1} and S_D is the shear direction in degrees clockwise from the north (°). Intensity is the maximum tangential wind speed in m s^{-1} at 1800 UTC from the SHIPS dataset. The 10R* distances in km for each day is also provided. From Nelson et al. (2019a). ©American Meteorological Society. Used with permission.

Day	Name	N_t	Intensity	S	S_D	10R*
27 Sept	Marty	50	26	11.21	98	370
28 Sept	Marty	58	36	11.00	89	210
02 Oct	Joaquin	44	57	4.90	151	310
03 Oct	Joaquin	43	67	13.20	127	270
04 Oct	Joaquin	55	44	4.90	66	380
05 Oct	Joaquin	53	39	3.90	39	490
20 Oct	Patricia	12	15	5.25	42	770
21 Oct	Patricia	51	26	2.93	195	400
22 Oct	Patricia	43	59	0.62	146	190
23 Oct	Patricia	28	93	4.58	21	110
TOTAL	——	437	46 (avg)	6.25 (avg)	——	350 (avg)

Table 3.2: Mean, median, and standard deviation of vertical velocity in m s^{-1} for all radii, within the core, and outside of the core. From Nelson et al. (2019a). ©American Meteorological Society. Used with permission.

Section	Mean	Median	St. Dev.
0–10R*	0.20	0.00	1.43
0–3R*	0.30	0.06	1.74
3–10R*	0.09	−0.04	0.98

Table 3.3: Number of updrafts and downdrafts from each TC (N) and the mean, median, and maximum/minimum of the peak updraft and downdraft strengths in m s^{-1}. From Nelson et al. (2019a). ©American Meteorological Society. Used with permission.

Updrafts				
Name	N	Mean	Median	Maximum
Marty	17	5.11	4.90	7.23
Joaquin	48	5.91	5.11	18.33
Patricia	38	8.72	6.77	23.89
TOTAL	103	6.58 (avg)	5.59 (avg)	16.48 (avg)
Downdrafts				
Name	N	Mean	Median	Minimum
Marty	9	−5.15	−5.16	−5.90
Joaquin	24	−5.40	−4.81	−8.70
Patricia	10	−4.54	−4.29	−5.95
TOTAL	43	−5.03 (avg)	−4.75 (avg)	−6.85 (avg)

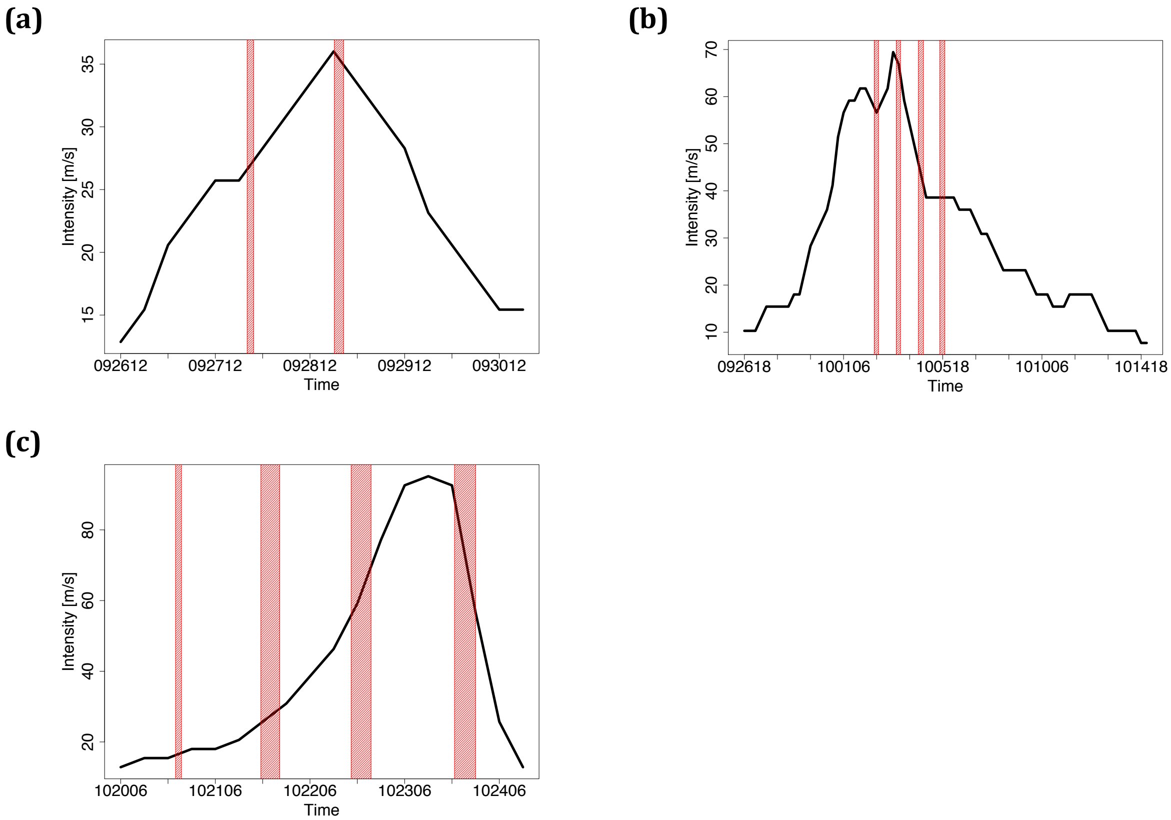

Figure 3.1: Observed NHC Best Track intensity (m s^{-1}) for Marty (a), Joaquin (b), and Patricia (c) over time (month, day, hour). Periods when TCI observed the TCs are shaded in red. From Nelson et al. (2019a). ©American Meteorological Society. Used with permission.

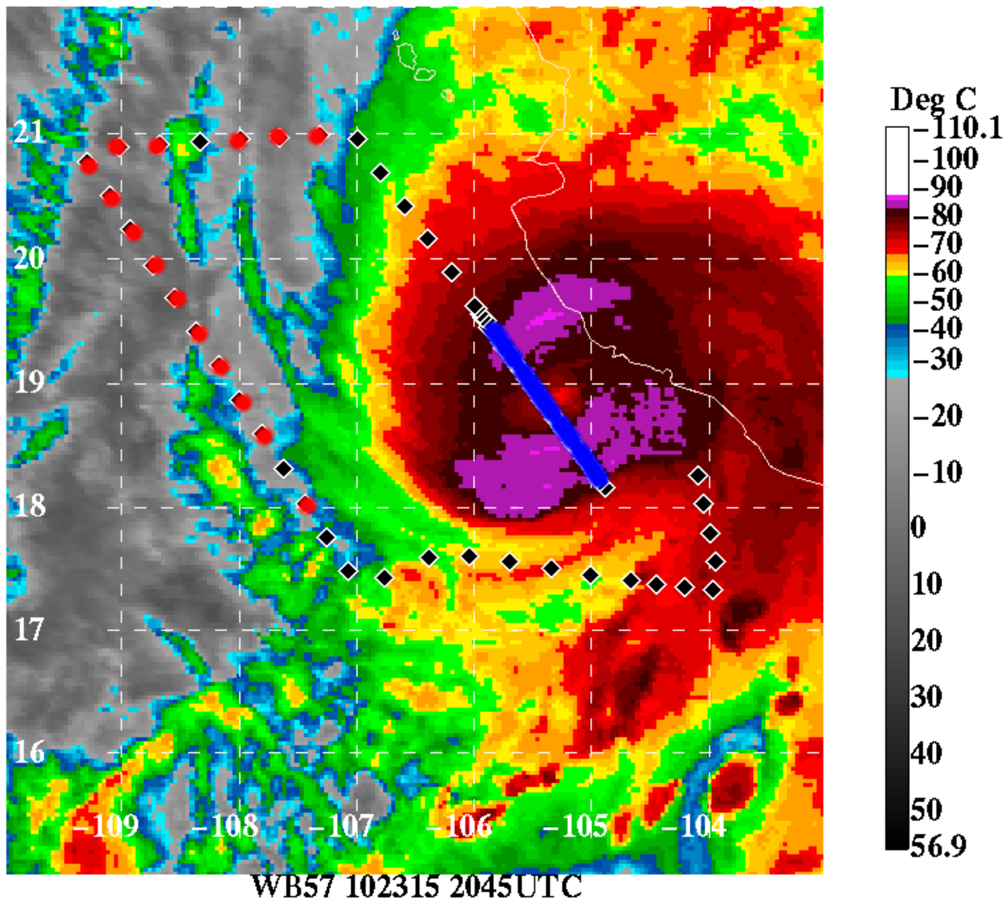

Figure 3.2: IR satellite image of Patricia at 2045 UTC 23 October 2015. Brightness temperatures (°C) are shaded. Launch locations for soundings outside of convection (red), soundings removed from the dataset by quality control or radial restriction (black diamonds), and soundings analyzed (blue) are also included. IR image courtesy of David Vollaro. From Nelson et al. (2019a). ©American Meteorological Society. Used with permission.

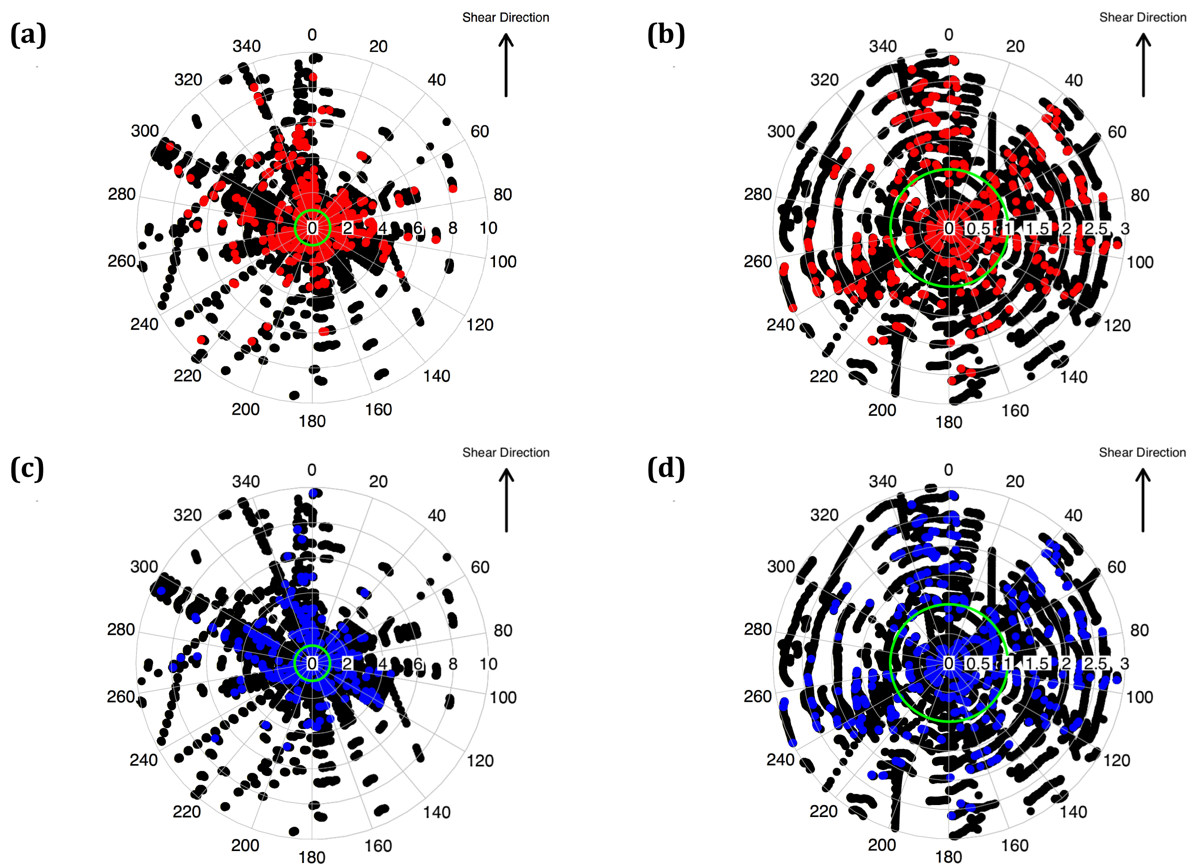

Figure 3.3: Distribution of data points in the total dataset in a shear-rotated framework. Azimuth is in degrees and radius is the radius divided by the RMW (R*). The RMW is the green ring. Panels (a, c) are plotted out to 10R* and panels (b, d) are plotted out to 3R*. Continuous positive vertical velocities within updrafts are in red in panels (a, b) and continuous negative vertical velocities within downdrafts are in blue in panels (c, d). From Nelson et al. (2019a). ©American Meteorological Society. Used with permission.

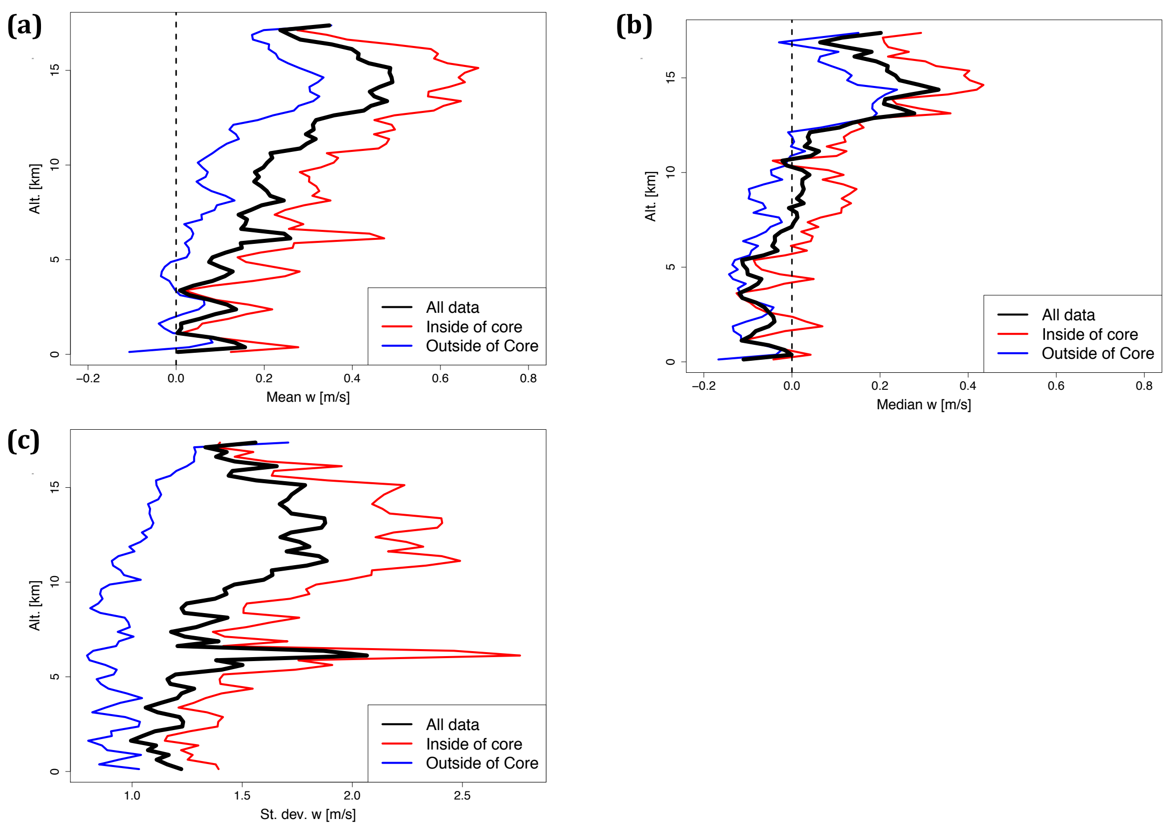

Figure 3.4: Mean (a), median (b), and standard deviation (c) profiles of vertical velocity for the full dataset (black), data within the core (red), and data outside of the core (blue). The dashed black line designates w = 0 m s^{-1}. From Nelson et al. (2019a). ©American Meteorological Society. Used with permission.

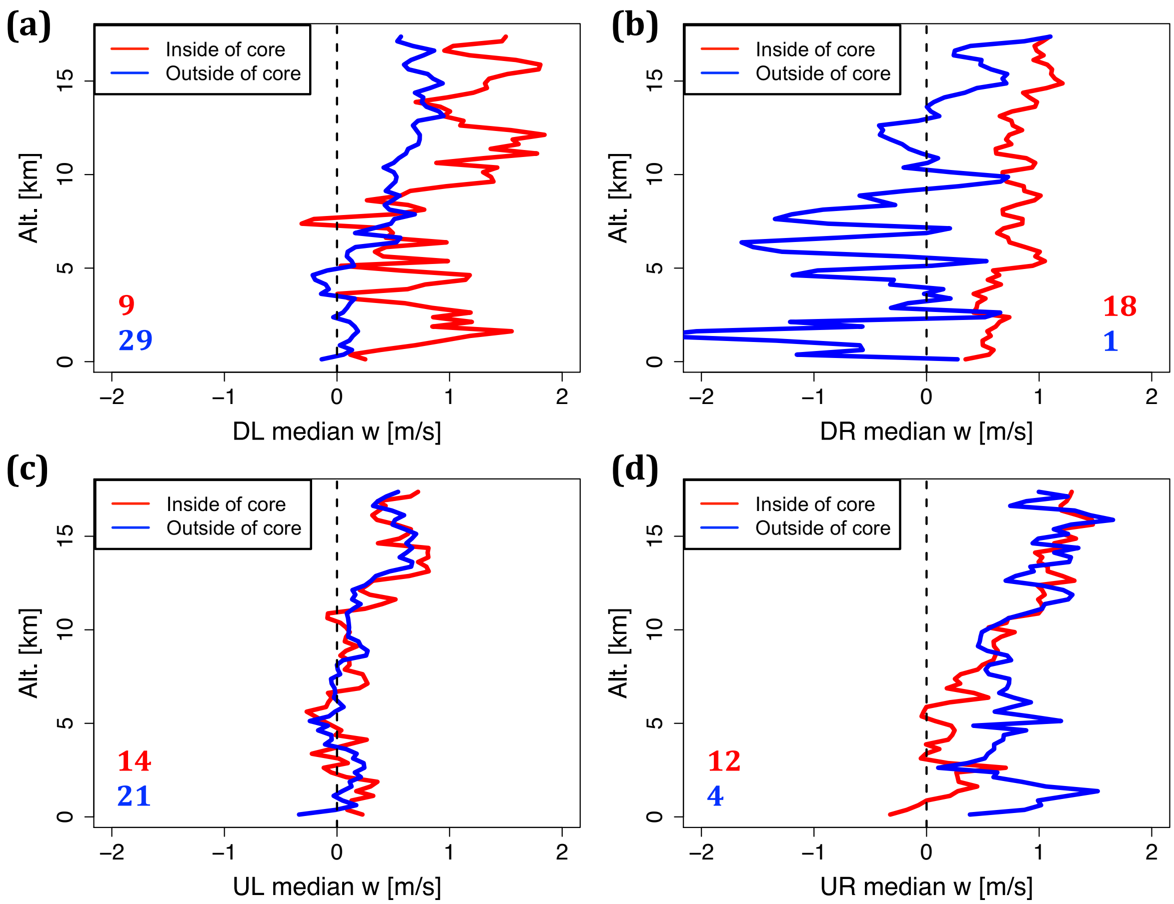

Figure 3.5: Median vertical velocity profiles for data within the core (red) and outside of the core (blue) and within the DL (a), DR (b), UL (c), and UR (d) quadrants in Marty. The dashed black line designates w = 0 m s^{-1}. The approximate number of soundings in each quadrant is provided for within the core (red) and outside of the core (blue). From Nelson et al. (2019a). ©American Meteorological Society. Used with permission.

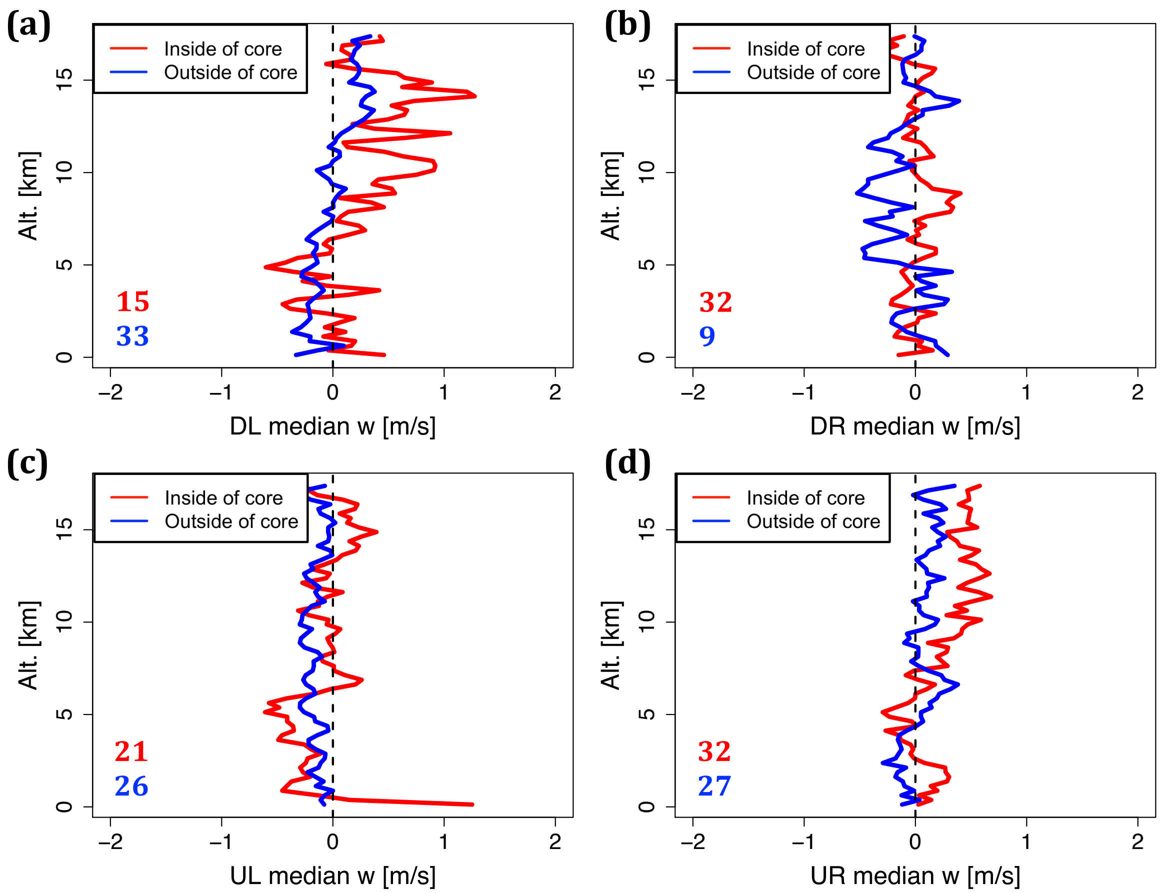

Figure 3.6: Same as Fig. 3.5, but for Joaquin. From Nelson et al. (2019a). ©American Meteorological Society. Used with permission.

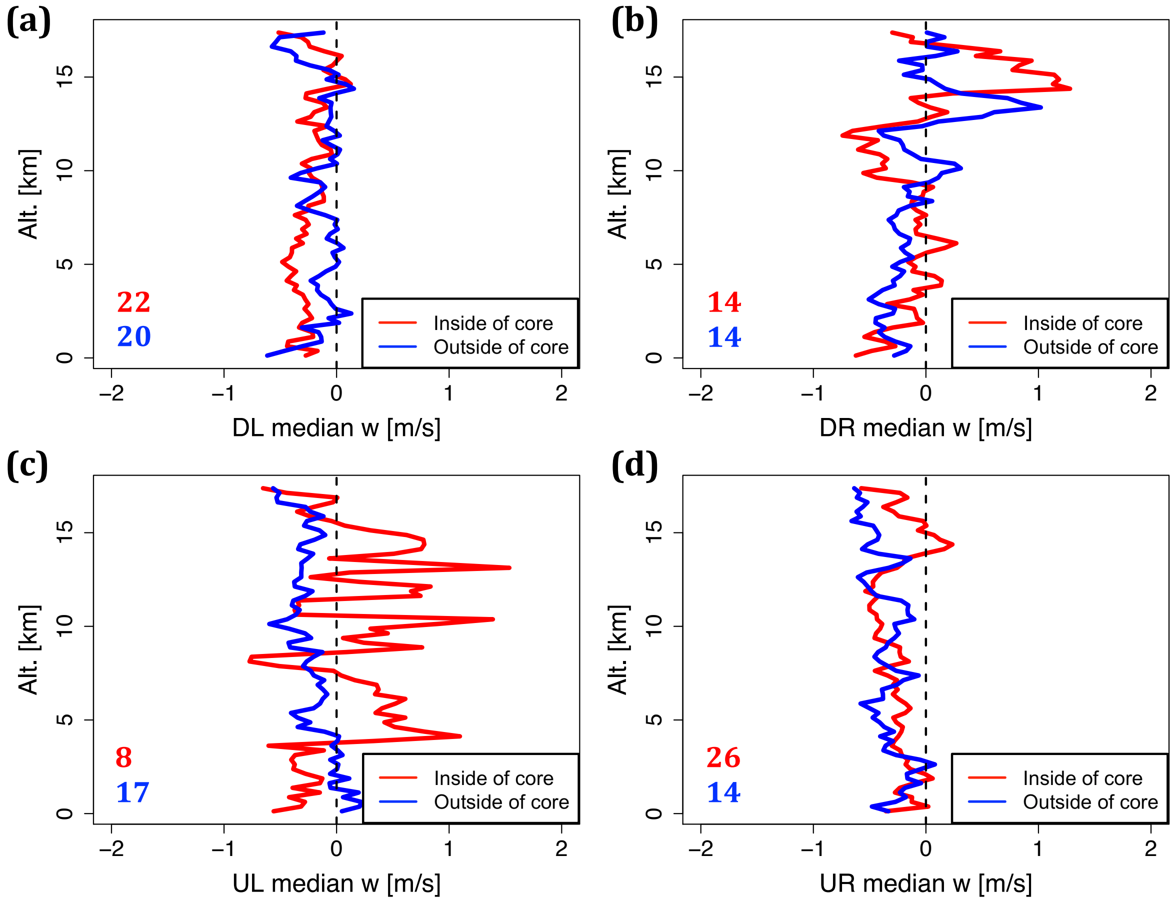

Figure 3.7: Same as Fig. 3.5, but for Patricia. From Nelson et al. (2019a). ©American Meteorological Society. Used with permission.

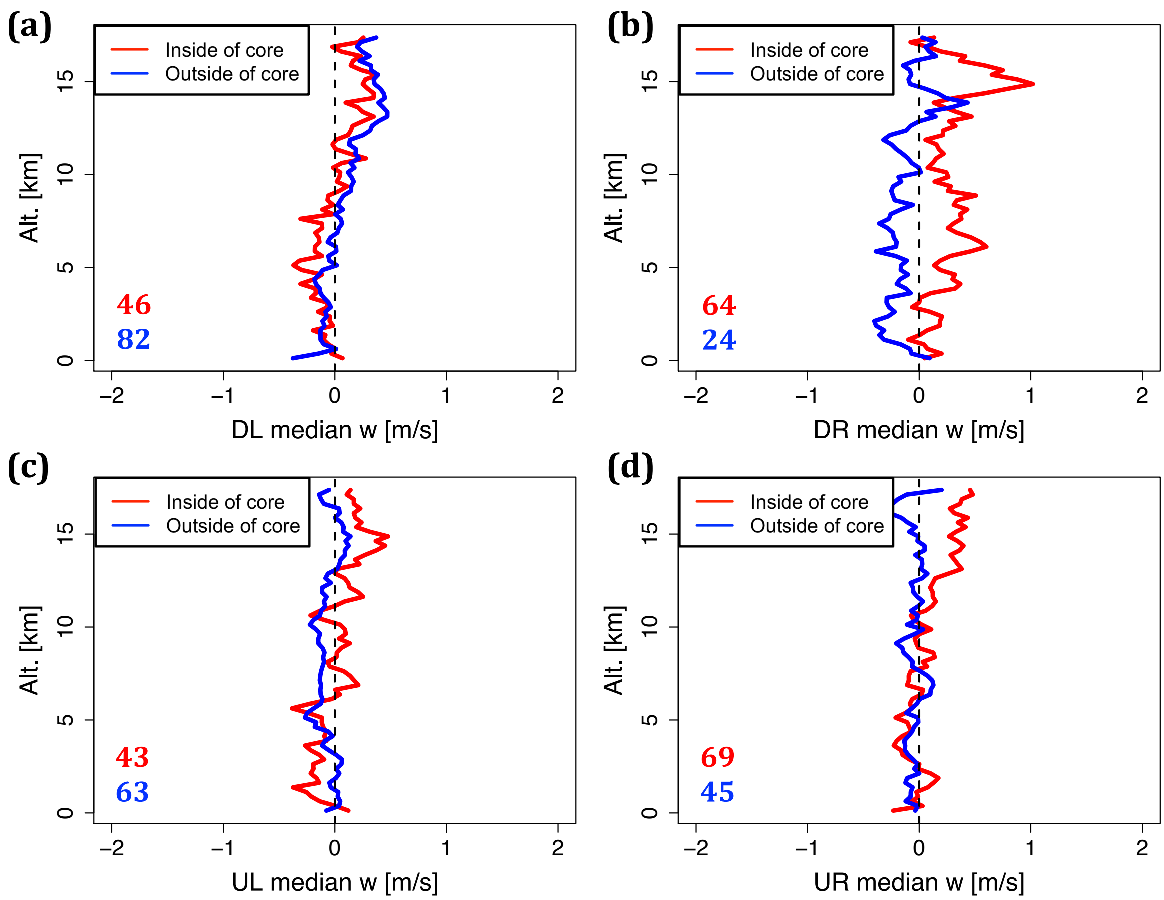

Figure 3.8: Same as Fig. 3.5, but for the total dataset. From Nelson et al. (2019a). ©American Meteorological Society. Used with permission.

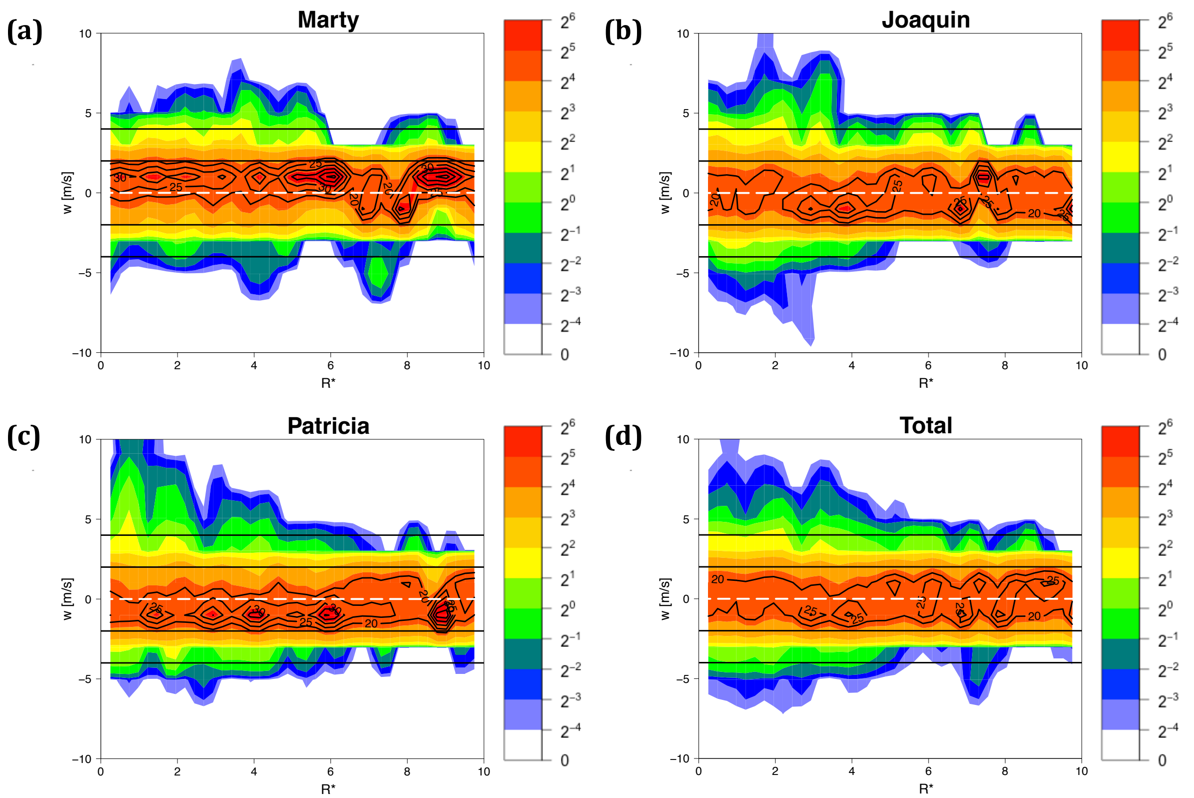

Figure 3.9: CFRD percentages of vertical velocities (m s^{-1}). Panel (a) is for Marty, panel (b) is for Joaquin, panel (c) is for Patricia, and panel (d) is for the entire dataset. Colored contours are percentages on a logarithmic scale. Black lined contours are percentages above 20% in intervals of 5%. The horizontal solid black lines denote the vertical velocity thresholds. The dashed white line designates $w = 0$ m s^{-1}. From Nelson et al. (2019a). ©American Meteorological Society. Used with permission.

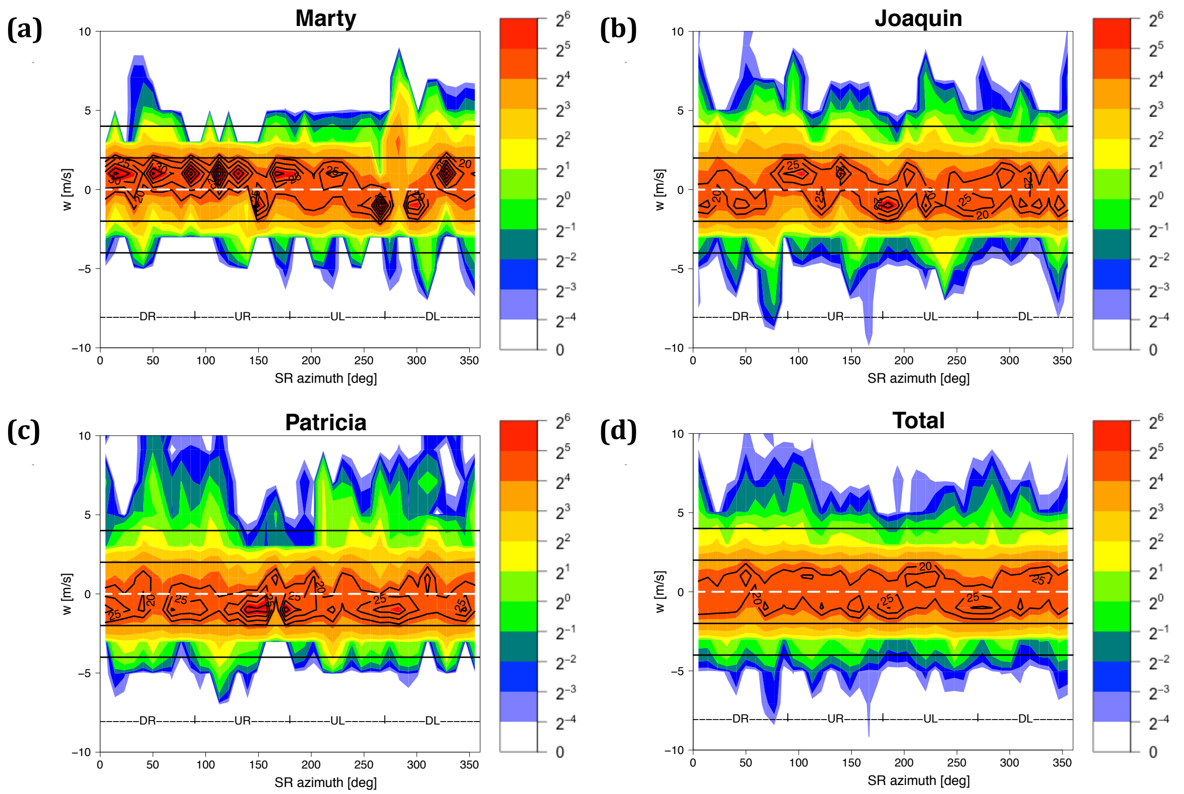

Figure 3.10: CFAzD percentages of vertical velocities (m s^{-1}). Panel (a) is for Marty, panel (b) is for Joaquin, panel (c) is for Patricia, and panel (d) is for the entire dataset. Colored contours are percentages on a logarithmic scale. Black lined contours are percentages above 20% in intervals of 5%. The horizontal solid black lines denote the vertical velocity thresholds. The dashed white line designates $w = 0$ m s^{-1}. From Nelson et al. (2019a). ©American Meteorological Society. Used with permission.

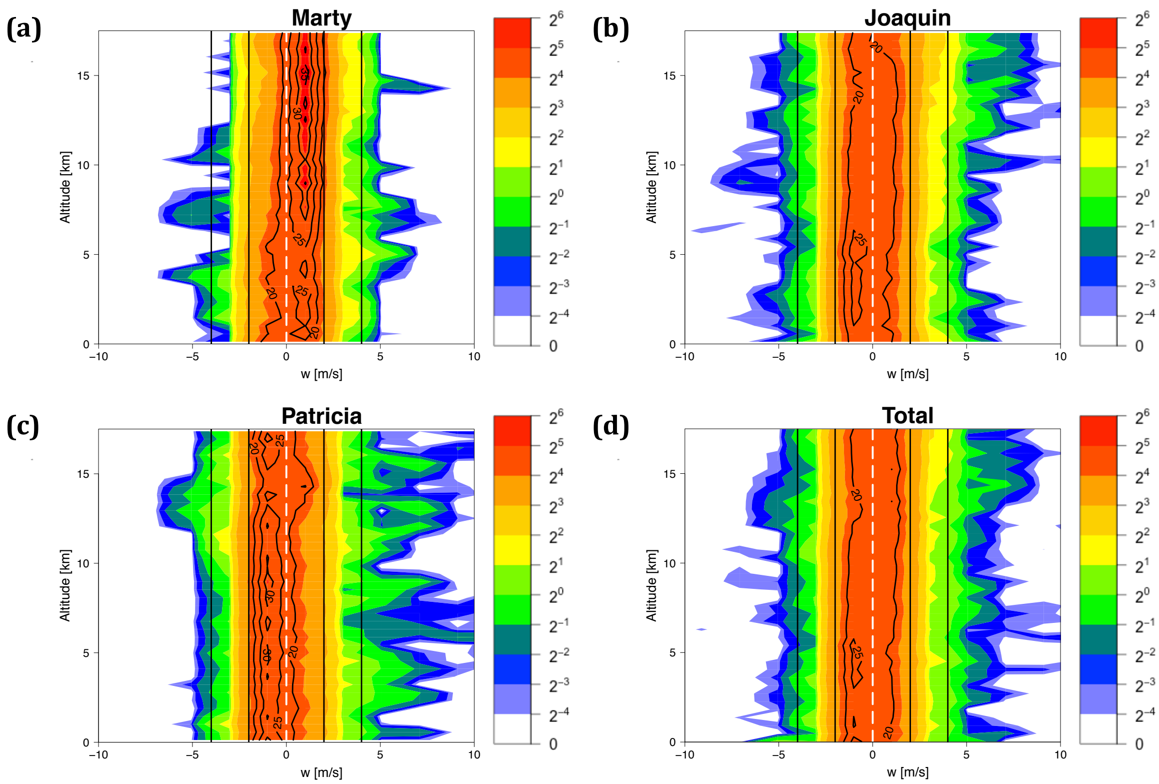

Figure 3.11: CFAD percentages of vertical velocities (m s^{-1}). Panel (a) is for Marty, panel (b) is for Joaquin, panel (c) is for Patricia, and panel (d) is for the entire dataset. Colored contours are percentages on a logarithmic scale. Black lined contours are percentages above 20% in intervals of 5%. The horizontal solid black lines denote the vertical velocity thresholds. The dashed white line designates $w = 0$ m s^{-1}. From Nelson et al. (2019a). ©American Meteorological Society. Used with permission.

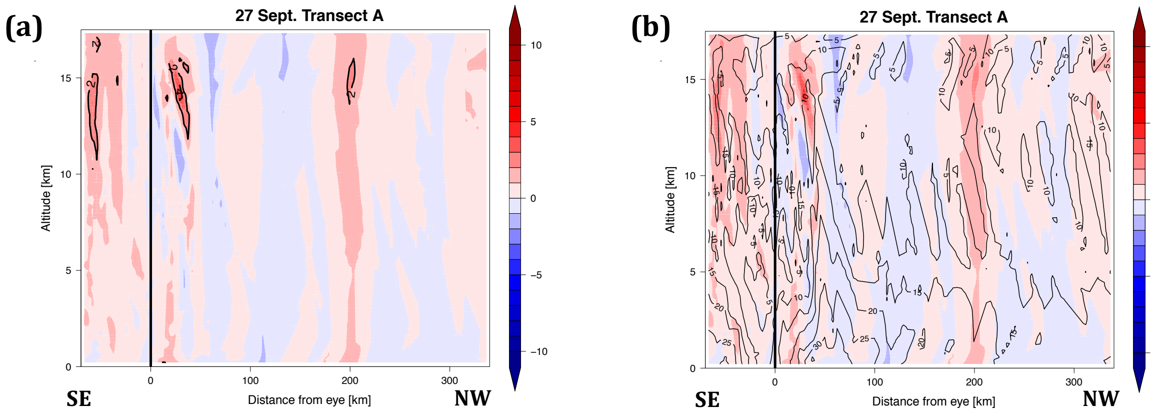

Figure 3.12: Transect cross section for Marty on 27 September. Panel (a) is a cross section of vertical velocity (m s^{-1}, shaded) with vertical velocities greater than |2 m s^{-1}| contoured. Panel (b) is a cross section of vertical velocity (m s^{-1}, shaded) and horizontal wind speed (m s^{-1}, contoured). The TC center is denoted with a solid vertical black line. From Nelson et al. (2019a). ©American Meteorological Society. Used with permission.

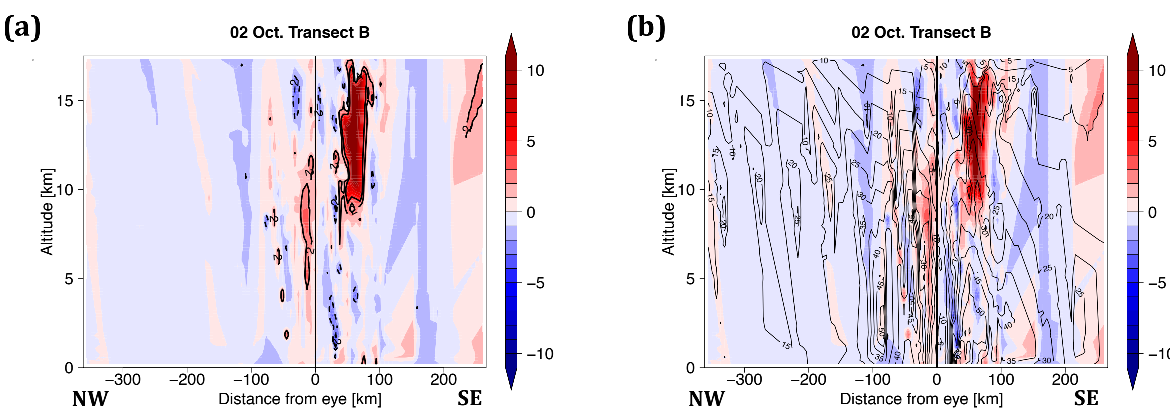

Figure 3.13: Same as Fig. 3.12, but for Joaquin on 02 October. From Nelson et al. (2019a). ©American Meteorological Society. Used with permission.

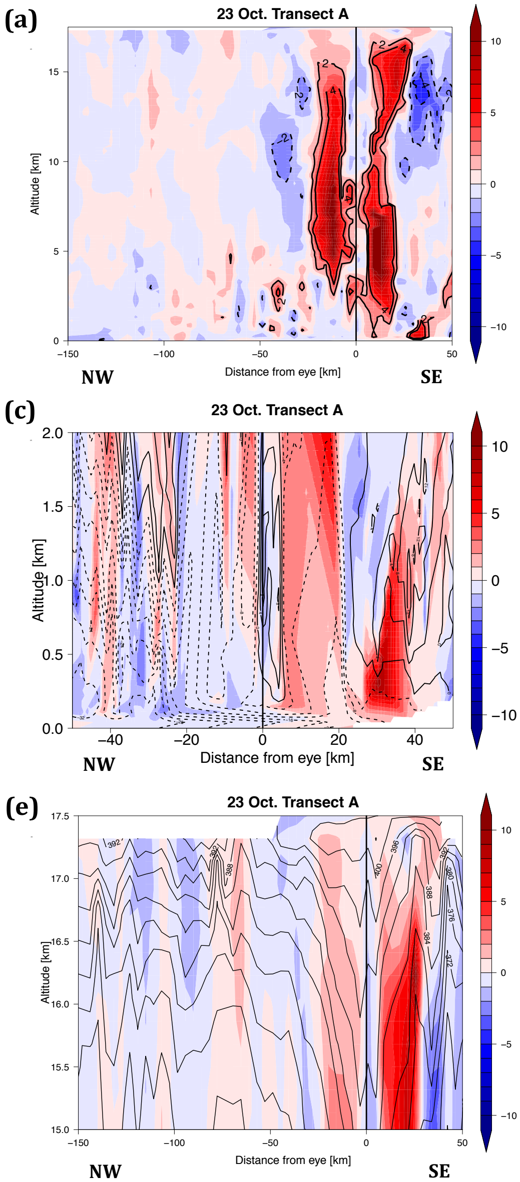

Figure 3.14: Transect cross section for Patricia on 23 October. Panel (a) is a cross section of vertical velocity (m s^{-1}, shaded), with vertical velocities greater than $|2$ m s$^{-1}|$ contoured. Panel (b) is a cross section of vertical velocity (m s^{-1}, shaded) and horizontal wind speed (m s^{-1}, contoured). Panel (c) is a low-level zoom-in of panel (a) showing vertical velocity (m s^{-1}, shaded) and radial velocity (m s^{-1}, contoured), where inflow is negative and outflow is positive. An upper-level zoom-in of panel (a) for vertical velocity (m s^{-1}, contoured) and pressure (hPa, contoured) is shown in panel (d). An upper-level zoom-in of panel (a) for vertical velocity (m s^{-1}, contoured) and potential temperature (K, contoured) is shown in panel (e). From Nelson et al. (2019a). ©American Meteorological Society. Used with permission.

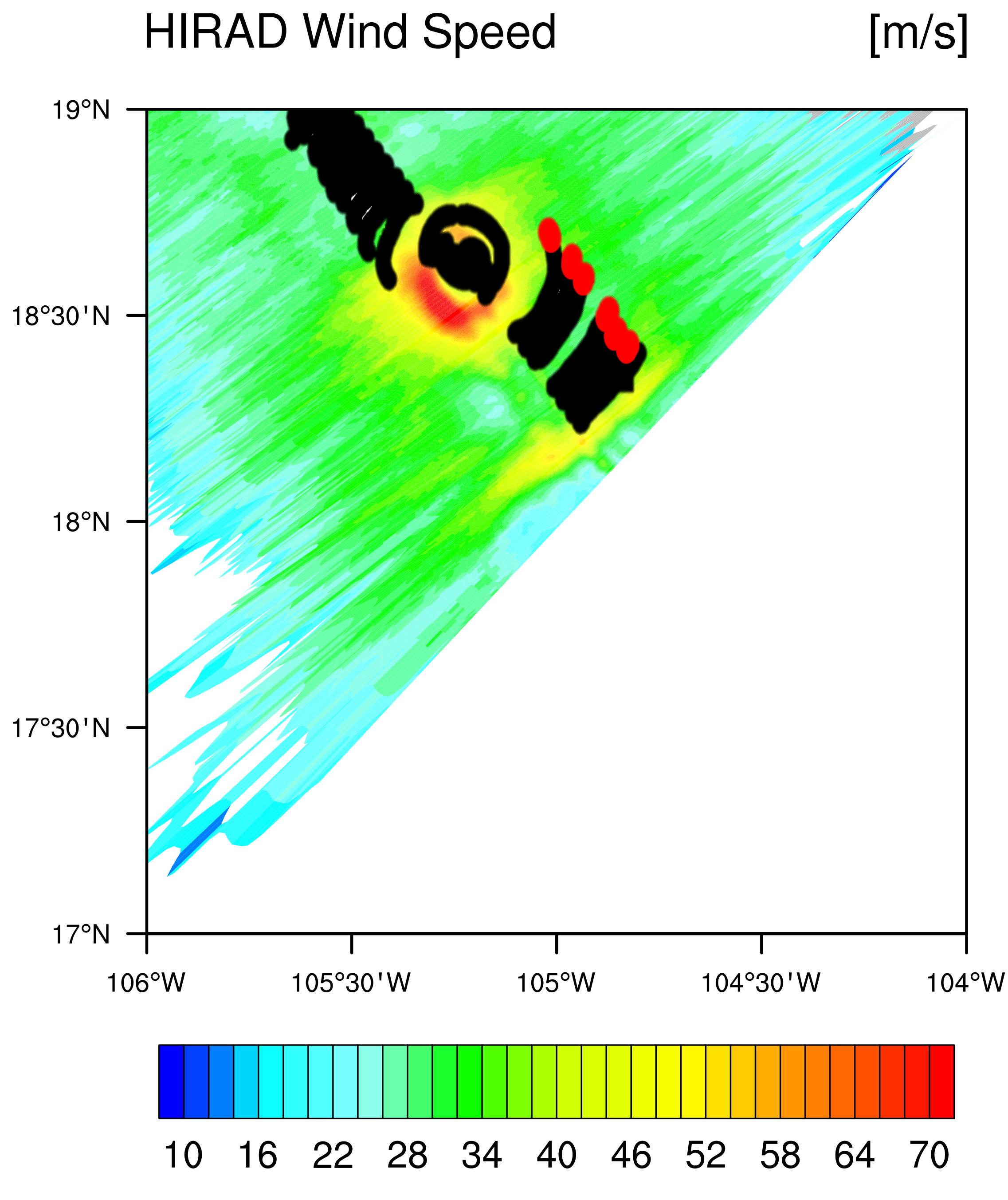

Figure 3.15: HIRAD-derived horizontal wind speeds for a transect over the center of Patricia on 23 October. Sounding trajectories are plotted in black and data points that sampled the low-level radial circulation are plotted in red. From Nelson et al. (2019a). ©American Meteorological Society. Used with permission.

Table 3.4: Mean, median, and standard deviation of the absolute differences between the HF99 methodology and xy-methodology horizontal winds in m s^{-1} ($|V2 - V1|$), LM12a methodology and xy-methodology horizontal winds ($|V3 - V1|$), and full WFE methodology and xy-methodology horizontal winds ($|V4 - V1|$). Also included are the p-values from Student's t-test between the methods compared. From Nelson and Harrison (2019).

	$\|V2 - V1\|$	$\|V3 - V1\|$	$\|V4 - V1\|$
Mean	0.57	0.59	0.58
Median	0.32	0.33	0.32
St. dev.	0.87	0.93	0.90
P-value	0.02	< 0.01	< 0.01

Table 3.5: Mean, median, and standard deviation of the absolute differences between the HF99 methodology and full WFE methodology horizontal winds in m s^{-1} ($|V2 - V4|$), LM12a methodology and full WFE methodology horizontal winds ($|V3 - V4|$), and xy-methodology and full WFE methodology horizontal winds ($|V1 - V4|$). Also included are the p-values from Student's t-test between the methods compared. From Nelson and Harrison (2019).

	$\|V2 - V4\|$	$\|V3 - V4\|$	$\|V1 - V4\|$
Mean	1.10	0.61	0.58
Median	0.64	0.26	0.32
St. dev.	1.55	1.08	0.90
P-value	< 0.01	< 0.01	< 0.01

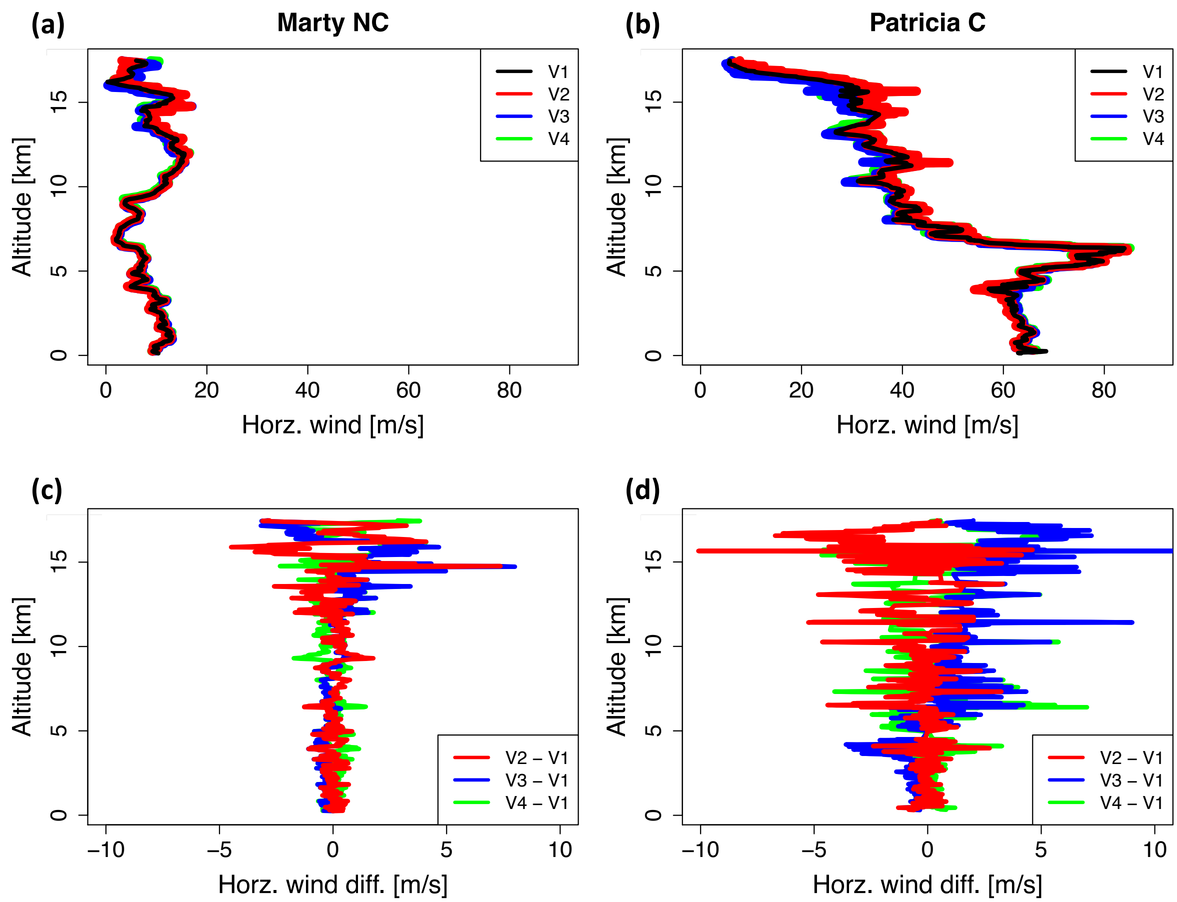

Figure 3.16: Sample NC sounding from Marty on 27 September (a), and C sounding from Patricia on 23 October (b). The xy-methodology, HF99 methodology, LM12a methodology, and full WFE methodology horizontal winds in panels (a) and (b) are in black, red, blue, and green, respectively. The horizontal wind differences between methodologies for Marty (c) and for Patricia (d). The difference between the HF99 methodology and the xy-methodology horizontal winds is in red, the LM12a methodology and the xy-methodology horizontal winds is in blue, and the full WFE methodology and the xy-methodology horizontal winds is in green in panels (c) and (d). From Nelson and Harrison (2019).

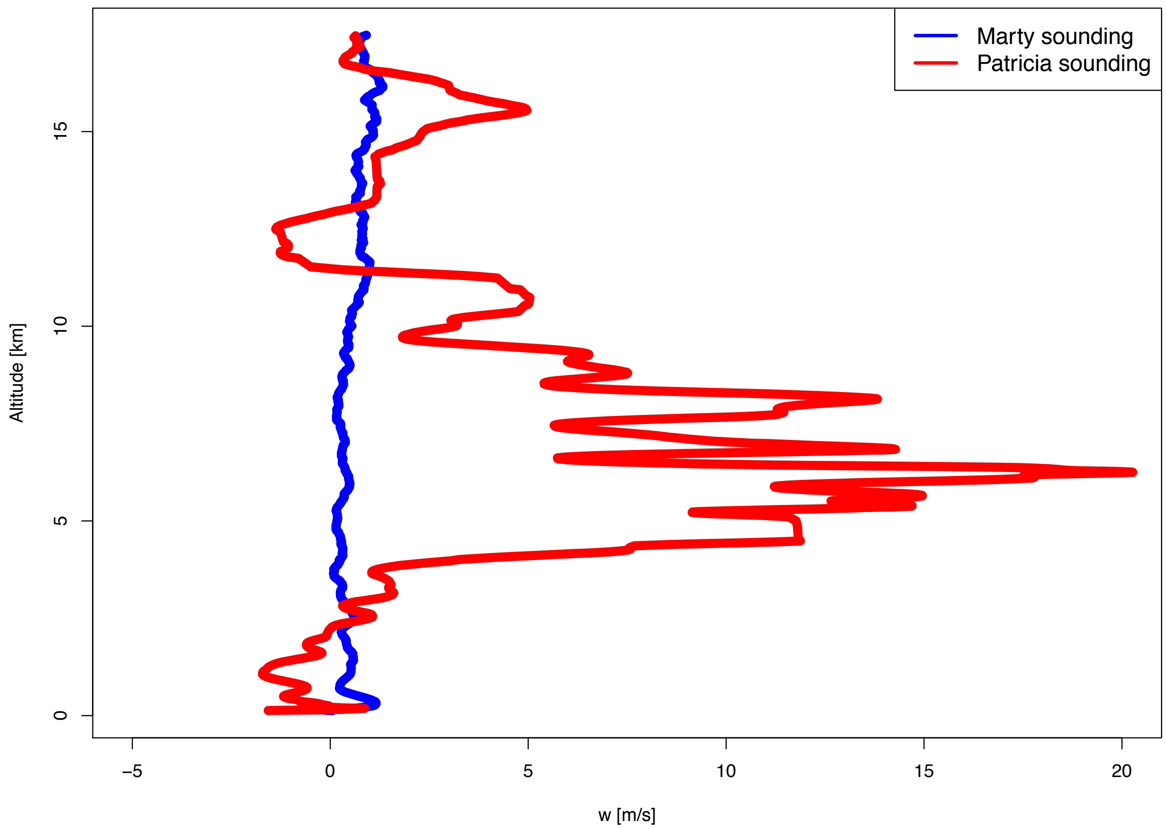

Figure 3.17: Vertical velocity (m s^{-1}) from the Marty NC sounding on 27 September (blue) and the Patricia C sounding (red). From Nelson and Harrison (2019).

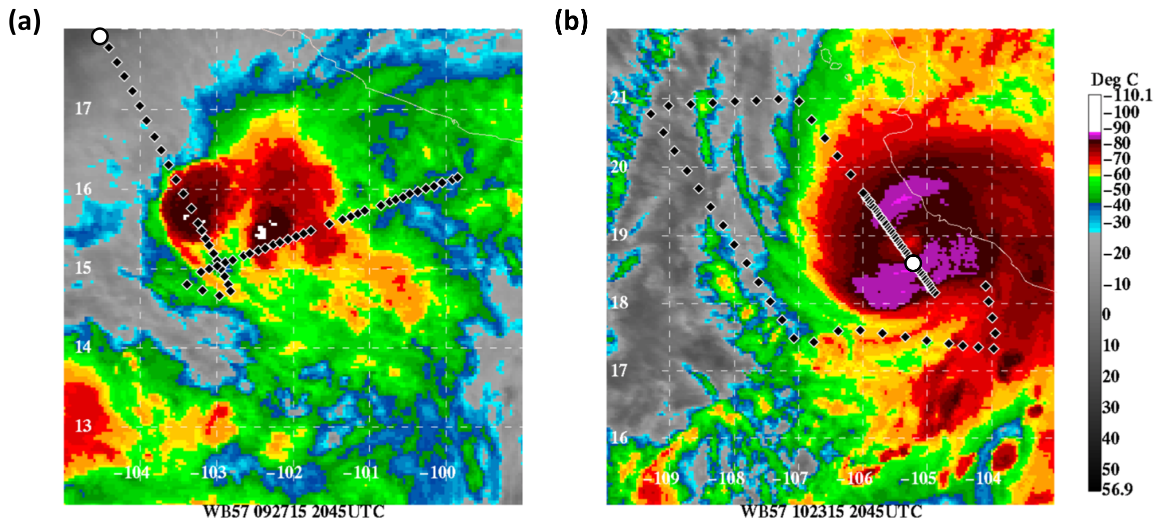

Figure 3.18: IR satellite image of Marty at 2045 UTC 27 September (a) and Patricia at 2045 UTC 23 October (b). Brightness temperatures (°C) are shaded. Sounding launch locations are shown as black diamonds. The sample soundings locations in Figures 3.16 and 3.17 are shown in white. IR image courtesy of David Vollaro. From Nelson and Harrison (2019).

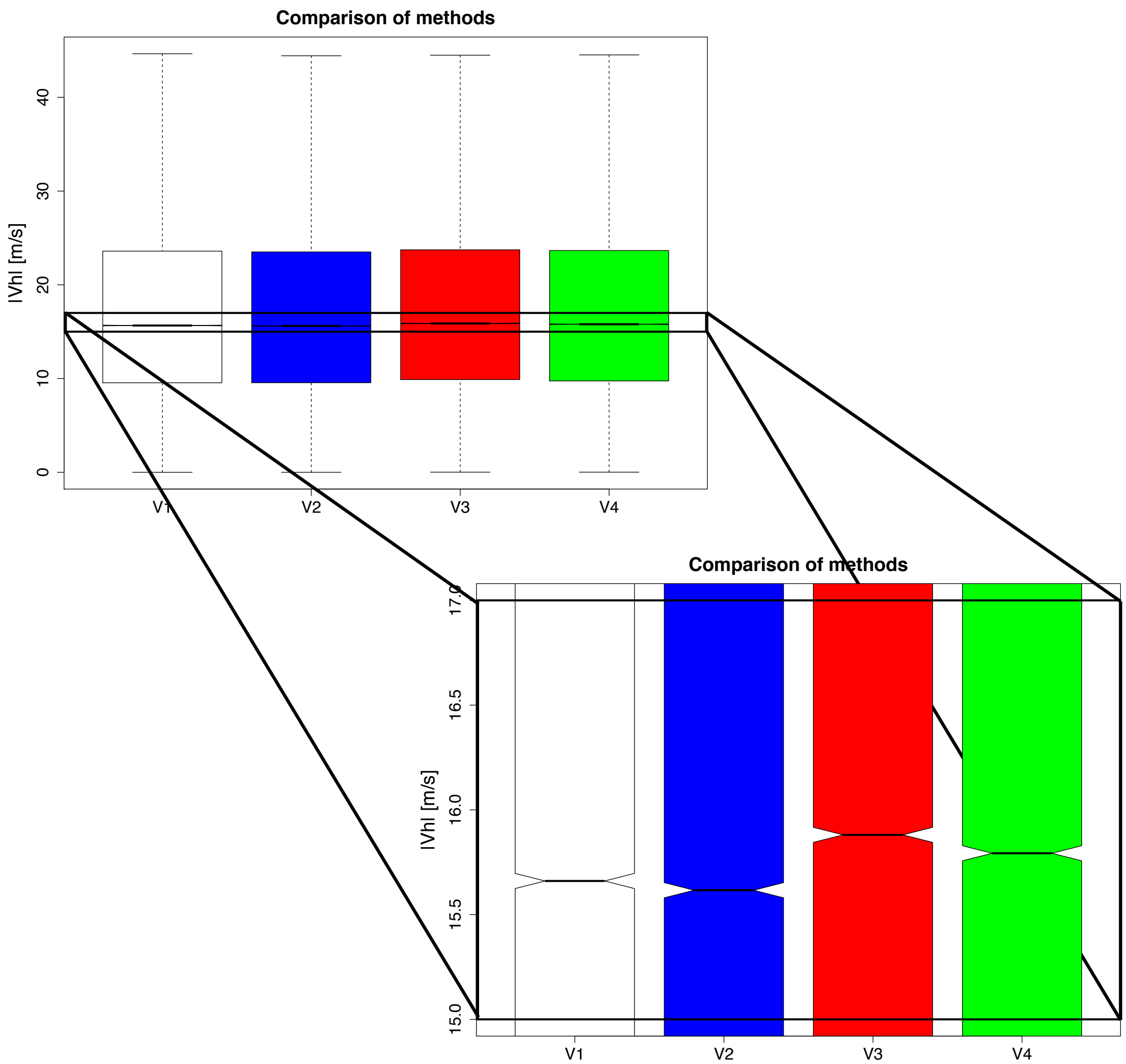

Figure 3.19: Notched box plot comparisons between the horizontal wind speeds from V1, V2, V3, and V4. The inset to the bottom right shows that only the notches of the box plots for V1 and V2 overlap. From Nelson and Harrison (2019).

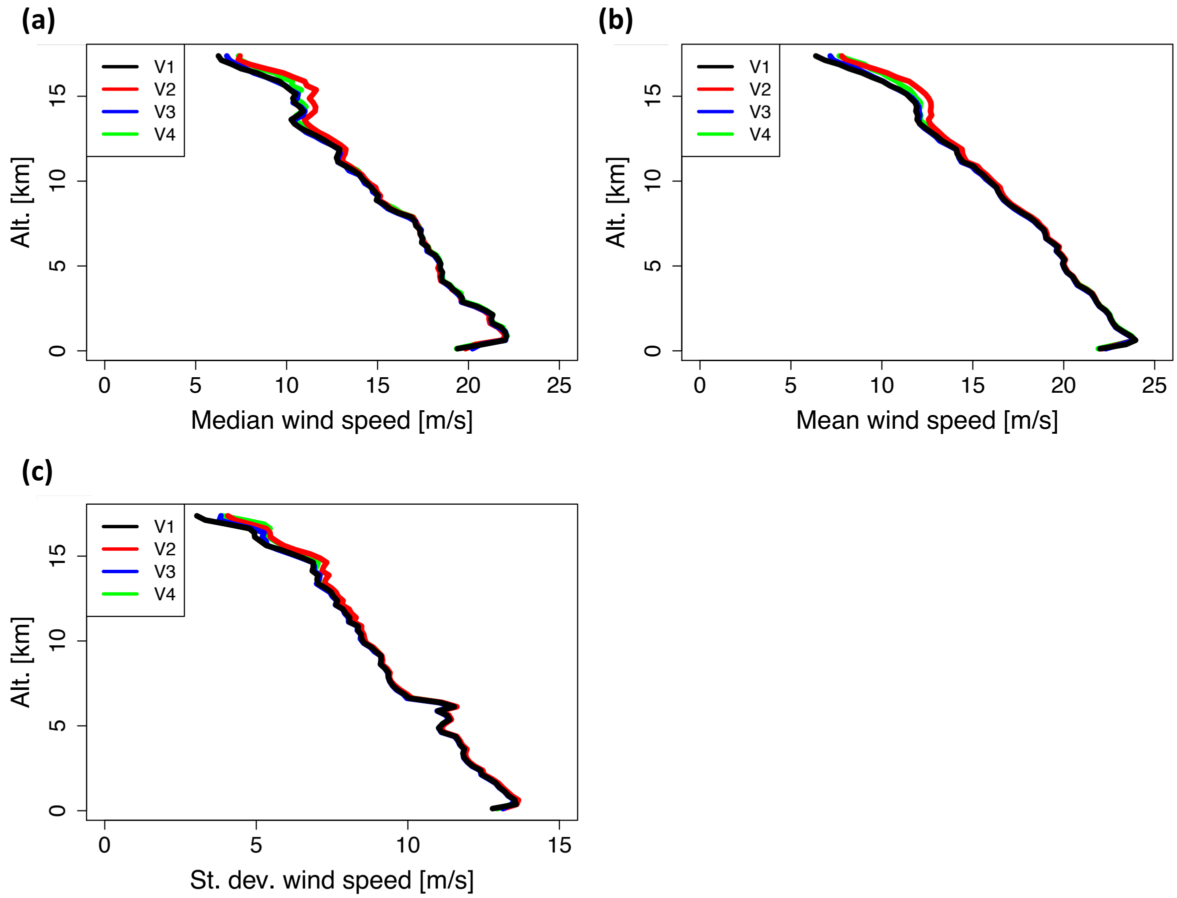

Figure 3.20: Median (a), mean (b), and standard deviation (c) profiles of V1, V2, V3, and V4 (black, red, blue, and green, respectively). From Nelson and Harrison (2019).

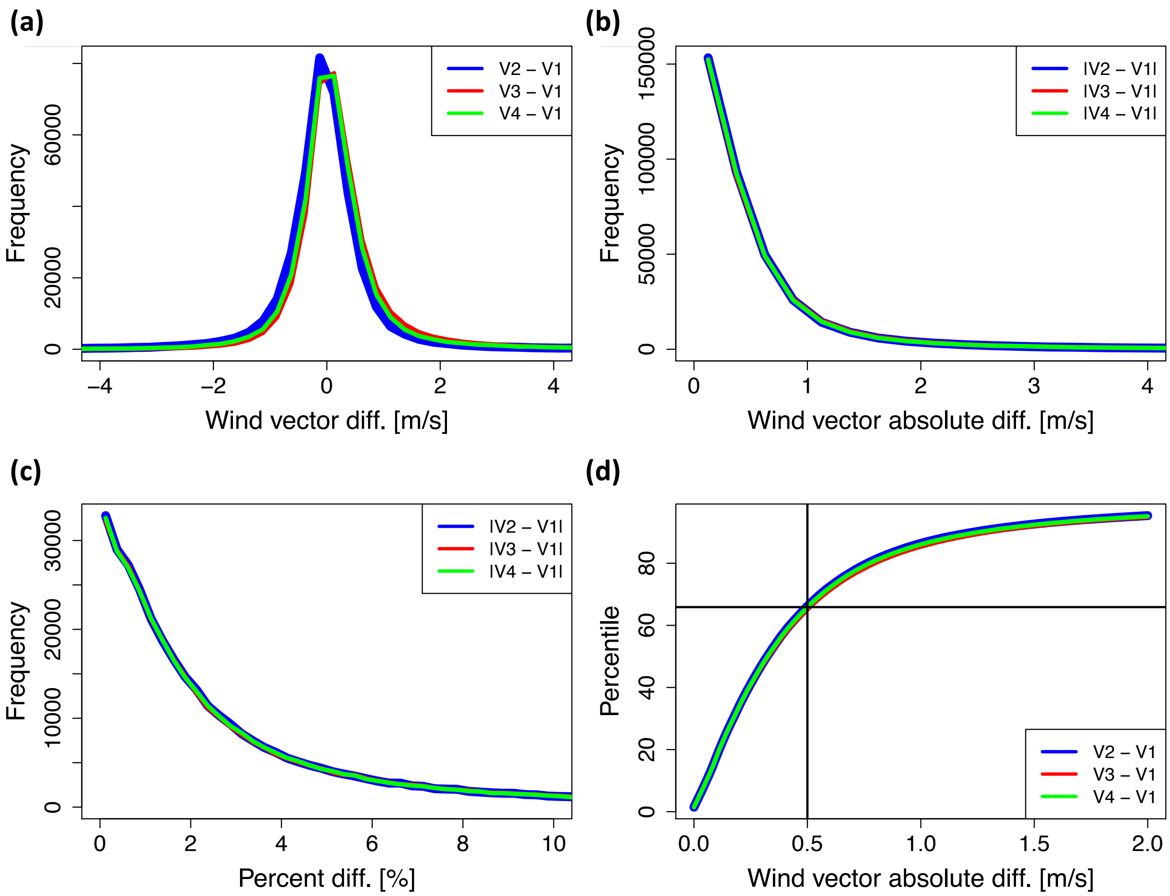

Figure 3.21: Comparison of the horizontal wind differences between the HF99 (blue), LM12a (red), and full WFE methods (green) to the xy-method. Panel (a) is a histogram of the wind speed differences. Panel (b) is a histogram of the absolute wind speed differences. Panel (c) is the percent difference histogram relative to the xy-method. Panel (d) is the percentiles of the absolute wind speed differences. The black solid lines in panel (d) denote the percentile for the 0.5 m s^{-1} absolute wind speed difference for the HF99 method difference. From Nelson and Harrison (2019).

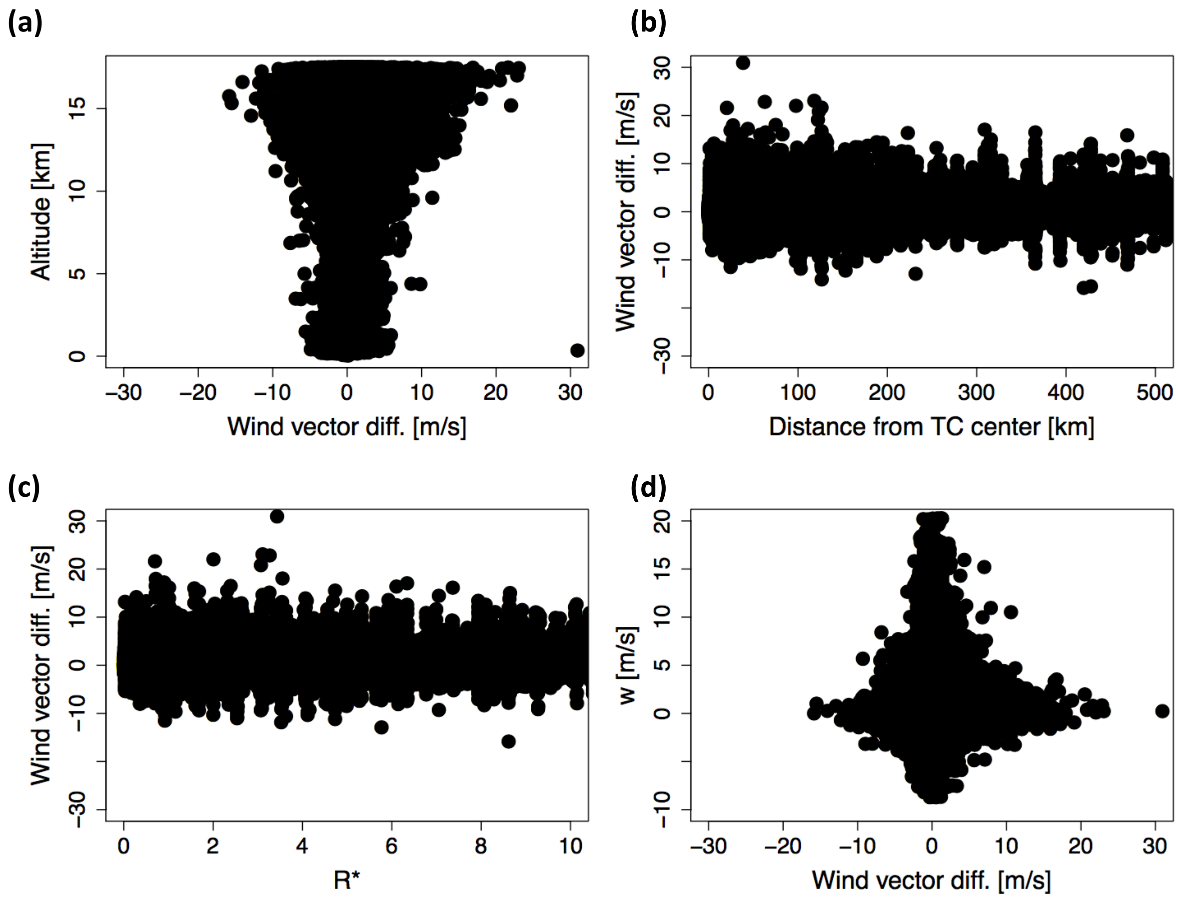

Figure 3.22: Wind speed differences between the xy-methodology and the full WFE methodology with respect to altitude (a), distance from the TC center (b), R^* (c), and vertical velocity (d). From Nelson and Harrison (2019).

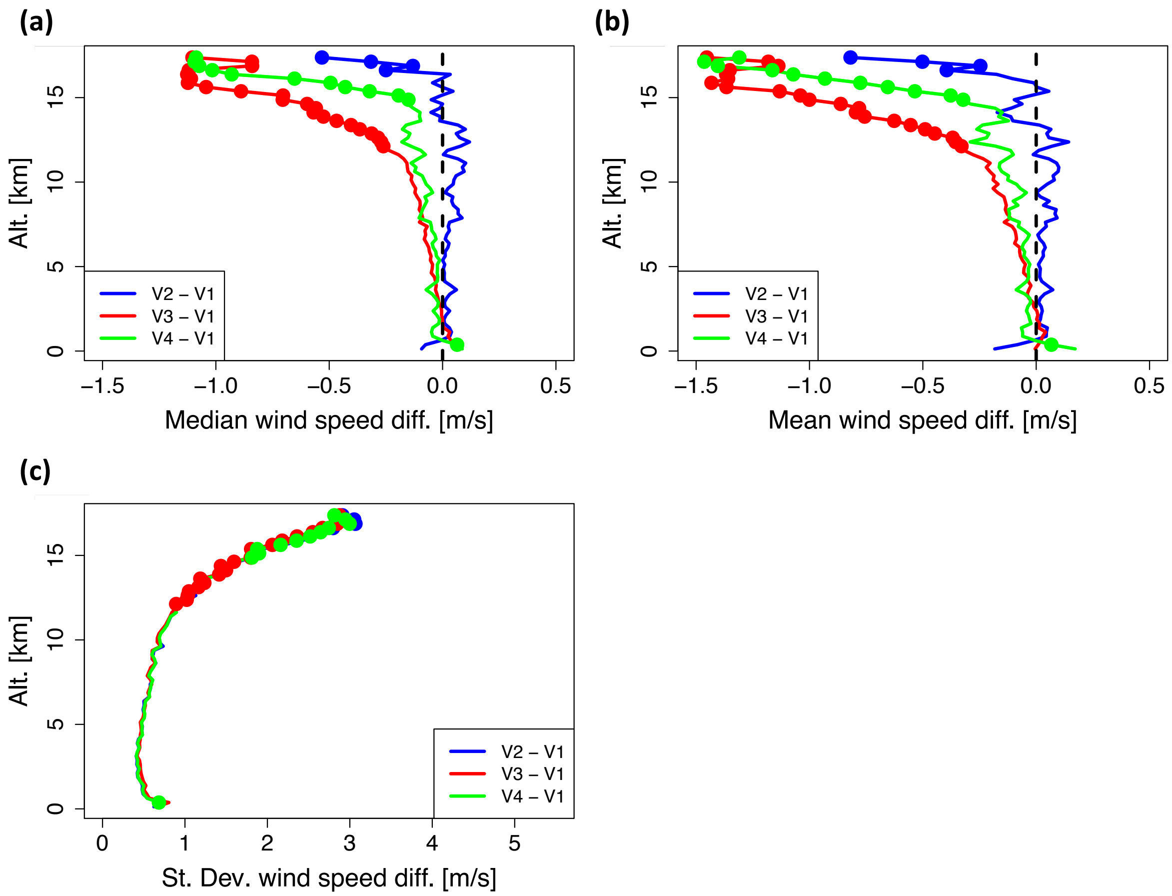

Figure 3.23: Median (a), mean (a), and standard deviation (c) profiles of wind speed differences for $|V2 - V1|$ (blue), $|V3 - V1|$ (red), $|V4 - V1|$ (green). Differences that are statistically different at the 95% level using Student's t-test are denoted with dots. From Nelson and Harrison (2019).

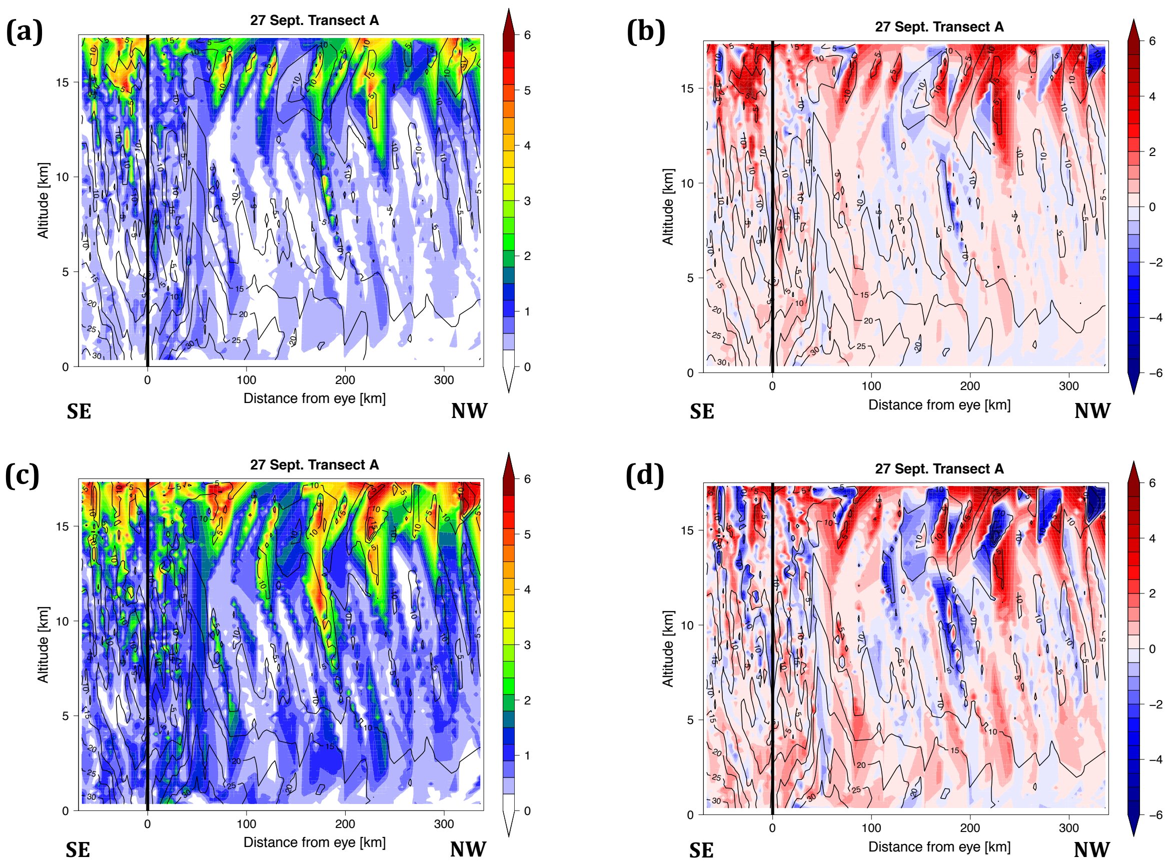

Figure 3.24: Cross section of horizontal wind from Marty on 27 September. Shown in solid black contours are the horizontal winds using the xy-methodology (a, b) or the HF99 methodology (c, d). Absolute differences to the full WFE methodology horizontal winds are shown in panels (a) and (c) and differences to the full WFE methodology horizontal winds are shown in panels (b) and (d). The TC center is denoted with a thick solid black line. From Nelson and Harrison (2019).

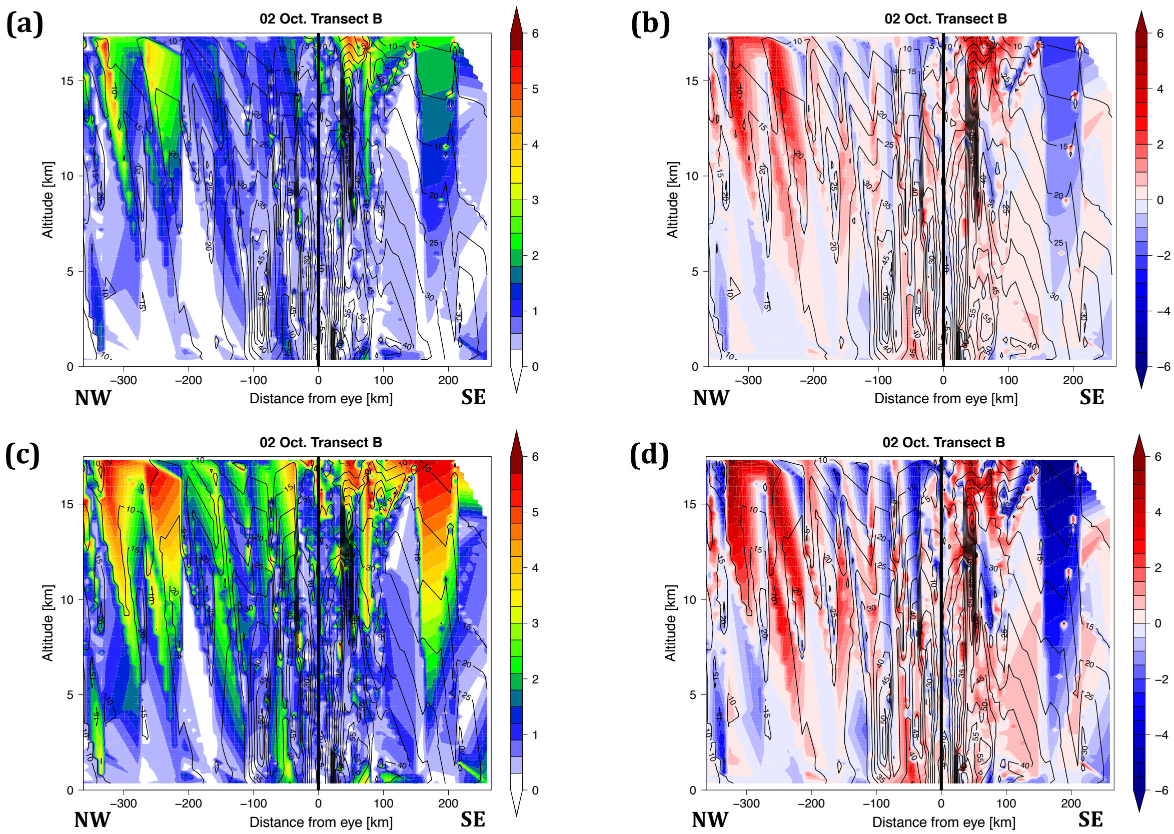

Figure 3.25: Same as Fig. 3.24, but for Joaquin on 2 October. From Nelson and Harrison (2019).

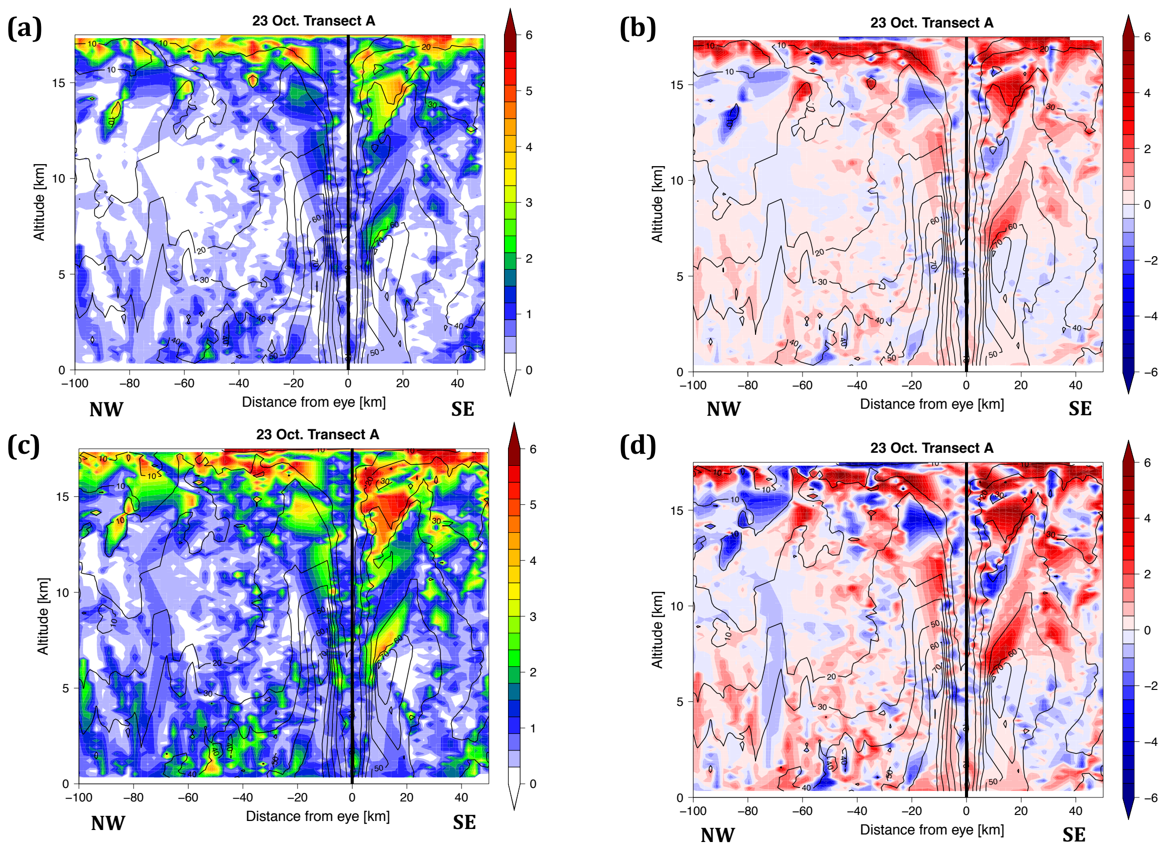

Figure 3.26: Same as Fig. 3.24, but for Patricia on 23 October. From Nelson and Harrison (2019).

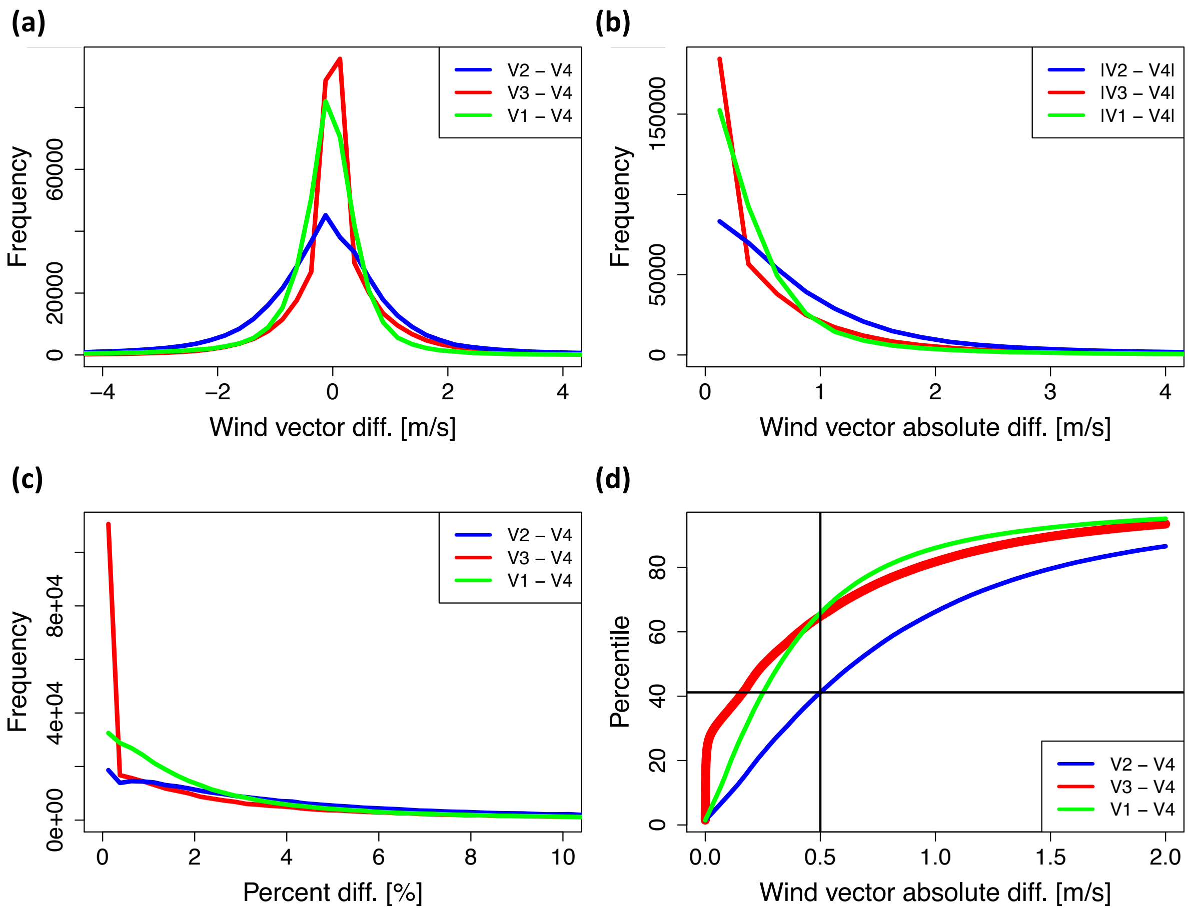

Figure 3.27: Same as Fig. 3.20, but for wind differences between the HF99 (blue), LM12a (red), and xy-methods (green) to the full WFE method. From Nelson and Harrison (2019).

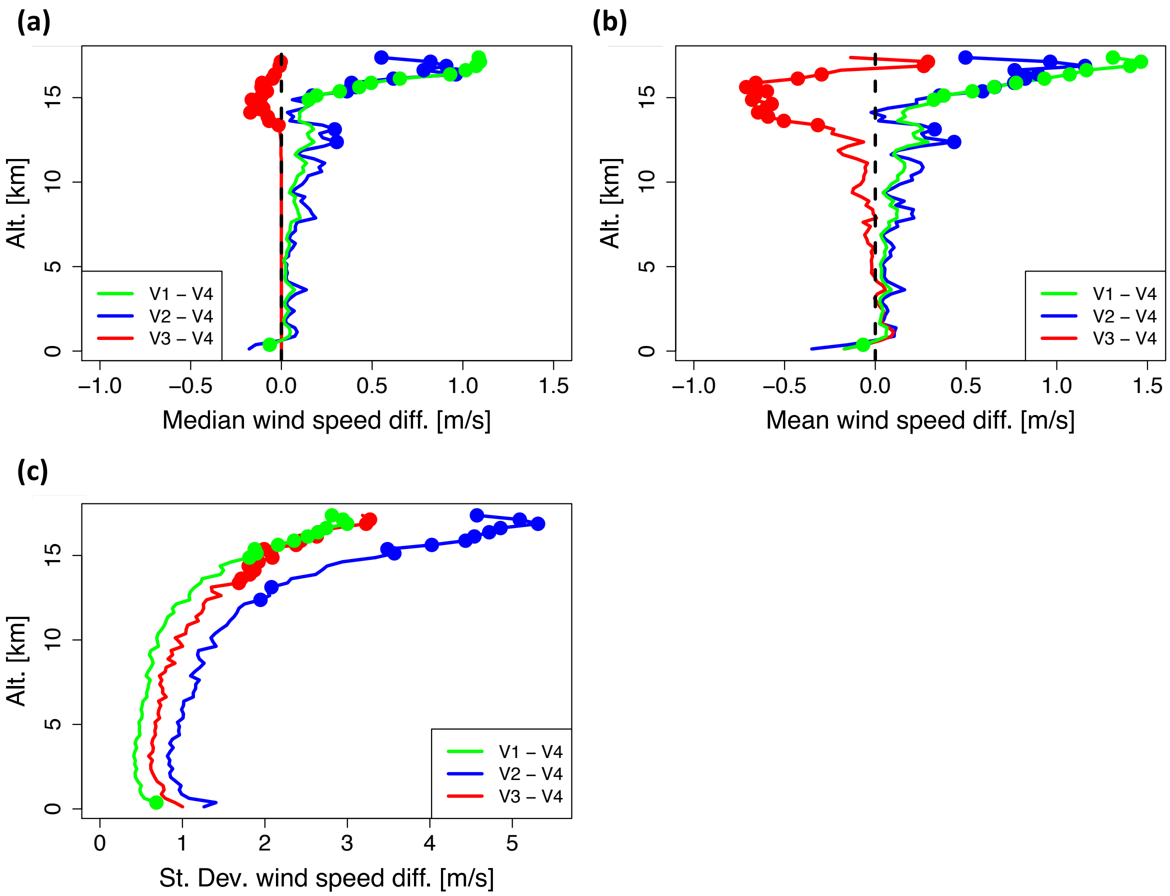

Figure 3.28: Same as Fig. 3.23, but for wind speed differences for $|V1 - V4|$ (green), $|V2 - V4|$ (blue), $|V3 - V4|$ (red). From Nelson and Harrison (2019).

Table 3.6: Summary of spatial (horizontal and vertical) and temporal autocorrelation scales referenced in the text based upon correlation thresholds of either 0.5, 0.37, or 0.2 for horizontal wind ($|V_h|$), temperature (T), water vapor, rainfall, rain rate, and vertical velocity (w). Correlation length scales that were specifically for convective regions are denoted as "C" and non-convective regions are denoted as "NC". Observation types (obs. type) are listed and the locations of the observations are noted for each referenced study. Observation types include: surface (Sfc. stations), boat (boat stations), radio acoustic sounding system (RASS), satellite, Lidar, S-band radar, or X-band radar. From Nelson et al. (2019b).

Var.	Corr.	Vert. dist.	Horz. dist.	Time	Obs. type	Location	Ref.
$\|V_h\|$	0.5	——	0–100 km	——	Sfc. stations	Land	Wylie et al. 1985
$\|V_h\|$	0.5	——	400 km	——	Boat stations	Ocean	Wylie et al. 1985
$\|V_h\|$	0.5	——	——	4–6 h	Sfc. stations	Land	Brett and Tuller 1991
$\|V_h\|$	0.37	——	——	11 h (at 40 m)	RASS	Land	Pérez et al. 2004
$\|V_h\|$	0.37	——	——	5 h (at 300 m)	RASS	Land	Pérez et al. 2004
T	0.5	——	800–1000 km	——	Sfc. stations	Land	Gunst 1995
T	0.5	——	200–600 km	——	Satellite	Upper air	Nichol and Wong 2008
T	0.37	——	——	7 h (at 40 m)	RASS	Land	Pérez et al. 2004
T	0.37	——	——	8 h (at 140 m)	RASS	Land	Pérez et al. 2004
T	0.5	——	——	12 h	Satellite	Over ITCZ	Raymond et al. 2003

Table 3.7: Table 3.6 continued. From Nelson et al. (2019b).

Var.	Corr.	Vert. dist.	Horz. dist.	Time	Obs. type	Location	Ref.
Water vapor	0.37	0.45 km (C)	——	——	Lidar	Airborne	Fisher et al. 2013
Water vapor	0.37	0.2–0.3 km (NC)	——	——	Lidar	Airborne	Fisher et al. 2013
Rainfall	0.5	——	4 km	——	Rain gauge	Land	Habib et al. 2001
Rain rate	0.5	——	10 km (NC)	——	S-band radar	Land	Brigni et al. 2015
Rain rate	0.5	——	4 km (C)	——	S-band radar	Land	Brigni et al. 2015
Rainfall	0.5	——	1.5–4 km	——	Reports/radar	Land	Jameson 2017
w	0.5	0.2–0.3 km	0.2–0.3 km	——	Lidar	Land	Lothon et al. 2006
w	0.2	4–7 km	4–6 km	——	X-band radar	TC eyewall	Black et al. 1996
w	0.2	2–4 km	1–4 km	——	X-band radar	TC rainband	Black et al. 1996

Table 3.8: List of the minimum, maximum, mean, and median dropsonde spacing for each day to the nearest km. From Nelson et al. (2019b).

Day	Name	Minimum	Maximum	Mean	Median
27 Sept	Marty	6	44	18	17
28 Sept	Marty	3	83	21	13
02 Oct	Joaquin	7	150	39	41
03 Oct	Joaquin	5	344	54	38
04 Oct	Joaquin	8	120	37	27
05 Oct	Joaquin	9	121	33	28
20 Oct	Patricia	18	267	87	44
21 Oct	Patricia	7	69	26	24
22 Oct	Patricia	4	142	26	11
23 Oct	Patricia	3	73	22	25

Table 3.9: List of the number of dropsondes within each of the four radial sections and in total on each day. From Nelson et al. (2019b).

Day	Name	$\leq$1.25R*	1.25–3R*	3–5R*	5–10R*	Total
27 Sept	Marty	11	13	6	20	50
28 Sept	Marty	13	16	15	14	58
02 Oct	Joaquin	15	13	6	10	44
03 Oct	Joaquin	11	11	7	14	43
04 Oct	Joaquin	13	16	15	11	55
05 Oct	Joaquin	9	13	7	24	53
20 Oct	Patricia	5	5	2	0	12
21 Oct	Patricia	13	18	13	7	51
22 Oct	Patricia	5	13	12	13	43
23 Oct	Patricia	5	6	9	8	28

Table 3.10: List of dropsonde-to-dropsonde spatial 0.5-autocorrelation thresholds (in km) for each day in the dataset for vertical velocity (w), horizontal wind speed ($|V_h|$), relative humidity (RH), temperature (T), and equivalent potential temperature (θ_e). The size of the RMW (in km) and TC intensity (in m s^{-1}) are also noted.

Day	Name	w	$\|V_h\|$	RH	T	θ_e	RMW	Intensity
27 Sept	Marty	4.8	9.6	6.9	6.9	6.9	37	26
28 Sept	Marty	3.8	7.3	3.4	4.6	3.8	21	36
02 Oct	Joaquin	3.8	7.0	3.8	5.4	4.8	31	57
03 Oct	Joaquin	3.2	5.1	3.2	4.6	3.2	27	67
04 Oct	Joaquin	4.9	18.9	6.0	15.1	7.6	38	44
05 Oct	Joaquin	4.5	11.5	6.4	7.0	5.1	49	39
20 Oct	Patricia	17.2	15.3	18.4	16.0	17.6	77	15
21 Oct	Patricia	4.8	15.7	5.2	14.4	5.2	40	26
22 Oct	Patricia	3.8	12.7	4.1	8.9	4.4	19	59
23 Oct	Patricia	1.4	7.2	2.1	2.1	1.3	11	93
Mean	——	5.2	11.0	6.0	8.5	6.0	35	46
Median	——	4.2	10.5	4.7	7.0	5.0	34	41
St. Dev.	——	4.3	4.6	4.6	5.0	4.5	18	22

Table 3.11: Same as Table 3.10, but for the temporal 0.5-autocorrelation thresholds (in s) for each day in the dataset and any given individual sounding. The size of the RMW (in km) and TC intensity (in m s^{-1}) are also noted.

Day	Name	w	$\|V_h\|$	RH	T	θ_e	RMW	Intensity
27 Sept	Marty	19	25	30	22	28	37	26
28 Sept	Marty	23	31	27	24	31	21	36
02 Oct	Joaquin	23	41	31	27	25	31	57
03 Oct	Joaquin	25	38	33	35	34	27	67
04 Oct	Joaquin	22	31	36	23	31	38	44
05 Oct	Joaquin	20	31	35	21	30	49	39
20 Oct	Patricia	8	21	30	15	19	77	15
21 Oct	Patricia	22	32	26	13	22	40	26
22 Oct	Patricia	21	27	32	17	25	19	59
23 Oct	Patricia	20	33	19	17	20	11	93
Mean	——	20.3	31.0	29.9	21.4	26.5	35	46
Median	——	21.5	31.0	30.5	21.5	26.5	34	41
St. Dev.	——	4.4	5.5	4.7	6.1	5.1	18	22

Table 3.12: Number of updraft (U) and downdraft (D) soundings for each day.

Day	Name	U	N
27 Sept	Marty	4	3
28 Sept	Marty	9	5
02 Oct	Joaquin	13	15
03 Oct	Joaquin	15	4
04 Oct	Joaquin	4	0
05 Oct	Joaquin	5	0
20 Oct	Patricia	8	1
21 Oct	Patricia	5	1
22 Oct	Patricia	3	2
23 Oct	Patricia	12	6
Total	——	78	37

Table 3.13: Same as Table 3.11, but for soundings containing an updraft. Also included are the p-values (p) for the Student‘s t-test comparisons between the temporal scales in Table 3.11 and the temporal scales in updraft soundings for each variable.

Day	Name	w	$\lvert V_h \rvert$	RH	T	θ_e	RMW	Intensity
27 Sept	Marty	24	28	21	34	29	37	26
28 Sept	Marty	30	42	21	27	34	21	36
02 Oct	Joaquin	30	39	22	29	17	31	57
03 Oct	Joaquin	26	43	27	51	40	27	67
04 Oct	Joaquin	34	38	26	50	63	38	44
05 Oct	Joaquin	10	24	28	25	27	49	39
20 Oct	Patricia	5	19	37	14	17	77	15
21 Oct	Patricia	33	25	21	27	25	40	26
22 Oct	Patricia	19	28	20	15	14	19	59
23 Oct	Patricia	26	37	21	22	27	11	93
Mean	——	23.7	32.3	24.4	29.4	29.3	35	46
Median	——	26	32.5	21.5	27.0	27.0	34	41
St. Dev.	——	9.7	8.5	5.3	12.7	14.3	18	22
p	——	0.34	0.69	0.03	0.10	0.57		

Table 3.14: Same as Table 3.13, but for soundings containing a downdraft.

Day	Name	w	$\lvert V_h \rvert$	RH	T	θ_e	RMW	Intensity
27 Sept	Marty	8	21	22	10	32	37	26
28 Sept	Marty	27	23	20	23	29	21	36
02 Oct	Joaquin	26	41	25	28	21	31	57
03 Oct	Joaquin	32	47	43	67	38	27	67
04 Oct	Joaquin	0	0	0	0	0	38	44
05 Oct	Joaquin	0	0	0	0	0	49	39
20 Oct	Patricia	27	19	15	18	5	77	15
21 Oct	Patricia	21	31	24	21	24	40	26
22 Oct	Patricia	22	34	48	40	31	19	59
23 Oct	Patricia	20	71	18	17	20	11	93
Mean	——	22.9	35.9	26.9	28.0	25.0	35	46
Median	——	24.0	32.5	23.0	22.0	26.5	34	41
St. Dev.	——	6.7	16.1	11.2	16.9	10.1	18	22
p	——	0.40	0.47	0.52	0.35	0.71		

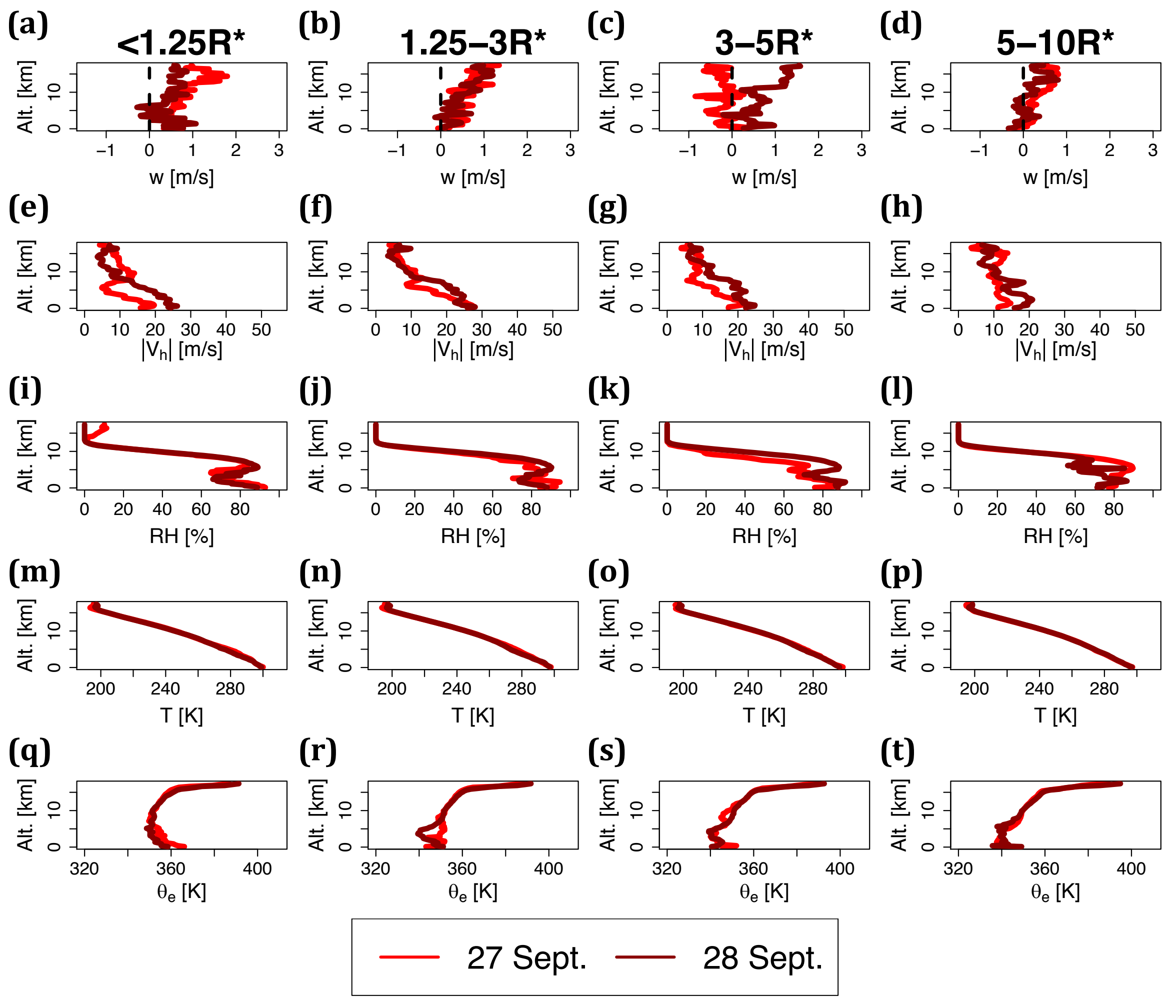

Figure 3.29: Median atmospheric profiles of (a, b, c, d) w (m s^{-1}), (e, f, g, h) $|V_h|$ (m s^{-1}), (i, j, k, l) RH (%), (m, n, o, p) T (K), and (q, r, s, t) θ_e (K) during Marty for data (a, e, i, m, q) within 1.25R*, (b, f, j, n, r) 1.25–3R*, (c, g, k, o, s) 3–5R*, and (d, h, l, p, t) 5–10R*.

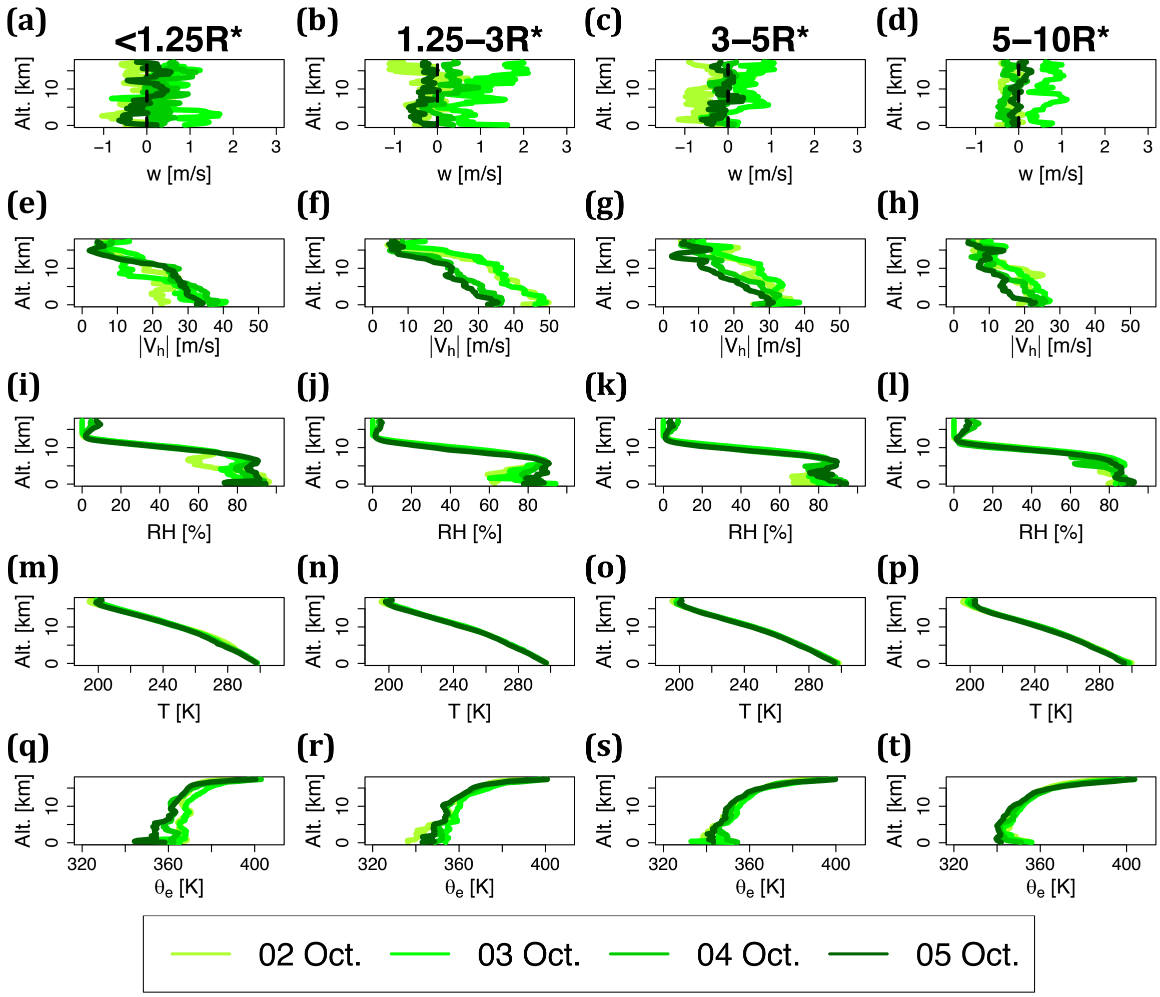

Figure 3.30: Same as Fig. 3.29, but for Joaquin.

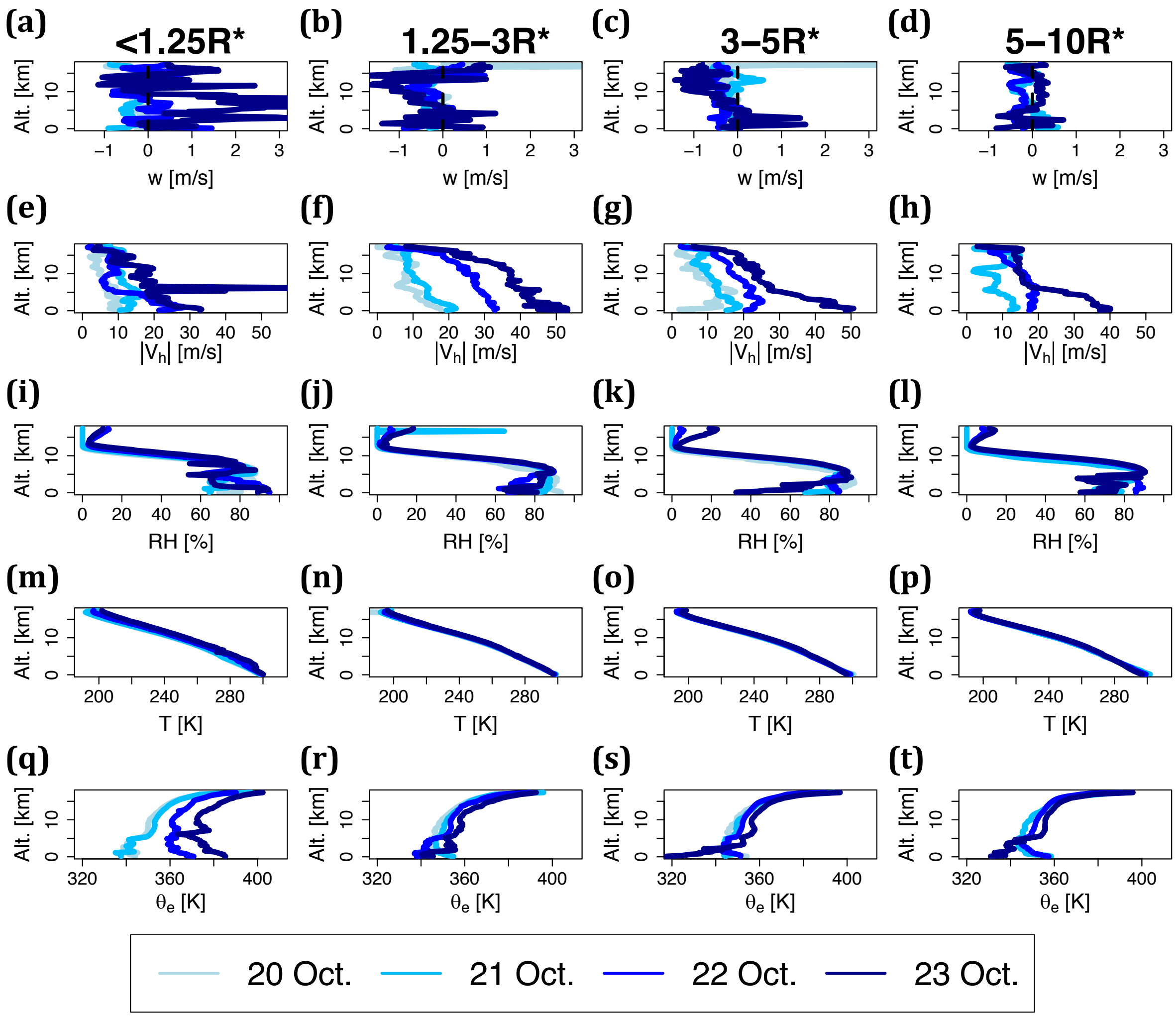

Figure 3.31: Same as Fig. 3.29, but for Patricia.

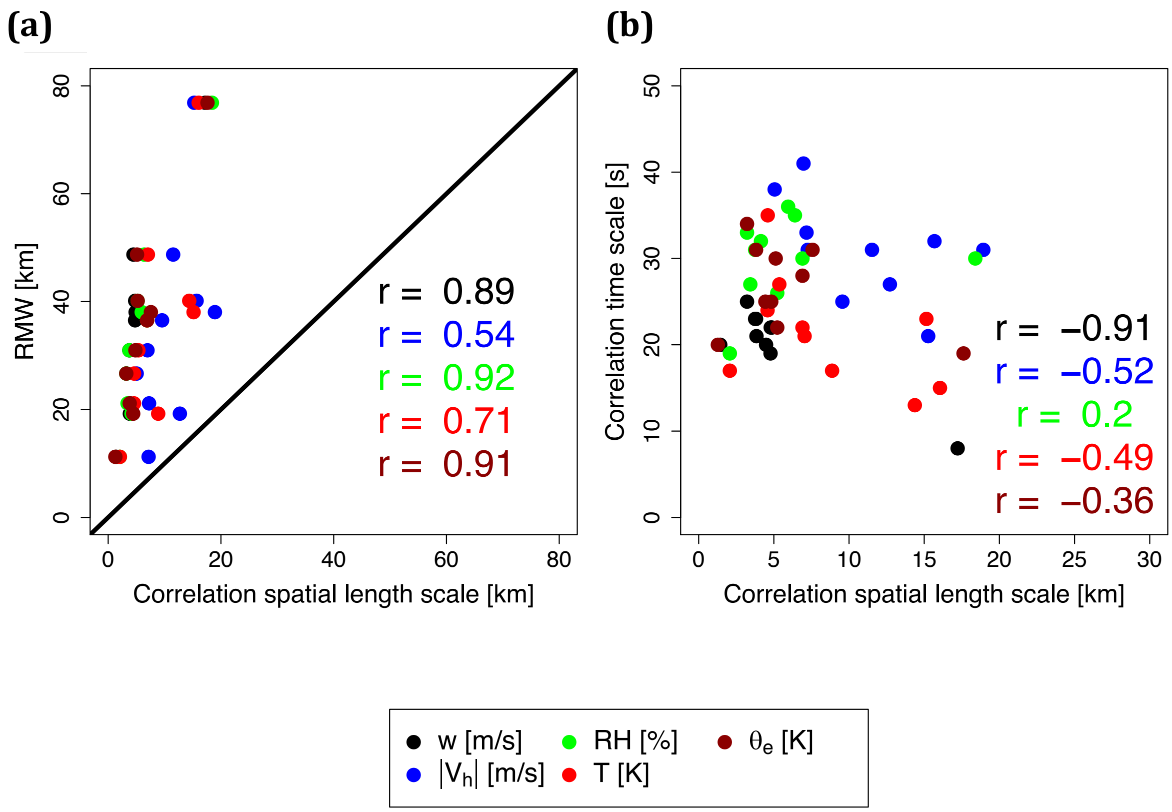

Figure 3.32: Comparison of the (a) daily dropsonde-to-dropsonde horizontal 0.5-autocorrelation length scales (km) to the RMWs (km), and (b) daily dropsonde-to-dropsonde horizontal 0.5-autocorrelation length scales to the daily temporal 0.5-autocorrelation length scales (s) for w, T, $|V_h|$, RH, and θ_e (black, red, blue, green, and dark red, respectively). The 1:1 (or x = y) line (black) is shown in (a).

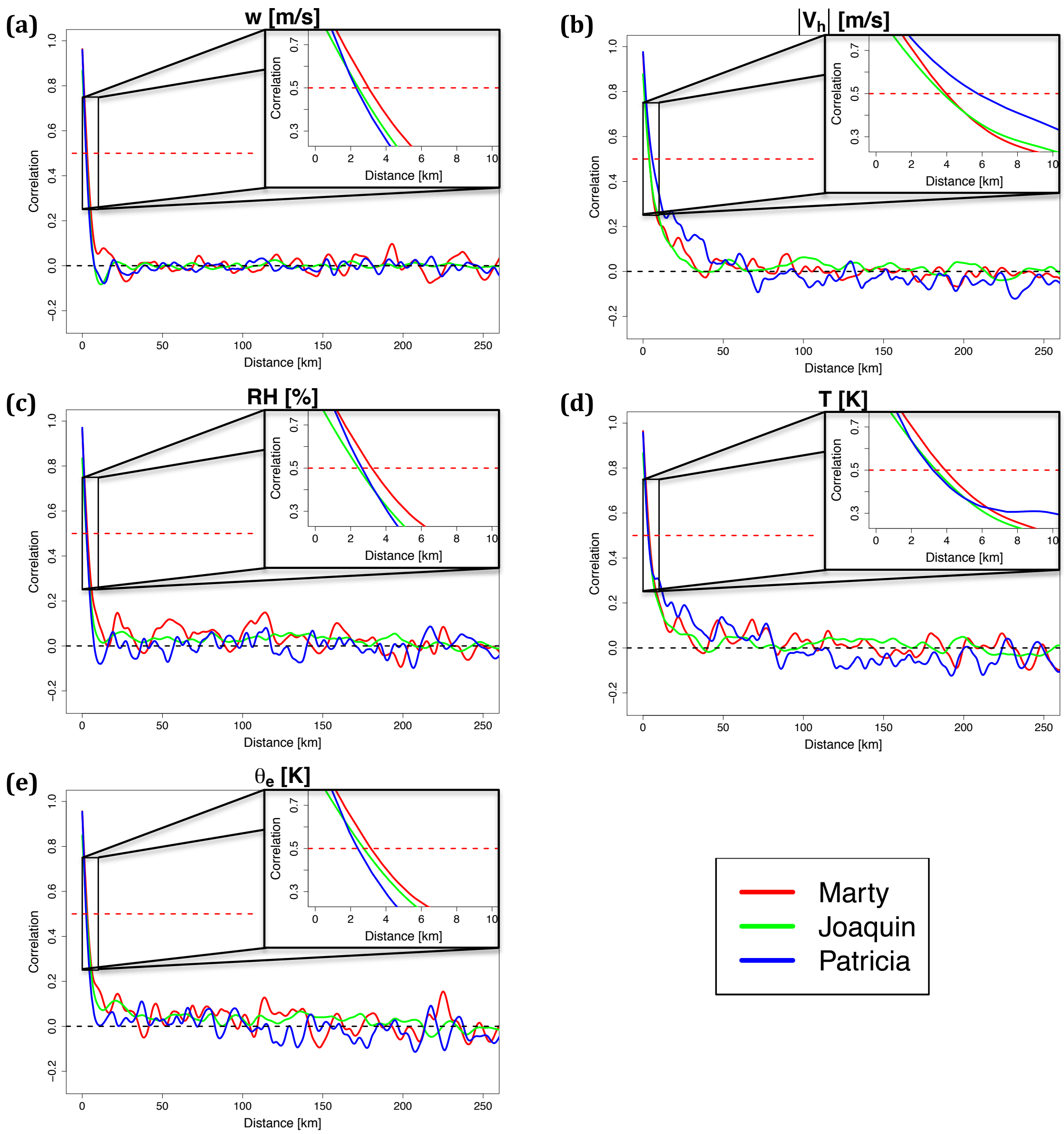

Figure 3.33: Spatial autocorrelations for XDDs launched into Marty (red), Joaquin (green), and Patricia (blue). The spatial autocorrelations for w, $|V_h|$, RH, T, and θ_e are provided in panels (a)–(e), respectively. Correlations of 0.5 and 0.0 are denoted with dashed red and black lines, respectively. Each panel has an inset in the upper-right corner that shows the variations in the 0.5-autocorrelation crossings.

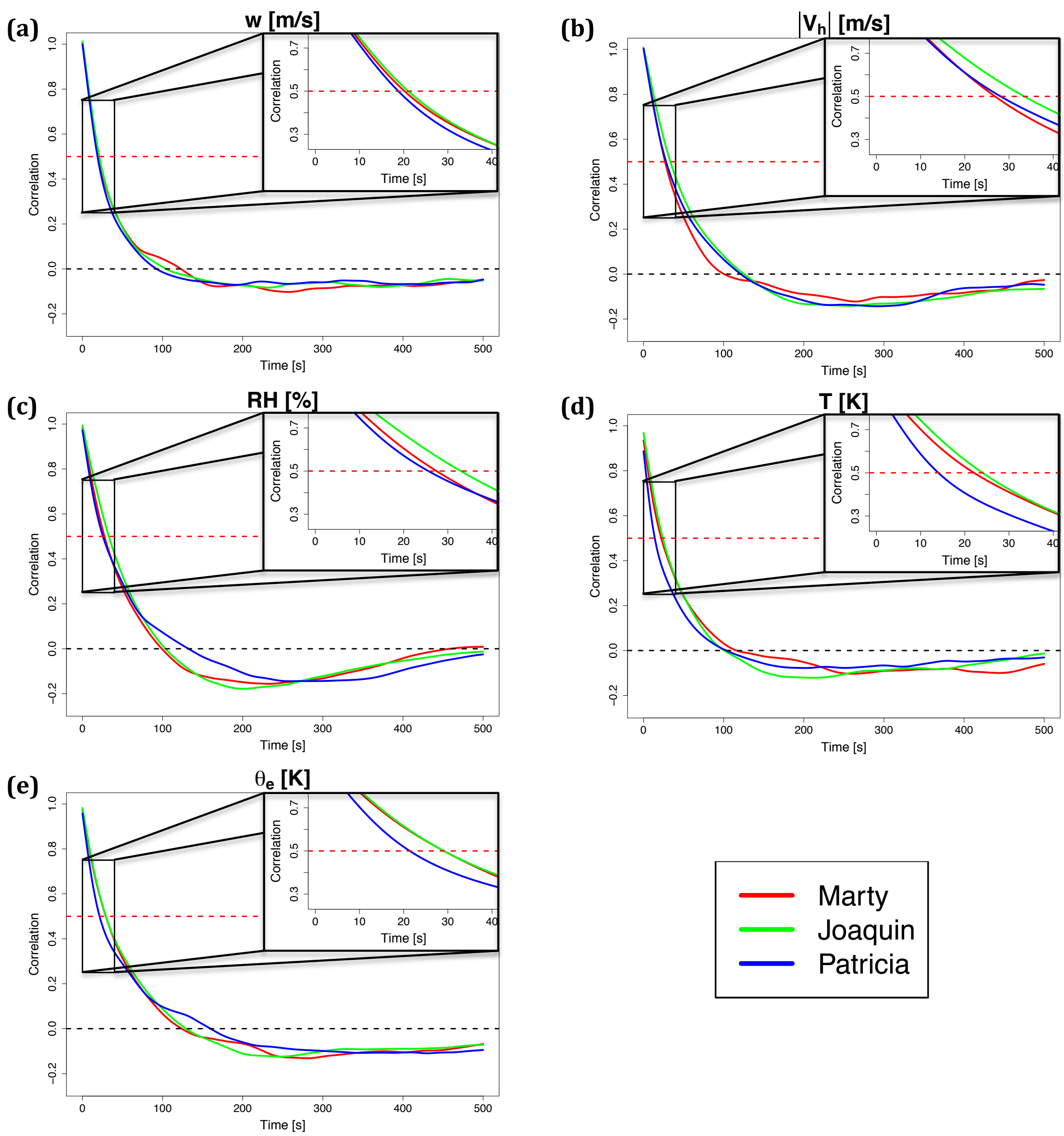

Figure 3.34: Same as Fig. 3.33, but for temporal autocorrelations in each sounding.

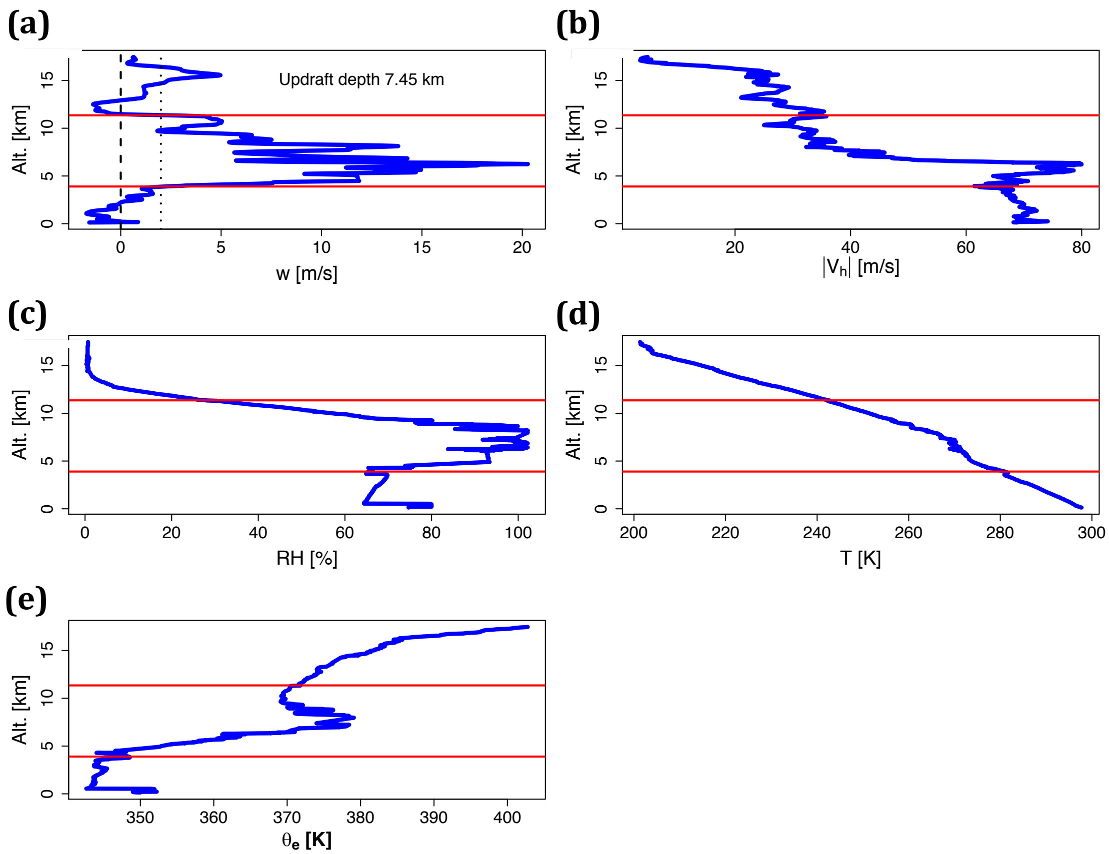

Figure 3.35: Vertical profiles of (a) w, (b) $|V_h|$, (c) RH, (d) T, and (e) θ_e from an updraft sounding (dropsonde 72CC) launched into the eyewall of Patricia on 23 October. The red horizontal lines denote the depth of the updraft. The black long dashed vertical line in panel (a) denotes $w = 0$ m s^{-1}. The black short dashed vertical line in panel (a) denotes $w = 2$ m s^{-1}, which is the minimum w strength required for an updraft.

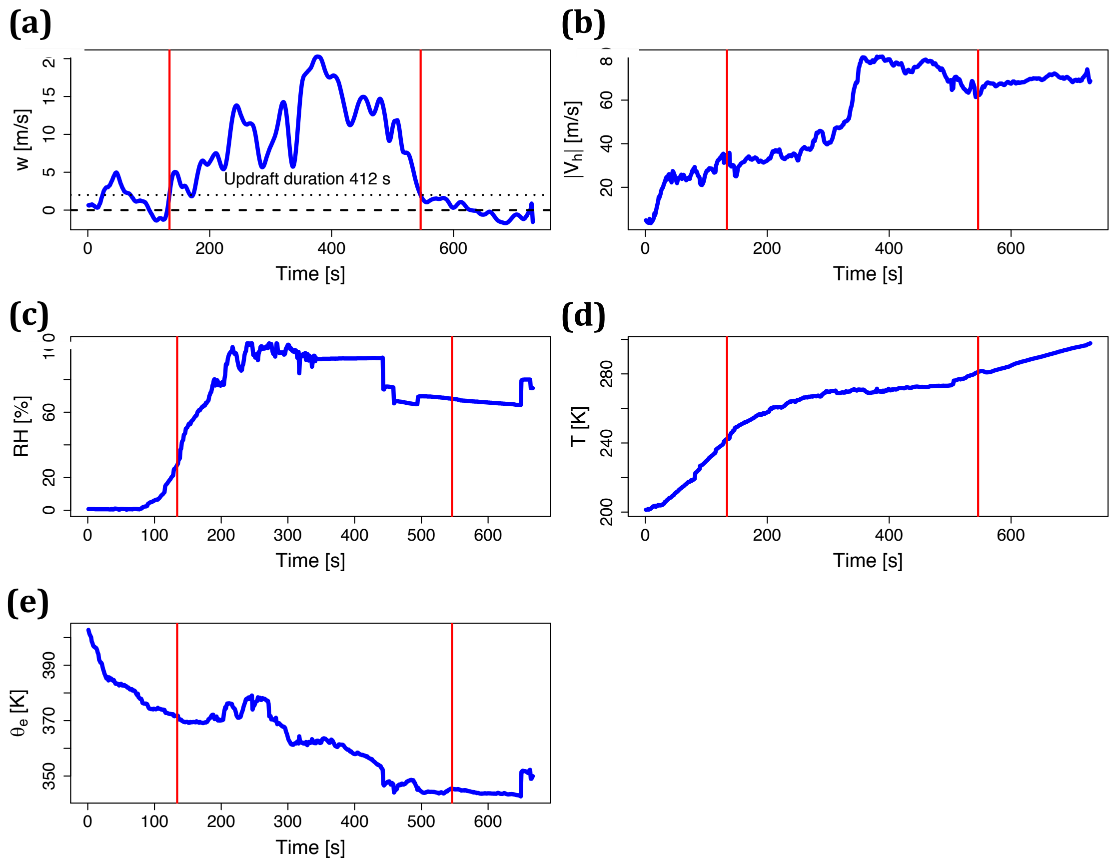

Figure 3.36: Same as Fig. 3.35, but with respect to time. The red vertical lines denote the time of the updraft. The black long dashed horizontal line in panel (a) denotes $w = 0$ m s^{-1}. The black short dashed horizontal line in panel (a) denotes $w = 2$ m s^{-1}, which is the minimum w strength required for an updraft.

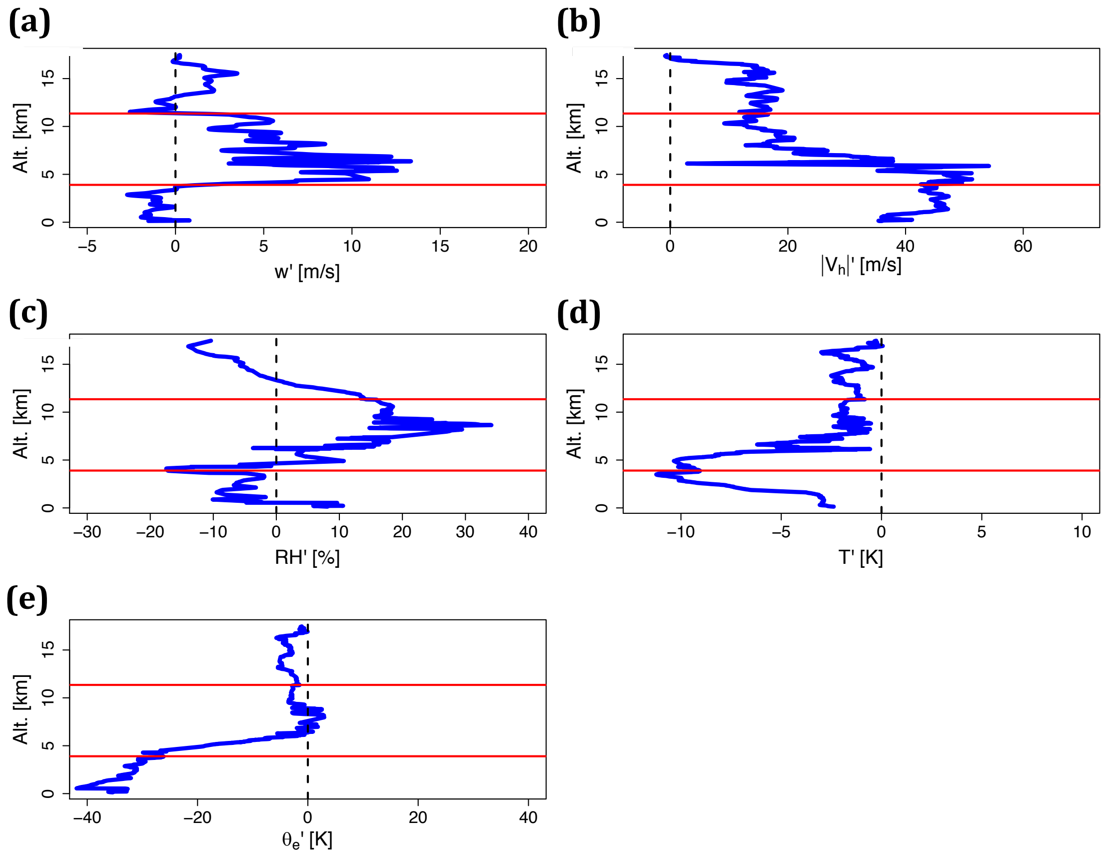

Figure 3.37: Same as Fig. 3.35, but for profiles of perturbation (a) w, (b) $|V_h|$, (c) RH, (d) T, and (e) θ_e. The black dashed vertical line denotes zero-perturbation.

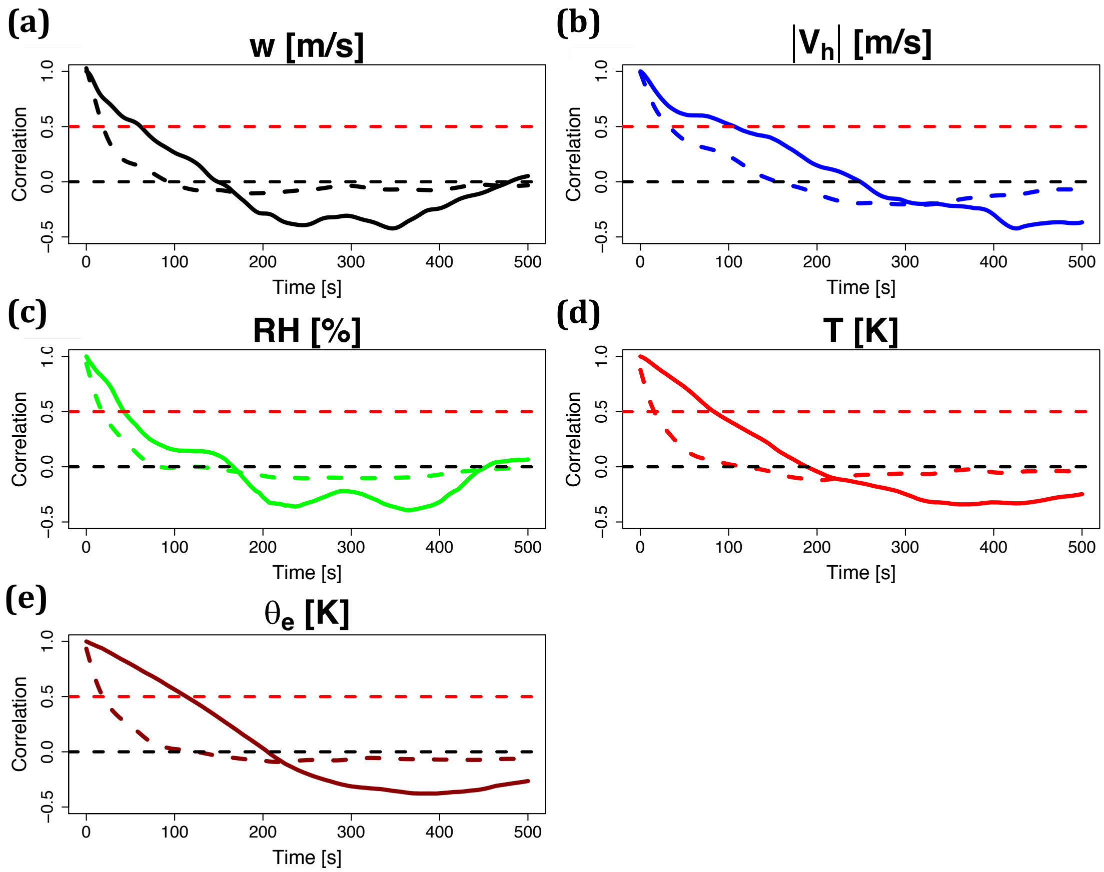

Figure 3.38: Temporal autocorrelation correlograms of (a) w (black), (b) $|V_h|$ (blue), (c) RH (green), (d) T (red), and (e) θ_e (dark red). Correlations of 0.5 and 0.0 are denoted with horizontal dashed red and black lines, respectively. Correlograms for the single updraft sounding in Figs. 3.35–3.37 are in solid color lines, and correlograms for all soundings on 23 October are in dashed color lines.

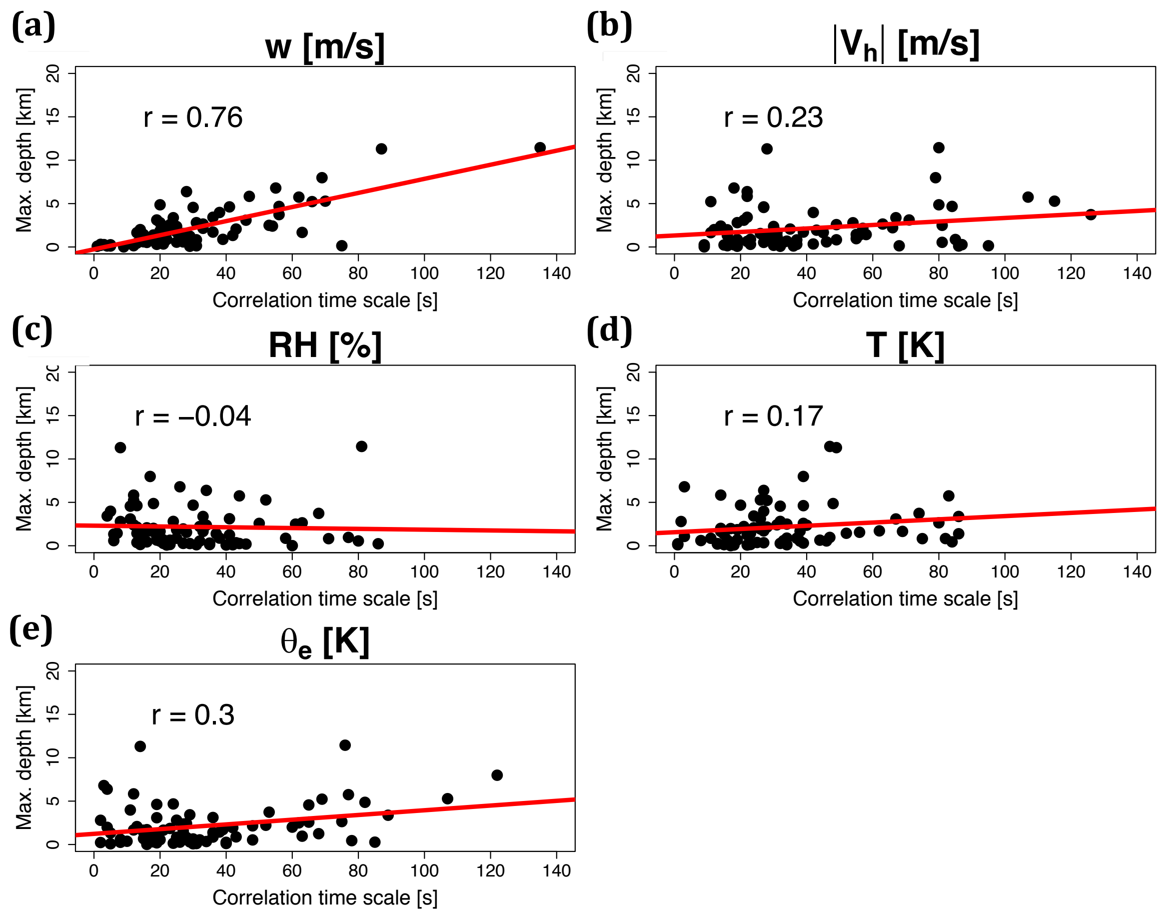

Figure 3.39: 0.5-autocorrelation temporal thresholds for (a) w, (b) $|V_h|$, (c) RH, (d) T, and (e) θ_e within individual soundings that recorded an updraft as a function of maximum updraft depth in the sounding. Correlations and linear fits (red lines) are also provided.

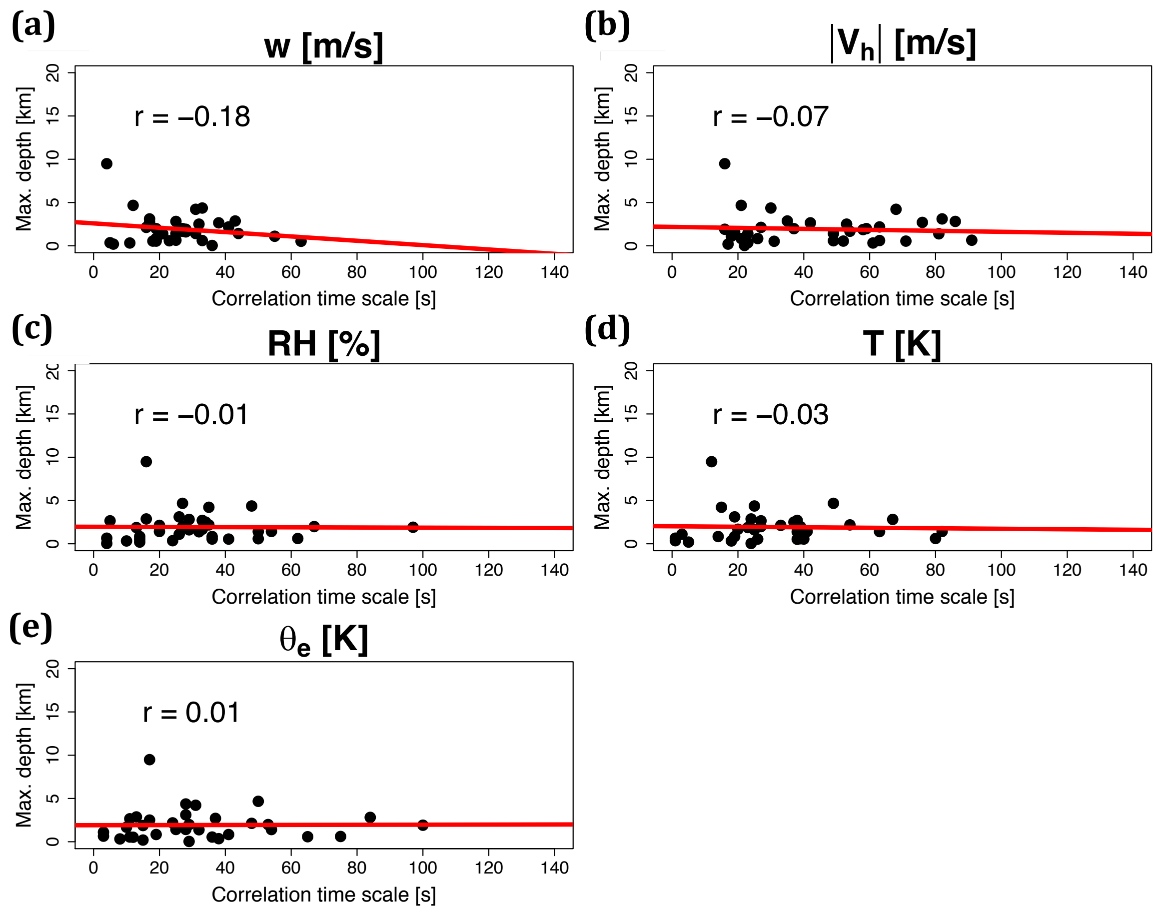

Figure 3.40: Same as Fig. 3.39, but for individual downdraft soundings.

CHAPTER 4

Computational fluid dynamics modeling

4.1 Introduction and methods

Prior to performing any physical test drops of the new XDDs with the p_d sensors, three-dimensional modeling of the typical airflow and pressure anomaly distribution around a falling XDD was examined. A three-dimensional model of a falling XDD, using a basic computational fluid dynamics (CFD) model, is useful to obtain estimates of optimal port location, pitot-static calibration coefficients (ratio of the true Bernoulli p_d to the true airspeed to the pitot-static-indicated p_d), drag force, and errors associated with angle of attack. A three-dimensional model of the XDD itself, obtained from computer-aided design and drafting (CAD) files provided by Yankee Environmental Systems, was imported into the '*simFlow*' three-dimensional CFD model (Fig. 4.1). The three-dimensional model is not a perfect representation of the XDDs or their fall characteristics, but it is reasonable to use the CFD model for basic simulations and to estimate the behavior of the XDD as it falls. The CAD file itself is not included in this dissertation due to proprietary concerns.

simFlow has been established as an adequate and robust CFD modeling software package (e.g., Lodh et al., 2017). *simFlow* uses the *ParaView* and *OpenFOAM* open source tools, which are commonly used in engineering studies. It can model both incompressible and compressible flows, include turbulence and simple chemical reactions, and simulate heat transfer. All values of pressure, wind speed, and turbulence are normalized by the density of the fluid, even though the units for these values are reported as Pa, m s^{-1}, and J, respectively.

In order to compute the wind flow around the XDD as it falls, and the pressure perturbations observed during descent, a non-uniform gridded mesh of the XDD and the space around the XDD was created (Fig. 4.2). *simFlow* creates the non-uniform gridded mesh from a user defined initial fixed grid. The specifications for the mesh size and CFD model are provided in Table 4.1. The CFD model was run for 250 s with a 1-s time step, incompressible free-stream airflow of 20 m s^{-1}, and Reynolds-averaged NavierStokes (RANS) k-ω shear stress transport (SST) turbulence. The RANS k-ω SST turbulence model performs well in conditions of adverse pressure gradients or separating flows around an object and in both high and low Reynolds number situations (Menter, 1993). Adverse pressure gradients occur when the pressure increases in the direction of the flow, such as for an XDD falling through the atmosphere in a motion-relative, Langrangian framework (e.g., Figs. 4.3c, 4.4c). The CFD model was also run at free-stream airflows of 20 m s^{-1} at different angles of incidence from 0–360°, every 5° to simulate the behavior of the XDD as it falls near terminal fall speed. Note that in *simFlow*, the horizontal axes are x and z and the vertical axis is y.

4.2 Results

4.2.1 Airflow characteristics

The CFD model runs show that, at 20 m s^{-1} true, the apparent airflow decreases to approximately 10 m s^{-1} at the nose of the XDD, which corresponds to an increase in pressure of 170–215 Pa (Figs. 4.3a, c, 4.4a, c). The flow diverges around the nose and either enters the twisted slots in the foam or flows parallel to the contours of the dropsonde body (Figs. 4.3b, 4.4b). There is a slight increase in the apparent airspeed outside of the dropsonde body along the sides, which corresponds to a relatively weak low-pressure anomaly along the sides of the dropsonde body (Figs. 4.3a, c, 4.4a, c). The flow then converges in the aft of the dropsonde and a weak wake low forms, with high turbulent kinetic energy (TKE) approximately half an inch behind the quadrifilar antenna and rotation of the airflow immediately behind the foam body (Figs. 4.3b, c, d, 4.4b, c, d). The low-pressure anomaly in the aft dissipates quickly, indicating that the pressure recovery is quick for the XDDs and that the low pressure is not appreciably strong, deep, or steady in the aft of the dropsonde (Figs. 4.3c, 4.4c). The airflow immediately behind the quadrifilar antenna is relatively calm, with weak airflow and a weak, but steady, 30–40 Pa low-pressure anomaly (Figs. 4.3a, c, d, 4.4a, c, d)

The tail of the dropsonde (Fig. 4.5) has four pockets of strong negative pressure anomalies (−80 to −90 Pa) associated with the blocked flow from the foam body of the XDD (Fig. 4.5c) and a weaker, −30 to −40 Pa, pocket of low pressure behind the antenna (Fig. 4.5a). But, these negative pressures are comparable to the negative pressures along the side of the dropsonde body (e.g., Fig. 4.5c), which would produce a weak or near-zero p_d for the venturi-static methods. Weak or near-zero p_d values are more prone to large percent errors associated with signal saturation as previously described in section 2.4. This means that the venturi-static method may not work well despite being the least prone to icing conditions.

A venturi port somewhere in the aft of the XDD is still plausible if a pitot-venturi method was used. Even though there is appreciable turbulence associated with the wake low in towards the aft of the XDD, the high TKE zone is far enough away from the end of the antenna (Fig. 4.3d), and the negative pressure anomaly and airflow strength immediately behind the antenna is reasonably uniform (Fig. 4.5a, b), to justify an antenna venturi port. The pressure behind the antenna varies by only 0.2 Pa within 0.25 in. of the center point. The low pressure (and airspeed) behind the antenna is more uniform than the low pressure and airflow behind the foam body of the XDD (Fig. 4.5c, d), and the rotor-like feature in the airflow behind the foam body is problematic (Fig. 4.3b). This collectively suggests that a venturi port at the end of the quadrifilar antenna would be the most optimal venturi method. The strength of the low-pressure anomaly behind the foam body and to either side of the antenna is also a stronger function of the angle of incidence of the XDD to the flow (Fig. 4.8, discussed below) and, subsequently, the phase of the XDD in its rotation, which complicates the analysis of the p_d and pitot-indicated TAS data.

The variance in the low pressure along the sides of the dropsonde presents a challenge for the pitot-static method. If a pitot-static was used, then the static port should be located towards the back end of the foam body to obtain a pressure measurement closer to the true static air pressure (0 Pa; Figs. 4.3c, 4.4c). A side static port is also logistically and operationally challenging, because of the effort it takes to route the pitot tube around the circuit board and electronics and puncturing the side wall of the XDD sleeve (Table 2.1). The pitot-static method would also suffer the same strong angle of incidence and dropsonde rotation issues as the pitot-venturi with a body venturi. Further, both nose-pitot methods will be less resilient to icing. These problems make the pitot-static method arduous, despite the previous hypothesis that it would be the most reproducible from dropsonde-to-dropsonde.

The nose of the dropsonde has little variance in the ram pressure caused by the airflow (Fig. 4.6a, b). The pressure along the leading edge/nose of the dropsonde foam body varies by approximately 20 Pa, but along the central line (shown in black in Fig. 4.6a, b) it only varies by 1–5 Pa at most. The strongest pressure occurs in the area between the nose and side wall and the corners of the rounded nose (Fig. 4.6a). The pressure along the central line is constant within 0.1 in. of the center point of the nose and varies by only 4 Pa within 0.25 in. A 4 Pa difference due to port placement would correspond to a velocity difference of 0.2 m s^{-1}. This means that little variation in the pressure should exist with port placement along the central line of the nose of the dropsonde and that the two pitot methods should be highly reproducible from dropsonde-to-dropsonde. These results indicate that the TAS from a pitot-static would more closely represent the true airspeed, but the operational limitations of the pitot-static and the strong influence of dropsonde tilt on the static pressure make it infeasible for use on the XDDs. The pitot-venturi method with an antenna port, therefore, is likely the most robust methodology out of the three modeled in the CFD, despite its limitations (Table 2.1).

The results from the CFD model indicate that any method used would not accurately obtain the TAS without a calibration coefficient. Because the pitot-venturi method appears to be the most reproducible and most operationally viable method, it was tested in the CFD model to estimate an airspeed calibration coefficient by placing "zero-mass" pressure probes on the nose and the antenna at the geometric center of the dropsonde and an aft body probe to one side of the XDD (Fig. 4.7). These probes report the exact pressure at a specific location in the CFD model output without adding in an actual probe to the XDD model. The pitot-venturi method using the antenna port was compared to the pitot-venturi method using an aft body port, and both were rotated with respect to both of the vertical planes (x-y plane and z-y plane) to examine the impact of dropsonde tilt or tumbling on the observed p_d.

The calibration coefficient (P^*) for each method is calculated by:

$$P^* = \frac{0.5V^2}{p_d}, \tag{4.1}$$

note that density is not included in the calculation, because the differential pressure obtained from the CFD model is normalized by density. In order to obtain the TAS, one would need to multiply the observed p_d by P^* and use equation 2.3. The estimated P^* value for the pitot-venturi with the antenna venturi port is 0.97, which is larger than for the pitot-venturi with the body venturi port at 0.81. This means that the pitot-venturi with the body port should overestimate the airspeed by approximately 20%, whereas the pitot-venturi with the tail port is closer to the true airspeed.

Figure 4.8 shows the response of p_d for the pitot-venturi method with an antenna port or a body port to the angle of incidence. The model XDD was rotated in both the x-y plane and the z-y plane and the average zero-incidence normalized signal (S^*) was plotted. Cross sections of the typical airflow and pressure at incidences of 0, 90, 180, and 270° in both the x-y and z-y plane are provided in Figures 4.9 and 4.10. S^* rises slightly above unity over an 80° span (±40°), then decreases rapidly to zero at approximately ±80°. At large incidences to the flow, the signal changes sign and indicates an incorrect, negative, p_d that minimizes at incidences of 140 and 220°. The pitot-venturi method with an antenna port has S^* values closer to unity at ±40° incidences, but stronger (more negative) S^* values outside of ±40° (Fig. 4.8). The pitot-venturi method with an antenna port has errors within ±0.5 m s^{-1} at ±5° incidences and ±1 m s^{-1} at ±10°. The angle of incidence, therefore, is an appreciable error that can affect the measurement beyond the desired error budget of ±0.1 m s^{-1}. At present, the severity of the tilt of the XDDs during descent is not known and further study of dropsonde dynamics is needed to obtain a realistic measure of tilt effects on the TAS measurement. Measurements of dropsonde tilt during descent can be used to make adjustments to the measured differential pressure TAS and account for most of these errors. Further error estimates of the pitot-venturi-derived TAS and vertical velocity, provided in chapters 5–7, assume an angle of incidence of 0°.

4.2.2 Drag coefficient estimate

The *simFlow* CFD model monitors density normalized drag forces (F^*) in the three-dimensional framework (x, z, y). The drag coefficient can be obtained using a modified version of equation 2.9:

$$C_d = \frac{2F^*}{AV^2}, \tag{4.2}$$

for each x, y, and z component. The drag coefficient was computed at an airspeed of 20 m s^{-1} and in both axial (nose-on) and cross-flow (side-on). The frontal area of the XDD can be approximated as a circle, with a diameter of 0.066 m (Black et al., 2017). The side area of the XDD can be approximated by a rectangle, with a length of 0.178 m and a width of 0.066 m (Black et al., 2017). For reference, the length to diameter ratio of the XDDs is approximately 2.7.

Using these approximated areas, the CFD model indicated C_d for the XDDs in axial flow (y-direction) is 0.93, which is close to the 0.95 estimate in section 2.4. Both of these estimated C_d values are slightly larger than what is expected for a cylinder (with a length to diameter ratio of 2.7) in axial flow by approximately 0.1–0.15 (Higuchi et al., 2006). The C_d for cross-flow (x-, z-direction) is an average of 1.30, which is not appreciably different than the axial drag coefficient and is representative for a smooth cylinder in cross-flow at the expected Reynolds numbers for the XDDs (Fig. 2.13) (e.g., Munson et al., 2006).

Table 4.1: Specifications for the *simFlow* CFD model for the XDDs.

	Value or description
Time step	1-s
Duration	250 s
Compression	Incompressible
Airspeed	20 m s^{-1}
Wind direction	0–360°
Turbulence	RANS k-ω SST
Boundary conditions	Free slip or inflow/outflow
Number of initial grid points	10x10x10
Grid spacing (x; z; y)	0.016 m; 0.034 m; 0.016 m
Transport model	Newtonian: ν=1.5x10^{-5} m^2 s^{-1}
Solver	Geometric agglomerated algebraic multigrid solver (GAMG)

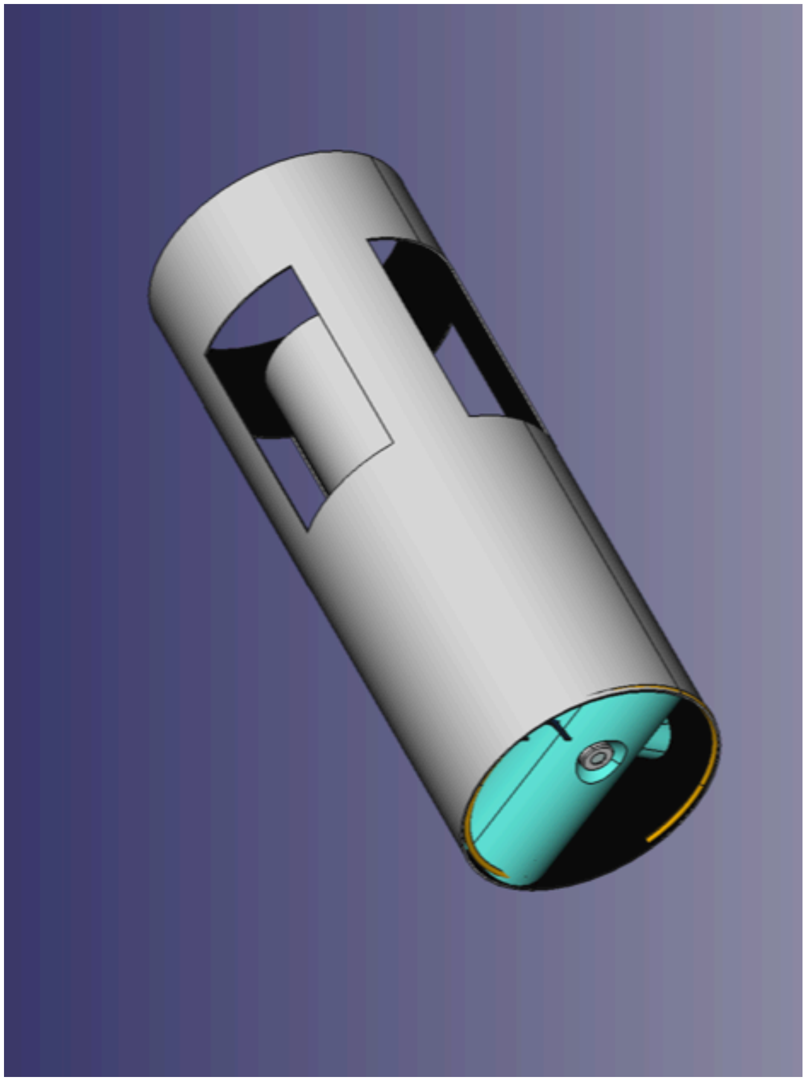

Figure 4.1: Three-dimensional model of the XDDs provided by Yankee Environmental Systems.

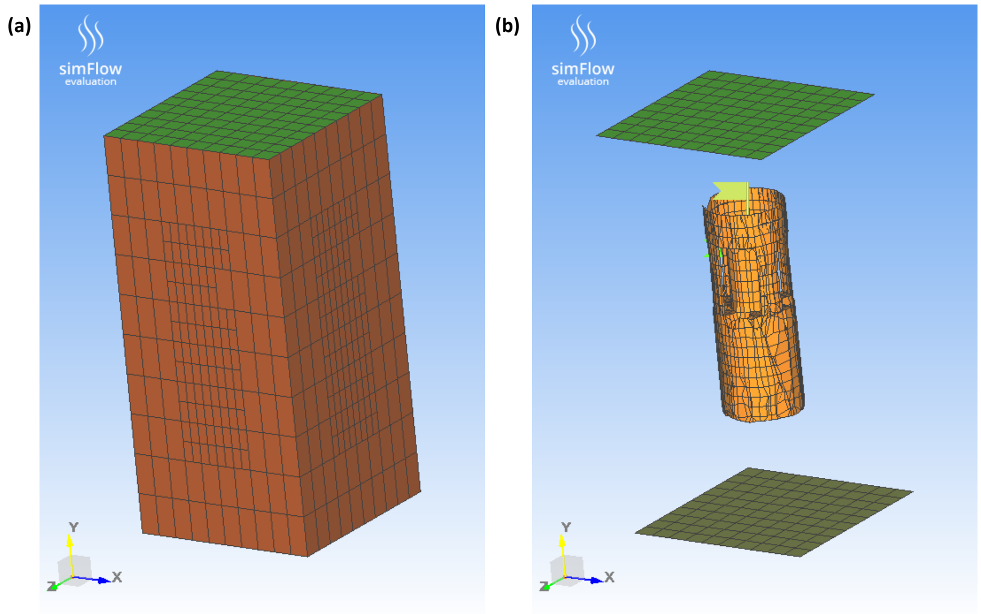

Figure 4.2: Three-dimensional non-uniform grid (brown and green in panel (a) and mesh around the XDDs (orange in panel (b)). Note, the vertical axis is denoted in *simFlow* as 'y' rather than the traditional 'z'.

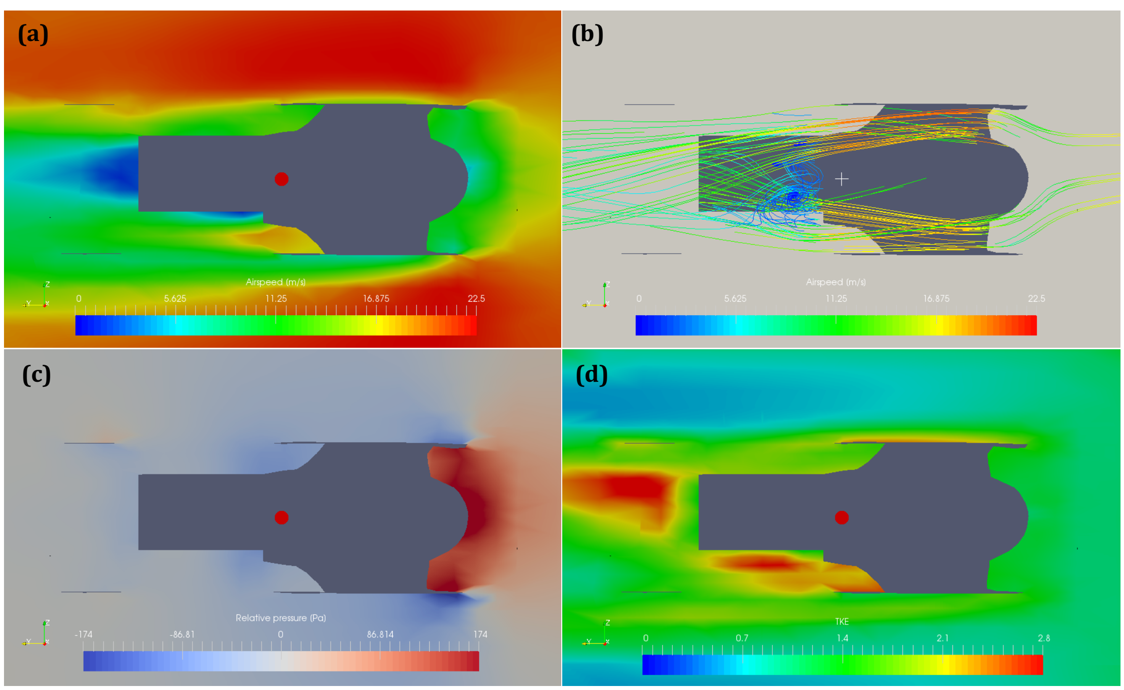

Figure 4.3: Results of the CFD model at zero angle of incidence in the x-direction. Panel (a) is the airflow (m s^{-1}; shaded). Panel (b) shows the streamlines of the airflow, with the airspeed shaded in m s^{-1}. Panel (c) is the anomalous pressure relative to the ambient pressure (Pa; shaded). Panel (d) is TKE (J; shaded).

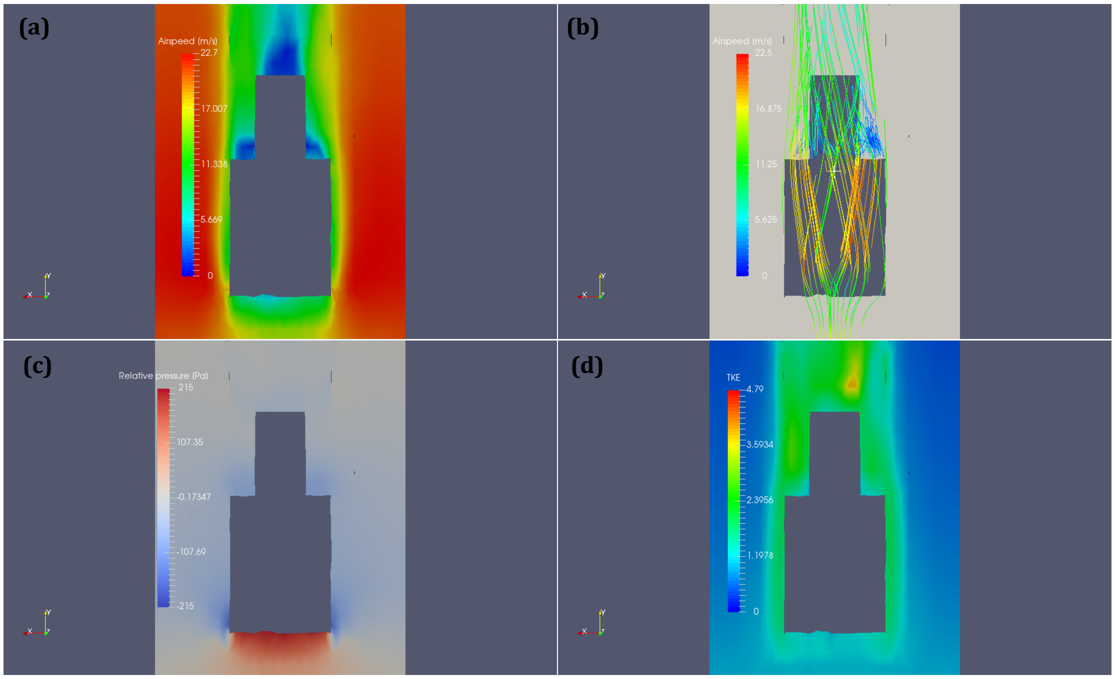

Figure 4.4: Same as Fig. 4.3, but for the z-direction.

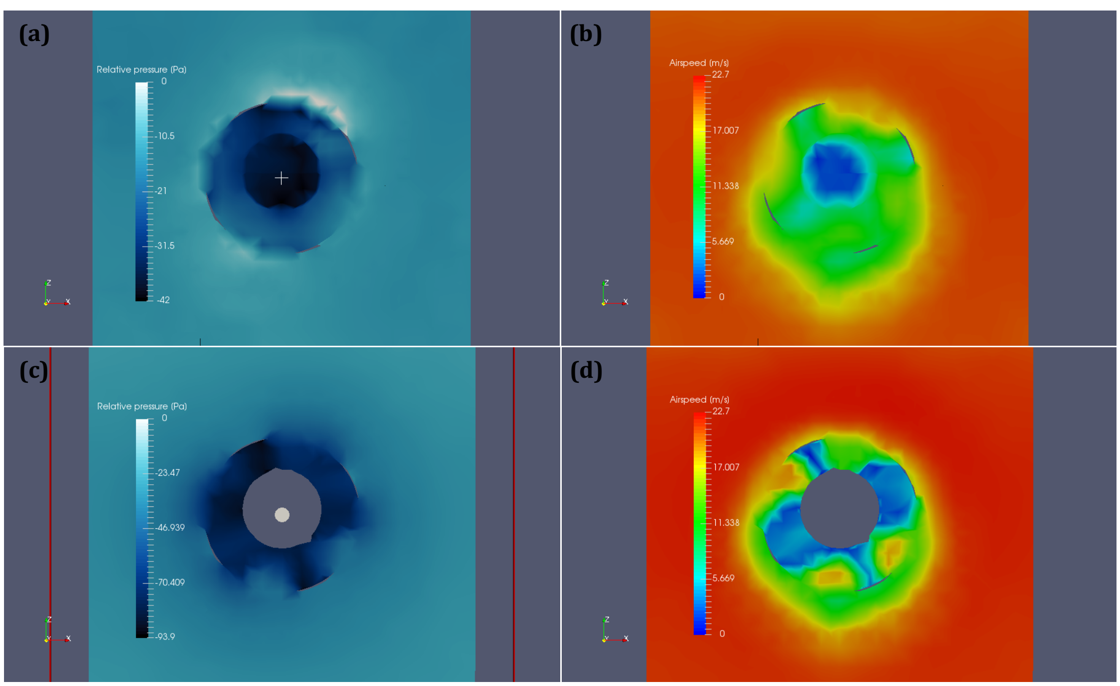

Figure 4.5: Anomalous pressure (Pa; shaded) and airflow (m s^{-1}; shaded) behind the main body of the dropsonde. Panels (a) and (b) are immediately behind the quadrifilar antenna, whereas panels (c) and (d) are immediately behind the foam body of the dropsonde.

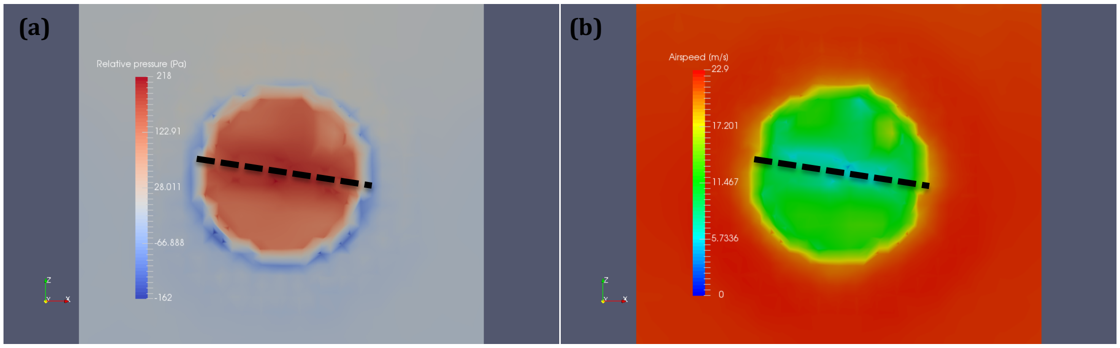

Figure 4.6: Anomalous pressure (Pa; shaded) and airflow (m s^{-1}; shaded) at the nose of the dropsonde. The center-line of the XDD foam body is shown as a dashed black line.

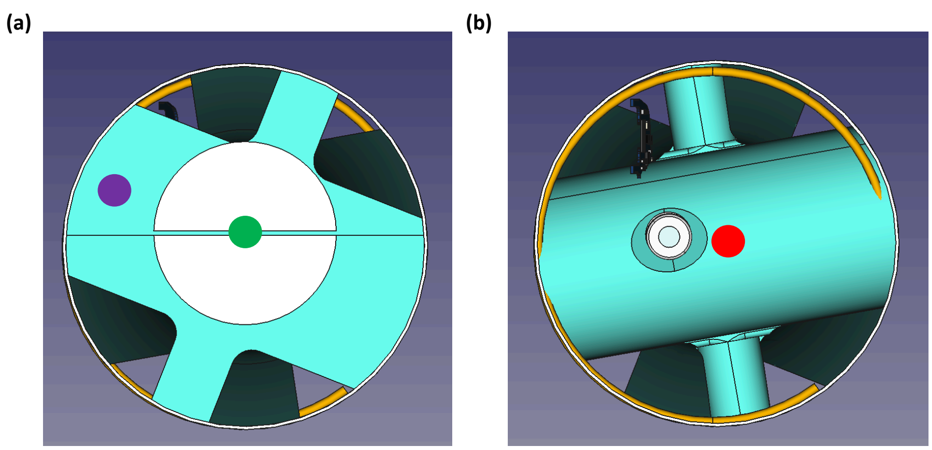

Figure 4.7: Location of pressure probes/ports for the CFD model analysis. The nose pitot port is the red dot in panel (b), the antenna venturi port is the green dot in panel (a), and the venturi body port is the purple dot in panel (a).

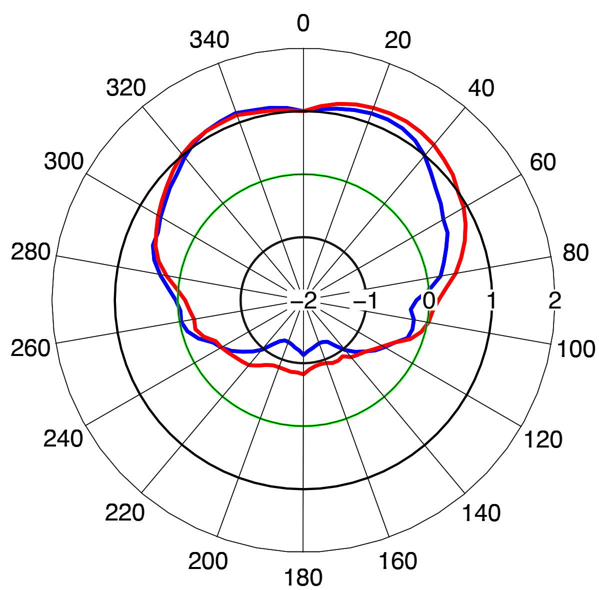

Figure 4.8: Polar plot of S^* for the pitot-venturi with the antenna port (blue) and the body port (red). S^* values of 1 and 0 are highlighted in black and green, respectively.

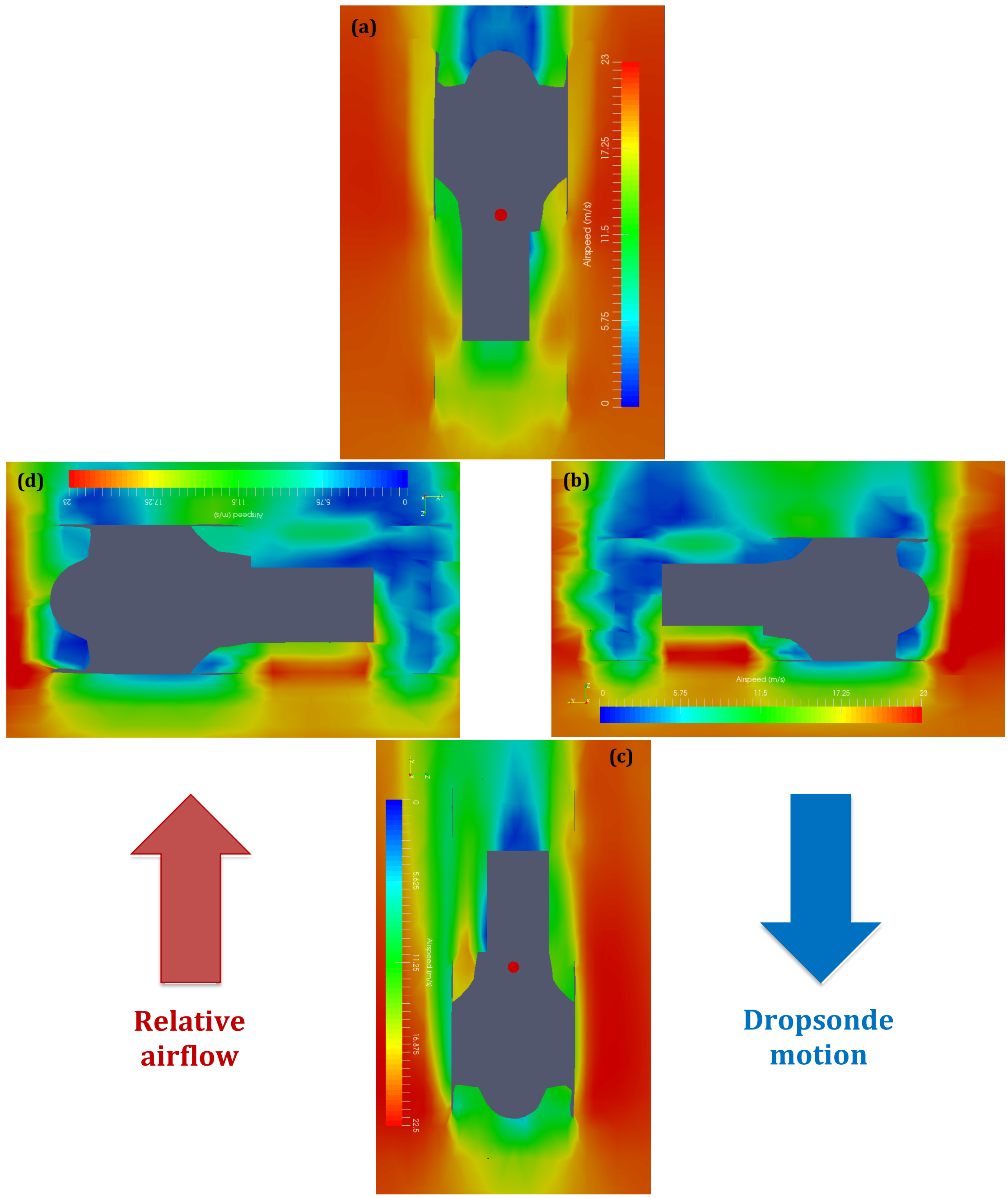

Figure 4.9: Airflow around the XDD as it falls (m s^{-1}; shaded) rotated in the x-y plane. Panel (a) is at an angle of 180°, panel (b) is at an angle of 90°, panel (c) is at an angle of 0°, and panel (d) is at an angle of 270°.

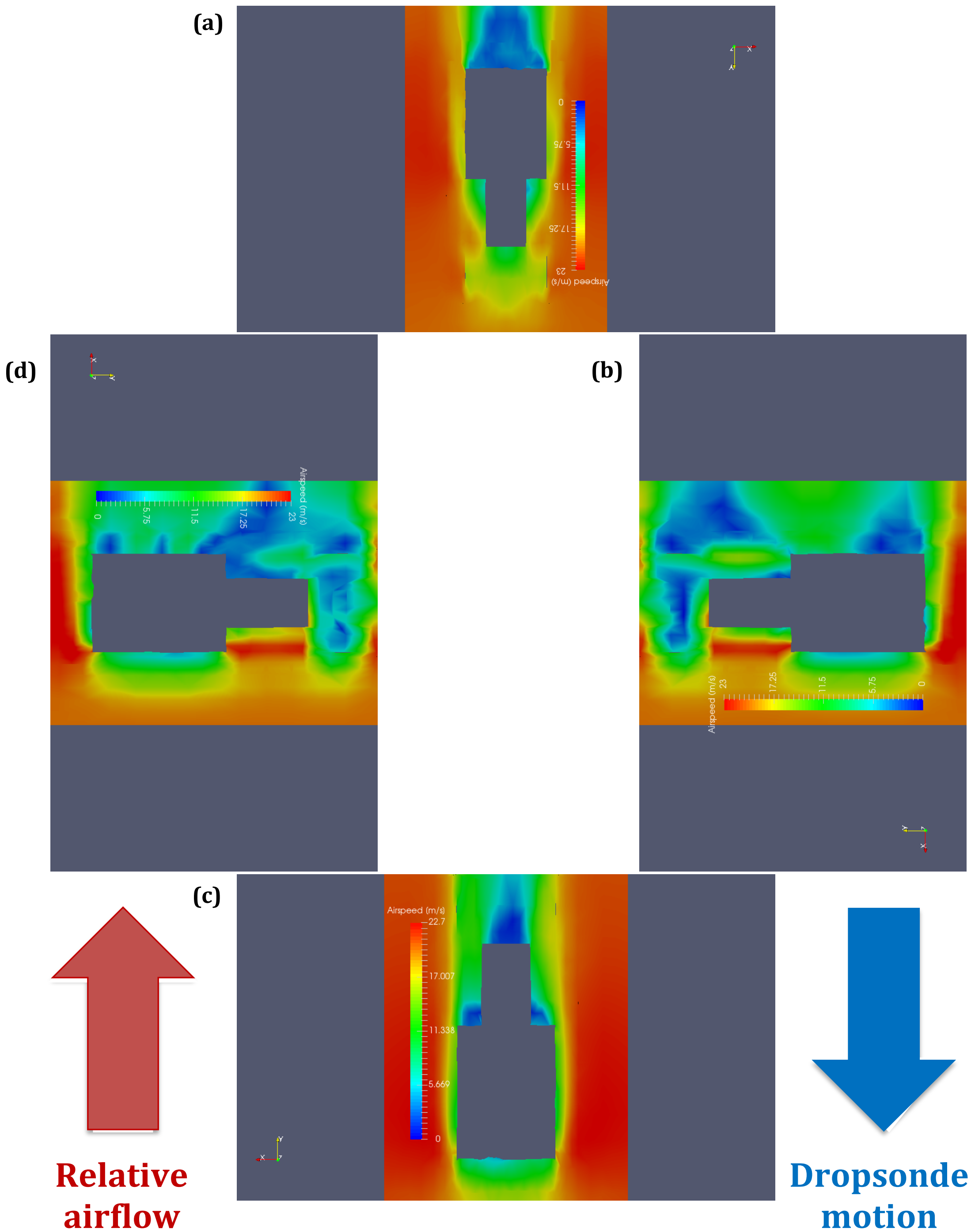

Figure 4.10: Same as Fig. 4.9 but rotated in the z-y plane.

CHAPTER 5

Clear air tests and calibrations

While the CFD model analysis is useful for beginning to understand the port location sensitivity and discerning the optimum port configuration, the pitot-venturi with an aft antenna port should be tested in clear air conditions prior to operational drops, and the dropsonde-to-dropsonde variance should be tested in reality. Moreover, the actual P^* for the chosen method needs to be established by comparing P^* values for a small subset of dropsondes. To accomplish this, individual P^* values using the pitot-venturi, with the aft antenna port, were obtained and compared using a rotating arm device. The final error estimate for the pitot-venturi-derived vertical velocities was calculated after conducting full-scale meteorological flights (chapter 6).

5.1 Methods and data

All clear air rotating arm tests documented here were conducted at Yankee Environmental Systems in Turners Fall, MA. All data were telemetered using a similar protocol and forward error correction as in TCI, but the receivers were located at Yankee Environmental Systems rather than on an aircraft. The telemetered data include: date, time, p, T, p_d, GPS fall speed, and GPS altitude. The p_d sensor used for all tests was the AllSensors DLHR-L05D-E1BD described in section 2.5. The pitot and venturi ports themselves are blunt ends of standard pitot tubing for model airplanes, with an inner diameter of 1.5 mm and an outer diameter of 2.5 mm. The ends of the tubing were placed flush to the foam exterior (e.g., Fig. 5.1).

The p_d for the DLHR-L05D-E1BD sensor is calculated by the following transfer function:

$$p_d = 248.84\frac{1.25(D - D_o)F_{SS}}{N^2}, \tag{5.1}$$

where D is the digital output (units as decimal counts, hereafter called DO), D_o is the zero-p_d offset, F_{SS} is the full-scale span of the measurement (2^5 DO), and N is the number of bits in the measurement (18). This equation was obtained from All Sensors (2019) and was modified to produce differential pressure values with units of Pa. The TAS was calculated using equation 2.3.

During the prototyping and development stage, eight XDDs were placed on the ground and allowed to transmit for approximately $1-10$ minutes, depending on the dropsonde. The mean DO bias for each XDD during this time period was assumed to be representative of the D_o term. By subtracting the mean D_o from the raw DO in equation 5.1, the observed p_d values were calibrated for any zero-p_d/zero-airspeed bias. The zero-p_d/zero-airspeed digital output is provided in Figure 5.4. The results from Figure 5.4 indicate that a single, universal zero-p_d offset correction for all XDDs cannot be used, because the mean values are appreciably different from dropsonde-to-dropsonde. The offset value should be calculated for each XDD individually prior to launch and automatically subtracted. The zero-p_d values are nearly constant over time for each XDD, with small standard deviations of $3-16$ DO (0.002–0.012%).

5.1.1 Rotating arm

In order to obtain true P^* values, estimate the dropsonde-to-dropsonde variance in the P^* value, and verify port sensitivity from the CFD model (chapter 4), a large rotating arm was built to swing the XDDs in a circle, with a constant radius. This was done in lieu of wind tunnel testing due to time and budget constraints, as well as the availability of wind tunnels suitable for the size of the XDDs and their expected fall speeds. The rotating arm (Fig. 5.2a) was designed to swing the XDDs in a circle with a diameter of approximately 5 m at a speed of 20 m s^{-1} to match the speeds used in the CFD model and the approximate sea-level fall speed of the XDDs. The rotating arm tests were conducted on 15 May 2019.

The rotating arm consists of a WEG 1 HP single phase AC motor, with a nominal speed of 3480 RPM, a Lexar Industrial MRV063 40:1 worm gear speed reducer, with a 2.95-in pulley head that connects to a stepped 3, 4, 5, or 6-in pulley head by a v-belt, a truck axle bearing, and an adjustable arm (Fig. 5.2b). The worm gear speed reducer slows down the speed of the output shaft to approximately 87 RPM. The speed is then modified by the ratio of the diameters of the chosen pulley heads. For example, the use of the 2.95-in pulley head on the output shaft with the 6-in option on the arm reduces the speed by approximately a factor of two (approximately 43 RPM). At an arm length of exactly 5 m, this would, theoretically, correspond to a tangential speed of approximately 22 m s^{-1}.

Ultimately, the 3-in pulley head option on the arm was used, with a total arm length of approximately 2.65 m (104.24 in) (Fig. 5.2a, b). This was done to get the theoretical speed of the arm as close to 20 m s^{-1} as possible and to keep the arm well balanced without a support strut system. The dropsonde was attached to the adjustable arm using a wiring rig (Fig. 5.2c). The wiring rig consists of a 1x2x3 in. block of wood, with copper tubing glued into holes drilled into the wood. Wire loops (14 gauge) threaded through the copper tubing were used to hold the dropsondes in place. The loops were tightened around the dropsondes each time the rotating arm was used.

The rig of the rotating arm was mounted to planks of wood to provide extra stability and anchored into to the ground using four metal stakes (Fig. 5.2a, b). Plastic feet were used under the wood planks to make sure that the rotating arm was level. The dropsonde mount was manually leveled prior to testing.

The true speed of the rotating arm was monitored three ways: 1) a Hall Effect sensor; 2) 30 FPS video; and, 3) a manual stop watch timer. Hall Effect sensors are traditionally used to detect changes in magnetic field (e.g., Ejsing et al., 2004). In this case, the Hall Effect sensor, controlled by an Arduino nano microprocessor board, triggers upon the passage of a set of neodymium magnets on the arm above it (Figs. 5.2b and 5.3b). The Arduino nano calculates the time between triggers and outputs the time onto an LCD screen (Fig. 5.3a). The Hall Effect sensor is attached to a short rod to place the sensor close enough to the magnets on the arm to correctly trigger. The Hall Effect speed monitor is powered by a 9 V battery (Fig. 5.3a).

The arm speed from the 30 FPS video was calculated by slowing the film down frame-by-frame and calculating the mean time it took to complete one full rotation of the arm. The speed from the manual stop watch calculation was obtained by calculating the mean time it took for the arm to complete ten revolutions at the start of each minute that the arm was rotating. The arm was ran for four minute intervals. Mean arm speeds and mean pitot-venturi-indicated speeds were used, rather than instantaneous speeds, in an effort to diminish the effect of ambient wind and wind gusts. It took approximately ten minutes to set up and complete the calibration of one dropsonde. The p_d values were recorded at a 1-Hz rate.

5.2 Results and analysis

A total of eight different dropsondes with the nose pitot port and antenna venturi port were used in the rotating arm calibration tests. The location of the ports was measured for each dropsonde using calipers after testing. The location of the nose port had a standard deviation of 0.02–0.03 in. and the antenna port had a standard deviation of 0.03 in. for the eight dropsondes. The total standard deviation of the port location was 0.04 in. Given the results of the CFD model analysis in chapter 4, p_d is expected to vary negligibly by 0.1–0.2 Pa at most; a TAS error of ± 0.01 m s^{-1}.

The Hall Effect sensor speed monitor indicated that the arm took approximately 1.16–1.17 s to complete one revolution. This agreed well with the mean manual stopwatch calculations and mean video calculated speeds of 1.155–1.165 s rev^{-1}. This corresponds to tangential speeds of 19.2–19.4 m s^{-1}, depending on the dropsonde and test run. The mean speeds for each test run/dropsonde were used to calibrate the TAS and calculate the mean P^* value for each dropsonde and the eight dropsonde dataset using equation 4.1.

The mean TAS for the eight test runs was 20.6–21.4 m s^{-1}. This variance between runs accounts for any persistent or mean errors for a given dropsonde, differences in mean arm rotational speed, any mean wind biases, small port placement errors, and any true dropsonde-to-dropsonde variance. The plots for all eight test runs are provided in Figure 5.5. The data have some noise across all eight runs associated with ambient wind, inconsistent arm speed, or true precision of the measurement. The standard deviation for seven of the eight tests was low at 0.43–0.57 m s^{-1}. The first test, dropsonde 8121, had a higher standard deviation at 0.74 m s^{-1}, but the ambient wind was relatively stronger at that time, compared to the other seven runs.

A histogram of the mean P^* values for each of the eight XDDs is provided in Figure 5.6.

While the total number of dropsondes (samples) is small, these tests provide validation for the CFD-estimated P^*. Further testing of a larger number of dropsondes is required to fully understand dropsonde-to-dropsonde variance in P^* and the true distribution of P^* values for the XDDs. The distribution is positively skewed, with a peak in frequency between P^* values of 0.84 and 0.86 (Fig. 5.6). Both the mean and median P^* values are 0.85, which is less than but comparable to the CFD-estimated P^*.

The absolute difference between the mean arm speed and the mean TAS calibrated with a mean P^* value for all eight tests was 0–0.45 m s^{-1}, with a mean absolute difference of 0.16 m s^{-1} (Table 5.1). Using individualized P^* values for each dropsonde reduces the mean absolute differences to 0–0.01 m s^{-1}, with a mean absolute difference of 0.006 m s^{-1} (Table 5.1). As the mean arm speed was used in this analysis, and the instantaneous arm speed or pitot-venturi-indicated speed may differ due to ambient wind or wind gusts, the traditional root mean square error (RMSE) for each dropsonde cannot be accurately calculated. A 'mean speed' RMSE (MS-RMSE) was computed for both the mean P^*-calibrated TAS and the individually P^*-calibrated TAS across all eight runs. The MS-RMSE for the mean P^*-calibrated TAS was 0.6 m s^{-1}, whereas the MS-RMSE for the individually P^*-calibrated TAS was considerably smaller at 0.02 m s^{-1}.

These results suggest that individually calibrated dropsondes would produce a more accurate pitot-venturi-indicated TAS and errors well within the allowed $\pm$0.1 m s^{-1} bounds. The individual calibration, however, presents a challenge operationally. For example, to complete the same calibration for the 785 XDDs launched into Marty, Joaquin, and Patricia (chapter 3), it would take an estimated 131 hours (or 5.5 days) to complete the calibration. On the other hand, using a single P^* value increases the error to approximately 0–0.5 m s^{-1}.

Table 5.1: Mean and absolute mean difference between the mean arm speed and the mean TAS calibrated with a mean P^* or individual P^* values.

Dropsonde	Mean diff. (mean P^* cal.)	Mean diff. (ind. P^* cal.)
8121	0.33	0.01
F424	−0.21	0.01
B0C5	−0.05	0.01
FE03	0.13	0.01
70C5	0.10	0.01
AF12	−0.01	0.00
B645	−0.45	0.00
9425	0.00	0.00
Mean	−0.02	−0.006
Absolute mean	0.16	0.006
MS-RMSE	0.62	0.018

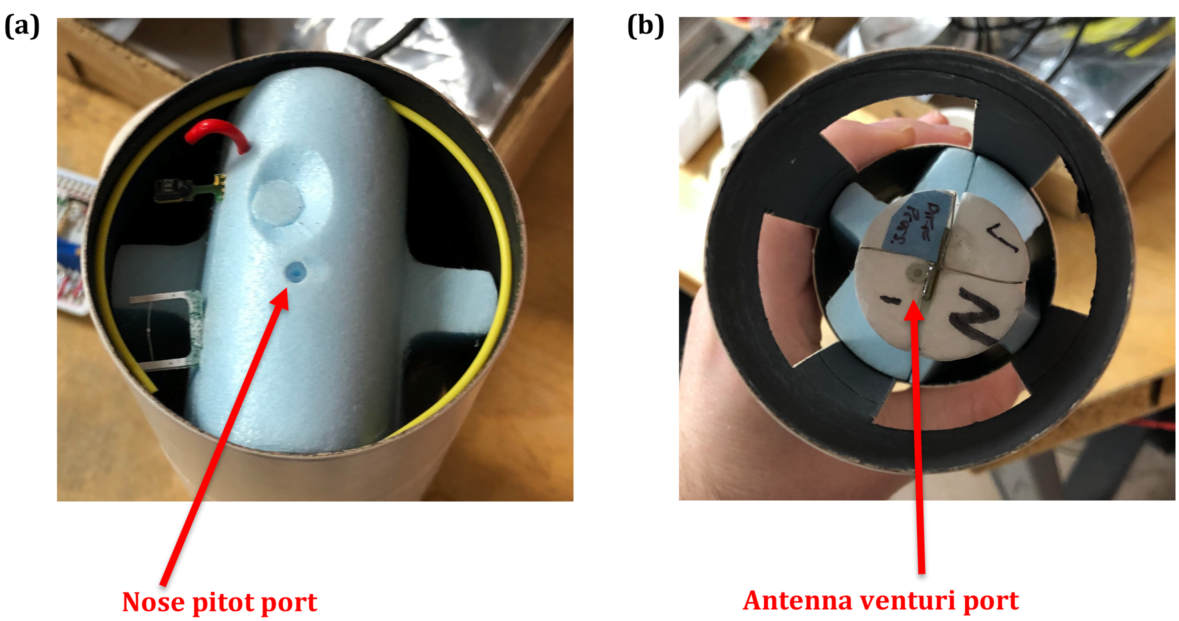

Figure 5.1: Pitot-venturi XDD prototype, with the nose pitot port (a) and antenna venturi port (b).

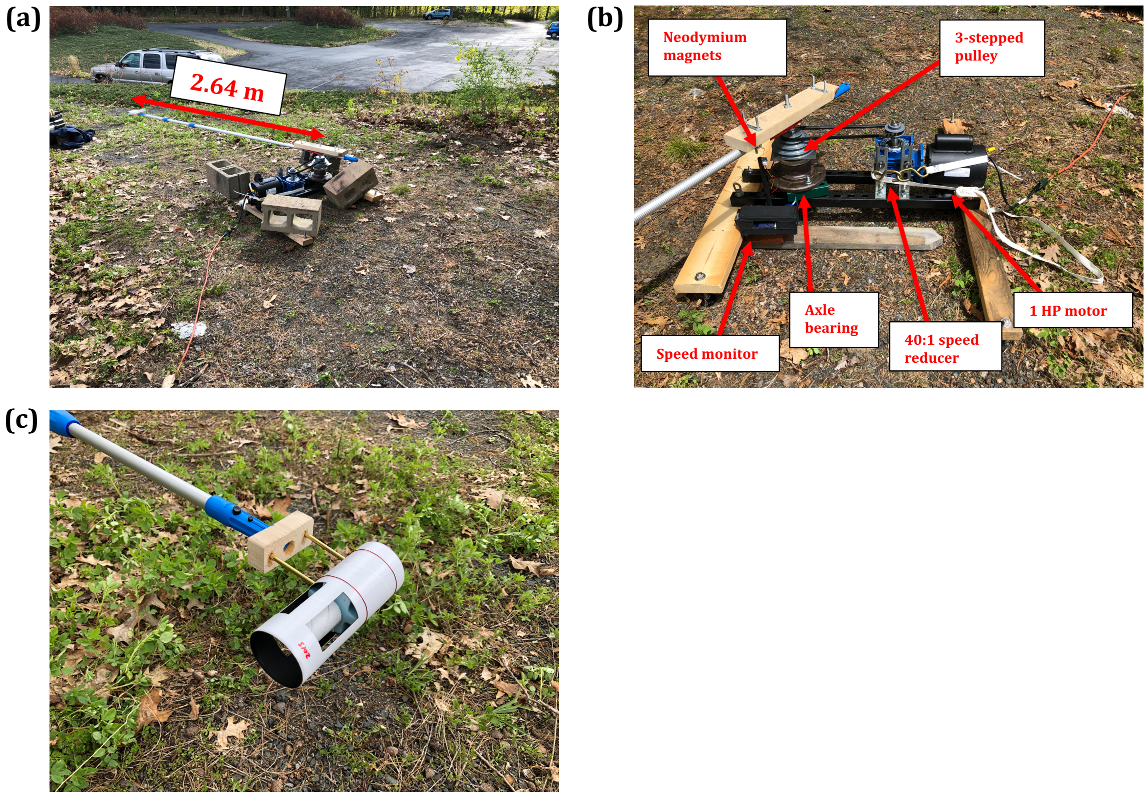

Figure 5.2: Images of the rotating arm used to calibrate the dropsondes. Panel (a) shows the arm length and overall scale. Panel (b) shows the general layout of the controlling mechanisms for the rotating arm. Panel (c) shows the wiring rig to hold dropsondes onto the end of the arm.

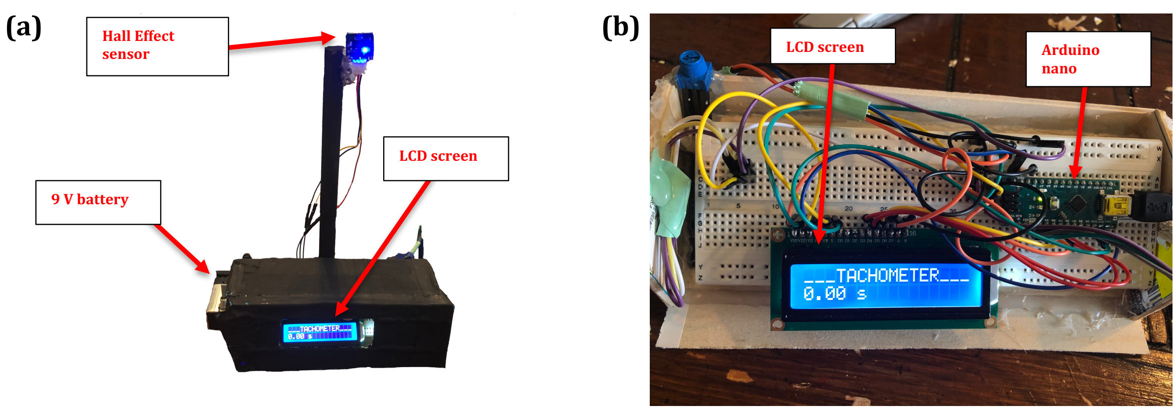

Figure 5.3: Images of the Hall Effect speed monitor. Panel (a) shows the monitor with the Hall Effect sensor attached to a post and an LCD screen output. Panel (b) shows the internals, circuit board, and Arduino nano used to control the sensor.

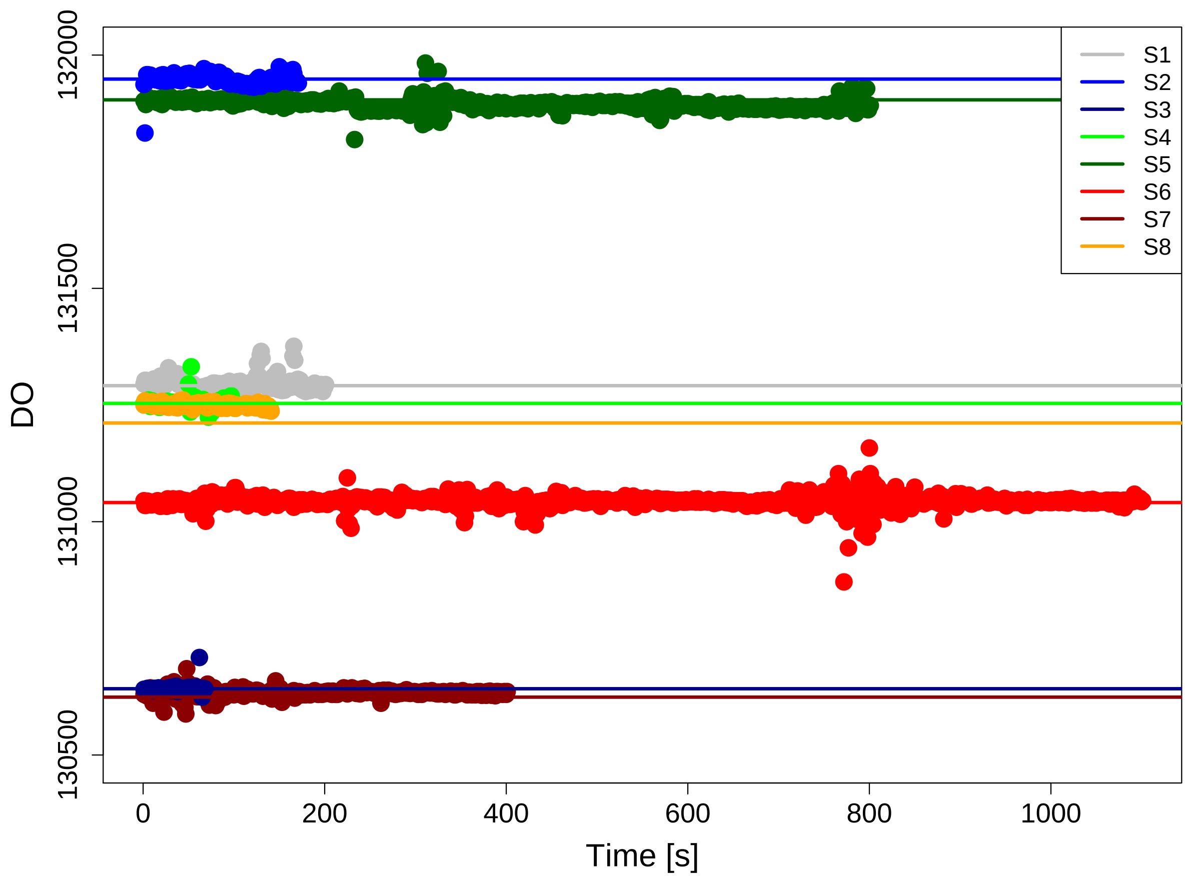

Figure 5.4: Digital output from eight XDDs (S1–S8; gray, blue, dark blue, green, dark green, red, dark red, and orange, respectively).

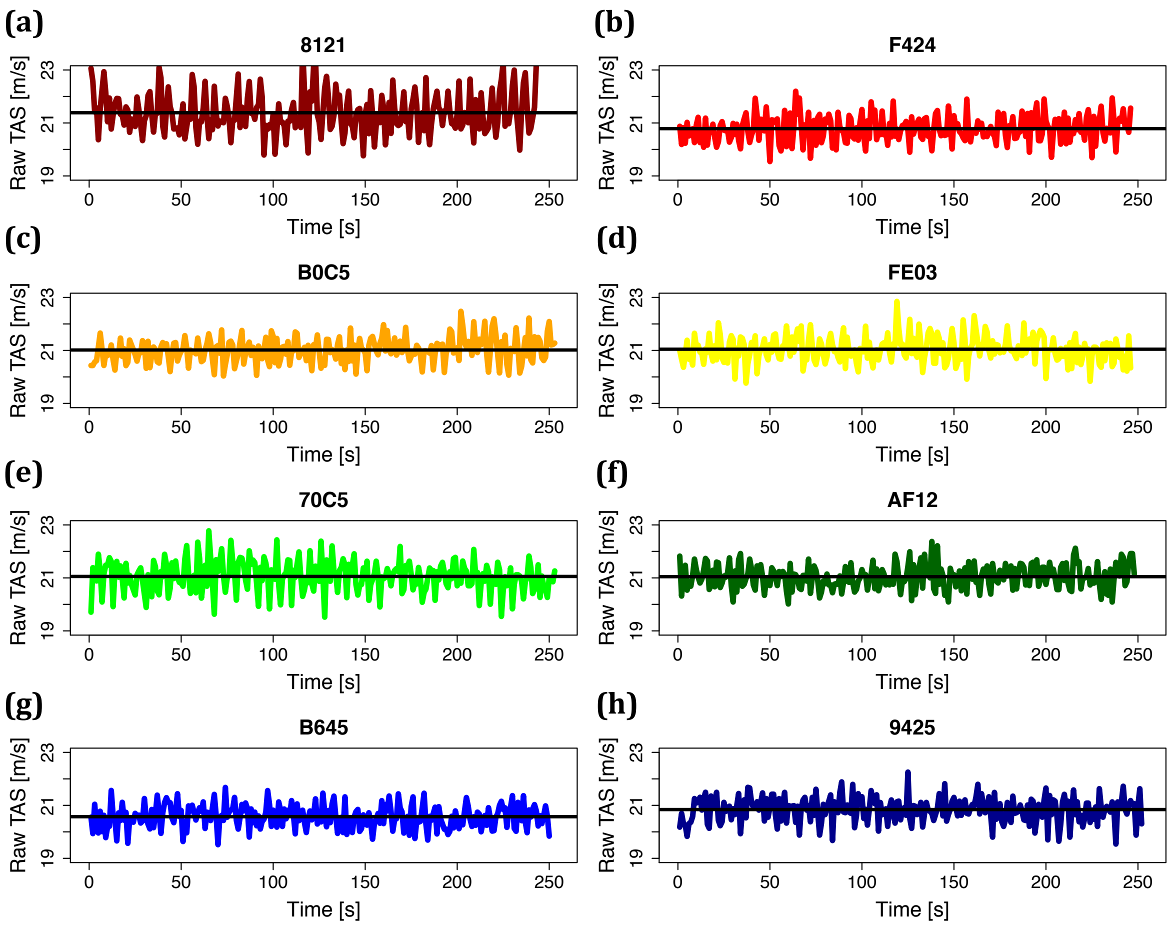

Figure 5.5: Raw, uncalibrated TAS from the eight dropsondes rotating arm tests. The black horizontal lines denote the mean TAS during the testing period.

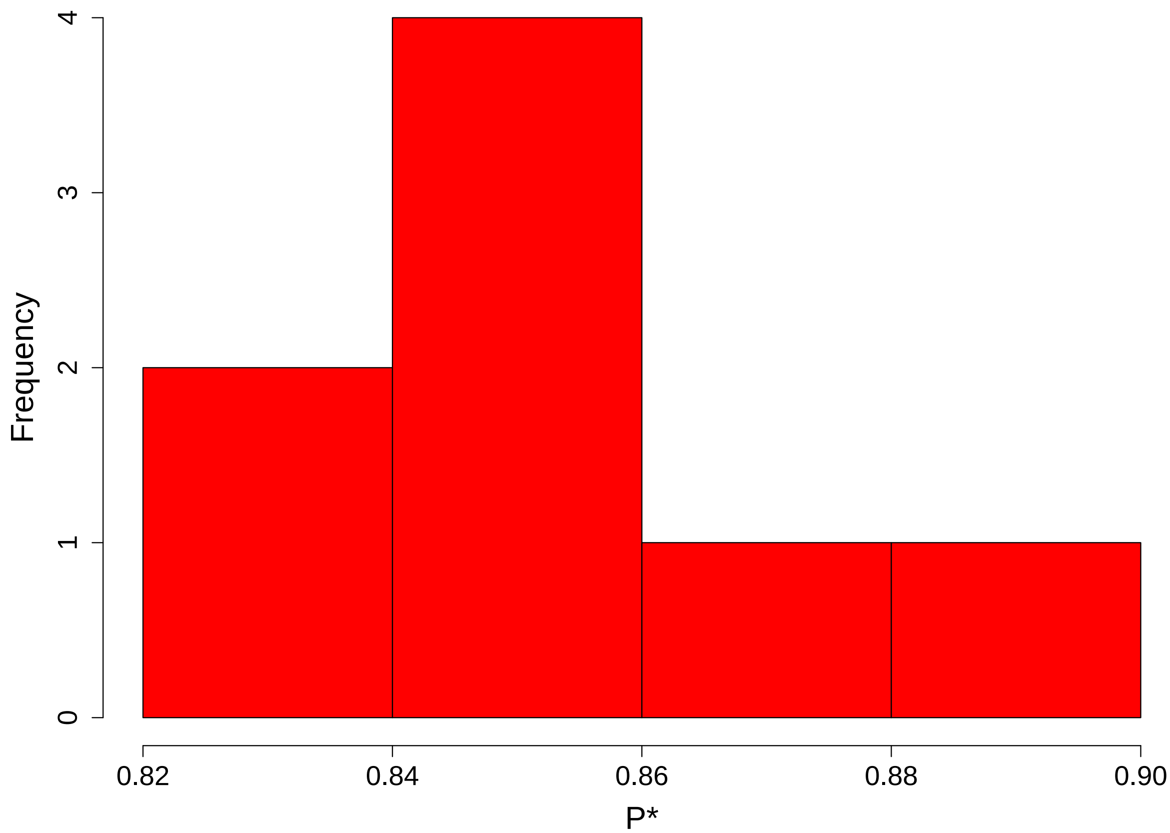

Figure 5.6: Histogram of the observed P^* values for the rotating arm calibration tests.

CHAPTER 6

Meteorological flights

6.1 Introduction

NASA conducted the Doppler Aerosol Wind (DAWN) Lidar verification field campaign from 15–28 April 2019 out of the NASA Armstrong Flight Research Center in Palmdale, CA. The goal of the campaign was to test the capabilities of the DAWN Lidar (Kavaya et al., 2014) onboard a DC-8 aircraft and validate the observations with coincident data from the Atmospheric Laser Doppler Instrument (ALADIN) wind Lidar on the European Space Agency Aeolus satellite (Paffrath et al., 2009; Reitebuch et al., 2009) and soundings of horizontal wind from the XDDs.

A total of four XDDs, with the p_d sensor and antenna aft port pitot-venturi configuration, were launched from the DC-8 aircraft at an altitude of approximately 8–9 km. All flights and XDD drops occurred over the northeastern Pacific between California, Hawaii, and Alaska. One sounding, launched approximately 1000 km off the coast of southern British Columbia (47.86°, −139.18°) at 03:09 UTC on 18 April, failed to record p_d data due to issues associated with start up of the XDD. The other three soundings recorded p_d data and were launched on 28 April approximately 700 km to the west of the Baja California Peninsula from 02:04–2:10 UTC. The soundings were launched approximately 40 km apart.

The three soundings are the first successful operational deployments of XDDs with the p_d sensor. In this chapter, the pitot-venturi-indicated fall speeds and vertical velocities are examined and compared to the other fall speeds and dropsonde-derived vertical velocity methods (e.g., the GPS fall speed-based drag force methodology and the M3 methodology). The synoptic meteorological conditions for the series of drops is also analyzed. An error analysis is also made, assuming that the true mean vertical velocity in the profiles is zero.

Unfortunately, the vertical velocity profiles observed by the XDDs cannot be truly verified at this time. The DAWN Lidar data was either not pointed downward or was pointed at a shallow, 30° angle (M. Beaubien and D. Emmitt, personal communication). This means that either vertical velocity profiles were not obtained or could be erroneous due to the shallow observation angle. Further, both the ALADIN and DAWN data were not fully post-processed, quality controlled, and readily available for inclusion in the dissertation. It is also unknown what the accuracy or quality of the ALADIN vertical velocities would have been. The specifications for the ALADIN and DAWN Lidars are provided in section 6.2. Comparisons of dropsonde pitot-venturi-derived vertical velocity to Lidar data will be a subject of future work.

6.2 Data and methods

6.2.1 ALADIN

The ALADIN Lidar, launched on the Aeolus satellite on 22 August 2018, is a direct-detection Doppler Lidar that detects the phase shifts in both the Rayleigh (molecular) and Mie (aerosols and cloud particle) regimes (European Space Agency, 2019a,b). It has a wavelength of 355 nm and a 100-Hz pulse rate (Reitebuch et al., 2009). The ALADIN Lidar is stated to have a $0.5-2$ km vertical resolution and a 1–3 m s^{-1} horizontal wind speed precision (Reitebuch et al., 2009). Additional specifications and simulated perfomance can be found in Reitebuch et al. (2009) and Paffrath et al. (2009). The ALADIN Doppler Lidar samples wind profiles below 30 km (Reitebuch et al., 2009; Paffrath et al., 2009; European

Space Agency, 2019a), whereas the XDDs and DAWN sample horizontal winds below flight level (approximately 8 km). Validations of the ALADIN Lidar-derived winds are ongoing and are part of the 2019 DAWN Lidar verification field campaign.

6.2.2 DAWN

The DAWN Lidar was developed by NASA to be used on a Earth-orbiting satellite to measure vertical profiles of horizontal wind (Kavaya et al., 2014). DAWN is a 2-μm pulsed-wave instrument that relies upon the Doppler shift of high-energy interacting with atmospheric aerosols to obtain the three-dimensional wind vector. The laser has a pulse rate of 10-Hz and a pulse length of 1 ns. Additional specifications can be found in Kavaya et al. (2014).

Comparisons between the DAWN horizontal wind speed and direction to XDD horizontal wind speed and direction was previously analyzed as part of the 2017 NASA Convective Processes Experiment (CPEX; Emmitt et al., 2018). The root mean square difference was 1–2 m s^{-1} for horizontal wind speeds and 14–16° for horizontal wind direction (Emmitt et al., 2018). This agrees well with the differences between dropsonde horizontal winds and DAWN horizontal winds during the 2010 NASA hurricane Genesis and Rapid Intensification Processes (GRIP) campaign (Kavaya et al., 2014). Emmitt et al. (2018) state that majority of the differences between the two were due to spatial and temporal separation of the DAWN and XDD soundings.

The DAWN horizontal wind soundings are approximately 30 seconds in duration, but cover a horizontal spatial scale of approximately 65 km when flown at 8 km on the DC-8 (Emmitt et al., 2018). In contrast, the XDDs would only traverse 5–10 km horizontally when launched from 8 km, assuming a hypothetical mean horizontal wind speed of 10 m s^{-1}. When the mean horizontal wind speed increases, however, the horizontal displacement of the XDD also increases (e.g., the XDDs launched near the core of Patricia on 23 October; section 3.1 and 3.3). Therefore, these differences in sampling could lead to slight differences between the profiles and not represent true error in the measurements of either instrument.

6.2.3 Flight and dropsonde data

Shown in Figure 6.1 is the flight track of the DC-8 for the 28 April drops. The p_d data obtained by the three dropsondes replaced the $IR\ SST$ data in the data processing and telemetry. Therefore, all variables in Table 1.2 were observed, except for the SST. The data acquisition frequency for p_d was 1-Hz for the DC-8 flights. The p_d values for each dropsonde were already calibrated for their individual zero-p_d offset (see section 5.1) prior to launch and were converted to the desired format using equation 5.1. The three XDDs were not calibrated individually with the rotating arm due to time constraints. Instead, the mean P^* value of 0.85 was used to calibrate the three XDDs. Like in section 3.1, data above a specific altitude, in this case 7.5 km, were removed due to dropsonde adjustments after launch.

There are three possible geometric fall speeds to use in the calculation of vertical velocity (e.g., equations 2.4 or 2.5): 1) GPS altitude calculated fall speed ($\frac{dz}{dt}$); 2) calculated hydrostatic differential pressure fall speed (equation 2.11); and, 3) hydrostatic height-calculated fall speed ($\frac{dz_p}{dt}$). The GPS altitude calculated fall speed is different than the actual GPS fall speed, which is obtained by Doppler shift. The three geometric fall speeds were calculated using a 15-point center difference similar to the methodology of section 3.1. However, only equation 2.4, with the hydrostatic fall speed, was used to calculate the final pitot-venturi-indicated vertical velocity due to uncertainties in the hydrostatic height-calculated fall speed.

6.3 Meteorological conditions

The 40-km North American Model (NAM) 00 UTC initialization for 28 April 2019 is used in this section to examine the synoptic and local conditions during the drops. The 40-km NAM data was obtained from the University at Albany, State University of New York, Department of Atmospheric and Environmental Sciences data repository. The 03 UTC valid forecast is shown here, because it is the closest in time to the drops. The analysis of the 00 UTC output, however, is not appreciably different from the 03 UTC forecast. Artificial, fixed-point, model soundings were created from the all of the data at the nearest grid points to the launch locations. The fixed-point model soundings were used to compare to the observed XDD soundings. The fixed-point model soundings were approximately 20–23 km to the northwest of the actual drops. The drop locations for the three soundings are provided in Figure 6.2 as black dots. Geostationary Operational Environmental Satellite (GOES) IR data, obtained from the San Francisco State University data archives, from 03 UTC on 28 April 2019 shows that the three XDDs were dropped in an area of relatively clear conditions with little cloud cover (Fig. 6.3).

6.3.1 28 April 2019: 00–03 UTC

The surface temperatures of the eastern Pacific were relatively cool, ranging from 290–292 K (62.33–65.93°F) off of the Baja California Peninsula (Fig. 6.2c). There was a weak surface low pressure (1016 hPa), which was not completely closed off, that was associated with an upper-level trough (Fig. 6.2). The trough was stacked and closed off at both the 500-hPa and 250-hPa levels (Fig. 6.2a, b). The northern jet was decoupled from the weaker southern jet at the 250-hPa level (Fig. 6.2a). There was a weak jet streak (closed 70 kt contour, red) on eastern side of low, adjacent to the location of the XDD drops, which could affect the observed vertical velocity (Fig. 6.2a). The upper-level forcing, however, was relatively weak, and the soundings may be too far enough removed from the influence of the weak jet streak. The only precipitation forecasted with the low pressure was to the northwest of the XDD drops (Fig. 6.2d).

The fixed-point model soundings, corresponding to each XDD drop, had slightly positive vertical velocities in the lowest 800 m but negative vertical velocities of -1 m s^{-1} to -2 m s^{-1} (Fig. 6.4a). The mean vertical velocity for the soundings was approximately -1.1 m s^{-1}. The horizontal wind speed was similar for all three drops, with weak winds below 800 m that increase in strength aloft (Fig. 6.4b). The flight-level horizontal wind speeds were forecasted to be between 22–28 m s^{-1} (Fig. 6.4b). The winds were veering below 800 m, indicating warm air advection (Fig. 6.4b). This low-level region also was fairly moist. The air above 800 m was mostly dry (excluding the 4–6 km layer)(Fig. 6.4d). The modeled weak horizontal winds, veering/warm air advection, moist air, and weakly positive vertical velocities, occurred below an inversion and 1 km deep stable layer, which would have suppressed the ability to have deep, strong convection and limited the strength of vertical velocity observed by the XDDs (Fig. 6.4c).

6.4 Results

6.4.1 Sounding analysis

Upon close examination of the fall speeds above 7.5 km (not shown), the pitot-venturi-indicated TAS profiles show instances where the dropsonde enters a stable descent earlier than what the GPS fall speed would suggest. There are also small, but distinct, features in the two fall speeds that are dislocated in time or altitude (Fig. 6.5). To examine this observation further, lagged time correlations were created between the two fall speeds for all three drops (Fig. 6.6). The GPS fall speed for the three soundings lagged behind the uncalibrated pitot-venturi-derived fall speed by 1–2 s, with a mean of −1.3 s (Fig. 6.6). All correlations (r values) outside of ±0.1 are statistically significant. These results imply that the GPS altitudes and GPS fall speeds likely correspond to data at lower true altitudes.

The mean difference between the GPS fall speed (unadjusted for time lag) and the pitot-venturi-derived fall speed for all three drops was 4.4 m s^{-1}. If a single P^* value of 0.85 was used, the mean difference reduces to 2.5 m s^{-1}, with largest mean difference being 4.7 m s^{-1} for the first sounding. The third sounding had the smallest mean absolute difference at 0.09 m s^{-1}.

The GPS fall speeds show the most variability from dropsonde-to-dropsonde, with a standard deviation of the mean fall speed at 2.4 m s^{-1} (Fig. 6.5). The hydrostatic fall speed and hydrostatic height-calculated fall speeds have standard deviations of the mean fall speeds of 0.25 and 0.48 m s^{-1}, respectively. The mean P^*-calibrated pitot-venturi TAS has the smallest standard deviation at 0.1 m s^{-1}. The mean P^*-calibrated TAS agrees exceptionally well with the hydrostatic fall speed for all three drops (Fig. 6.5). All three fall speeds, except for the hydrostatic height-calculated fall speed, agree well for the third sounding (FE38; Fig. 6.5c).

Shown in Table 6.1 are the mean and mean absolute differences between the P^*-calibrated pitot-venturi-derived fall speeds and hydrostatic fall speeds for each sounding and for the combined three sounding dataset. The mean P^*-calibrated pitot-venturi-derived fall speeds and mean hydrostatic fall speeds differ by −0.18 m s^{-1}, with a mean absolute difference of 0.28 m s^{-1} for the combined three sounding dataset (Table 6.1). The mean differences for 2FEF and FE38 were approximately −0.1 m s^{-1}, with mean absolute differences between 0.2–0.3 m s^{-1} (Table 6.1). 9C30 had larger differences, which biased the overall mean differences (Table 6.1).

The observed soundings for horizontal wind speed, T, and RH (Fig. 6.7b, c, d) agree well with the 03 UTC 40-km NAM model fixed-point soundings (Fig. 6.4b, c, d). The horizontal winds above 6 km and below 1 km were stronger in the XDD soundings (Fig. 6.7b). The inversion and stable layer were more shallow in the XDD soundings and the lapse rates above the inversion are steeper (Fig. 6.7c). The XDD soundings were also drier below 1 km, with the mid-level moisture peak occurring at a lower altitude of 3.5 km (Fig. 6.7d).

The observed vertical velocity, however, is different from the model fixed-point soundings. The pitot-venturi-derived vertical velocity profiles were weak and relatively near zero for the entire depth of the sounding (Fig. 6.7a). Sounding 2FEF had weakly negative vertical velocities below 2 km, then weakly positive velocities above 2 km (green; Fig. 6.7a). Sounding FE38 showed a similar, but weaker and shallower, transition from negative vertical velocities below 1.5 km and positive above 1.5 km (blue; Fig. 6.7a). Sounding 9C30 was primarily positive throughout the depth of the sampled atmosphere (red; Fig. 6.7a).

As the model soundings in Figure 6.4 indicate, one would expect positive, or weakly positive, vertical velocities capped below the stable inversion and downward motion associated with subsidence above the inversion and relatively high surface pressure (Fig. 6.2c). Shown in Figure 6.8 are the vertical velocity profiles using the pitot-venturi, M3 methodology with the hydrostatic fall speed, and drag force methodology with the GPS fall speed and assuming a C_d value of 0.95. The M3 methodology vertical velocities were negative for all three soundings, but sounding 2FEF had a similar structure and shift to more positive vertical velocities at 2 km as the pitot-venturi vertical velocity profile (Fig. 6.2a and 6.8b). The GPS fall speed-based drag force vertical velocity profiles had high-amplitude noise and unrealistically large dropsonde-to-dropsonde variance in the fall speeds (Fig 6.8c). While the M3 methodology vertical velocities agree more with the primarily negative NAM model vertical velocities, none of the dropsonde-derived vertical velocity methods produce the same canonical subsidence inversion vertical velocity structure as in the NAM model. It is possible, however, that the model soundings do not accurately represent the true vertical velocity structure and that the true vertical velocity profile was weak and close to zero. It is also possible that the vertical velocity profiles do not agree between the NAM model and the observations, because the NAM model is a rigid fixed-grid sounding and the observational soundings are not at a fixed point in space. The XDDs drifted approximately 0.5–1 km during their descent.

6.4.2 Error analysis

Bushnell et al. (1973) claim that the total mean vertical velocity error using a pitot-static method can be calculated directly from the fall speed or TAS data under the assumption that the true mean vertical velocity is zero in relatively quiescent environments. The synoptic conditions during the ED drops documented by Bushnell et al. (1973), are comparable to the synoptic conditions for the XDD DC-8 drops. Given that the soundings were in an area of weak upper-level forcing and relatively calm conditions, the zero-mean vertical velocity assumption is not likely to severely impact the error analysis. The fixed-point model soundings, however, indicated that the mean vertical velocity was not zero (approximately -1 m s^{-1}). Unfortunately, there are no readily available datasets to verify the vertical velocity from the DC-8 drops at present.

If the mean vertical velocity over the sampling depth is truly zero, then there should be no difference between the mean actual geometric fall speed and the mean P^*-calibrated pitot-static-derived fall speed over that depth (i.e., $\overline{V_{TAS}} - \overline{V_{geometric}} = 0$). If this difference for any given sounding is not zero, then the difference is the mean vertical velocity error in the sounding. In this section, the Bushnell et al. (1973) mean vertical velocity error calculation is used to estimate the errors in the pitot-venturi-derived vertical velocity from the DC-8 soundings.

If the true mean vertical velocity in the profiles is zero, then the mean differences in Table 6.1 represent the mean error in the pitot-venturi-derived TAS and pitot-venturi-derived vertical velocity. In that situation, the mean absolute vertical velocity errors would be approximately 0.1–0.4 m s^{-1}. The RMSE of the vertical velocity in this case would be 0.23–0.44 m s^{-1}. It is unrealistic, however, that the true mean vertical velocity was exactly zero or that the true vertical velocity was zero for the majority of the descent. Therefore, these mean differences in Table 6.1 are the combination of the true mean vertical velocity and true mean error.

The error estimates are based upon the assumption that the mean P^* value can be applied for all XDDs. It is possible that the mean P^* of 0.85 is wrong or that it is unrepresentative for these three XDDs. It is also likely that the XDDs should be individually calibrated with the rotating arm or a highly accurate wind tunnel. One additional possibility is that the hydrostatic fall speed is not the true geometric fall speed of the XDDs. As shown by Figure 6.9, however, the use of the hydrostatic height-calculated fall speed or GPS fall speed does not improve the results and produces large, positive vertical velocity profiles that are highly unrepresentative of a subsidence inversion sounding. The TAS-derived vertical velocities with the GPS fall speed also have large, unrealistic peaks above 5.5 km (Fig. 6.9). The results indicate that the hydrostatic fall speed is the most realistic and consistent measure of the true geometric fall speed of the XDDs. It is also possible, but highly unlikely, that the nose pitot tubes were blocked (see section 2.4) for all three XDDs, causing the TAS to be close to, but slightly more than, the geometric fall speed.

The repeatability of the measurement can be estimated from the root mean square noise (RMSN) of the difference between the pitot-venturi-derived fall speed to the calculated hydrostatic differential pressure fall speed ("true" Bernoulli fall speed). The RMSN is the root mean square error after removing any mean bias in the difference between the predicted and actual value, and it is calculated by:

$$RMSN = \sqrt{\frac{\sum_{i=1}^{N}[(P-A) - \overline{(P-A)}]^2}{N}}, \tag{6.1}$$

where P is the predicted value (pitot-venturi-derived fall speed), A is the actual, or true, value (calculated hydrostatic fall speed), and N is the number of observations. The RMSN of the three soundings was 0.2–0.35 m s^{-1}. With additional smoothing, such as the nine-point binomial filter used in section 3.1, the noise in the signal can be reduced. The filtering will not, however, reduce the true precision of the measurement itself.

Table 6.1: Mean and mean absolute differences between the mean P^*-calibrated pitot-venturi-derived fall speed and hydrostatic fall speed (e.g., $\overline{V_{TAS}} - \overline{V_{geometric}}$) for each sounding and the combined three soundings. Values are in m s^{-1}.

Dropsonde	Mean difference	Mean absolute difference
9C30	−0.37	0.38
2FEF	−0.07	0.29
FE38	−0.10	0.18
Total	−0.18	0.28

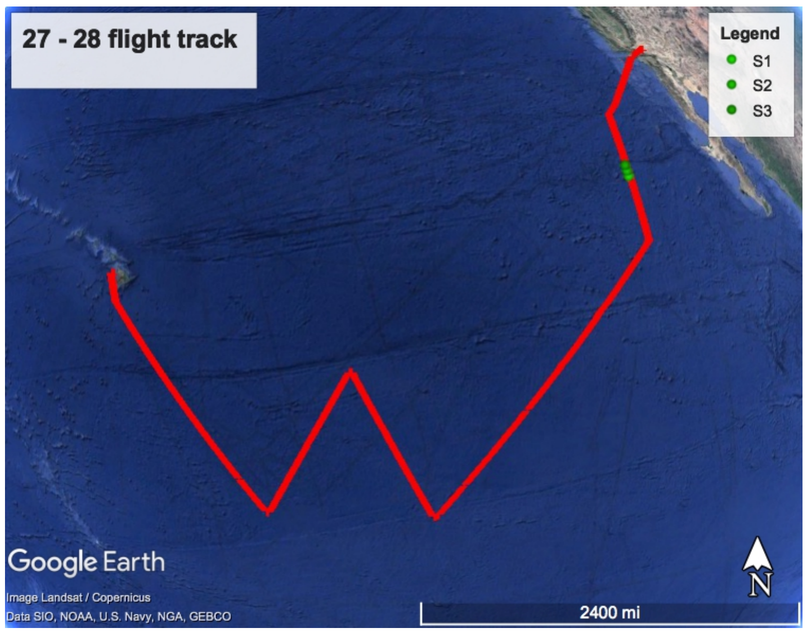

Figure 6.1: Flight path (red) of the DC-8 aircraft on 27–28 April 2019. The drop locations of the three XDDs with the p_d sensor is shown in green. Satellite imagery obtained from Google Earth. S1 is dropsonde 9C30. S2 is dropsonde 2FEF. S3 is dropsonde FE38.

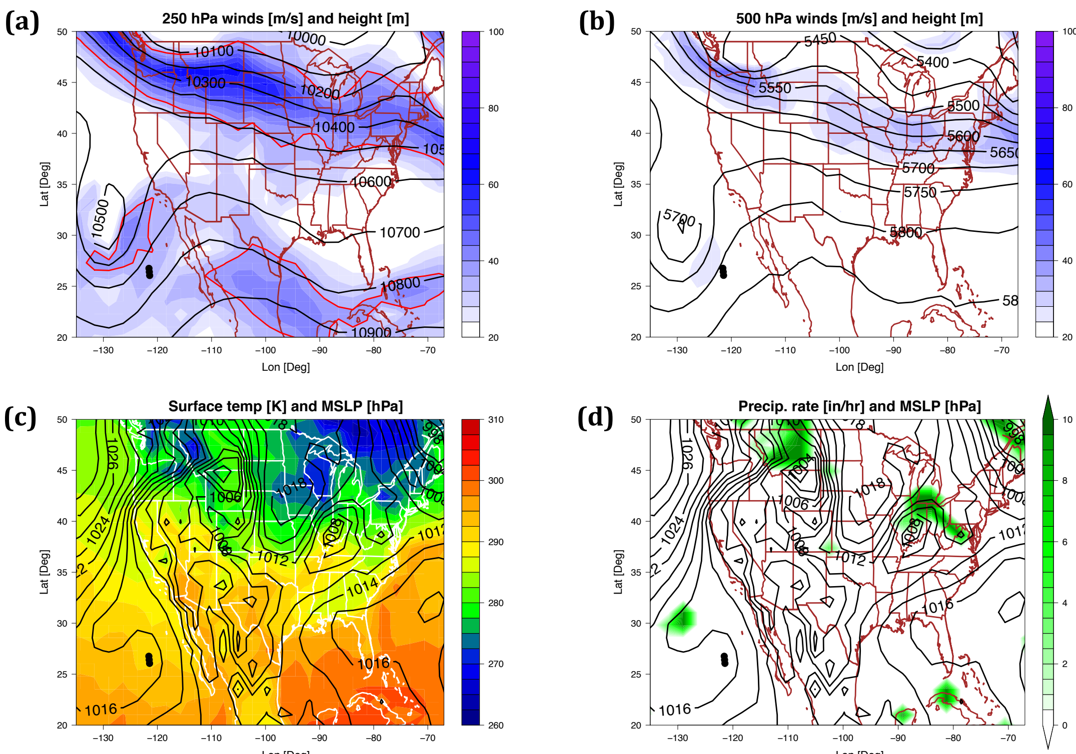

Figure 6.2: NAM 00 UTC synoptic conditions on 28 April 2019 at 03 UTC. Panel (a) is the 250 hPa height (m, contoured) and wind speed (kts, shaded). Panel (b) is the 500 hPa height (m, contoured) and wind speed (kts, shaded). Panel (c) is the surface temperature (K, shaded) and MSLP (hPa, contours). Panel (d) is the precipitation rate (in hr^{-1}, shaded) and MSLP (hPa, contours). The location of the drops are shown as the black dots.

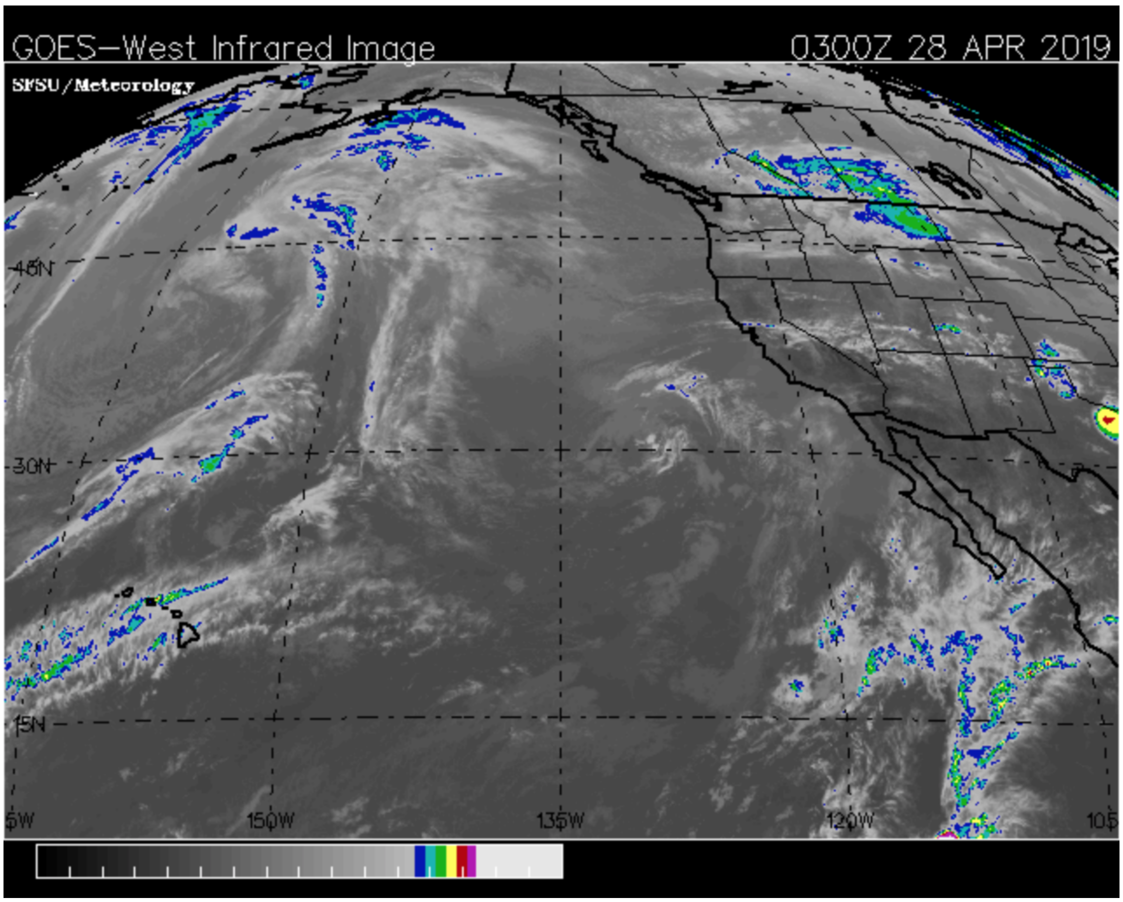

Figure 6.3: IR GOES-West imagery for 28 April at 03 UTC. Obtained from the San Francisco State University satellite image archive.

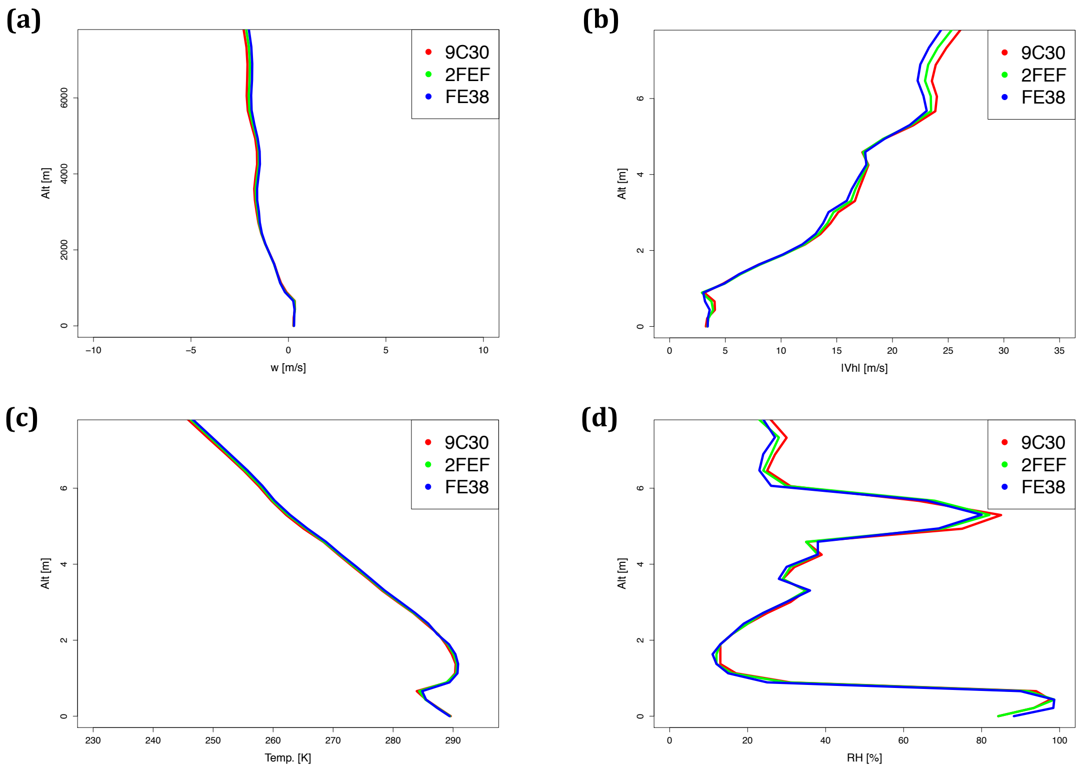

Figure 6.4: NAM 00 UTC fixed-point model soundings 28 April 2019 at 03 UTC. Panel (a) is the vertical velocity sounding (m s^{-1}). Panel (b) is the horizontal wind speed sounding (m s^{-1}). Panel (c) is the relative humidity sounding (%). Panel (d) is the temperature sounding (K). The first sounding, 9C30, is in red. The second sounding, 2FEF, is in green. The third sounding, FE38, is in blue.

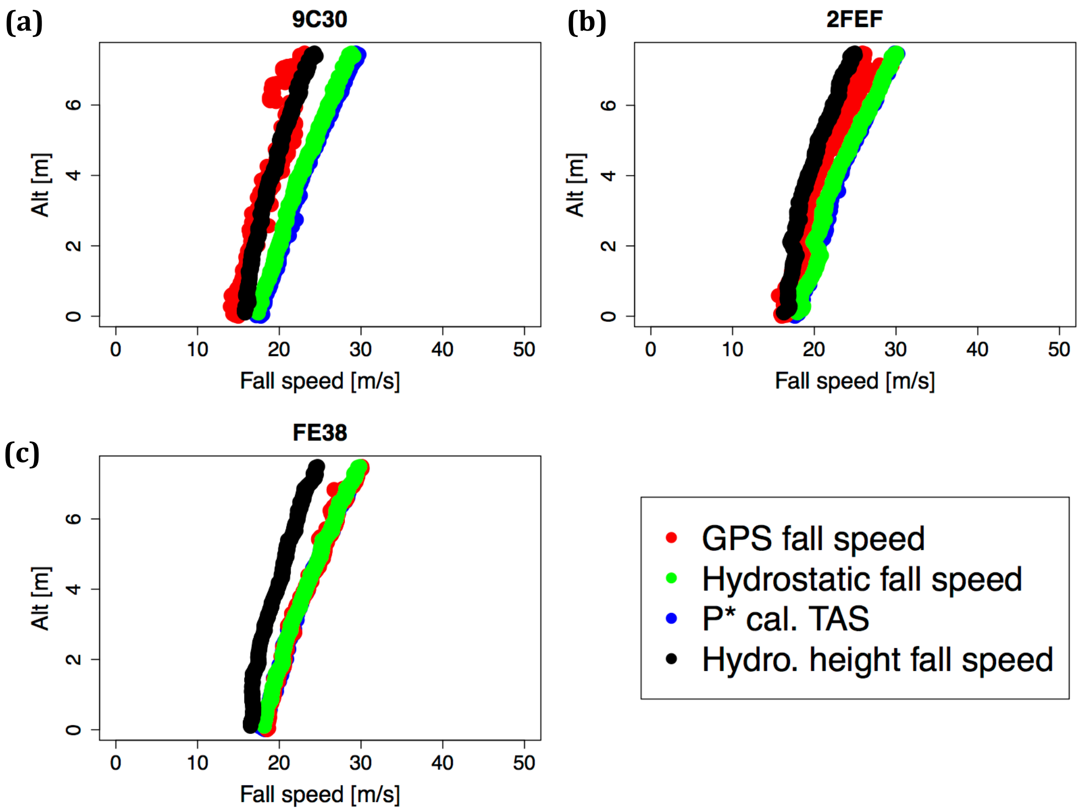

Figure 6.5: Fall speeds for the three XDDs launched on 28 April 2019. Panel (a) is for dropsonde 9C30 (northern sounding). Panel (b) is for dropsonde 2FEF (middle sounding). Panel (c) is for dropsonde FE38 (southern sounding). The GPS fall speed is in red. The hydrostatic fall speed is in green. The pitot-venturi-indicated TAS is in blue. The hydrostatic height-calculated fall speed is in black.

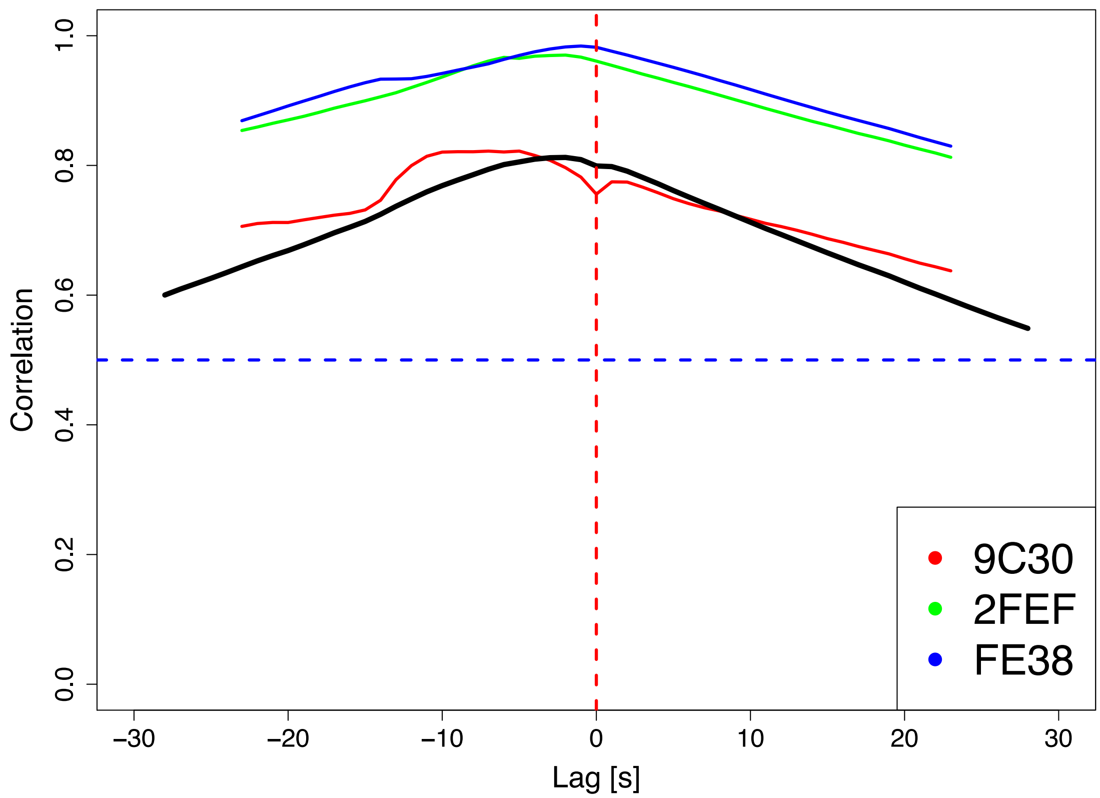

Figure 6.6: Correlograms of GPS fall speed and the TAS from the three soundings (9C30, 2FEF, and FE38) individually (red, blue, and green, respectively) and collectively (black). Negative lags indicate that the GPS fall speed lags behind the pitot-venturi-indicated TAS. The blue dashed line denotes the 0.5-correlation level. The vertical dashed red line denotes a time lag of zero.

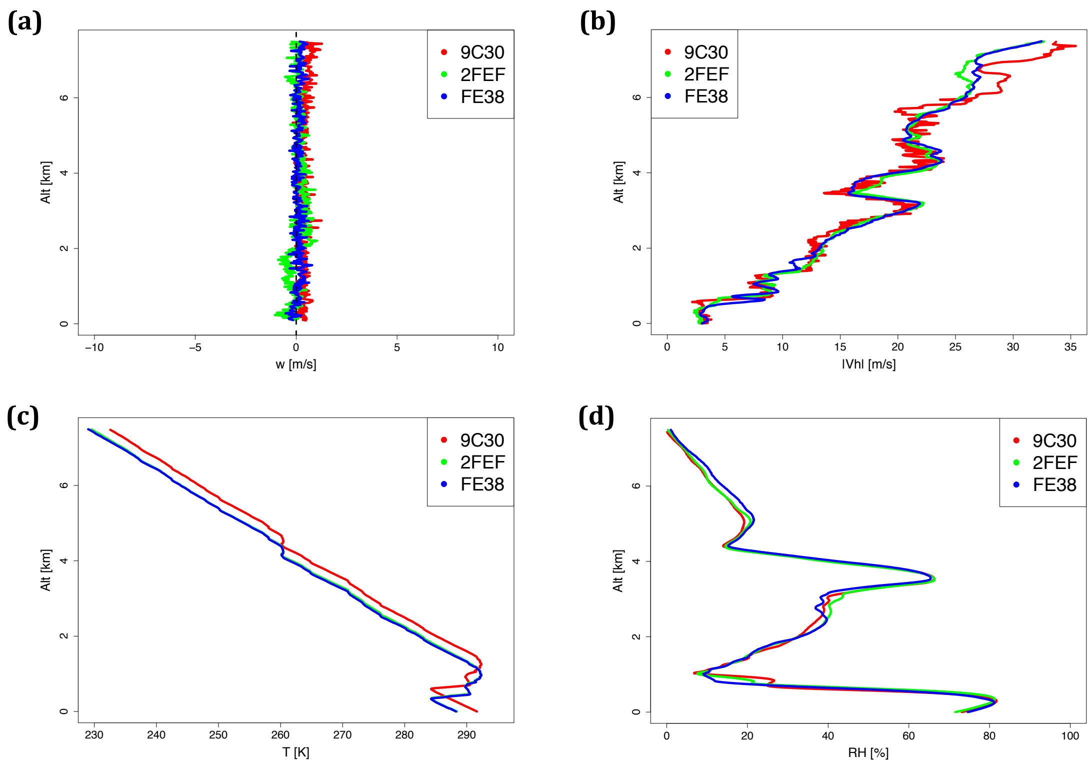

Figure 6.7: Same as Fig. 6.4, but for the actual XDD soundings on 28 April 2019.

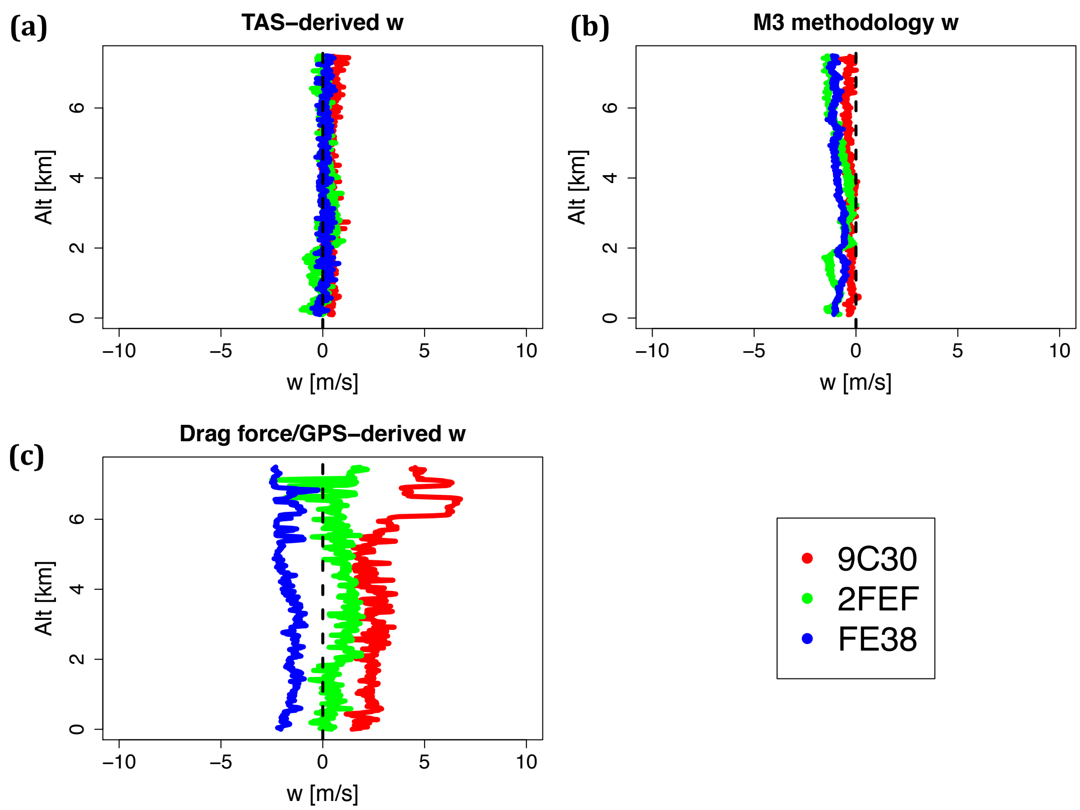

Figure 6.8: Vertical velocity profiles from 28 April 2019 using the pitot-venturi methodology (a), M3 methodology (b), and GPS drag force methodology (c). The first sounding, 9C30, is in red. The second sounding, 2FEF, is in green. The third sounding, FE38, is in blue. The vertical dashed black line denotes $w = 0$ m s^{-1}.

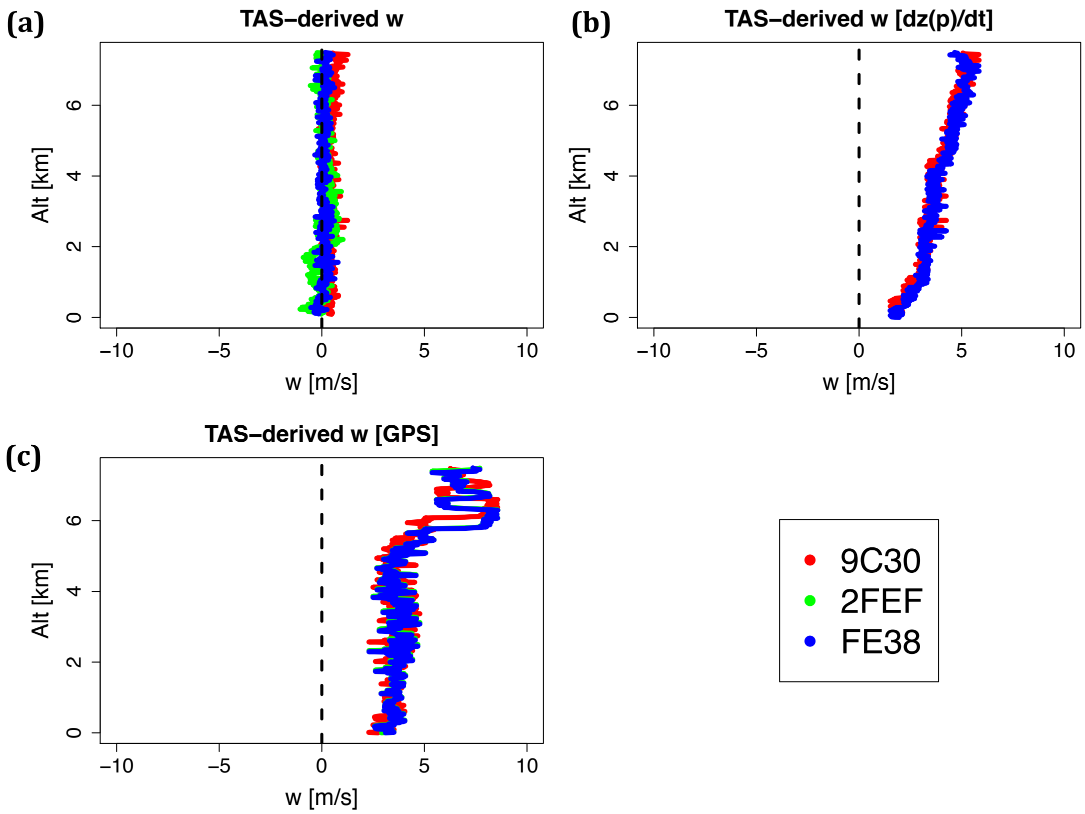

Figure 6.9: Vertical velocity profiles from 28 April 2019. Panel (a) is the TAS-derived vertical velocity using the hydrostatic fall speed. Panel (b) is the TAS-derived vertical velocity using the hydrostatic height-calculated fall speed. Panel (c) is the TAS-derived vertical velocity using the GPS fall speed. The first sounding, 9C30, is in red. The second sounding, 2FEF, is in green. The third sounding, FE38, is in blue. The vertical dashed black line denotes $w = 0$ m s^{-1}.

CHAPTER 7

Conclusions

7.1 Summary

Dropsonde technology, and dropsonde-derived vertical velocities, are a relatively young area of research compared to traditional balloon-borne observations (e.g., Rykatcheff, 1990; Bushnell, 1966; Bushnell et al., 1973). Observations of dropsonde-derived vertical velocities and research on their accuracies began in the early 1960's (Bushnell et al., 1973). Early dropsonde iterations, such as the EDs, used a pitot-static probe to measure the TAS of the dropsonde and subtract the geometric fall speed from it to obtain vertical velocity (equations 2.4–2.6). The errors for this methodology were claimed to be ± 1 m s^{-1} (Bushnell et al., 1973).

With the development of GPS chip set technology, vertical velocity methods transitioned away from direct physical measurements and instead relied upon a drag force method (equations 2.9 and 2.10). Recent studies have concluded that GPS fall speeds are often erroneous and a hydrostatic fall speed should be used with the drag force methods (e.g., Wang et al., 2015; Stern et al., 2016; Nelson et al., 2019a). The results in chapter 6 support this claim. In section 2.3, a modified drag force method was proposed to obtain the vertical velocity without direct, a priori knowledge of the exact dropsonde mass, area, or drag coefficient. Regardless of the method used, drag force based vertical velocities have ± 1–2 m s^{-1} errors (e.g, Figs. 2.11 and 2.12).

Technological advancements over the past 50–60 years have allowed for smaller and more accurate p_d sensors. This should lead to improved pitot-static-derived TAS and vertical velocity. In this dissertation, it was proposed to reintroduce, revisit, and revise the pitot-static-derived vertical velocity methodology for use on the XDDs. The goal was to decrease clear-air vertical velocity errors to ± 0.1 m s^{-1} and develop a highly-accurate vertical velocity dropsonde for use in TC research.

The major objectives, accomplishments, and results of this dissertation are as follows:

1. Estimated drag force methods (e.g., the M3 methodology) can be used to examine individual updrafts and downdrafts in the TCI dataset

2. High-spatial resolution vertical velocity measurements can be used to examine and document convective features such as gravity waves, eyewall updrafts, and secondary eyewalls in TCs

3. While the estimated drag force methods provided a unique opportunity to document cross sections of the vertical velocity in individual TCs, the majority of the vertical velocity distribution occurs within ± 1–2 m s^{-1}

    (a) This presents a major problem, considering that the error estimate for drag force based vertical velocities are ± 1–2 m s^{-1}

4. Not only is addressing the vertical velocity accuracy important to documenting vertical velocities in TCs, but it is also an important parameter needed to document the horizontal wind in TCs from dropsondes

5. In order to adequately "resolve" TC kinematics and structure within dropsonde transects, the spatial resolution should be less than approximately 5–10 km

    (a) Specifically, the 0.5-autocorrelation spatial scales from the TCI data suggest that dropsondes should be launched at fine spatial scales less than 3 km to document convection and convection-related variables

6. Three modified versions of the traditional pitot-static and their configurations were presented
   (a) It was hypothesized that the venturi-static, with an aft venturi port and side static port, would be the most optimal configuration as it would be more resilient to ice accumulation
7. CFD model runs of the XDD in 20 m s^{-1} flow indicated that the pitot-venturi, with an antenna aft port, would be the most optimum configuration, because it had a better response to angle of attack and the observed p_d was not sensitive to the exact position of the port within approximately 0.1–0.25 in
   (a) The CFD model results indicated that the drag coefficient is 0.93, which is close to the estimate of 0.95 from the TCI data in section 3.1
   (b) The CFD model results indicated that the p_d calibration coefficient, P^*, for the pitot-venturi, with an antenna aft port, is 0.91
8. Eight pitot-venturi XDDs, with the antenna aft port, were tested using a rotating arm at a nominal speed of 19.2–19.4 m s^{-1}.
   (a) The actual P^* values for these XDDs was approximately 0.85
   (b) Dropsonde-to-dropsonde variance in the port locations was low at approximately 0.04 in, which should negligibly affect the TAS by approximately 0.01 m s^{-1}
   (c) Using a mean P^* value for all of the XDDs introduces mean errors of 0–0.45 m s^{-1}, whereas individualized P^* leads to mean errors of less than 0.01 m s^{-1}

9. Three pitot-venturi XDDs were successfully launched operationally from a DC-8 aircraft downwind of an upper level trough and surface high pressure as part of the NASA DAWN Lidar verification field campaign from 15–28 April 2019

   (a) The pitot-venturi-indicated vertical velocities obtained by the XDDs cannot be verified with the collocated Lidar data at present

   (b) The GPS fall speed lagged behind the pitot-venturi-indicated TAS by approximately 1–2 s

   (c) The observed horizontal wind, temperature, and relative humidity soundings agreed well with fixed-grid point NAM soundings

   (d) The pitot-venturi vertical velocity profiles did not agree with the fixed-grid point NAM soundings, but this discrepancy is not likely due to port blockage or incorrect geometric fall speed

   (e) The observed pitot-venturi vertical velocity profiles were weak and near zero for the majority of the sampled atmosphere

   (f) The hydrostatic fall speed should be used for the geometric fall speed in the calculations of vertical velocity rather than the GPS fall speed or hydrostatic height-calculated fall speed

   (g) The mean vertical velocity errors and RMSN from the DC-8 drops were presented (discussed further in section 7.2)

7.2 Final error estimate

From the CFD model analysis (chapter 4), rotating arm tests (section 5.2), and the DC-8 drops (chapter 6), a final vertical velocity error estimate for the pitot-venturi methodology can be obtained. It is important to note that the final vertical velocity error estimates presented here are for quiescent conditions, where icing and high angle of attack are not likely and assume that the true mean vertical velocity from the DC-8 drops was zero. Even in relatively quiescent conditions, with weak ± 1 m s^{-1} low-level vertical velocities, drag force-based vertical velocity errors are approximately ± 1–2 m s^{-1}, depending on altitude (section 2.4). In order for the pitot-venturi vertical velocity XDDs to be used operationally in convective environments like TCs, more extensive testing should be completed to understand dropsonde icing and the response of the dropsonde and the angle of attack to local wind and local wind shear.

The initial error budget attributed ± 0.05 m s^{-1} to instrumentation error and ± 0.05 m s^{-1} tube/port placement error for a total error of ± 0.1 m s^{-1}. The final expected error analysis is provided in Table 7.1. Table 7.1 includes error estimates for port position error, P^* calibration error, and instrumentation error based upon the CFD model analysis and rotating arm tests, and the observed mean, observed absolute mean, and observed RMSE from the DC-8 flights. The final estimated errors for the pitot-venturi XDD vertical velocities are estimated by the mean absolute errors of these components and the observed mean absolute errors and RMSE. Error estimates for mean P^*-calibrated XDDs and individual P^*-calibrated XDDs are also provided, as well as a maximum error estimate.

Given the small dropsonde-to-dropsonde variance in the port location, it is unlikely that port placement would cause more than approximately ± 0.01 m s^{-1} errors in vertical velocity (section 5.2). Based upon the dropsonde-to-dropsonde variance in the value of P^* for the rotating arm tests, which was conducted a known speed unlike the DC-8 drops, the use of a mean P^* leads to larger vertical velocity errors with an absolute mean of 0.16 m s^{-1} (Table 5.1, 7.1) and an absolute median of 0.11 m s^{-1}. All of the dropsondes in the rotating arm test had errors less than 0.5 m s^{-1} when using a mean P^* value. These errors depend upon the combined dropsonde-to-dropsonde variance in port placement, dropsonde body characteristics, performance of the sensor, and the airflow around the dropsonde. The use of an individualized P^* value decreases these errors to approximately 0.01 m s^{-1}, which is attributed to the expected errors due to port placement (Table 7.1).

The specifications for the DLHR-L05D-E1BD state that the typical errors of the sensor are 0.2% of the full scale span (-5 to 5 inches of water) (Table 2.2, All Sensors, 2019). This corresponds to $\pm$5-Pa or $\pm$0.25 m s^{-1} at typical XDD sea-level fall speeds (Table 7.1). The three DC-8 drops had total vertical velocity errors of 0.1–0.4 m s^{-1}, with a mean absolute error of 0.28 m s^{-1} (Table 6.1). As discussed in section 6.4.2, this assumes that the true mean vertical velocity in the observed soundings is zero.

The mean absolute error estimate of 0.28 m s^{-1} from the DC-8 drops is the total error of instrumentation error, port placement error, and mean P^* error (Table 7.1). It is possible that the three errors could compensate each other, leading to an estimated error comparable to the specified instrumentation error by All Sensors (2019). In the event that the three errors do not compensate each other at all, then the expected "maximum" mean vertical velocity error would be the sum of the three; a value of 0.42 m s^{-1} for a mean P^*-calibrated pitot-venturi XDD and 0.27 m s^{-1} for an individual P^*-calibrated pitot-venturi XDD (Table 7.1). The observed RMSE for all three soundings is comparable to, but less than, the maximum error estimate at 0.36 m s^{-1}.

7.3 Conclusions

Regardless if a mean P^* value or individualized P^* values are used, the results show that typical errors associated with the pitot-venturi-indicated TAS and, subsequently, vertical velocity are between ±0.2–0.4 m s^{-1}. Given that the typical error range of the drag force methods is ±1–2 m s^{-1}, this is an improvement in the vertical velocity accuracy by, approximately, a factor of five in quiescent conditions. The error estimate is also an improvement by a factor of two from the Bushnell et al. (1973) findings. The repeatability of the measurement is also 0.2–0.4 m s^{-1}. With an increased accuracy and decreased error to 0.2–0.4 m s^{-1}, analyses of dropsonde-derived vertical velocities in TCs, like in sections 3.1 and 3.3, can be improved and the unique convective features observed by dropsondes in TCs (like the gravity wave in Patricia; Fig. 3.14) can be discussed with more confidence. In order for the pitot-venturi vertical velocity XDDs to be used operationally in convective environments like TCs, however, more extensive testing should be completed to understand dropsonde icing and the response of the dropsonde to local wind and local shear.

While these expected errors are larger than the goal of 0.1 m s^{-1}, the use of a pitot-venturi method is an improvement upon the previous methods for dropsonde-derived vertical velocities and it is likely that, with further testing and calibration, the goal of ±0.1 m s^{-1} errors is achievable and the error estimates provided here can be more solidified. One option to further improve the accuracy would be to change the sensor to a much smaller surface mount sensor that would have a much smaller full scale span or smaller instrumentation error at the typical XDD fall speeds. Further testing of the calibration methods and P^* values would solidify the accuracy and error estimates. Individually calibrating each dropsonde prior to launch seems to decrease the errors by 40%. Finally, additional high-altitude (> 6 km) drops should be done over a larger range of XDDs in conjunction with other independent measurements of vertical velocity, such as flight-level or vertically pointing Lidar data, to increase the confidence in the error estimate.

Table 7.1: Expected mean (or absolute mean) errors for mean P^*-calibrated TAS vertical velocity and individual P^*-calibrated TAS vertical velocity.

Mean error type	Mean P^*-cal.	Individual P^*-cal.
Port placement	0.01 m s^{-1}	0.01 m s^{-1}
P^*	0.16 m s^{-1}	0.01 m s^{-1}
Instrumentation	0.25 m s^{-1}	0.25 m s^{-1}
Observed mean	-0.18 m s^{-1}	NA
Observed absolute mean	0.28 m s^{-1}	NA
Observed RMSE	0.36 m s^{-1}	NA
Maximum	0.42 m s^{-1}	0.27 m s^{-1}

APPENDIX A

American Meteorological Society Permission to Republish

Permission to reuse Monthly Weather Review manuscript in EOR

Inbox ×

Connor Nelson <ccnelson@albany.edu> 3:26 PM (2 hours ago)

to permissions

Hello,

I am T. Connor Nelson, a Ph.D. candidate at the University at Albany. I am currently in the process of finishing my dissertation and look to defend my dissertation on 16 July 2019. Two of the chapters in my dissertation are large excerpts and figures from a manuscript (and supplementary material) that I recently published in Monthly Weather Review. Specifically, the manuscript is: "Examination of the eXpendable Digital Dropsonde-derived vertical velocities from the Tropical Cyclone Intensity (TCI) experiment." I am the lead author on this manuscript and it is currently in EOR. I will certainly be sure to fully cite the material and include the AMS copyright information with the appropriate figures.

Would it be possible to obtain written permission to use the MWR/AMS manuscript in my dissertation?

Thank you for your consideration.

T. Connor Nelson

Gumbel, Erin <egumbel@ametsoc.org> 4:52 PM (45 minutes ago)

to Connor, permissions@ametsoc.org

Dear Connor,

Thank you for your email. This signed message constitutes permission to use the material requested below.

You may include your published article in your upcoming dissertation with the following conditions:

1. Include the complete bibliographic citation of the original source.
2. Include the following statement with that citation for each: **© American Meteorological Society. Used with permission.**

If you have any questions or need additional information, please feel free to contact me.

Congratulations on your publication and on the completion of your dissertation!

Best,

Erin Gumbel

Ms. Erin Gumbel, she/her/hers
Peer Review Support Assistant
American Meteorological Society
egumbel@ametsoc.org
617-226-3926

AMS100

APPENDIX B

Bootstrap Testing of Vertical Velocity Strength

While there was little sample bias in the three TCs altitudinally, there were radial and azimuthal biases, especially between shear-relative quadrants (see Fig. 3.3). The sampling bias in the TCI data makes the interpretation of the azimuthal vertical velocity distribution difficult. In consideration of sampling biases, bootstrapping, or bootstrap resampling, is a common method employed to obtain an equal number of samples from unequal populations to perform statistical comparisons over many sampling iterations (e.g., Ditchek et al., 2017). Notched box plots are used here to compare medians of bootstrapped samples of positive or negative vertical velocities over 1000 iterations. The median is used in lieu of the mean, as the median is more resistant to outliers in the data. The notched boxplots show the spread in the sample medians (whiskers), interquartile range (box), median (solid black line), and 95% confidence interval of the median (edges of the notches). If the notches of any box plots overlap, then the medians are considered to be statistically similar (Chambers et al., 1983). Sample sizes ranged from 296–380 data points, depending upon the population size in each quadrant for each TC, and are valid minimum sample sizes at the 95% confidence interval. It is important to note that the notched boxplots illustrate the quadrants with the strongest median positive or negative XDD-derived vertical velocities observed and are not a true measure of the strength of convection in each of the quadrants.

Data were split between each of the shear-relative quadrants (DR, UR, UL, and DL) within $3R^*$ and outside of $3R^*$. Figures B.1–B.8 show the notched box plots of the medians for all vertical velocities (teal) and positive (red) or negative (blue) vertical velocities. It should be noted that while there may be statistical differences in the medians in the boxplots, there may not be physically significant differences, since many of the medians differ by less than 0.1 m s^{-1}. Further, the boxplots compare the statistical similarity in the medians of the bootstrapped samples and not the similarities between the vertical velocity distributions themselves.

The box plots for Marty show that the downshear and right quadrants had more positive median vertical velocities (Fig. B.1). The median vertical velocities were mostly negative in the UL quadrant (Fig. B.1). For all radii, the DL and DR quadrants had the statistically strongest median positive and negative vertical velocities, respectively (Fig. B.5a, b). Within the core, the statistically strongest median positive and negative vertical velocities were in the left-of-shear quadrants (Fig. B.5c, d). Outside of 3R*, the strongest median vertical velocities were in the DR quadrant (Fig. B.5e), but the large gaps in the azimuthal distribution of Marty at outer radii (see Fig. D.2) could affect the interpretation of the notched boxplots.

In Joaquin, median vertical velocities were primarily positive in the UR quadrant (Fig. B.2). The DL quadrant within the core was also primarily positive (Fig. B.2a). The statistically strongest median positive and negative vertical velocities occurred in the DR quadrant (Fig. B.6a, b). Within the core, the median positive and negative vertical velocities in the downshear quadrants were stronger than the upshear quadrants (Fig. B.6c, d). Outside of 3R*, the statistically strongest vertical velocities were in the DR quadrant (Fig. B.6e, f).

Median vertical velocities in Patricia were interestingly primarily negative but were closer to zero (more positive) in the DR and UL quadrant within the core and the DL quadrant outside of the core (Fig. B.3). The statistically strongest median vertical velocities occurred in the right-of-shear quadrants for all radii (Fig. B.7a, b). Within the core, the statistically strongest median positive and negative vertical velocities were in the DR quadrant (Fig. B.7c, d). Outside of 3R*, median positive vertical velocities were statistically strongest in the downshear quadrants (Fig. B.7e) and median negative vertical velocities were statistically strongest in the UR quadrant (Fig. B.7f).

The median vertical velocities for the total dataset in the downshear quadrants were primarily positive, especially the DR quadrant within the core and DL quadrant outside of the core (Fig. B.4). The statistically strongest median positive vertical velocities for all radii occurred in the DR quadrant (Fig. B.8a). There was little spread in the medians of the negative vertical velocity bootstrap samples and all quadrants, except the UL quadrant, had similar medians (Fig. B.8b). Within the core, the statistically strongest median positive and negative vertical velocities occurred in the DR and UL quadrants, respectively (Fig. B.8c, d). Outside of 3R*, the statistically strongest median vertical velocities occurred in the UR quadrant (Fig. B.8e, f).

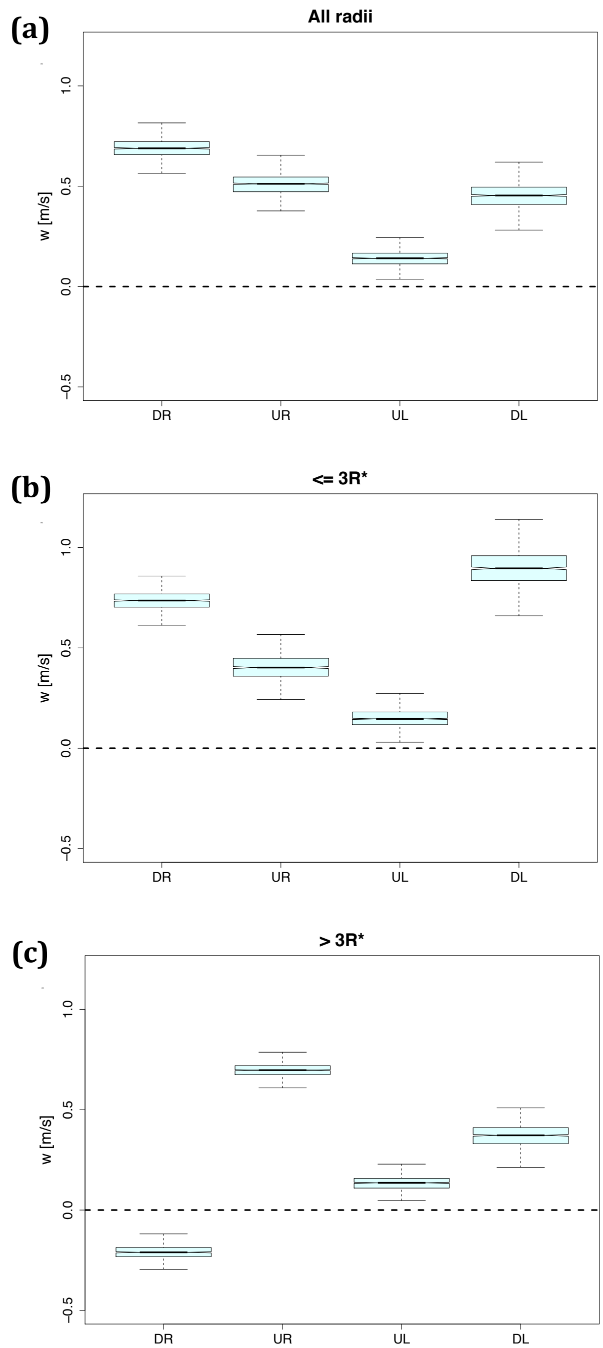

Figure B.1: Box plots of bootstrapped medians of vertical velocities in Marty for all radii (a), within 3R* (b), and outside of 3R* (c). The dashed black line denotes $w = 0$ m s^{-1}. From Nelson et al. (2019a). ©American Meteorological Society. Used with permission.

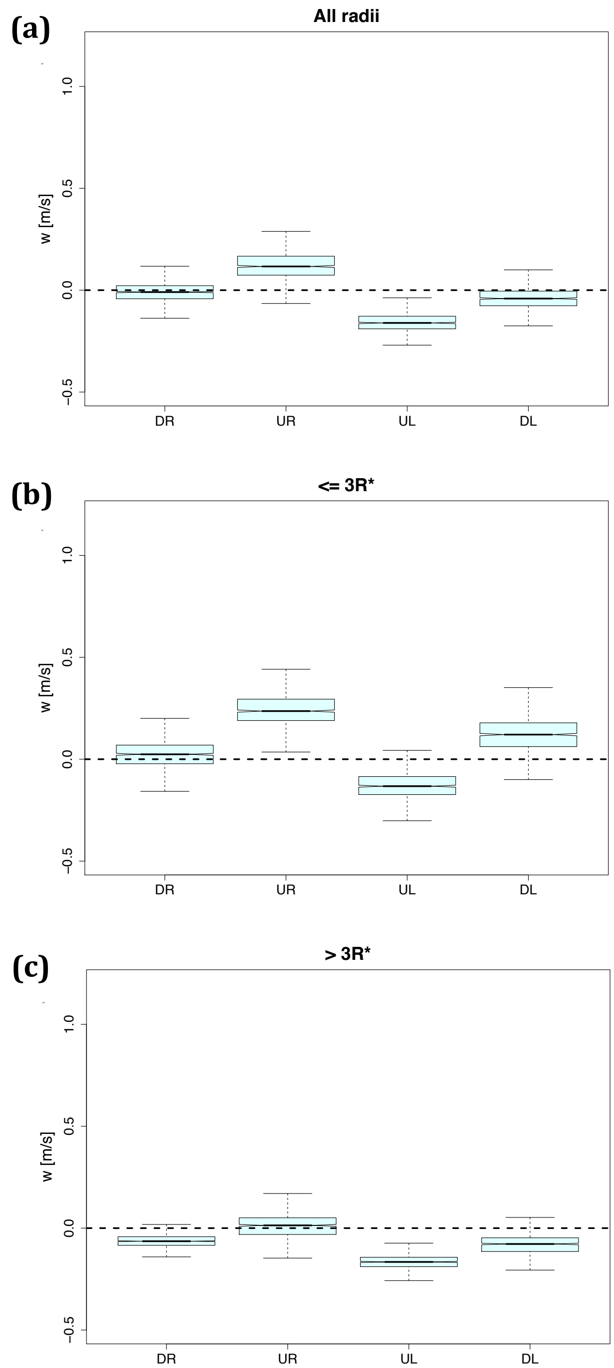

Figure B.2: Same as Fig. B.1, but for Joaquin. From Nelson et al. (2019a). ©American Meteorological Society. Used with permission.

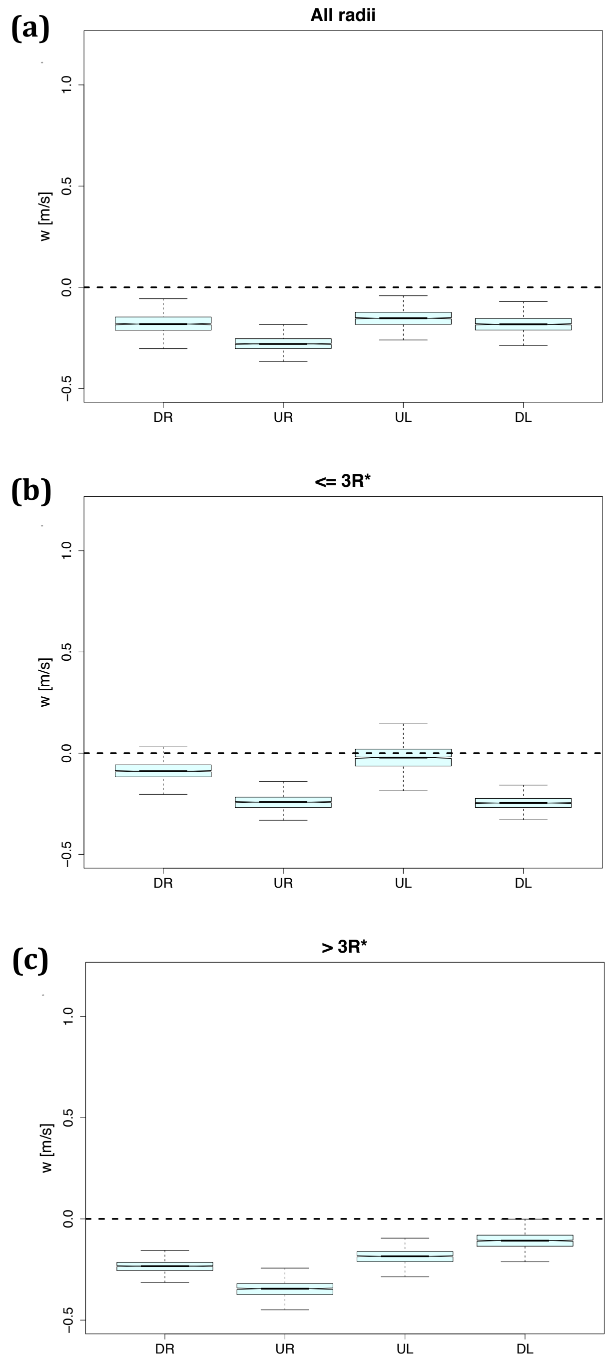

Figure B.3: Same as Fig. B.1, but for Patricia. From Nelson et al. (2019a). ©American Meteorological Society. Used with permission.

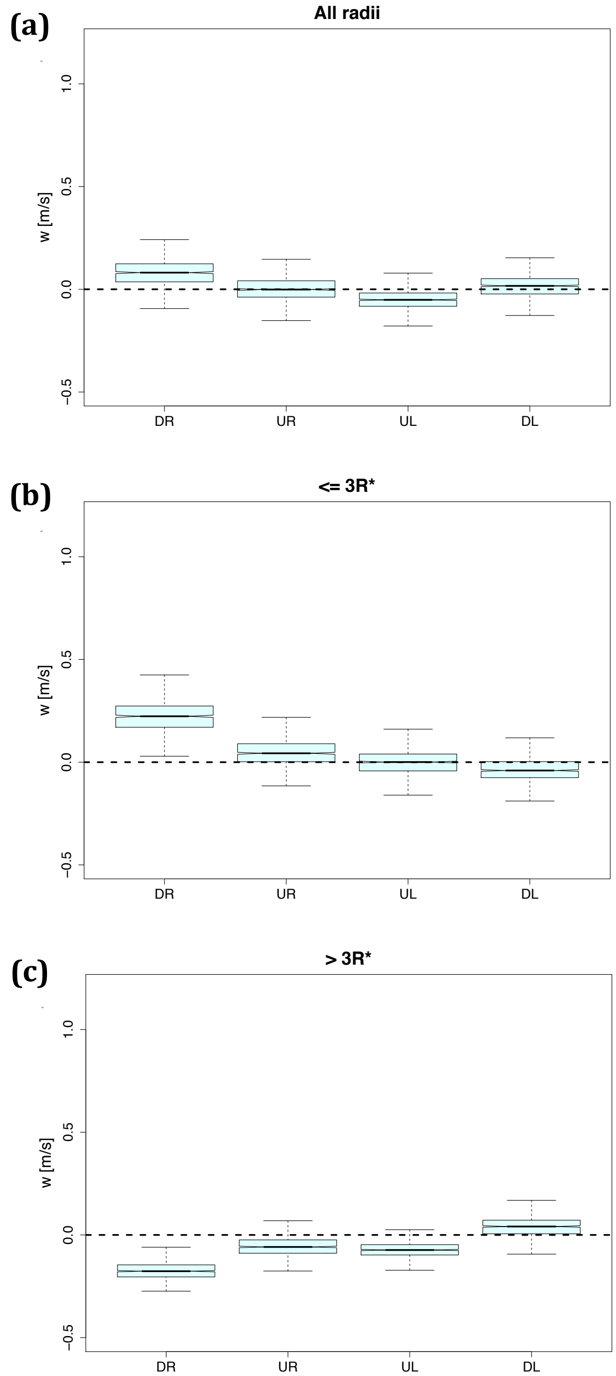

Figure B.4: Same as Fig. B.1, but for the total dataset. From Nelson et al. (2019a). ©American Meteorological Society. Used with permission.

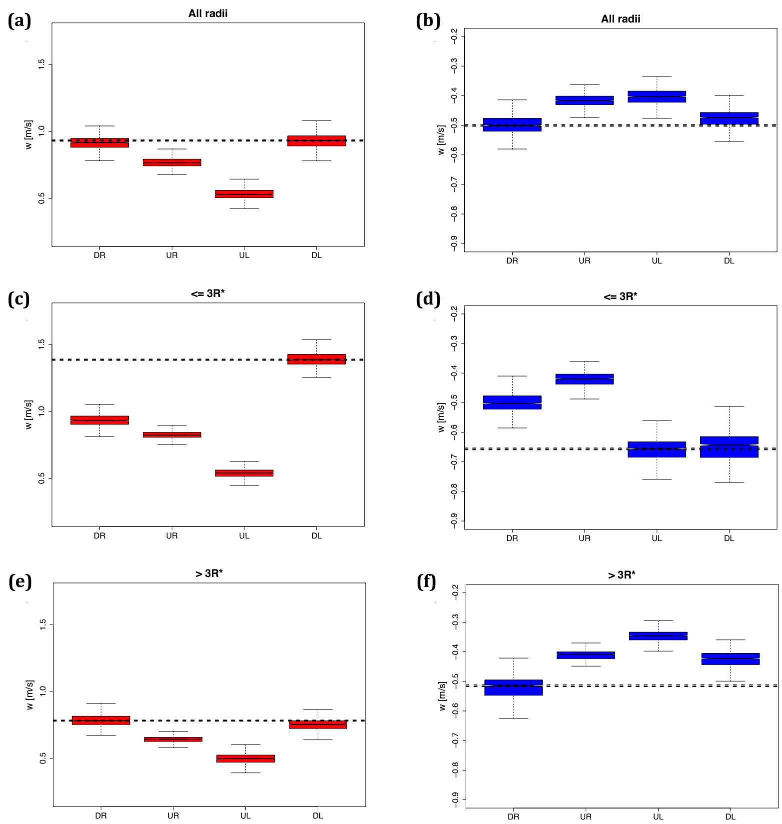

Figure B.5: Box plots of bootstrapped medians of positive vertical velocities (a, c, e) and negative vertical velocities (b, d, f) in Marty for all radii (a, b), within 3R* (c, d), and outside of 3R* (e, f). Dashed black lines denote the notches of the strongest median positive or negative vertical velocities. Note that the scales for positive vertical velocities are different than for negative vertical velocities. From Nelson et al. (2019a). ©American Meteorological Society. Used with permission.

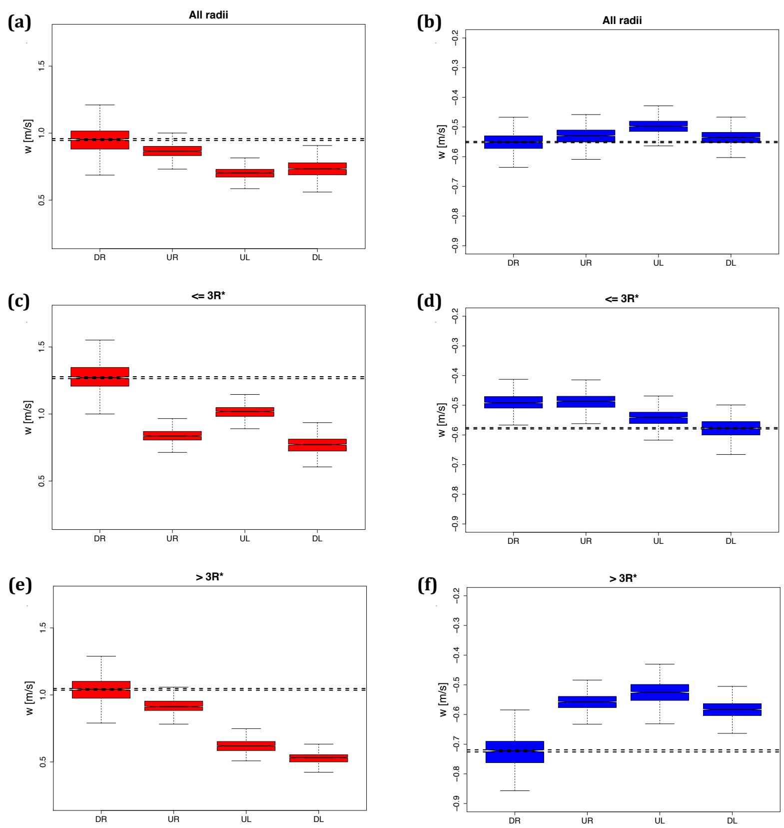

Figure B.6: Same as Fig. B.5, but for Joaquin. From Nelson et al. (2019a). ©American Meteorological Society. Used with permission.

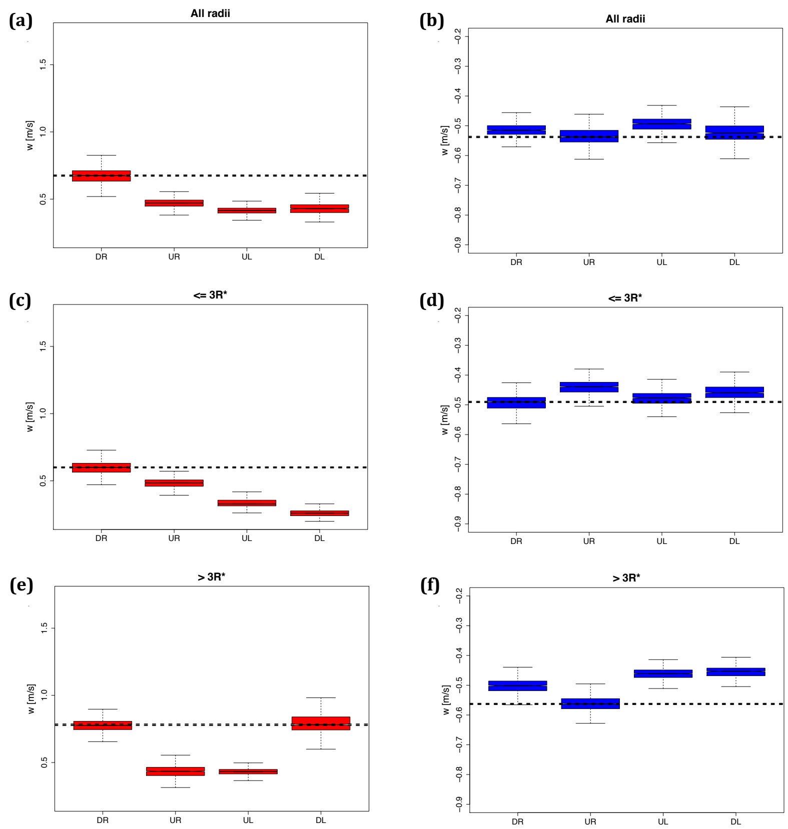

Figure B.7: Same as Fig. B.5, but for Patricia. From Nelson et al. (2019a). ©American Meteorological Society. Used with permission.

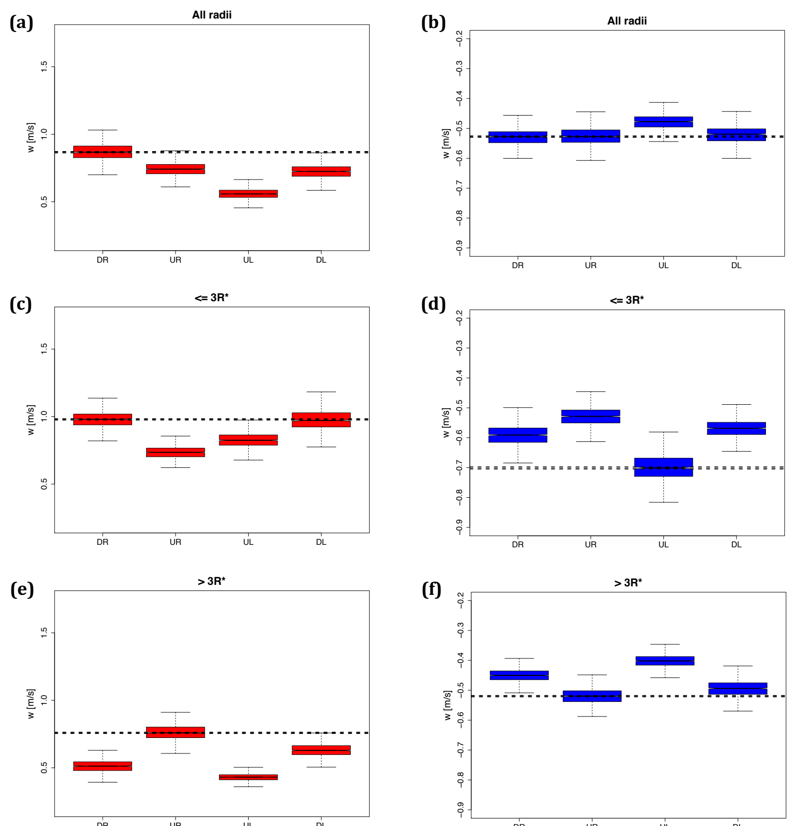

Figure B.8: Same as Fig. B.5, but for the total dataset. From Nelson et al. (2019a). ©American Meteorological Society. Used with permission.

APPENDIX C

Flight-level RMWs and HRD Centers

While there are well-documented high-resolution centers available from the Hurricane Research Division (HRD), they are not available for all observation days. Only seven of the ten observation days have HRD track, center, or flight-level RMW data. The mean and median difference between the ZWC tracks and the HRD high-resolution track is 17.2 and 14.6 km, respectively. The largest differences were for Joaquin, which has well-known TC center and track issues (e.g., Creasey and Elsberry, 2017) and for Patricia on 21 October as a tropical storm with an ill-defined center. Shown in Figures C.1–C.3 are the NHC Best Tracks (blue), ZWC tracks (red), and HRD high-resolution tracks (black; when available). Also shown in Figure C.4 are the histograms for the track differences between the ZWC tracks and HRD high-resolution tracks for each TC and in total. The tracks agree well when the TCs are strong and the TC cores are well sampled by the XDDs (e.g., Patricia on 23 October).

The mean difference between the ZWC track and the HRD track for Patricia on 23 October was approximately 6 km. It is possible that this 6 km mean difference can adversely affect the analysis of the horizontal and radial wind fields. This difference, however, minimally changes the cross sections in Figure 3.14 of the manuscript (Fig. C.5). The eyewall updraft to the southeast is weaker from 9–12 km when using the HRD track (Fig. C.5a). The vertical velocity at the TC center is stronger when using the HRD track (Fig. C.5a). The horizontal winds are not as symmetric or strong when using the HRD track (Fig. C.5b). Regardless of these small changes, the same results and conclusions can be drawn from the

Patricia cross section: 1) the eyewall features deep, exceptionally strong updrafts; 2) there is a low-level updraft associated with a localized horizontal wind maximum and a radial overturning circulation; and, 3) there appears to be an upper-level gravity wave to the northwest of the TC center. Because the same conclusions can be drawn from Figures 3.14 and C.5 and there is little difference between the two cross sections, the use of the ZWC track does not adversely impact the analysis of the cross section.

Six different variations of TC center and RMW combinations for the seven days that did have flight-level data and HRD track data were examined: 1) ZWCs and RMWs from the manuscript; 2) ZWC with single point maximum wind speed XDD-derived RMW; 3) ZWC with HIRAD-derived RMW; 4) HRD center with the RMWs from the manuscript; 5) HRD center with single point maximum wind speed XDD-derived RMW; and, 6) HRD center with flight-level RMW (closest flights in time to WB-57) overpass. The RMWs for all six methods agree reasonably well, with largest discrepancies at weak TC intensities (Fig. C.6). The RMWs used in the manuscript derived from both XDD and HIRAD data agree with flight-level data RMWs within a mean and median of 8–9 km, which is close to the resolution of the NHC Best Track RMWs. The use of a single data point maximum for obtaining the XDD-derived RMW doesn't change the results in the CFAzDs and CFADs appreciably, because the single data point maximum RMW and estimated RMW in the manuscript agree within a mean and median of 5–6 km.

The median profiles for the subset of seven dates at all radii, within the core, and outside of the core (Fig. C.7) agree reasonably well between the methods used in the manuscript and the HRD data, with the largest discrepancies aloft and outside of the core. The p-values for Student's t-test comparisons are 0.8, 0.25, and < 0.01 for all data, inside core, outside of core. This indicates that only the median profiles outside of the core are different by using the HRD centers and flight-level RMWs.

The CFRDs and CFAzDs for all radii (Fig. C.8) for the subset of seven days look extremely similar for the methods in the manuscript and for the flight-level RMW/HRD track method. Shown in Figure C.8 are also percent frequency difference plots (using the ZWC/XDD-derived RMW method using HRD center and flight-level RMW) for the CFRDs and CFAzDs for the combined seven dates with flight-level RMW/HRD track data. The difference plots show that the largest differences outside of $\pm 1\%$ occur within the error bounds of vertical velocity and, therefore, may not be significantly different. Further, Student's t-tests of the binned percentages in the CFRDs and CFAzDs have p-values above 0.97 for Marty, Joaquin, Patricia, and the combined seven days. This suggests that theres no statistical difference in the CFRDs or CFAzDs using either methodology. The CFADs (not shown) are not appreciably affected by the center or track, because it is a frequency distribution with respect to altitude and the lack of data at large radii limit the impact of differences in the 10R* values for the two methods.

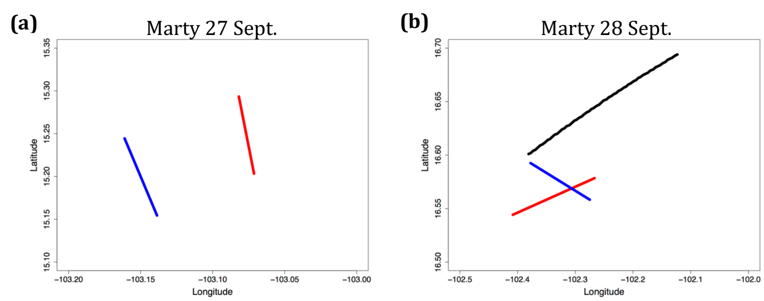

Figure C.1: TC center tracks for Marty. The NHC Best Track center track is in blue, the XDD-derived ZWC track is in red, and the HRD center track (when available) is in black. From Nelson et al. (2019a). ©American Meteorological Society. Used with permission.

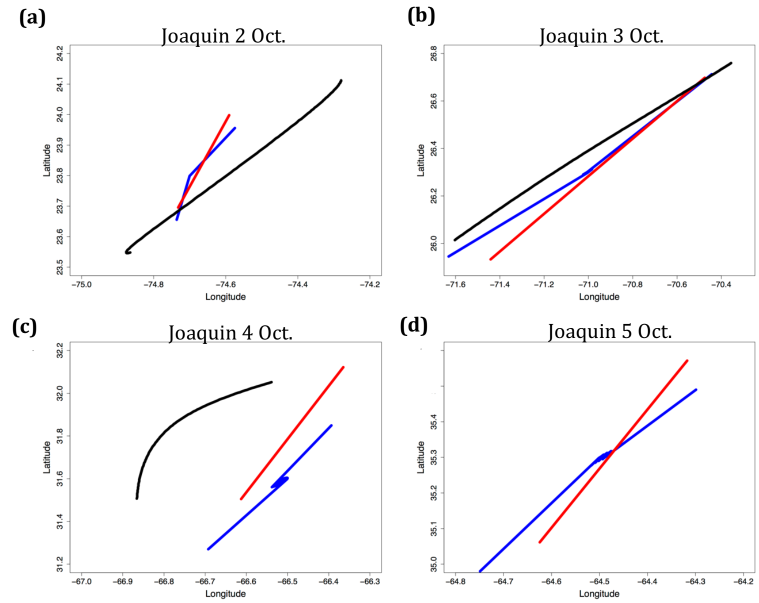

Figure C.2: Same as Fig. C.1, but for Joaquin. From Nelson et al. (2019a). ©American Meteorological Society. Used with permission.

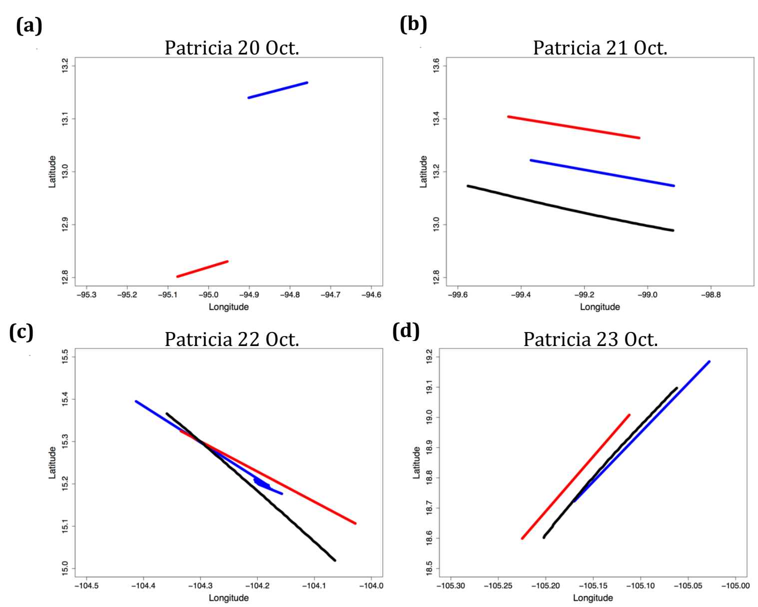

Figure C.3: Same as Fig. C.1, but for Patricia. From Nelson et al. (2019a). ©American Meteorological Society. Used with permission.

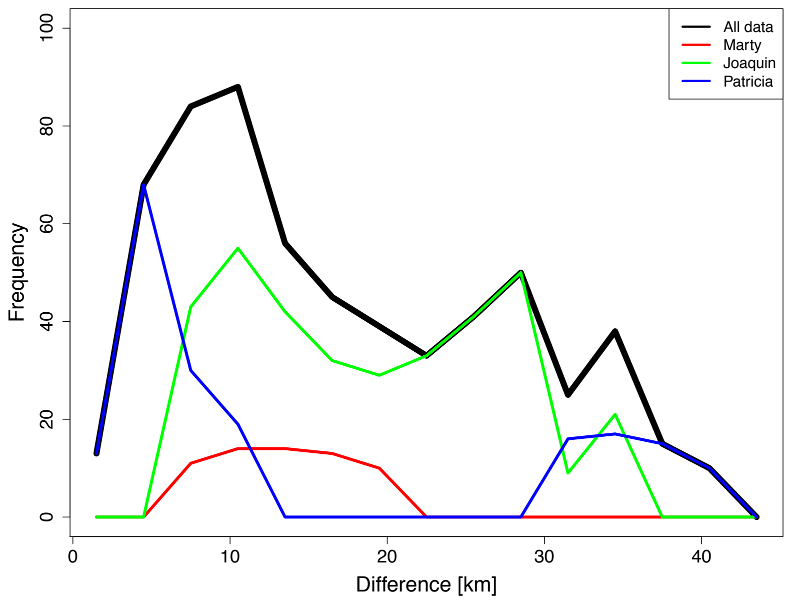

Figure C.4: Histogram of differences between XDD-derived ZWC tracks and HRD center tracks. The histogram for all of the seven-day subset is in black, Marty in red, Joaquin in green, and Patricia in blue. From Nelson et al. (2019a). ©American Meteorological Society. Used with permission.

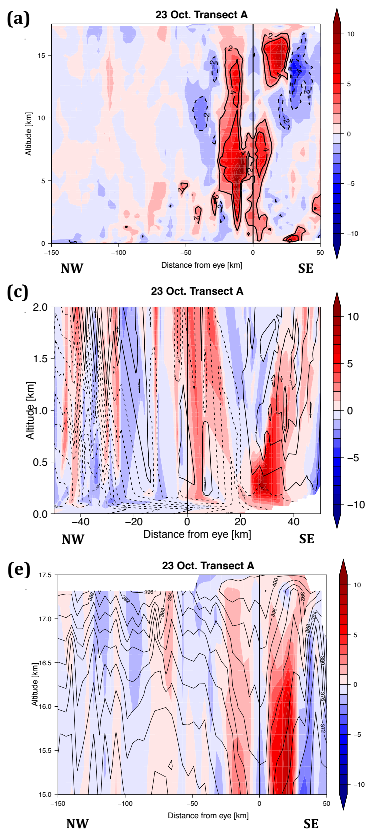

Figure C.5: Same as Fig. 3.14 but using the high-resolution HRD TC center tracks. From Nelson et al. (2019a). ©American Meteorological Society. Used with permission.

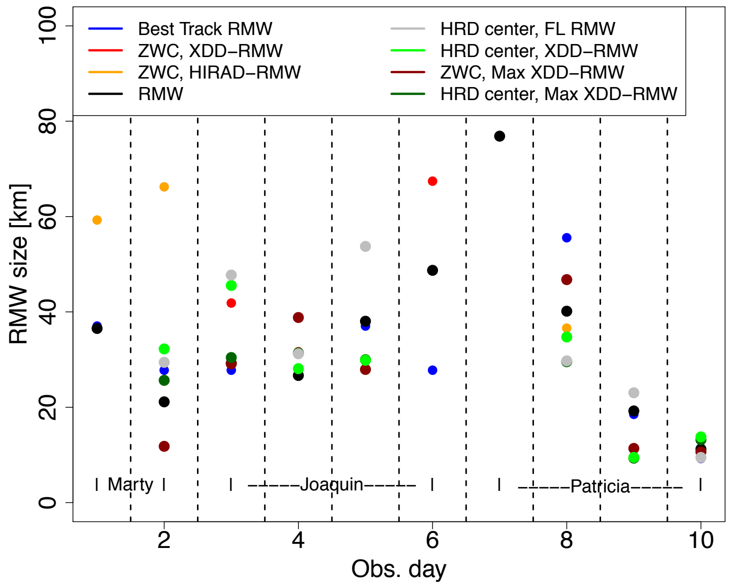

Figure C.6: Scatter plot of RMW size for each of the eight RMWs examined for the six total RMW/center methods. For reference, the RMWs used in this dissertation are in black and the flight-level RMWs are in gray. Vertical dashed lines separate the observation days. From Nelson et al. (2019a). ©American Meteorological Society. Used with permission.

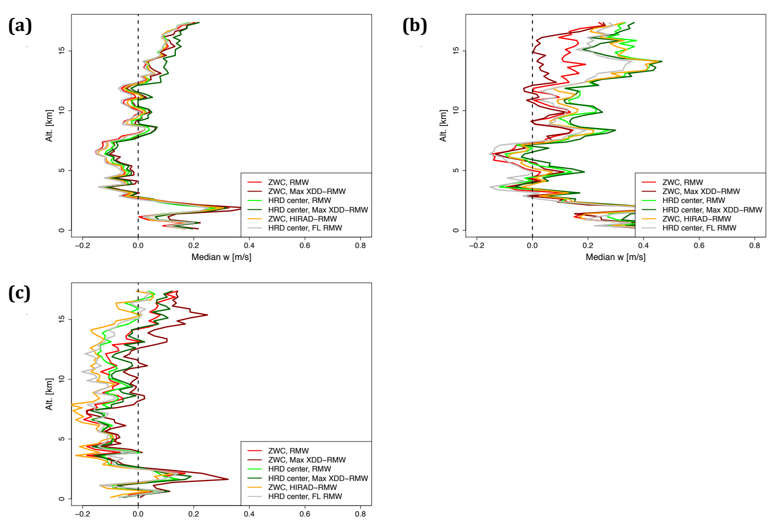

Figure C.7: Median $|V_h|$ profiles for all six RMW/center methods explored. Panel (a) is for all of the seven-day subset, panel (b) is for data within the core, and panel (c) is for data outside of the core. From Nelson et al. (2019a). ©American Meteorological Society. Used with permission.

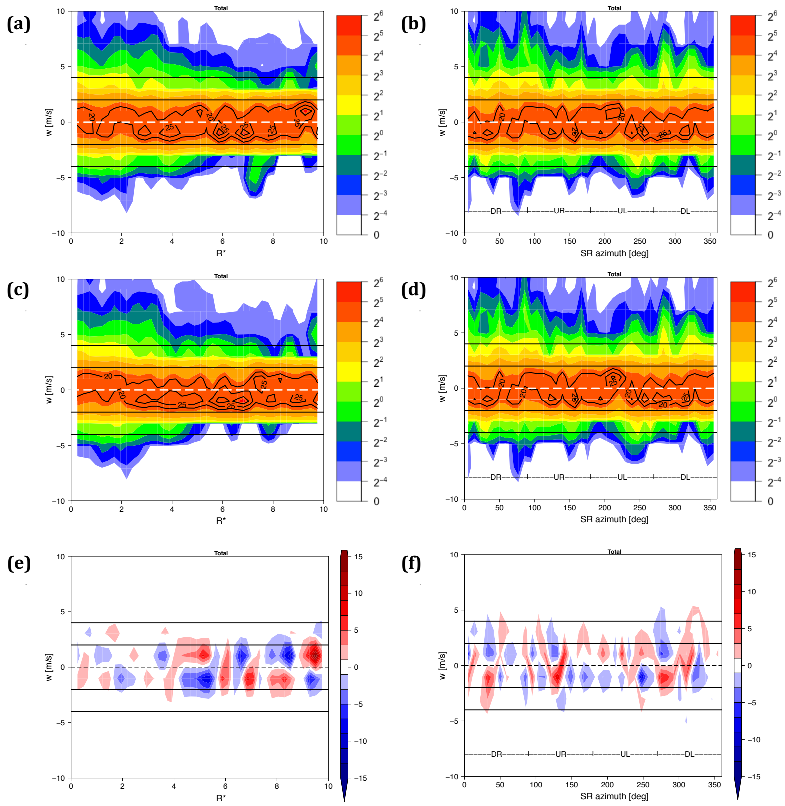

Figure C.8: CFRDs (a, c) and CFAzDs (b, d) for the seven-day subset using the XDD and HIRAD derived RMWs (a, b) and flight-level RMWs (c, d). Difference plots between the two methods are provided in panels (e) and (f). The horizontal solid black lines denote the vertical velocity updraft and downdraft thresholds. From Nelson et al. (2019a). ©American Meteorological Society. Used with permission.

APPENDIX D

Contour Frequency Diagrams for Data Inside and Outside of the Core

After restricting the data to within the core (Fig. D.1), similar azimuthal features as the CFAzD for all radii (Fig. 3.10) are present. One major difference between the two is in the azimuthal vertical velocity distribution in Marty, where vertical velocities between the UL and DL quadrants were more negative in the core (Fig. D.1a). The vertical velocity distributions within the cores of the three TCs are different than for outside of 3R* (Fig. D.2). The azimuthal distributions for all three TCs outside of the core have higher frequencies of lower vertical velocity strength, but little azimuthal variability exists in vertical velocity strength (Fig. D.2). This is similar to the azimuthal variability of the core CFAzDs (Fig. D.1). There were very few data points in the DR or UR quadrants in Marty due to sampling biases, which makes the distribution outside of the core of Marty not robust (Fig. D.2). There were also data gaps in the DR quadrant outside of the core in Joaquin. The similarities between the contoured frequency diagrams for all radii and the contoured frequency diagrams from the core reflect that: 1) approximately 50% of the data used to derive the full contoured frequency diagrams comes from the core; and, 2) the cores of the TCs have the most variation and spread in the strength of the observed vertical velocities.

Like the core CFAzD plots, the core CFADs (Fig. D.3) do not change appreciably from the total CFADs (Fig. 3.10). Larger differences were found between the CFADs for the core and the CFADs for data outside of 3R*, especially for Joaquin and Patricia (e.g., Fig. D.3c vs. Fig. D.4c). The shape of the CFAD remained similar for data inside and outside of the core, and the vertical velocity distribution spread in Marty was not appreciably different between the two (Figs. D.3a and D.4a). In Joaquin, the distribution was narrower for data outside of the core, and the strongest positive vertical velocities occurred primarily above 13.5 km (Fig. D.3a). Outside of 3R*, Patricia also had a narrower vertical velocity distribution, but the strongest vertical velocities occurred below 6 km for positive values and above 8 km for negative values.

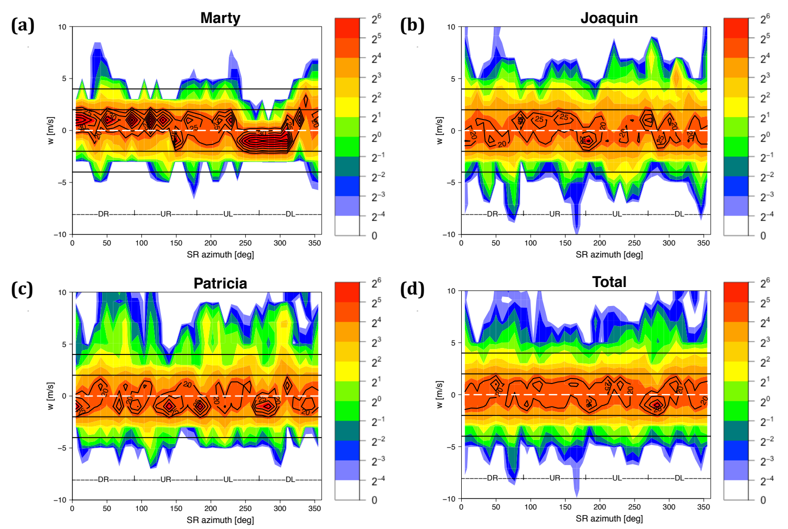

Figure D.1: CFAzD percentages of vertical velocities (m s^{-1}) within the core. Panel (a) is for Marty, panel (b) is for Joaquin, panel (c) is for Patricia, and panel (d) is for the entire dataset. Colored contours are percentages on a logarithmic scale. Black lined contours are percentages above 20% in intervals of 5%. The horizontal solid black lines denote the vertical velocity updraft and downdraft thresholds. The dashed white line designates $w = 0$ m s^{-1}. From Nelson et al. (2019a). ©American Meteorological Society. Used with permission.

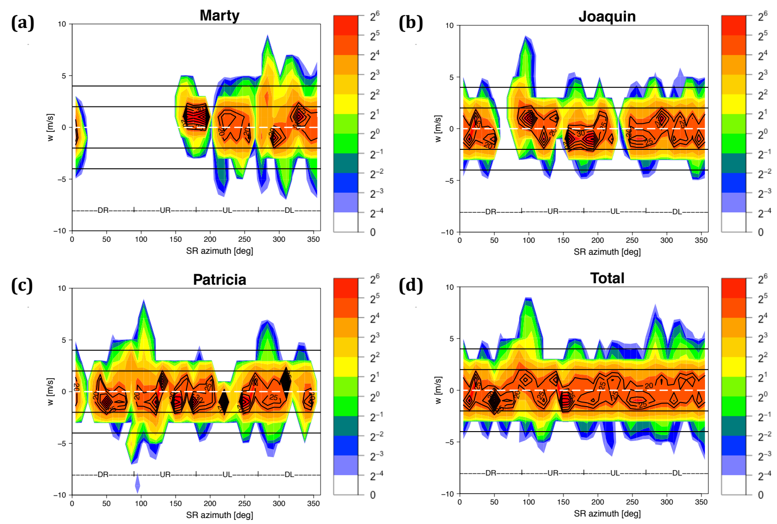

Figure D.2: Same as Fig. D.1, but for r > 3R*. From Nelson et al. (2019a). ©American Meteorological Society. Used with permission.

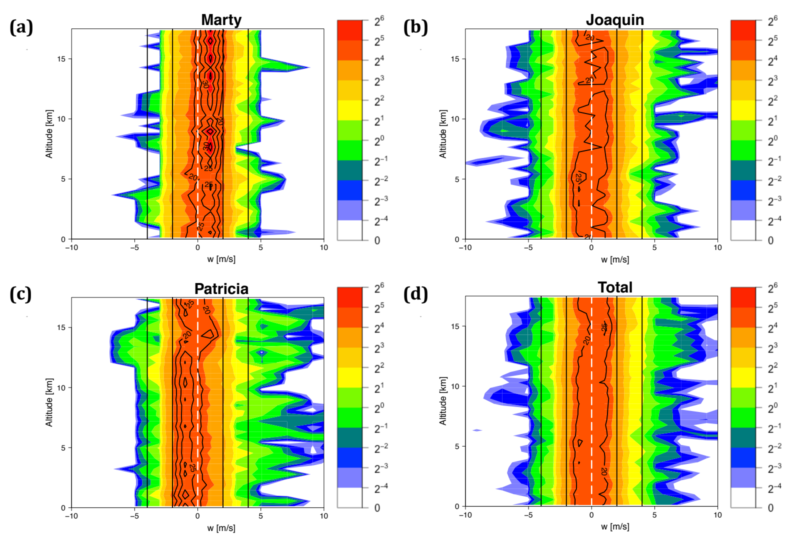

Figure D.3: CFAD percentages of vertical velocities (m s^{-1}) within the core. Panel (a) is for Marty, panel (b) is for Joaquin, panel (c) is for Patricia, and panel (d) is for the entire dataset. Colored contours are percentages on a logarithmic scale. Black lined contours are percentages above 20% in intervals of 5%. The vertical solid black lines denote the vertical velocity thresholds. The dashed white line designates $w = 0$ m s^{-1}. From Nelson et al. (2019a). ©American Meteorological Society. Used with permission.

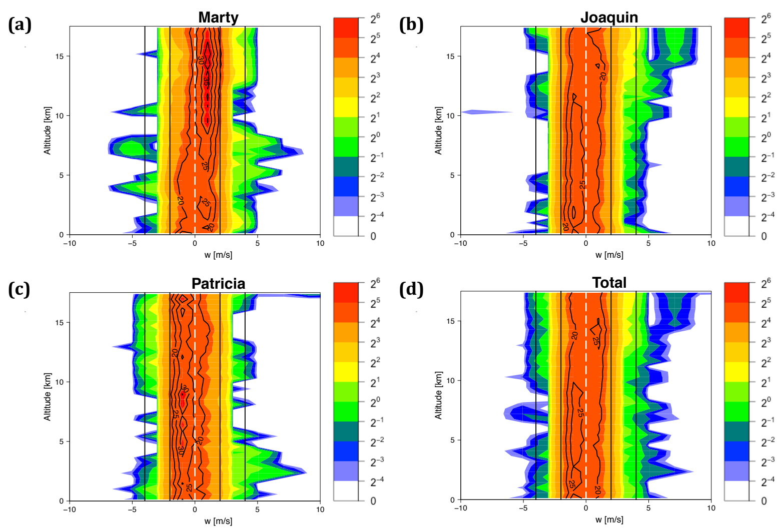

Figure D.4: Same as Fig. D.3, but for r > 3R*. From Nelson et al. (2019a). ©American Meteorological Society. Used with permission.

APPENDIX E

Contour Frequency Diagrams using the GPS Fall Speed

The contoured frequency diagrams for vertical velocities derived from the GPS fall speed rather than the hydrostatic differential pressure fall speed have vastly different frequency distributions. The vertical velocities tend to be stronger overall and peak in strength aloft, which agrees better with the CFADs in Black et al. (1996) (Fig. E.1). The vertical velocities using the GPS fall speed decrease in strength with increasing radius like for the differential pressure vertical velocities, but the decrease is stronger for the GPS fall speed vertical velocities (Figs. 3.9, E.2). There is little difference between the CFAzDs using either the GPS fall speed, or the differential pressure indicated fall speed other than overall strength (Figs. 3.10, E.3). Little azimuthal signal can be ascertained in both cases.

The justification for using the differential pressure indicated fall speeds was for two reasons: 1) the large discrepancies between the two fall speeds (Fig. 2.4); and, 2) Stern et al. (2016) state that the accuracy of the pressure is better than the GPS height derived fall speeds. Further, large, unrealistic GPS fall speeds, especially in the lowest few 100 m can be erroneous (Vömel et al., 2018). Currently, dropsonde manufacturers are working to fix these issues by filtering or improved GPS receivers and chip sets (e.g., Vömel et al., 2018). Figure 2.4 does not exhibit as strong of a low-level issue as in Vömel et al. (2018), but the profile still contains unrealistic, noisy GPS fall speeds. The differences between the two fall speeds are likely to be due to GPS errors rather than physical or smoothing scale differences in calculating the differential pressure fall speed.

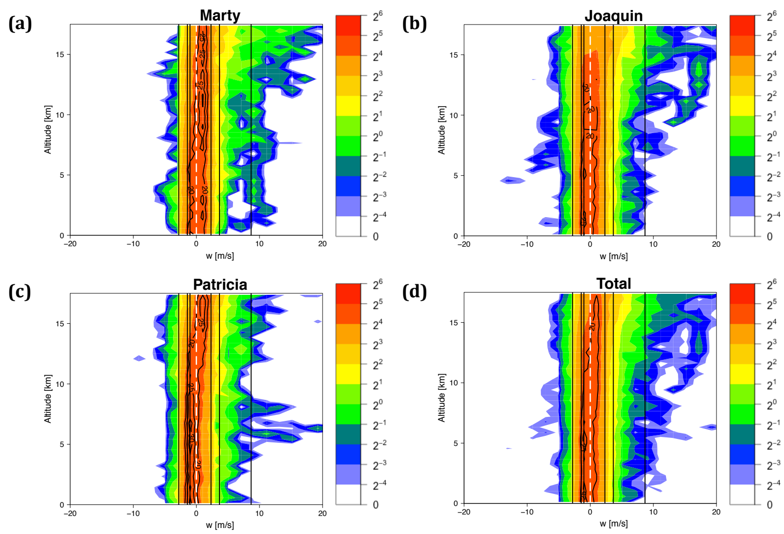

Figure E.1: CFAD percentages of vertical velocities (m s^{-1}) derived from GPS fall speed. Panel (a) is for Marty, panel (b) is for Joaquin, panel (c) is for Patricia, and panel (d) is for the entire dataset. Colored contours are percentages on a logarithmic scale. Black lined contours are percentages above 20% in intervals of 5%. The vertical solid black lines denote the vertical velocity thresholds. The dashed white line designates $w = 0$ m s^{-1}. Note the difference in the vertical velocity (x-axis) scale to the previous CFADs. From Nelson et al. (2019a). ©American Meteorological Society. Used with permission.

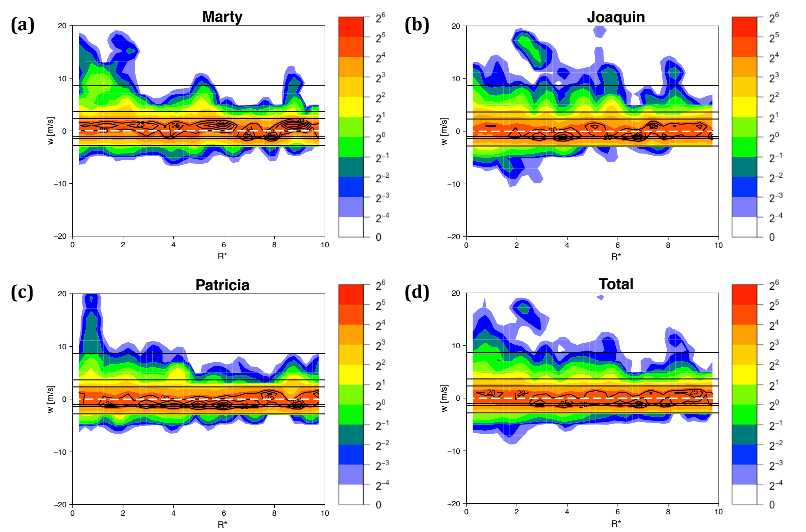

Figure E.2: CFRD percentages of vertical velocities (m s^{-1}) derived from GPS fall speed. Panel (a) is for Marty, panel (b) is for Joaquin, panel (c) is for Patricia, and panel (d) is for the entire dataset. Colored contours are percentages on a logarithmic scale. Black lined contours are percentages above 20% in intervals of 5%. The horizontal solid black lines denote the vertical velocity thresholds. The dashed white line designates $w = 0$ m s^{-1}. Note the difference in the vertical velocity (y-axis) scale to the previous CFRDs. From Nelson et al. (2019a). ©American Meteorological Society. Used with permission.

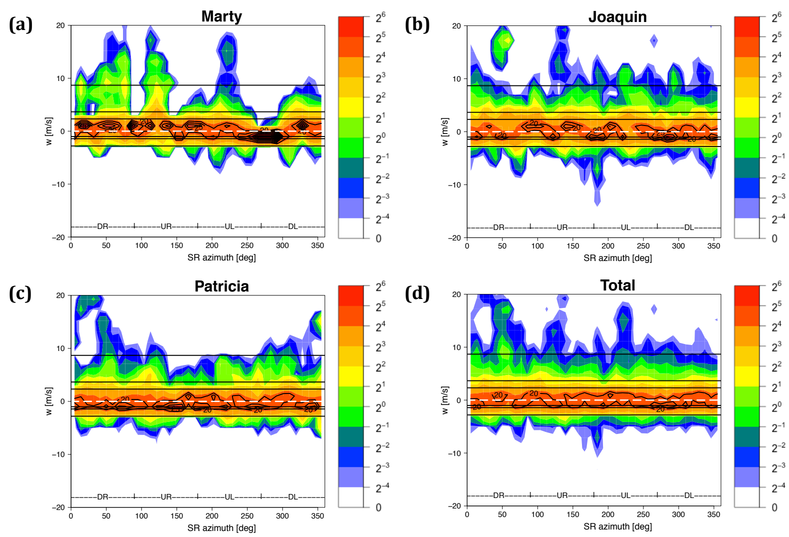

Figure E.3: CFAzD percentages of vertical velocities (m s^{-1}) derived from GPS fall speed. Panel (a) is for Marty, panel (b) is for Joaquin, panel (c) is for Patricia, and panel (d) is for the entire dataset. Colored contours are percentages on a logarithmic scale. Black lined contours are percentages above 20% in intervals of 5%. The horizontal solid black lines denote the vertical velocity thresholds. The dashed white line designates $w = 0$ m s^{-1}. Note the difference in the vertical velocity (y-axis) scale to the previous CFAzDs. From Nelson et al. (2019a). ©American Meteorological Society. Used with permission.

APPENDIX F

Six Detrending Methods for Dropsonde Autocorrelations

Autocorrelations with respect to space and time can be computed for raw data or for data that have been detrended for any linear, polynomial, or non-linear base state. A total of six detrend methods were explored: 1) non-detrend; 2) detrend using median profiles from a specific date (date detrend); 3) detrend using median profiles from a specific TC (storm detrend); 4) detrend using median profiles from the entire dataset (total detrend); 5) detrend using median profiles within the four radial sections noted below from the entire dataset (radial detrend); and, 6) detrend using median profiles within the four radial sections from a specific date (D+R detrend). The purpose of this section is to document and compare the six detrend methods for vertical velocity (w), horizontal wind speed ($|V_h|$), relative humidity (RH), temperature (T), and equivalent potential temperature (θ_e). The four radial sections are: 1) $\leq$1.25R*; 2) 1.25–3R*; 3) 3–5R*; and, 4) 5–10R*. The 1.25R* radius was chosen because DeHart et al. (2014) found that the highest frequencies of updrafts and downdrafts in the core occurred between 0.75R* and 1.25R*. 3R* was also chosen to reflect the outermost region of the core (Rogers et al., 2013), and 5R* was chosen because it is the midpoint of the R* values. Beyond 5R*, composite low-level azimuthal winds decreased substantially in strength (not shown).

The median base states for methods 2−5 are provided in Figures F.1−F.6. The median base states for the D+R detrend method is provided in Figures 3.29−3.31 of the manuscript. Figures F.1−F.3 are the date detrend median profiles for Marty, Joaquin, and Patricia, respectively. The date detrend profiles show that there were large variances between the median profiles from day-to-day, especially with w and $|V_h|$ (Figs. F.1−F.3). T and θ_e have similar profiles from day-to-day (Figs. F.1−F.3). The variance in the RH profiles from day-to-day was largest in the lowest 6 km below the freezing level (Figs. F.1−F.3).

The storm detrend median profiles show similar variances from storm-to-storm, with the largest variances with w and $|V_h|$ (Fig. F.4). Patricia had the strongest median $|V_h|$, but had the weakest (more negative) median vertical wind speeds (Fig. F.4a, b), which is problematic as Patricia had the strongest updraft speeds. The total detrend median profiles (Fig. F.5) most closely resemble the Joaquin median profiles (Fig. F.4). Radial median profiles (Fig. F.6) better capture the radial variance in the median profiles, but they do not capture the variance from storm-to-storm (Fig. F.4) or day-to-day (Figs. F.1-F.3). The radial and date median profiles (D+R) capture the variances daily, radially, and from storm-to-storm (Figs. 3.29–3.31).

An example of a detrended sounding that sampled an updraft from Patricia on 23 October is provided in Figure F.7. All detrended w profiles show positive perturbations within the updraft zone and a sharp decrease in speed within the updraft zone (Figs. F.7a, b). This specific convective eyewall sounding shows strong variances in the detrended RH, T, and θ_e profiles (Figs. F.7c, d, e). Date, storm, total, and radial detrend methods produced qualitatively similar thermal profiles, but D+R detrended thermal profiles are weaker and more negative (Figs. F.7d, e). The differences in the median profiles changes the temporal autocorrelations within the sounding (Fig. F.8). 0.5-autocorrelation temporal thresholds range from 62−76 s for w, 91−110 s for $|V_h|$, 23−92 s for RH, 82−126 s for T, and 77−115 s for θ_e (Fig. F.8).

The 0.5-autocorrelation spatial thresholds for detrend methods 1−6 show that little variation exists for w (Tables F.1−F.5, 3.10). There was also little variation for RH and θ_e

when detrended by the latter five methods (Tables F.1−F.5). Larger variations were observed for T and $|V_h|$ (Tables F.1−F.5, 3.10). Overall, the D+R detrended spatial autocorrelation scales are smaller than the other methods and the non-detrended variables had the largest spatial autocorrelation scales (Tables F.1−F.5, 3.10). Table F.6 shows the pairwise Student's t-test p-values for the spatial autocorrelation thresholds for each variable for methods 1−6. The non-detrend method for $|V_h|$, RH, T, and θ_e exhibited statistically significant differences and some of the other detrend methods for T were also statistically different (Table F.6). The 0.5-autocorrelation temporal thresholds for detrend methods 1−5 show that the non-detrend method produces the largest temporal scales and the D+R detrend method produces the smallest temporal scales (Tables F.7−F.11, 3.11). This result is supported by pairwise Student's t-tests, which show that for all variables, except w, the non-detrend method produces statistically larger temporal autocorrelation scales (Table F.12). Similarly, Student's t-test p-values indicate statistical differences for the D+R detrend method and all other methods, except for w and the date detrend method (Table F.12).

Figures F.9−F.11 show the spatial autocorrelation correlograms for Marty (Fig. F.9), Joaquin (Fig. F.10), and Patricia (Fig. F.11). The spatial correlograms for w were similar for all six detrend methods (Figs. F.9a, F.10a, F.11a). The non-detrend method produces correlograms that do not decrease appreciably with increasing distance, which rarely cross the 0.5-autocorrelation threshold (Fig. F.9−F.11). Variations in the $|V_h|$ correlograms exist for the other five detrend methods, but the shapes of the correlograms are similar (Figs. F.9b, F.10b, F.11b). The T and θ_e spatial correlograms have the largest differences between the five other detrend methods, especially within the inner 100 km (Figs. F.9d, e, F.10d, e, F.11d, e).

Figures F.12−F.14 show the temporal autocorrelation correlograms for Marty (Fig.

F.12), Joaquin (Fig. F.13), and Patricia (Fig. F.14). The detrend methods does not drastically affect the temporal autocorrelation correlograms for w (Figs. F.12a, F.13a, F.14a). The largest differences in the correlograms were between the non-detrend temporal autocorrelation correlograms for $|V_h|$, RH, T, and the other five methods (Figs. F.12b, c, d, F.13b, c, d, F.14b, c, d). The non-detrended temporal autocorrelation correlograms for all variables (except w) do not saturate to near-zero at large lags. Rather, the autocorrelations drop to large, negative values because of the presence of a mean state in the data (Janert, 2011).

Table F.1: List of dropsonde-to-dropsonde spatial 0.5-autocorrelation thresholds (in km) for each day in the dataset without detrending. Distances larger than 500 km were not considered and are labeled as "> 500". From Nelson et al. (2019b).

Date	Storm	w	$\|V_h\|$	RH	T	θ_e
27 Sept.	Marty	4.8	28.1	> 500	> 500	> 500
28 Sept.	Marty	4.2	364.6	> 500	> 500	> 500
2 Oct.	Joaquin	3.8	17.6	> 500	> 500	> 500
3 Oct.	Joaquin	3.2	274.7	> 500	> 500	> 500
4 Oct.	Joaquin	4.3	> 500	> 500	> 500	> 500
5 Oct.	Joaquin	5.1	383.6	> 500	> 500	> 500
20 Oct.	Patricia	19.6	27.4	> 500	> 500	> 500
21 Oct.	Patricia	5.7	98	> 500	> 500	> 500
22 Oct.	Patricia	3.8	225.7	> 500	> 500	> 500
23 Oct.	Patricia	1.4	> 500	> 500	> 500	41.9
Mean	All	5.6	192	> 500	> 500	> 500
Median	All	4.3	237.8	> 500	> 500	> 500
St. Dev	All	5	139.2	NA	NA	NA

Table F.2: Same as Table F.2, but for the date detrend method. From Nelson et al. (2019b).

Date	Storm	w	$\|V_h\|$	RH	T	θ_e
27 Sept.	Marty	4.2	23.4	12.7	47.3	50.5
28 Sept.	Marty	3.4	8.4	3.1	16.8	5.3
2 Oct.	Joaquin	3.8	9.1	24.7	40.8	33.3
3 Oct.	Joaquin	3.2	7.4	4.6	17.5	5.5
4 Oct.	Joaquin	4.9	21.1	7	25.4	9.2
5 Oct.	Joaquin	4.5	63.4	10.2	90.9	12.2
20 Oct.	Patricia	20	24.3	50.9	25.4	36
21 Oct.	Patricia	5.2	15.2	6.5	17.4	8.3
22 Oct.	Patricia	4.1	22.8	4.7	19.8	5.3
23 Oct.	Patricia	1.3	15.5	3.8	11.8	4.9
Mean	All	5.5	21	12.8	31.3	17
Median	All	4.2	18.3	6.8	22.6	8.7
St. Dev	All	5.2	16.2	14.8	23.8	16.5

Table F.3: Same as Table F.2, but for the storm detrend method. From Nelson et al. (2019b).

Date	Storm	w	$\|V_h\|$	RH	T	θ_e
27 Sept.	Marty	4.2	30.8	12.2	71.7	79.1
28 Sept.	Marty	3.4	11.4	3.1	15.7	5.3
2 Oct.	Joaquin	3.8	8.6	30.6	53.6	35.4
3 Oct.	Joaquin	3.2	7.8	5.1	18.8	5.5
4 Oct.	Joaquin	4.9	22.2	7	25.4	34.1
5 Oct.	Joaquin	4.5	36.5	7.7	86.5	8.3
20 Oct.	Patricia	19.6	173	25.1	45.8	28.2
21 Oct.	Patricia	5.7	17.9	6.5	41.8	7.4
22 Oct.	Patricia	3.8	25.4	4.7	32.8	5.6
23 Oct.	Patricia	1.3	1.9	4	45.8	11.8
Mean	All	5.4	33.5	10.6	43.8	22.1
Median	All	4	20	6.8	43.8	10.1
St. Dev	All	5.1	50.2	9.5	22.6	23.5

Table F.4: Same as Table F.2, but for the total detrend method. From Nelson et al. (2019b).

27 Sept.	Marty	4.2	47.3	11.7	121.1	78.6
28 Sept.	Marty	3.8	10.7	3.1	24.4	5.3
2 Oct.	Joaquin	3.8	9.1	32.2	45.6	35.4
3 Oct.	Joaquin	3.2	6.9	5.1	20.7	5.5
4 Oct.	Joaquin	4.9	25.4	7	35.7	29.2
5 Oct.	Joaquin	4.5	65.3	7	195.6	7.7
20 Oct.	Patricia	19.2	387.2	29	320.6	25.1
21 Oct.	Patricia	5.7	24.4	6.5	195.6	9.1
22 Oct.	Patricia	4.4	26.9	4.7	126.3	6.5
23 Oct.	Patricia	1.4	2.1	3.7	38.4	12
Mean	All	5.5	60.5	11	43.8	21.3
Median	All	4.3	24.9	6.8	43.8	10.6
St. Dev	All	4.9	116.4	10.6	22.6	22.8

Table F.5: Same as Table F.2, but for the radial detrend method. From Nelson et al. (2019b).

Date	Storm	w	$\lvert V_h \rvert$	RH	T	θ_e
27 Sept.	Marty	4.2	72.8	8.5	163.6	49.4
28 Sept.	Marty	3.8	9.5	3.4	29	4.6
2 Oct.	Joaquin	3.8	9.7	27.4	39.7	31.6
3 Oct.	Joaquin	3.2	6	4.6	14.7	4.1
4 Oct.	Joaquin	4.9	20.6	7	30.3	21.6
5 Oct.	Joaquin	4.5	35.2	7	194	6.4
20 Oct.	Patricia	19.6	> 500	38.8	312.4	104.5
21 Oct.	Patricia	5.2	76.2	6.5	83.6	11.3
22 Oct.	Patricia	4.4	26.3	4.4	38.2	6.5
23 Oct.	Patricia	1.4	2.1	4	36.5	5.4
Mean	All	5.5	50.8	11.2	94.2	24.6
Median	All	4.3	23.4	6.8	38.9	8.6
St. Dev	All	5.1	74.8	12	98.1	31.8

Table F.6: Pairwise Student's t-test p-values for the 0.5-autocorrelation spatial thresholds for each variable and each detrend method. Statistically different spatial thresholds have p-values below 0.05. From Nelson et al. (2019b).

w	No detrend	Date detrend	Storm detrend	Total detrend	Radial detrend
Date detrend	0.95	-	-	-	-
Storm detrend	0.94	0.99	-	-	-
Total detrend	0.97	0.98	0.97	-	-
Radial detrend	0.97	0.98	0.98	1	-
D+R detrend	0.87	0.91	0.92	0.9	0.9
$\|V_h\|$	No detrend	Date detrend	Storm detrend	Total detrend	Radial detrend
Date detrend	2.50E-05	-	-	-	-
Storm detrend	8.00E-05	0.73819	-	-	-
Total detrend	0.00083	0.29223	0.46997	-	-
Radial detrend	0.00037	0.42577	0.64271	0.795	-
D+R detrend	9.90E-06	0.78791	0.54683	0.18781	0.2881
RH	No detrend	Date detrend	Storm detrend	Total detrend	Radial detrend
Date detrend	2.00E-16	-	-	-	-
Storm detrend	2.00E-16	0.89	-	-	-
Total detrend	2.00E-16	0.91	0.98	-	-
Radial detrend	2.00E-16	0.92	0.97	0.99	-
D+R detrend	2.00E-16	0.67	0.77	0.75	0.75
T	No detrend	Date detrend	Storm detrend	Total detrend	Radial detrend
Date detrend	2.80E-11	-	-	-	-
Storm detrend	1.60E-10	0.63592	-	-	-
Total detrend	2.50E-06	0.00322	0.01178	-	-
Radial detrend	2.10E-07	0.01989	0.05969	0.49711	-
D+R detrend	1.10E-12	0.38789	0.18374	0.00023	0.00188
θ_e	No detrend	Date detrend	Storm detrend	Total detrend	Radial detrend
Date detrend	2.00E-16	-	-	-	-
Storm detrend	2.00E-16	0.74	-	-	-
Total detrend	2.00E-16	0.78	0.96	-	-
Radial detrend	2.00E-16	0.62	0.87	0.83	-
D+R detrend	2.00E-16	0.46	0.29	0.31	0.22

Table F.7: List of the temporal 0.5-autocorrelation thresholds (in s) for each day in the dataset without detrending. From Nelson et al. (2019b).

Date	Storm	w	$\|V_h\|$	RH	T	θ_e
27 Sept.	Marty	22	39	51	98	36
28 Sept.	Marty	27	77	50	99	39
2 Oct.	Joaquin	24	63	45	94	39
3 Oct.	Joaquin	28	71	50	103	46
4 Oct.	Joaquin	22	77	78	104	39
5 Oct.	Joaquin	22	74	72	104	43
20 Oct.	Patricia	8	42	56	99	53
21 Oct.	Patricia	24	53	48	101	46
22 Oct.	Patricia	22	59	75	94	42
23 Oct.	Patricia	25	74	52	95	46
Mean	All	22.4	62.9	57.7	99.1	42.9
Median	All	23	67	51.5	99	42.5
St. Dev	All	5.5	14.3	12.3	3.9	5

Table F.8: Same as Table F.7, but for the date detrend method. From Nelson et al. (2019b).

Date	Storm	w	$\|V_h\|$	RH	T	θ_e
27 Sept.	Marty	20	38	35	29	44
28 Sept.	Marty	23	35	29	29	39
2 Oct.	Joaquin	24	45	40	37	44
3 Oct.	Joaquin	26	38	40	38	41
4 Oct.	Joaquin	22	36	40	25	39
5 Oct.	Joaquin	21	44	36	26	33
20 Oct.	Patricia	8	26	46	20	35
21 Oct.	Patricia	23	37	41	18	34
22 Oct.	Patricia	21	29	41	21	40
23 Oct.	Patricia	25	50	23	27	24
Mean	All	21.3	37.8	37.1	27	37.3
Median	All	22.5	37.5	40	26.5	39
St. Dev	All	5	7.2	6.7	6.7	6

Table F.9: Same as Table F.7, but for the storm detrend method. From Nelson et al. (2019b).

Date	Storm	w	$\lvert V_h \rvert$	RH	T	θ_e
27 Sept.	Marty	20	46	36	28	45
28 Sept.	Marty	24	39	30	29	37
2 Oct.	Joaquin	24	42	44	36	43
3 Oct.	Joaquin	26	40	39	37	40
4 Oct.	Joaquin	22	36	41	22	41
5 Oct.	Joaquin	21	45	39	26	33
20 Oct.	Patricia	8	39	54	32	43
21 Oct.	Patricia	24	39	41	19	35
22 Oct.	Patricia	22	35	43	19	45
23 Oct.	Patricia	25	59	27	43	34
Mean	All	21.6	42	39.4	29.1	39.6
Median	All	23	39.5	40	28.5	40.5
St. Dev	All	5.1	6.9	7.5	8	4.6

Table F.10: Same as Table F.7, but for the total detrend method. From Nelson et al. (2019b).

Date	Storm	w	$\lvert V_h \rvert$	RH	T	θ_e
27 Sept.	Marty	20	54	35	32	42
28 Sept.	Marty	25	34	31	26	38
2 Oct.	Joaquin	25	42	43	34	42
3 Oct.	Joaquin	26	42	39	47	44
4 Oct.	Joaquin	22	42	42	29	43
5 Oct.	Joaquin	21	49	39	38	36
20 Oct.	Patricia	8	50	56	30	40
21 Oct.	Patricia	25	43	41	24	32
22 Oct.	Patricia	22	35	42	23	41
23 Oct.	Patricia	26	57	28	40	35
Mean	All	22	44.8	39.6	32.3	39.3
Median	All	23.5	42.5	40	31	40.5
St. Dev	All	5.4	7.6	7.6	7.6	3.9

Table F.11: Same as Table F.7, but for the radial detrend method. From Nelson et al. (2019b).

Date	Storm	w	$\|V_h\|$	RH	T	θ_e
27 Sept.	Marty	20	48	31	45	40
28 Sept.	Marty	25	34	31	28	33
2 Oct.	Joaquin	24	42	42	34	41
3 Oct.	Joaquin	26	40	38	44	39
4 Oct.	Joaquin	22	39	42	26	39
5 Oct.	Joaquin	21	44	38	33	34
20 Oct.	Patricia	8	52	59	39	42
21 Oct.	Patricia	25	49	39	30	34
22 Oct.	Patricia	22	38	36	22	39
23 Oct.	Patricia	26	60	29	36	34
Mean	All	21.9	44.6	38.5	33.7	37.5
Median	All	23	43	38	33.5	39
St. Dev	All	5.3	7.7	8.5	7.5	3.4

Table F.12: Pairwise Student's t-test p-values for the 0.5-autocorrelation temporal thresholds for each variable and each detrend method. Statistically different spatial thresholds have p-values below 0.05. From Nelson et al. (2019b).

w	No detrend	Date detrend	Storm detrend	Total detrend	Radial detrend
Date detrend	0.64	-	-	-	-
Storm detrend	0.73	0.9	-	-	-
Total detrend	0.86	0.76	0.86	-	-
Radial detrend	0.83	0.8	0.9	0.97	-
D+R detrend	0.37	0.67	0.58	0.47	0.49
$\lvert V_h \rvert$	No detrend	Date detrend	Storm detrend	Total detrend	Radial detrend
Date detrend	3.20E-08	-	-	-	-
Storm detrend	1.70E-06	0.28536	-	-	-
Total detrend	2.20E-05	0.0777	0.47502	-	-
Radial detrend	1.80E-05	0.08632	0.50699	0.95921	-
D+R detrend	4.80E-11	0.08632	0.00659	0.00082	0.00096
RH	No detrend	Date detrend	Storm detrend	Total detrend	Radial detrend
Date detrend	8.00E-07	-	-	-	-
Storm detrend	7.50E-06	0.536	-	-	-
Total detrend	9.10E-06	0.501	0.957	-	-
Radial detrend	3.10E-06	0.706	0.808	0.767	-
D+R detrend	5.70E-10	0.056	0.013	0.011	0.024
T	No detrend	Date detrend	Storm detrend	Total detrend	Radial detrend
Date detrend	< 2.00E-16	-	-	-	-
Storm detrend	< 2.00E-16	0.49499	-	-	-
Total detrend	< 2.00E-16	0.08862	0.29979	-	-
Radial detrend	< 2.00E-16	0.03271	0.13815	0.64876	-
D+R detrend	< 2.00E-16	0.07244	0.01475	0.00077	0.00018
θ_e	No detrend	Date detrend	Storm detrend	Total detrend	Radial detrend
Date detrend	0.011	-	-	-	-
Storm detrend	0.126	0.283	-	-	-
Total detrend	0.095	0.35	0.888	-	-
Radial detrend	0.014	0.925	0.327	0.4	-
D+R detrend	2.70E-10	4.60E-06	8.90E-08	1.50E-07	3.30E-06

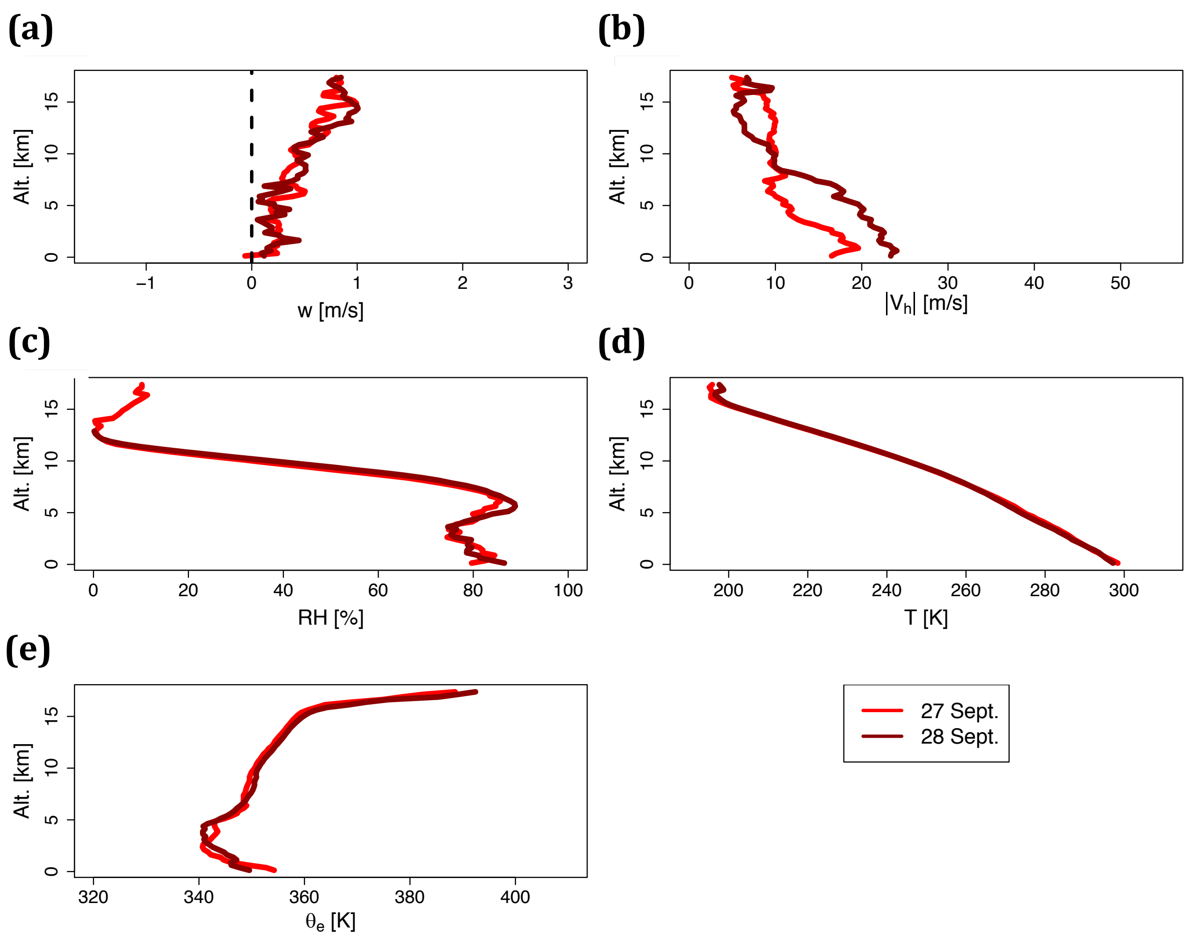

Figure F.1: Median atmospheric profiles of (a) w (m s^{-1}), (b) $|V_h|$ (m s^{-1}), (c) RH (%), (d) T (K), and (e) θ_e (K) for each observation day in Marty. From Nelson et al. (2019b).

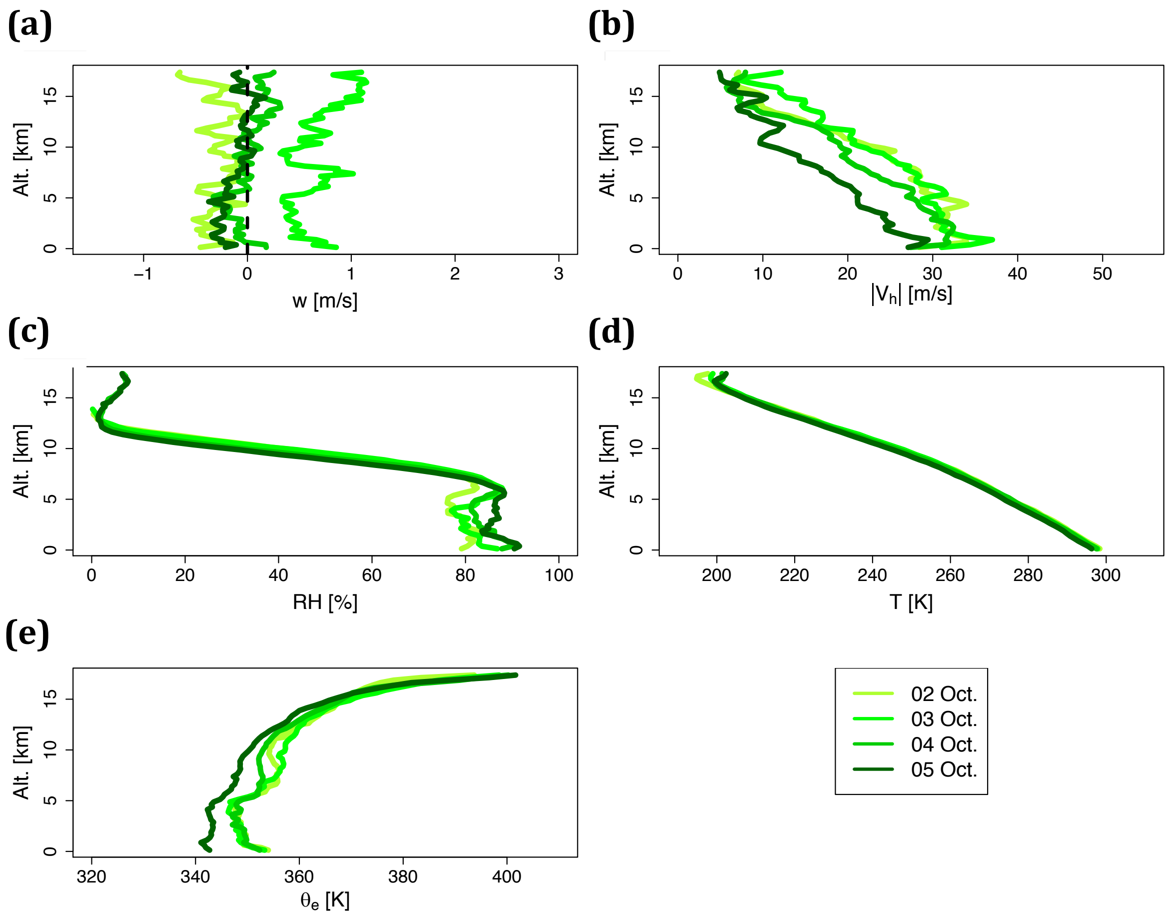

Figure F.2: Same as Fig. F.1, but for Joaquin. From Nelson et al. (2019b).

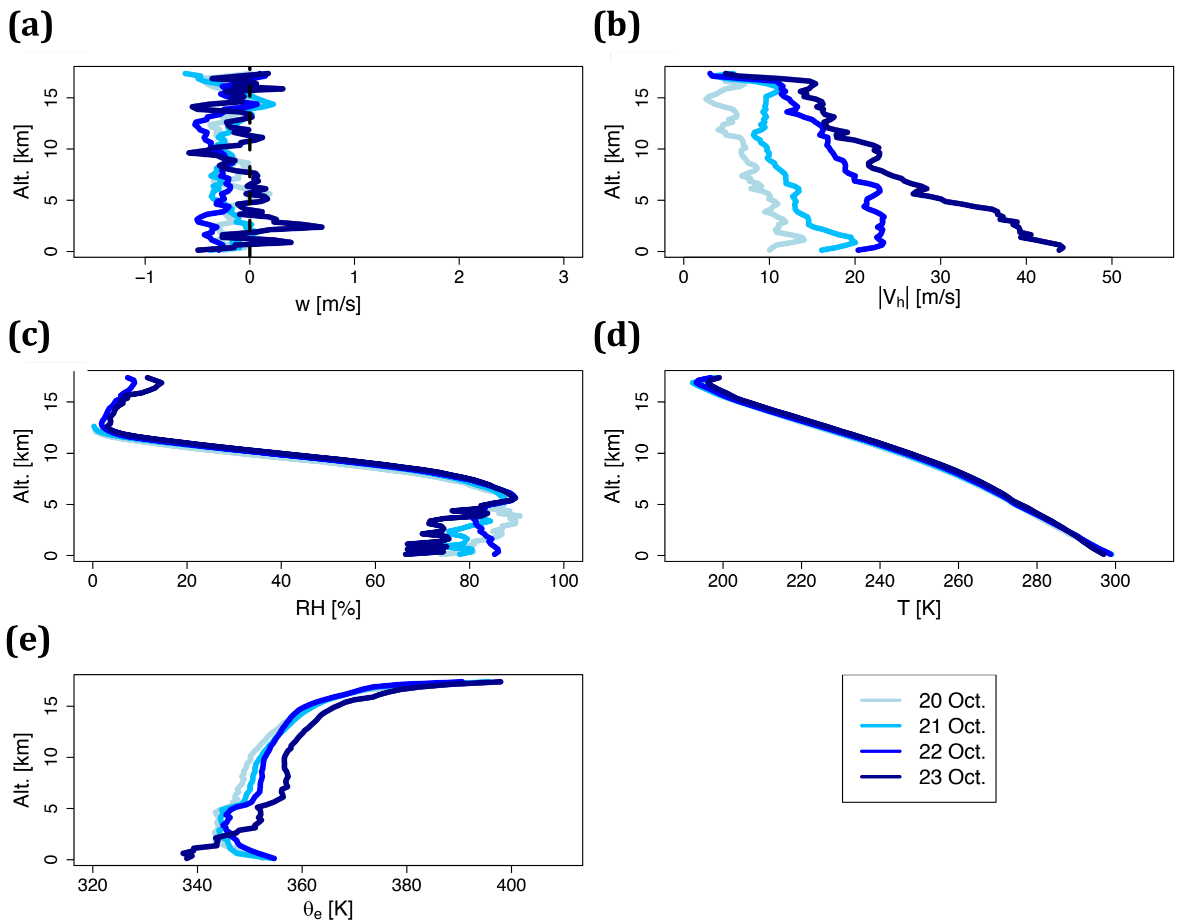

Figure F.3: Same as Fig. F.1, but for Patricia. From Nelson et al. (2019b).

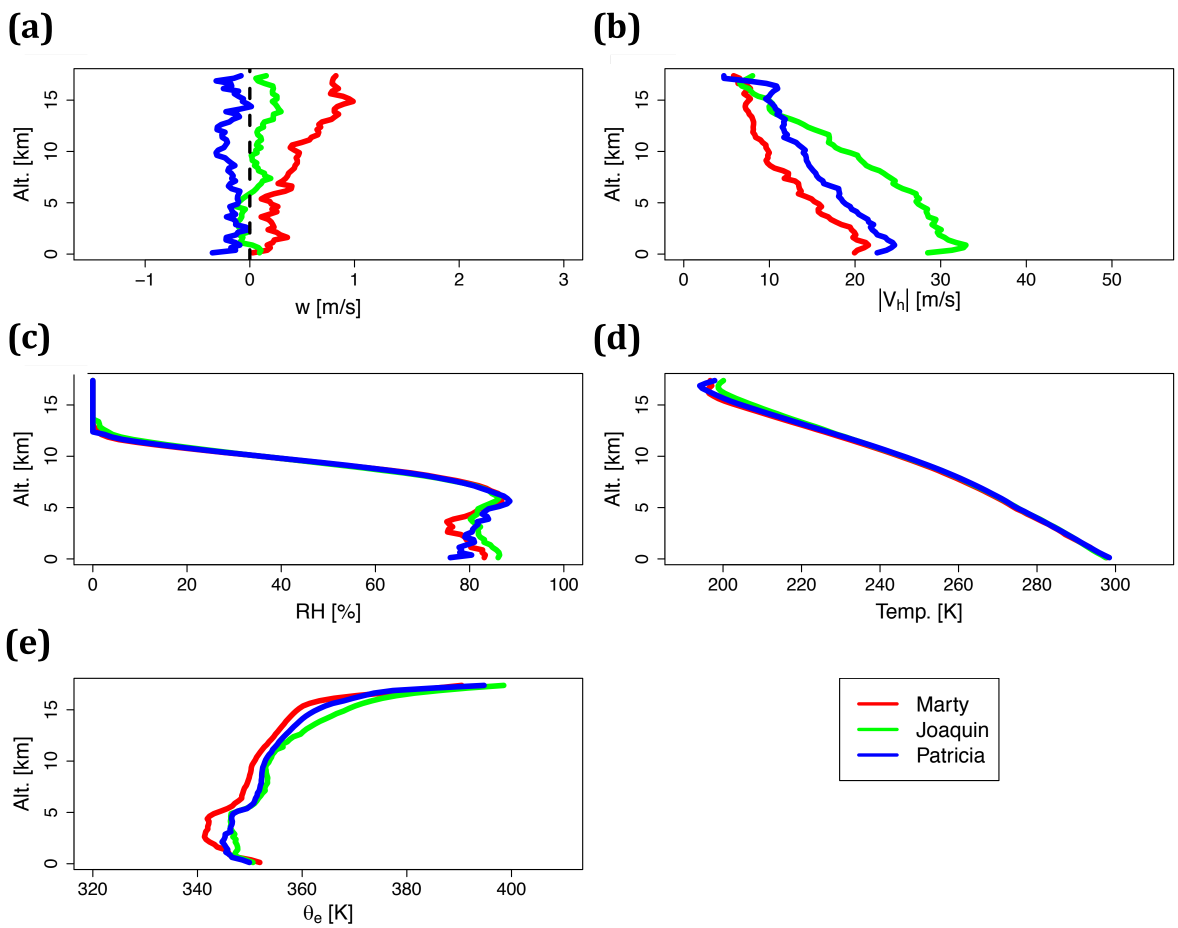

Figure F.4: Median atmospheric profiles of (a) w (m s^{-1}), (b) $|V_h|$ (m s^{-1}), (c) RH (%), (d) T (K), and (e) θ_e (K) for each tropical cyclone. From Nelson et al. (2019b).

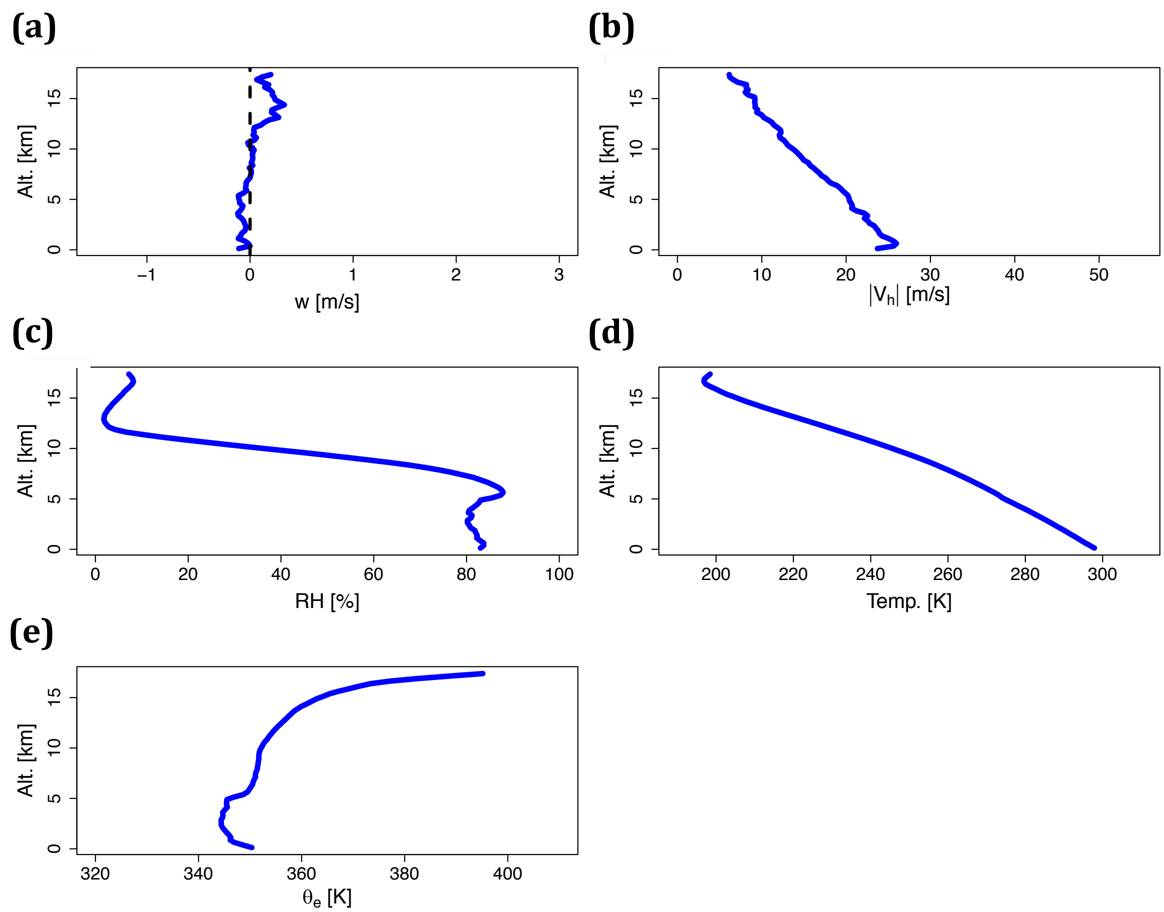

Figure F.5: Median atmospheric profiles of (a) w (m s^{-1}), (b) $|V_h|$ (m s^{-1}), (c) RH (%), (d) T (K), and (e) θ_e (K) for the entire dataset. From Nelson et al. (2019b).

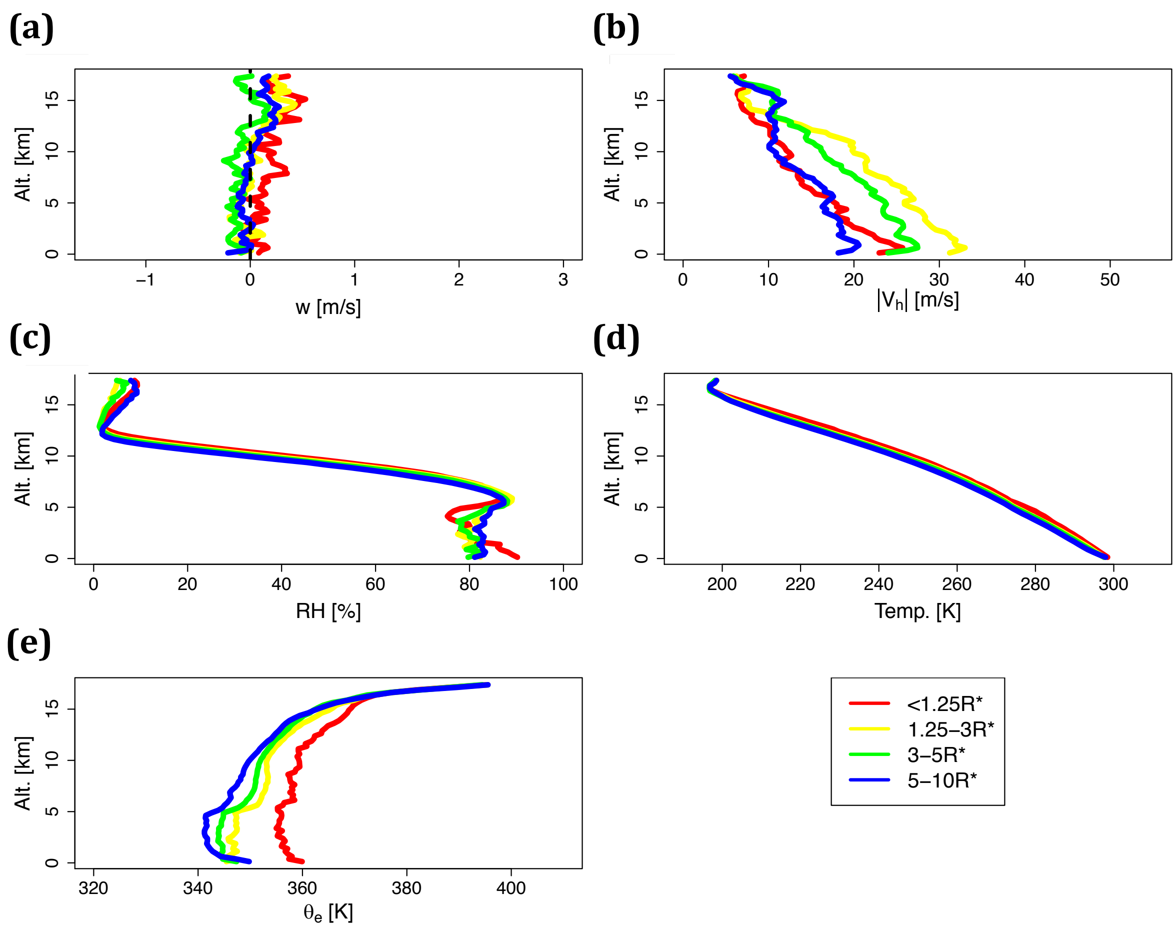

Figure F.6: Median atmospheric profiles of (a) w (m s^{-1}), (b) $|V_h|$ (m s^{-1}), (c) RH (%), (d) T (K), and (e) θ_e (K) for the entire dataset, divided into four radial sections: $< 1.25\text{R}^*$ (red), 1.25–3R* (yellow), 3–5R* (green), and 5–10R* (blue). From Nelson et al. (2019b).

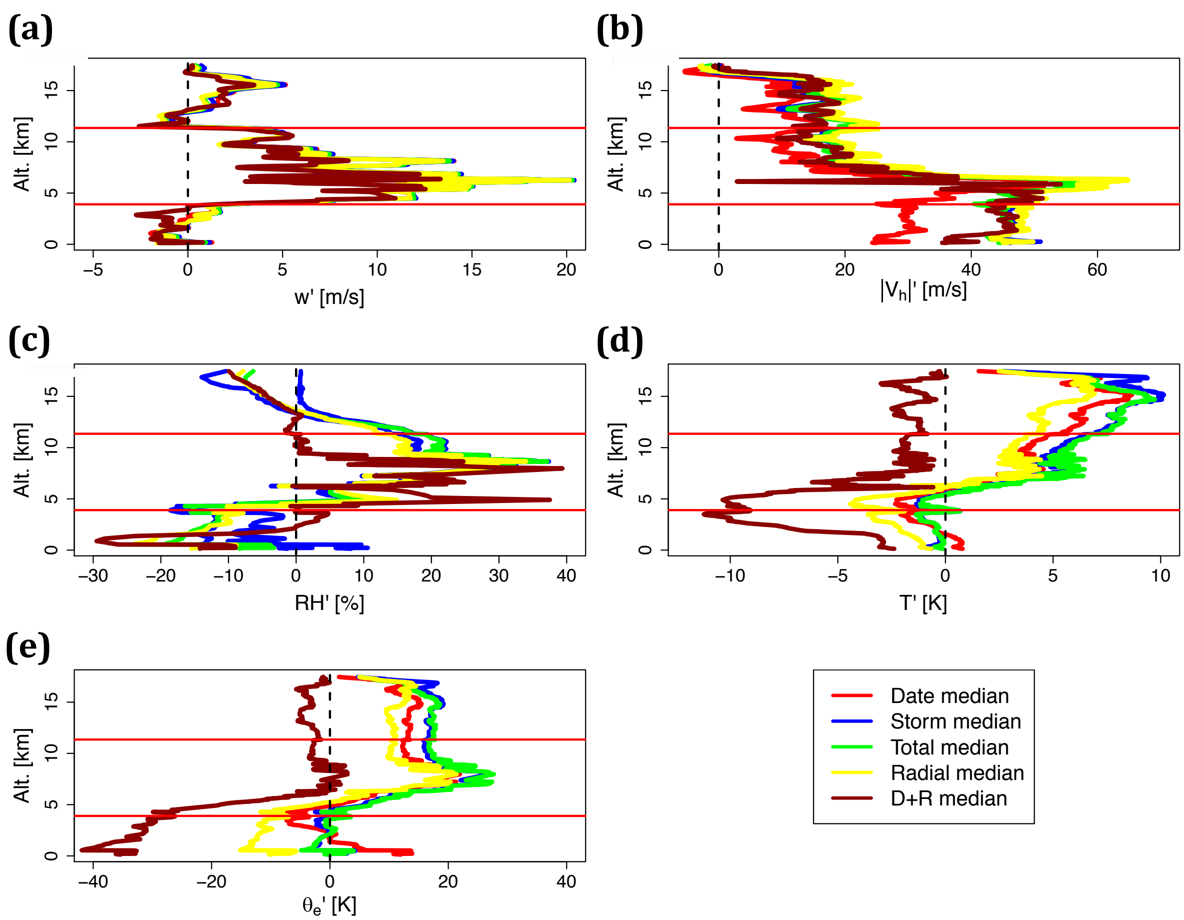

Figure F.7: Detrended atmospheric profiles of (a) w (m s^{-1}), (b) $|V_h|$ (m s^{-1}), (c) RH (%), (d) T (K), and (e) θ_e (K) from an updraft sounding (Droponde 72CC) launched into the eyewall of Patricia on 23 October. The red horizontal lines denote the depth of the updraft. From Nelson et al. (2019b).

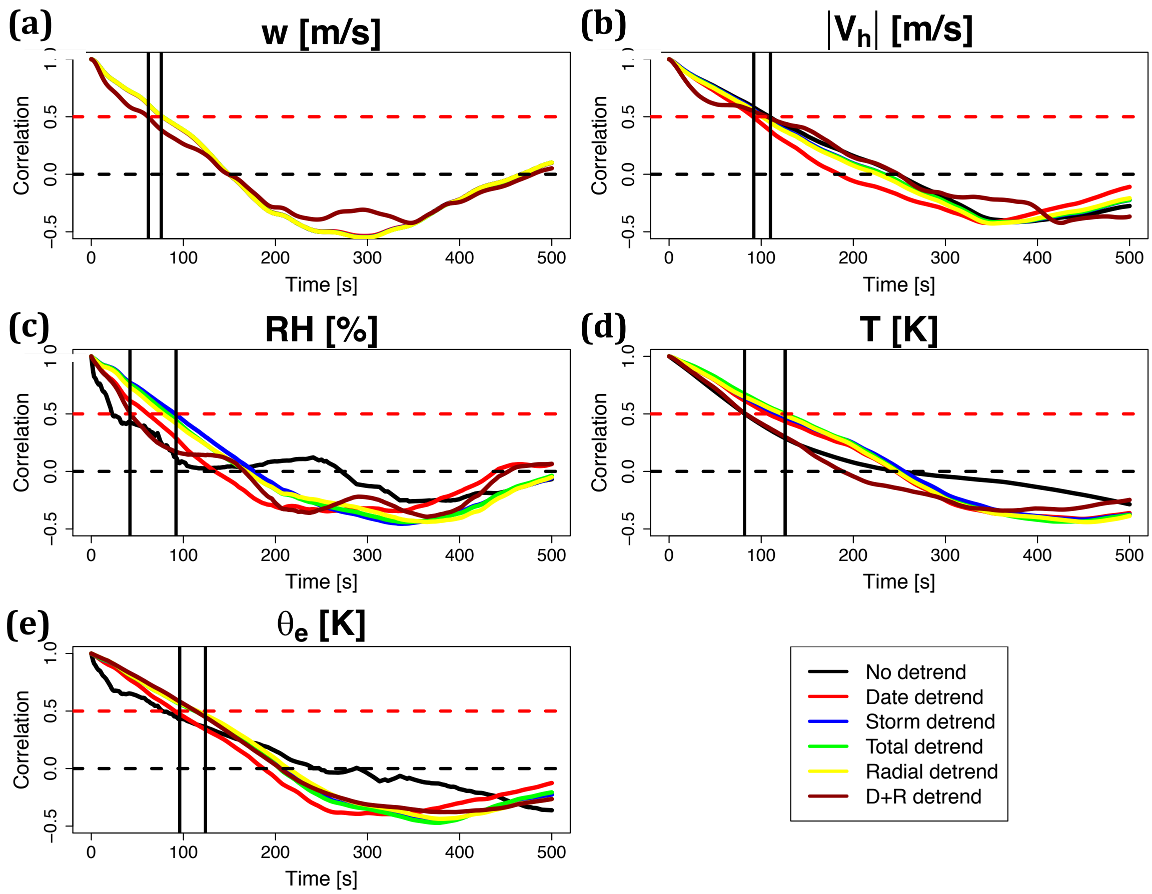

Figure F.8: Temporal autocorrelation correlograms of (a) w (m s^{-1}), (b) $|V_h|$ (m s^{-1}), (c) RH (%), (d) T (K), and (e) θ_e (K) from an updraft sounding (Dropsonde 72CC) launched into the eyewall of Patricia on 23 October. The black vertical lines denote the maximum and minimum 0.5-autocorrelation threshold. Correlations of 0.5 and 0.0 are denoted with horizontal dashed red and black lines, respectively. From Nelson et al. (2019b).

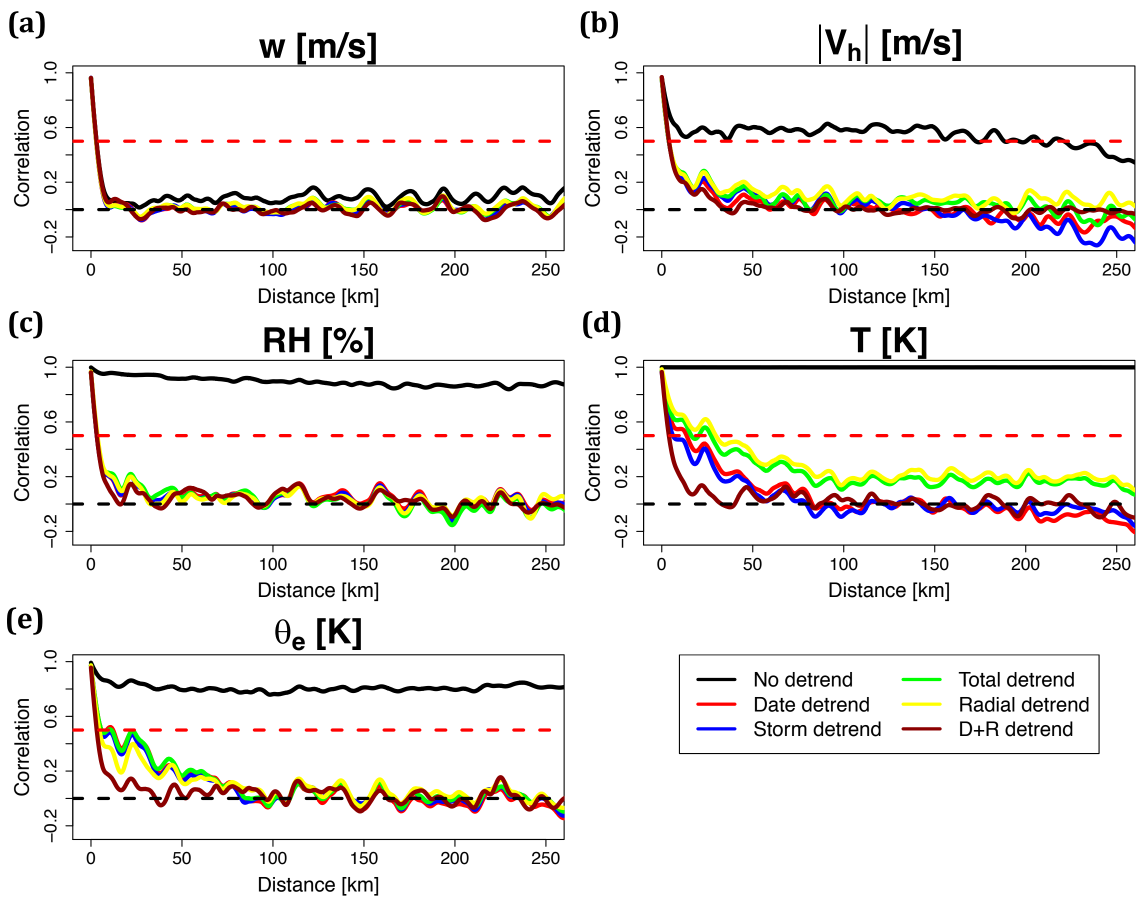

Figure F.9: Spatial autocorrelation correlograms of (a) w (m s^{-1}), (b) $|V_h|$ (m s^{-1}), (c) RH (%), (d) T (K), and (e) θ_e (K) for each of the six detrend methods in Marty. Correlations of 0.5 and 0.0 are denoted with horizontal dashed red and black lines, respectively. From Nelson et al. (2019b).

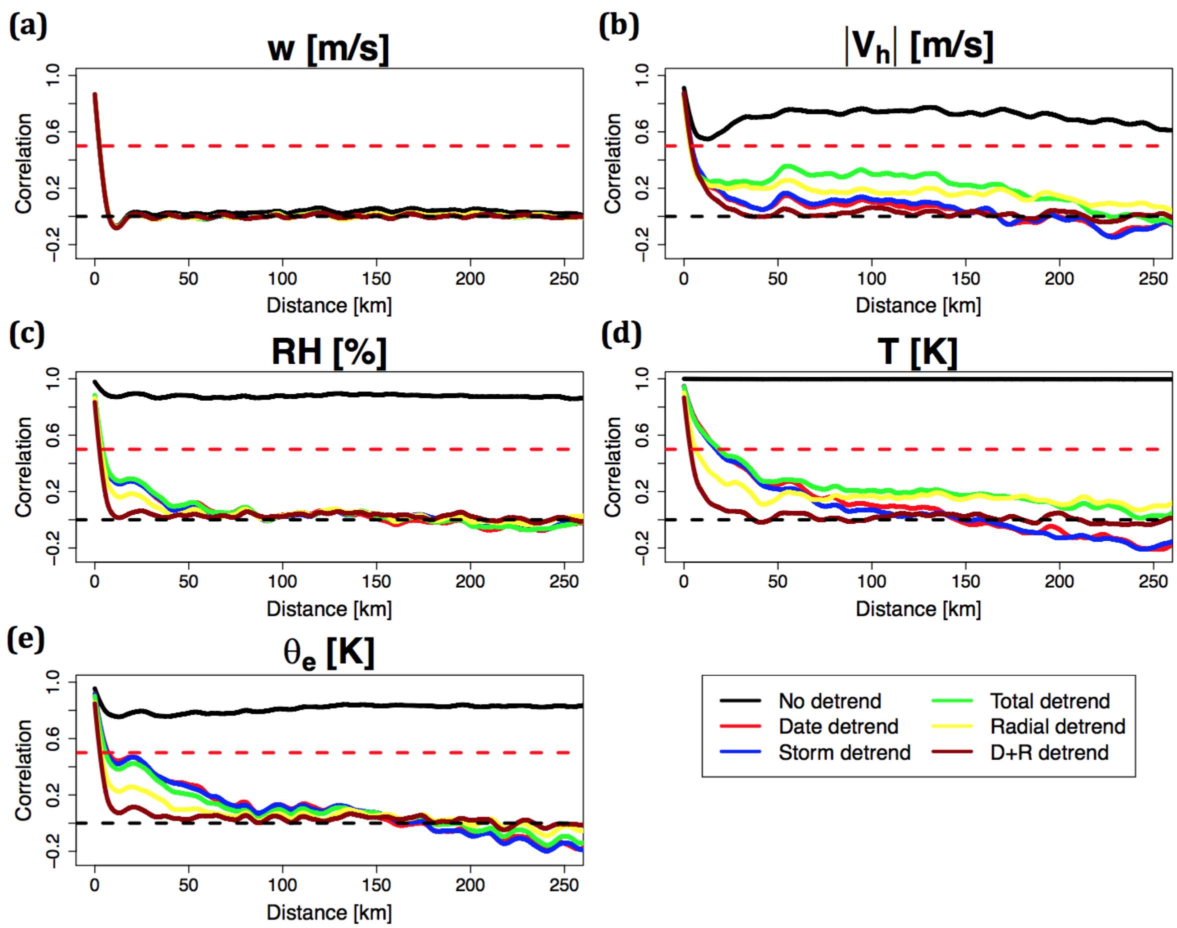

Figure F.10: Same as Fig. F.9, but for Joaquin. From Nelson et al. (2019b).

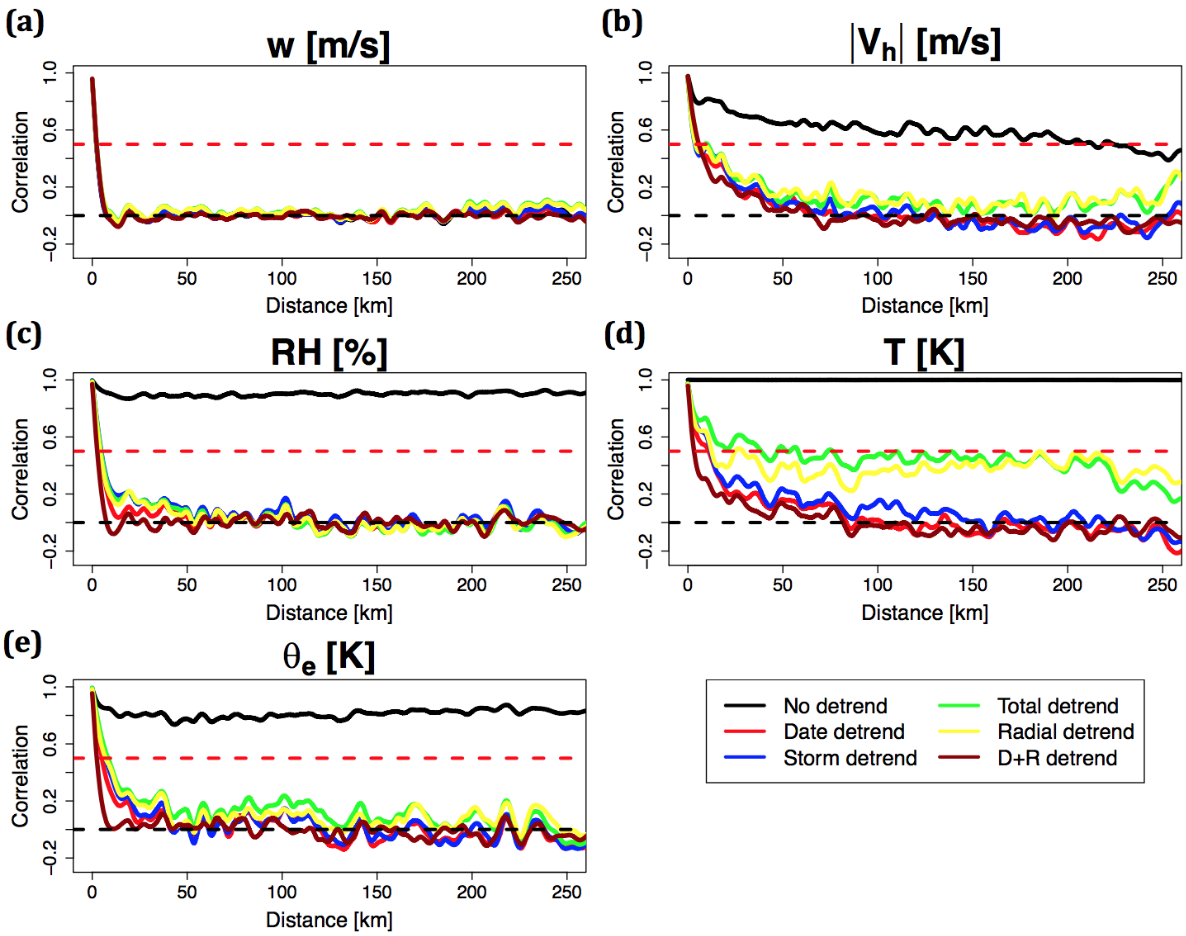

Figure F.11: Same as Fig. F.9, but for Patricia. From Nelson et al. (2019b).

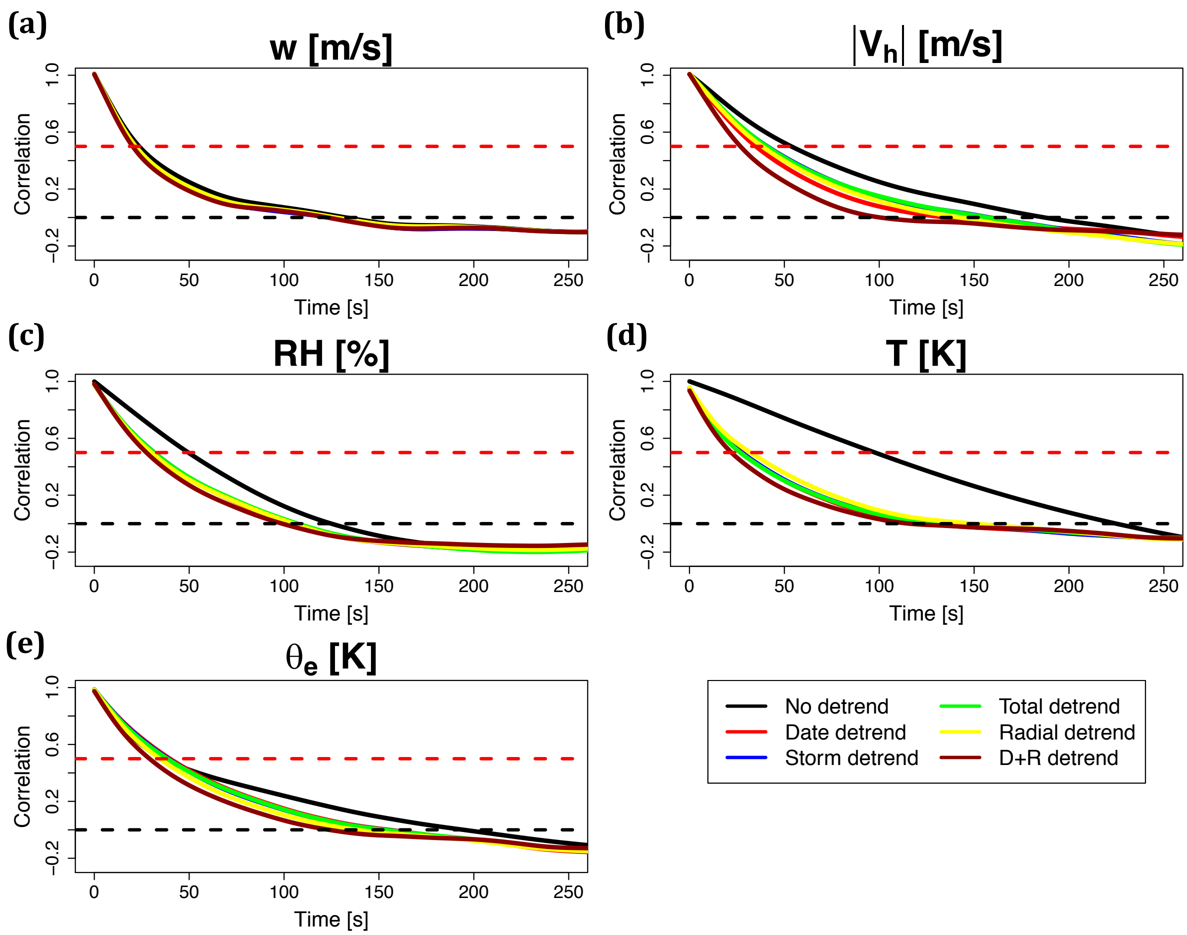

Figure F.12: Temporal autocorrelation correlograms of (a) w (m s^{-1}), (b) $|V_h|$ (m s^{-1}), (c) RH (%), (d) T (K), and (e) θ_e (K) for each of the six detrend methods in Marty. From Nelson et al. (2019b).

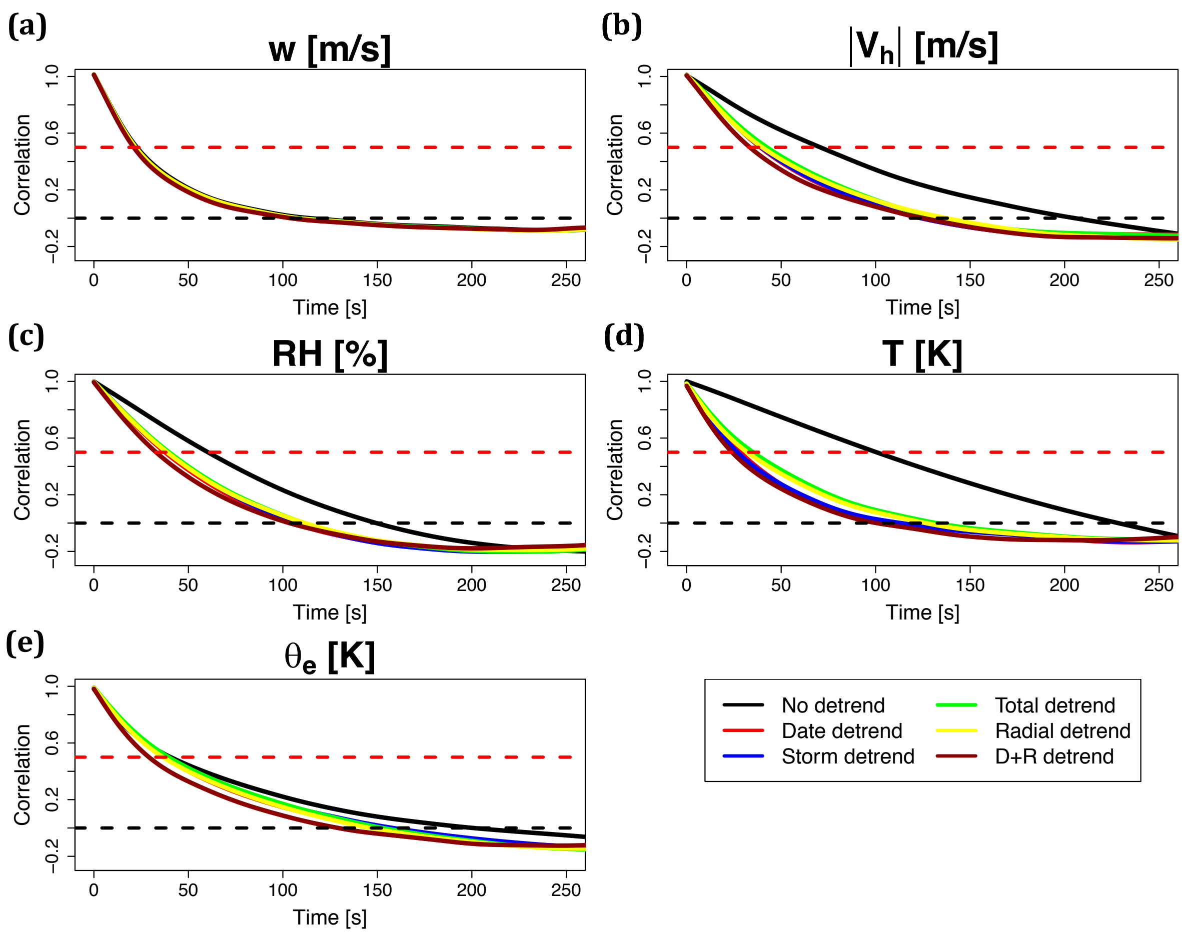

Figure F.13: Same as Fig. F.12, but for Joaquin. From Nelson et al. (2019b).

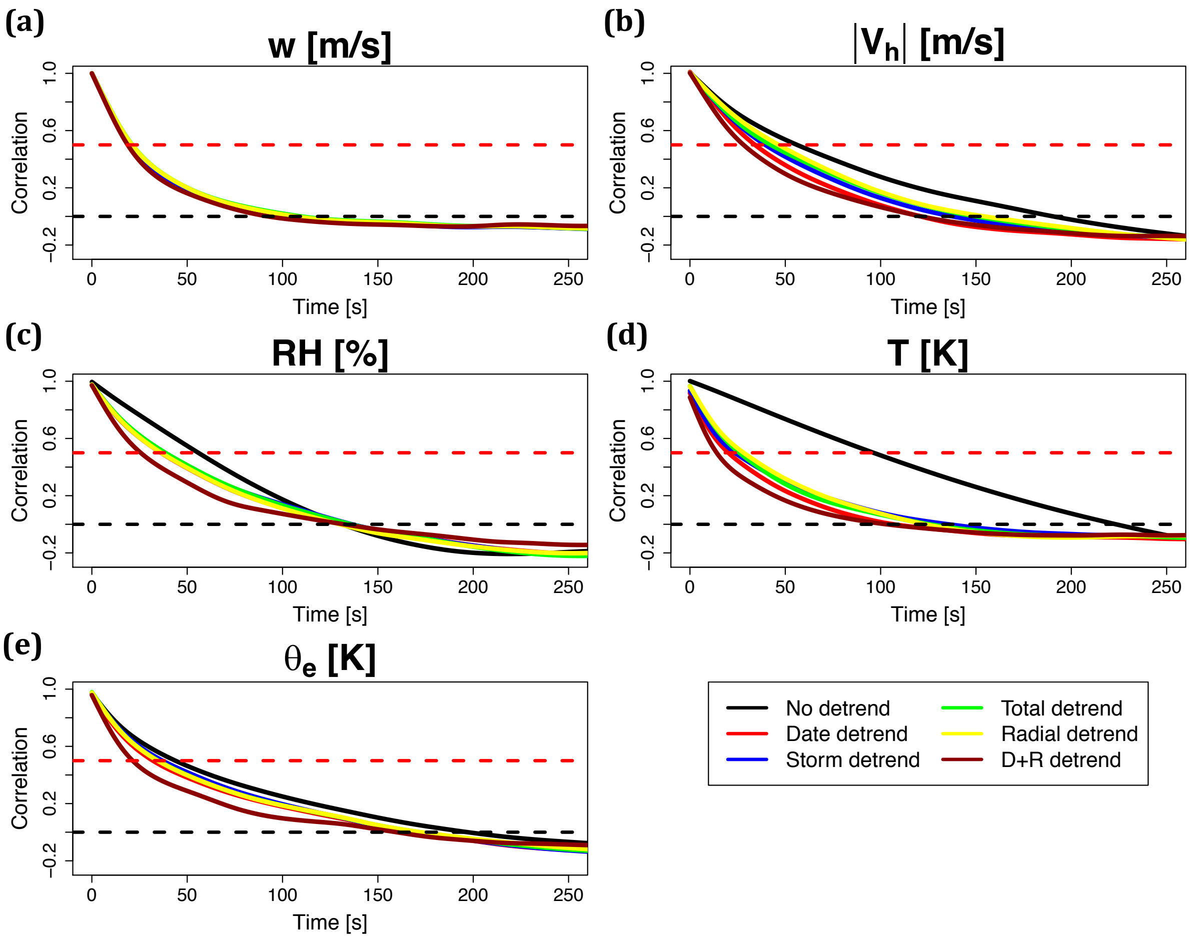

Figure F.14: Same as Fig. F.12, but for Patricia. From Nelson et al. (2019b).

BIBLIOGRAPHY

Abdelrahman, A. A. A., S. E. Suliman, A. B. A. Awad, Y. E. E. T. Alla, and A. A. A. Mohammed, 2015: Development of a computer based aircraft pitot-static instruments test system. *2015 International Conference on Computing, Control, Networking, Electronics and Embedded Systems Engineering*, 149–154.

Aberson, S. D., 2008: Large forecast degradations due to synoptic surveillance during the 2004 and 2005 hurricane seasons. *Mon. Wea. Rev.*, **136**, 3138–3150, doi:10.1175/2007MWR2192.1.

Aberson, S. D., M. T. Montgomery, M. Bell, and M. Black, 2006: Hurricane Isabel (2003): New insights into the physics of intense storms. Part II. *Bull. Amer. Meteor. Soc.*, **87**, 1349–1354, doi:10.1175/BAMS-87-10-1349.

All Sensors, 2019: DLHR series low voltage digital pressure sensors. All Sensors, accessed: 2019-03-11, https://www.allsensors.com/cad/DS-0350_Rev_B.PDF.

Atlas, D., R. C. Srivastava, and R. S. Sekhon, 1973: Doppler radar characteristics of precipitation at vertical incidence. *Rev. Geophys. Space Phys.*, **11**, 1–35.

Barfield, 2013: Automated pitot/static and air data test set specifications. Barfield, accessed: 2019-03-11, https://www.barfieldinc.com/assets/files/BIC%20Air%20Data%20Specification%20Comparison%20Chart.pdf.

Beck, B. T., G. Payne, and T. Heitman, 2010: Ac 2010-1803: The aerodynamics of the pitot-static tube and its current role in non-ideal engineering applications. *Proceedings of the ASEE 2010 Annual Conference and Exposition.*

Bell, M. M., and Coauthors, 2016: ONR Tropical Cyclone Intensity 2015 NASA WB-57 HDSS Dropsonde Data, Version 1.0. UCAR/NCAR - Earth Observing Laboratory, accessed: 2018-03-01, https://doi.org/10.5065/D6CF9NGC.

Berg, C. G., 2003: Low airspeed measuring devices for helicopter usage monitoring system. *Air Vehicles Division Platforms Sciences Laboratory, DSTO-TN-0495*, 33 pp., URL http://citeseerx.ist.psu.edu/viewdoc/download?doi=10.1.1.617.8859&rep=rep1&type=pdf.

Berg, R., 2016a: Hurricane Joaquin. *NHC Trop. Cycl. Rep. AL112015*, 36 pp., URL http://www.nhc.noaa.gov/data/tcr/AL112015_Joaquin.pdf.

Berg, R., 2016b: Hurricane Marty. *NHC Trop. Cycl. Rep. EP172015*, 17 pp., URL http://www.nhc.noaa.gov/data/tcr/EP172015_Marty.pdf.

Biau, G., E. Zorita, H. von Storch, and H. Wackernagel, 1999: Estimation of precipitation by kriging in the EOF space of the sea level pressure field. *J. Climate*, **12**, 1070–1085, doi:10.1175/1520-0442(1999)012,1070:EOPBKI.2.0.CO;2.

Black, M. L., R. W. Burpee, and F. Marks Jr., 1996: Vertical motion characteristics of tropical cyclones determined with airborne Doppler radial velocities. *J. Atmos. Sci.*, **53**, 1887–1909.

Black, M. L., J. F. Gamache, F. D. M. Jr., C. E. Samsury, and H. E. Willoughby, 2002: Eastern Pacific Hurricanes Jimena of 1991 and Olivia of 1994: The effect of vertical shear on structure and intensity. *Mon. Wea. Rev.*, **130**, 2291–2312.

Black, P., L. Harrison, M. Beaubien, R. Bluth, R. Woods, A. Penny, R. Smith, and J. Doyle, 2017: High Definition Sounding System (HDSS) for atmospheric profiling. *J. Atmos. Oceanic Technol.*, **34**, 777–796, doi:10.1175/JTECH-D-14-00210.1.

Black, R. A., H. B. Bluestein, and M. L. Black, 1994: Unusually strong vertical motions in a Caribbean hurricane. *Mon. Wea. Rev.*, **122**, 2722–2739.

Brett, A. C., and S. E. Tuller, 1991: The autocorrelation of hourly wind speed observations. *J. Appl. Meteor.*, 823–833.

Bringi, V. N., L. Tolstoy, M. Thurai, and W. A. Petersen, 2015: Estimation of spatial correlation of drop size distribution parameters and rain rate using NASA's S-band polarimetric radar and 2D video disdrometer network: Two case studies from MC3E. *J. Hydrometeor.*, **16**, 1207–1221, doi:10.1175/JHM-D-14-0204.1.

Brooks, C. E. P., and N. B. Carruthers, 1978: *Handbook of Statistical Methods in Meteorology.* AMS Press, 412 pp pp.

Brousaides, F. J., 1983: Meteorological sensors for battlefield weather support. *Rep. AD3.132623.*, 68 pp., URL https://apps.dtic.mil/docs/citations/AD3.132623.

Brown, G. O., 2003: Henry Darcy's perfection of the Pitot tube. *Henry P. G. Darcy and Other Pioneers in Hydraulics: Contributions in Celebration of the 200th Birthday of Henry Philibert Gaspard Darcy*, 14–23.

Bryan, G. H., and R. Rotunno, 2009: The influence of near-surface, high-entropy air in hurricane eyes on maximum hurricane intensity. *J. Atmos. Sci.*, **66**, 148–158, doi:10.1175/2008JAS2707.1.

Bushnell, R. H., 1966: The NCAR dropsonde program. *NCAR Tech. Note NCAR/TN-13+EDD*, 22 pp., doi:10.5065/D62V2D1B.

Bushnell, R. H., V. H. Glover, and R. D. Chu, 1973: Engineering report on a dropsonde for measuring vertical wind velocity in thunderstorms. *NCAR Tech. Note NCAR/TN-83+EDD*, 66 pp., doi:10.5065/D6K0727T.

Carlson, R., 2012: Accuracy of UAV pitot-static system. *UMTC Undergraduate Research Presentations and Papers (UROP) [1416]*, 9 pp., URL http://hdl.handle.net/11299/123252.

Cecil, D., S. Biswas, W. Jones, and F. Alquaied, 2016: Hurricane imaging radiometer (HIRAD) data. Version 2.1. UCAR/NCAR - Earth Observing Laboratory, accessed: 2017-07-26, https://doi.org/10.5065/D6CF9NGC.

Cecil, D. J., and S. K. Biswas, 2017: Hurricane imaging radiometer (HIRAD) wind speed retrievals and validation using dropsondes. *J. Atmos. Oceanic Technol.*, **34**, 1837–1851, doi:10.1175/JTECH-D-17-0031.1.

Chambers, J. M., W. S. Cleveland, B. Kleiner, and P. A. Tukey, Eds., 1983: *Graphical Methods for Data Analysis*. Wadsworth and Brooks/Cole.

Cole, H. L., S. Rossby, and P. K. Govind, 1973: The NCAR wind-finding dropsonde. *Atmos. Technol.*, **2**, 19–24.

Corbosiero, K. L., and J. Molinari, 2002: The effects of vertical wind shear on the distribution of convection in tropical cyclones. *Mon. Wea. Rev.*, **130**, 2110–2123.

Corbosiero, K. L., and J. Molinari, 2003: The relationship between storm motion, vertical wind shear, and convective asymmetries in tropical cyclones. *J. Atmos. Sci.*, **60**, 366–376.

Corbosiero, K. L., J. Molinari, A. R. Aiyyer, and M. L. Black, 2006: The structure and evolution of Hurricane Elena (1985). Part II: Convective asymmetries and evidence for vortex Rossby waves. *Mon. Wea. Rev.*, **134**, 3073–3091, doi:10.1175/MWR3250.1.

Creasey, R. L., and R. L. Elsberry, 2017: Tropical cyclone center positions from sequences of HDSS sondes deployed along high-altitude overpasses. *Wea. Forecasting*, **32**, 317–325, doi:10.1175/WAF-D-16-0096.1.

Darcy, H., 1858: Relative à quelques modifications à introduire dans le tube de pitot. *Annales des Ponts et Chaussées*, **15**, 351–359, doi:10.1175/WAF-D-16-0096.1.

DeHart, J. C., R. A. Houze Jr., and R. F. Rogers, 2014: Quadrant distribution of tropical cyclone inner-core kinematics in relation to environmental shear. *J. Atmos. Sci.*, **71**, 2713–2732, doi:10.1175/JAS-D-13-0298.1.

DeMaria, M., R. T. DeMaria, J. A. Knaff, and D. Molenar, 2012: Tropical cyclone lightning and rapid intensity change. *Mon. Wea. Rev.*, **140**, 1828–1842.

DeMaria, M., and J. Kaplan, 1994: A statistical hurricane intensity prediction scheme (SHIPS) for the Atlantic basin. *Wea. Forecasting*, **9**, 209–220.

Ditchek, S. D., T. C. Nelson, M. Rosenmayer, and K. L. Corbosiero, 2017: The relationship between tropical cyclones at genesis and their maximum attained intensity. *J. Climate*, **30**, 4897–4913, doi:10.1175/JCLI-D-16-0554.1.

Dolling, K., and G. M. Barnes, 2012: The creation of a high equivalent potential temperature reservoir in tropical storm Humberto (2001) and its possible role in storm deepening. *Mon. Wea. Rev.*, **140**, 492–505.

Doyle, J. D., and Coauthors, 2017: A view of tropical cyclones from above: The Tropical Cyclone Intensity (TCI) experiment. *Bull. Amer. Meteor. Soc.*, **98**, 2113–2134, doi:10.1175/BAMS-D-16-0055.1.

Duran, P., and J. Molinari, 2018: Dramatic inner-core tropopause variability during the rapid intensification of Hurricane Patricia (2015). *Mon. Wea. Rev.*, **146**, 119–134, doi:10.1175/MWR-D-17-0218.1.

Eastin, M. D., P. G. Black, and W. M. Gray, 2002a: Flight-level thermodynamic instrument wetting errors in hurricanes. Part I: Observations. *Mon. Wea. Rev.*, **130**, 825–841.

Eastin, M. D., P. G. Black, and W. M. Gray, 2002b: Flight-level thermodynamic instrument wetting errors in hurricanes. Part II: Implications. *Mon. Wea. Rev.*, **130**, 842–851.

Eastin, M. D., W. M. Gray, and P. G. Black, 2005a: Buoyancy of convective vertical motions in the inner core of intense hurricanes. Part I: General statistics. *Mon. Wea. Rev.*, **133**, 188–208.

Eastin, M. D., W. M. Gray, and P. G. Black, 2005b: Buoyancy of convective vertical motions in the inner core of intense hurricanes. Part I: General statistics. *Mon. Wea. Rev.*, **133**, 188–208.

Eastin, M. D., W. M. Gray, and P. G. Black, 2005c: Buoyancy of convective vertical motions in the inner core of intense hurricanes. Part II: Case studies. *Mon. Wea. Rev.*, **133**, 209–227.

Ejsing, L. W., M. F. Hansen, A. K. Menon, H. A. Ferreira, D. L. Graham, and P. P. Freitas, 2004: Planar Hall effect sensor for magnetic micro- and nanobead detection. *Appl. Phys. Letters*, **84**, 4729–4731, doi:10.1063/1.1759380.

Emmitt, G. D., S. Greco, M. Garstang, and M. Beaubien, 2018: CPEX 2017: Utilizing the Airborne Doppler Aerosol Wind Lidar and dropsondes for convective process studies. *2018 American Meteorological Society Annual Meeting.*

European Space Agency, 2019a: Introducing Aeolus. European Space Agency, accessed: 2019-05-05, https://www.esa.int/Our_Activities/Observing_the_Earth/Aeolus/Introducing_Aeolus.

European Space Agency, 2019b: Lasers in space. European Space Agency, accessed: 2019-05-05, https://www.esa.int/Our_Activities/Observing_the_Earth/Aeolus/Introducing_Aeolus.

Federal Aviation Administration, 2016: *Pilots Handbook of Aeronautical Knowledge. FAA-H-8083-25B.* Federal Aviation Administration, 8-1-8-23 pp.

Fisher, L., G. C. Craig, and C. Kiemle, 2013: Horizontal structure function and vertical correlation analysis of mesoscale water vapor variability observed by airborne Lidar. *J. Geophys. Res.*, **118**, 7579–7590, doi:10.1002/jgrd.50588.

Franklin, J. L., M. L. Black, and K. Valde, 2003: GPS dropwindsonde wind profiles in hurricanes and their operational implications. *Wea. Forecasting*, **18**, 32–44.

Franklin, J. L., S. J. Ford, S. E. Feuer, and F. Marks Jr., 1993: The kinematic structure of Hurricane Gloria (1985) determined from nested analyses of dropwindsonde and Doppler radar data. *Mon. Wea. Rev.*, **121**, 2433–2451.

Gentry, M. S., and G. M. Lackmann, 2010: Sensitivity of simulated tropical cyclone structure and intensity to horizontal resolution. *Mon. Wea. Rev.*, **138**, 688–704, doi: 10.1175/2009MWR2976.1.

Giammanco, I. M., J. L. Schroeder, and M. D. Powell, 2013: GPS dropwindsonde and WSR-88D observations of tropical cyclone vertical wind profiles and their characteristics. *Wea. Forecasting*, **28**, 77–99, doi:10.1175/WAF-D-11-00155.1.

Gorman, R. M., 2009: Intercomparison of methods for the temporal interpolation of synoptic wind fields. *J. Atmos. Oceanic Technol.*, **26**, 828–837, doi:10.1175/2008JTECHO588.1.

Govind, P. K., 1973: Dropsonde velocity measurements based on omega signals. *Atmos. Tech.*, **2**, 39–42.

Grasso, L. D., 2000: The difference between grid spacing and resolution and their application to numerical modeling. *Bull. Amer. Meteor. Soc.*, **81**, 579–580.

Griffith, D. A., 2003: *Spatial Autocorrelation and Spatial Filtering: Gaining Understanding through Theory and Scientific Visualization.* Springer, 247 pp.

Guimond, S. R., G. M. Heymsfield, and F. J. Turk, 2010: Multiscale observations of Hurricane Dennis (2005): The effects of hot towers on rapid intensification. *J. Atmos. Sci.*, **67**, 633–654.

Gunst, R. F., 1995: Estimating spatial correlations from spatial-temporal meteorological data. *J. Climate*, **8**, 2454–2470.

Habib, E., W. F. Krajewski, and G. J. Ciach, 2001: Estimation of rainfall interstation correlation. *J. Hydrometeor.*, **2**, 621–629.

Haering Jr., E. A., 1995: Airdata measurement and calibration. *NASA Technical Memorandum 104316*, 22 pp., URL https://www.nasa.gov/centers/dryden/pdf/88377main_H-2044.pdf.

Happel, J., and H. Brenner, 1965: *Low Reynolds Number Hydrodynamics*. Prentice-Hall, 533 pp.

Hazelton, A., R. Rogers, and R. Hart, 2017: Analyzing simulated convective bursts in two Atlantic hurricanes, Part I: Burst formation and development. *Mon. Wea. Rev.*, **145**, 3073–3094, doi:10.1175/MWR-D-16-0267.1.

Heymsfield, G. M., L. Tian, A. J. Heymsfield, L. Li, and S. Guimond, 2010: Characteristics of deep tropical and subtropical convection from nadir-viewing high-altitude airborne Doppler radar. *J. Atmos. Sci.*, **67**, 285–308, doi:10.1175/2009JAS3132.1.

Higuchi, H., P. Langen, H. Sawada, and C. E. Tinney, 2006: Axial flow over a blunt circular cylinder with and without shear layer reattachment. *J. Fluids and Structures*, **2**, 949–959, doi:10.1016/j.jfluidstructs.2006.04.020.

Hock, T. F., and J. L. Franklin, 1999: The NCAR GPS dropwindsonde. *Bull. Amer. Meteor. Soc.*, **80**, 407–420.

Houchi, K., A. Stoffelen, G. Marseille, and J. D. Kloe, 2015: Statistical quality control of high resolution winds of different radiosonde types for climatology analysis. *J. Atmos. Oceanic Technol.*, **32**, 1796–1812, doi:10.1175/JTECH-D-14-00160.1.

Incropera, F. P., D. P. Dewitt, T. L. Bergman, and A. S. Lavine, 2007: *Fundamentals of Heat and Mass Transfer*. John Wiley and Sons, 1070 pp.

Jameson, A. R., 2017: Spatial and temporal network sampling effects on the correlation and variance structures of rain observations. . *J. Hydrometeor.*, **18**, 187–196, doi:10.1175/JHM-D-16-0129.1.

Janert, P. K., 2011: *Data Analysis with Open Source Tools*. O'Reilly, 509 pp.

Jiang, H., 2012: The relationship between tropical cyclone intensity change and the strength of inner-core convection. *Mon. Wea. Rev.*, **140**, 1164–1176, doi:10.1175/MWR-D-11-00134.1.

Jiang, H., and E. M. Ramirez, 2013: Necessary conditions for tropical cyclone rapid intensification as derived from 11 years of TRMM data. *J. Climate*, **26**, 6459–6470, doi:10.1175/JCLI-D-12-00432.1.

Jiang, H., and C. Tao, 2014: Contribution of tropical cyclones to global very deep convection. *J. Climate*, **27**, 4313–4336, doi:10.1175/JCLI-D-13-00085.1.

Jorgensen, D. P., T. Matejka, and J. D. DuGranrut, 1996: Multi-beam techniques for deriving wind fields from airborne Doppler radars. *Meteor. Atmos. Phys.*, **59**, 83–104.

Jorgensen, D. P., E. J. Zipser, and M. A. LeMone, 1985: Vertical motions in intense hurricanes. *J. Atmos. Sci.*, **42**, 839–856.

Kaplan, J., and M. DeMaria, 2003: Large-scale characteristics of rapidly intensifying tropical cyclones in the North Atlantic basin. *Wea. Forecasting*, **18**, 1093–1108.

Kavaya, M. J., J. Y. Beyon, G. J. Koch, M. Petros, P. J. Petzar, U. N. Singh, B. C. Trieu, and J. Yu, 2014: The Doppler Aerosol Wind (DAWN) airborne, wind-profiling coherent-detection lidar system: Overview and preliminary flight results. *J. Atmos. Oceanic Technol.*, **31**, 826–842, doi:10.1175/JTECH-D-12-00274.1.

Khalili, M., R. Leconte, and F. Brissette, 2007: Stochastic multisite generation of daily precipitation data using spatial autocorrelation. *J. Hydrometeor.*, **8**, 396–412, doi:10.1175/JHM588.1.

Kimball, S. K., and M. S. Mulekar, 2004: A 15-year climatology of North Atlantic tropical cyclones. Part I: Size parameters. *J. Climate*, **17**, 3555–3575.

Kimberlain, T. B., E. S. Blake, and J. P. Cangialosi, 2016: Hurricane Patricia. *NHC Trop. Cycl. Rep. EP202015*, 32 pp., URL http://www.nhc.noaa.gov/data/tcr/EP202015_Patricia.pdf.

Komaromi, W. A., and J. D. Doyle, 2017: Tropical cyclone outflow and warm core structure as revealed by HS3 dropsonde data. *Mon. Wea. Rev.*, **145**, 1339–1359, doi:10.1175/MWR-D-16-0172.1.

LeMone, M. A., and E. J. Zipser, 1980: Cumulonimbus vertical velocity events in GATE. Part I: Diameter, intensity, and mass flux. *J. Atmos. Sci.*, **37**, 2444–2457.

Li, S., and C. Miller, 2014a: A study on the motion characteristics and their impact on the wind measurement post-processing of the GPS dropwindsonde Part I: Effects of the wind-finding equations. *Theo. Appl. Climatol.*, **117**, 221–231, doi:10.1007/s00704-013-0962-5.

Li, S., and C. Miller, 2014b: A study on the motion characteristics and their impact on the wind measurement post-processing of the GPS dropwindsonde Part II: Impacts of post-processing/composition schemes. *Theo. Appl. Climatol.*, **117**, 247–259, doi:10.1007/s00704-013-1003-0.

Lodh, B. K., A. K. Das, and N. Signh, 2017: Large eddy simulation turbulence modeling for wind flow over wall mounted cube. *Int. J. Chem. Eng. Res.*, **9**, 7–39.

Lothon, M., D. H. Lenschow, and S. D. Mayor, 2006: Coherence and scale of vertical velocity in the convective boundary layer from a Doppler lidar. *Boundary-Layer Meteor.*, **121**, 521–536, doi:10.1007/s10546-006-9077-1.

Marks, F. D., P. G. Black, M. T. Montgomery, and R. W. Burpee, 2008: Structure of the eye and eyewall of Hurricane Hugo (1989). *Mon. Wea. Rev.*, **136**, 1237–1259.

Matejka, T., and D. L. Bartels, 1998: The accuracy of vertical air velocities from Doppler radar data. *Mon. Wea. Rev.*, **126**, 92–117.

McFarquhar, G. M., B. F. Jewett, M. S. Gilmore, S. W. Nesbitt, and T. Hsieh, 2012: Vertical velocity and microphysical distributions related to rapid intensification in a simulation of Hurricane Dennis (2005). *J. Atmos. Sci.*, **69**, 3515–3534, doi:10.1175/JAS-D-12-016.1.

Menter, F. R., 1993: Zonal two-equation k-ω turbulence models for aerodynamic flows. *AIAA 24th Fluid Dynamics Conference*, 1993–2906.

Mitchell, C., 2013: Measuring the air speed created in a wind tunnel. M.S. thesis, Department of Physics, Pomona College, 24 pp. pp.

Molinari, J., D. Vollaro, and S. Skubis, 1993: Application of the Eliassen balanced model to real-data tropical cyclones. *Mon. Wea. Rev.*, **121**, 2409–2419.

Montgomery, M. T., M. M. Bell, S. D. Aberson, and M. L. Black, 2006: Hurricane Isabel (2003): New insights into the physics of intense storms. Part I. *Bull. Amer. Meteor. Soc.*, **87**, 1335–1347, doi:10.1175/BAMS-87-10-1335.

Moon, Y., and D. S. Nolan, 2015: Spiral rainbands in a numerical simulation of Hurricane Bill (2009). Part II: Propagation of inner rainbands. *J. Atmos. Sci.*, **72**, 191–215, doi:10.1175/JAS-D-14-0056.1.

Moum, J. N., 2015: Ocean speed and turbulence measurements using pitot-static tubes on moorings. *J. Atmos. Oceanic Technol.*, **32**, 1400–1413, doi:10.1175/JTECH-D-14-00158.1.

Mu, M., F. Zhou, and H. Wang, 2009: A method for identifying the sensitive areas in targeted observations for tropical cyclone prediction: Conditional nonlinear optimal perturbation. *Mon. Wea. Rev.*, **137**, 1623–1639, doi:10.1175/2008MWR2640.1.

Munson, B. R., D. F. Young, and T. H. Okiishi, 2006: *Fundamentals of Fluid Mechanics.* 5th ed., John Wiley and Sons, 526 pp pp.

Nelson, T. C., and L. C. Harrison, 2019: Revisiting the wind-finding equations for dropsondes. *In preparation.*

Nelson, T. C., L. C. Harrison, and K. L. Corbosiero, 2019a: Examination of the eXpendable Digital Dropsonde-derived vertical velocities from the Tropical Cyclone Intensity (TCI) experiment. *Mon. Wea. Rev.*, **147**, 2367–2386, doi:10.1175/MWR-D-18-0414.1.

Nelson, T. C., L. C. Harrison, and K. L. Corbosiero, 2019b: Temporal and spatial autocorrelations from expendable digital dropsondes (XDDs). *J. Atmos. Oceanic Technol., In revision.*

Nguyen, L. T., R. F. Rogers, and P. D. Reasor, 2017: Thermodynamic and kinematic influences on precipitation symmetry in sheared tropical cyclones: Bertha and Cristobal (2014). *Mon. Wea. Rev.*, **145**, 4423–4446, doi:10.1175/MWR-D-17-0073.1.

Nichol, J. E., and M. S. Wong, 2008: Spatial variability of air temperature and appropriate resolution for satellite-derived air temperature estimation. *Int. J. Remote Sens.*, **29**, 7213–7223, doi:10.1080/01431160802192178.

Niedzielski, T., and Coauthors, 2017: Are estimates of wind characteristics based on measurements with Pitot tubes and GNSS receivers mounted on consumer-grade unmanned aerial vehicles applicable in meteorological studies? *Environ. Monit. Assess.*, **189**, 1–19, doi:10.1007/s10661-017-6141-x.

Paffrath, U., C. Lemmerz, O. Reitebuch, B. Witschas, I. Nikolaus, and V. Freudenthaler, 2009: The airborne demonstrator for the direct-detection Doppler wind lidar ALADIN on ADM-Aeolus. Part II: Simulations and Rayleigh receiver radiometric performance. *J. Atmos. Oceanic Technol.*, **26**, 2516–2530, doi:10.1175/2009JTECHA1309.1.

Pearson, P. H. O., 1983: Investigation into the internal aerodynamic design and associated errors in a fast descent ducted sonde for the measurement of atmospheric pressure and temperatures (AMPARS phase 2). *Tech. Rep. WSRL-0343-TR.*, 30 pp., URL https://apps.dtic.mil/dtic/tr/fulltext/u2/3.143189.pdf.

Pérez, I. A., M. Á. García, M. L. Sánchez, and B. Torre, 2004: Autocorrelation analysis of meteorological data from a RASS sodar. *J. Appl. Meteor.*, **43**, 1213–1223.

Persing, J., and M. T. Montgomery, 2003: Hurricane superintensity. *J. Atmos. Sci.*, **60**, 2349–2371.

Pitot, H., 1732: Description d'une machine pour mesurer la vitesse des eaux courantes et le sillage des vaisseaux,. *Mémoires de L'Académie*, 363–376.

Privé, N. C., and R. M. Errico, 2016: Temporal and spatial interpolation errors of high-resolution modeled atmospheric fields. *J. Atmos. Oceanic Technol.*, **33**, 303–311, doi:10.1175/JTECH-D-15-0132.1.

Raymond, D. J., G. B. Raga, C. S. Bretherton, J. Molinari, C. López-Carrillo, and Ž. Fuchs, 2003: Convective forcing in the intertropical convergence zone of the eastern Pacific. *J. Atmos. Sci.*, **60**, 2064–2082.

Reasor, P. D., R. Rogers, and S. Lorsolo, 2013: Environmental flow impacts on tropical cyclone structure diagnosed from airborne Doppler radar composites. *Mon. Wea. Rev.*, **141**, 2949–2969, doi:10.1175/MWR-D-12-00334.1.

Reitebuch, O., C. Lemmerz, E. Nagel, U. Paffrath, Y. Durand, M. Endemann, F. Fabre, and M. Chaloupy, 2009: The airborne demonstrator for the direct-detection Doppler wind lidar ALADIN on ADM-Aeolus. Part I: Instrument design and comparison to satellite instrument. *J. Atmos. Oceanic Technol.*, **26**, 2501–2515, doi:10.1175/2009JTECHA1309.1.

Reuder, J., P. Brisset, M. Jonassen, M. Müller, and S. Mayer, 2009: The small unmanned meteorological observer SUMO: A new tool for atmospheric boundary layer research. *Meteorologische Zeitschrift*, **18**, 141–147, doi:10.1127/0941-2948/2009/0363.

Reuder, J., M. O. Jonassen, and H. Ólafsson, 2013: The small unmanned meteorological observer SUMO: Recent developments and applications of a micro-UAS for atmospheric boundary layer research. *Acta Geophysica*, **60**, 1454–1473, doi:10.2478/s11600-012-0042-8.

Rogers, R., P. Reasor, and S. Lorsolo, 2013: Airborne doppler observations of the inner-core structural differences between intensifying and steady-state tropical cyclones. *Mon. Wea. Rev.*, **141**, 2970–2991, doi:10.1175/MWR-D-12-00357.1.

Rogers, R. F., J. A. Zhang, J. Zawislak, H. Jiang, G. R. Alvey III, E. J. Zipser, and S. N. Stevenson, 2016: Observations of the structure and evolution of Hurricane Edouard (2014) during intensity change. Part II: Kinematic structure and the distribution of deep convection. *Mon. Wea. Rev.*, **144**, 3355–3376, doi:10.1175/MWR-D-16-0017.1.

Rogers, R. F., and Coauthors, 2017: Rewriting the tropical record books: The extraordinary intensification of Hurricane Patricia. *Bull. Amer. Meteor. Soc.*, **98**, 2092–2112, doi:10.1175/BAMS-D-16-0039.1.

Romine, G. S., C. S. Schwartz, R. D. Torn, and M. L. Weisman, 2016: Impact of assimilating dropsonde observations from MPEX on ensemble forecasts of severe weather events. *Mon. Wea. Rev.*, **144**, 3799–3823, doi:10.1175/MWR-D-15-0407.1.

Rykatcheff, M., 1990: Results of a balloon ascension at St. Petersburg, May 20 / June 1,1878. *Mon. Wea. Rev.*, **28**, 392–393.

Ryzhkov, A. V., 2007: Impact of beam broadening on the quality of radar polarimetric data. *J. Atmos. Oceanic Technol.*, **24**, 729–744, doi:10.1175/JTECH2003.1.

Salter, C., J. H. Warsap, and D. G. Goodman, 1965: A discussion of pitot-static tubes and of their calibration factors with a description of various versions of a new design. *Aeronautical Research Council Reports and Memoranda.*, **3365**, 1–53.

Shapiro, L. J., and H. E. Willoughby, 1982: The response of balanced hurricanes to local sources of heat and momentum. *J. Atmos. Sci.*, **39**, 378–394.

SpaceAge Control, 1998: Wind tunnel evaluation of pitot nose configurations on indicated airspeed accuracy. X003A(NC).Doc. SpaceAge Control, accessed: 2019-03-11, 16 pp. pp., https://spaceagecontrol.com/Main/uploads/Main.Freewtpubs/x003a.pdf.

Steranka, J., E. B. Rodgers, and R. C. Gentry, 1986: The relationship between satellite measured convective bursts and tropical cyclone intensification. *Mon. Wea. Rev.*, **114**, 1539–1546.

Stern, D. P., and S. D. Aberson, 2006: Extreme vertical winds measured by dropwindsondes in hurricanes. *27th Conf. on Hurricanes and Tropical Meteorology.*

Stern, D. P., and G. H. Bryan, 2018: Using simulated dropsondes to understand extreme updrafts and wind speeds in tropical cyclones. *Mon. Wea. Rev.*, **146**, 3901–3925, doi: 10.1175/MWR-D-18-0041.1.

Stern, D. P., G. H. Bryan, and S. D. Aberson, 2016: Extreme low-level updrafts and wind speeds measured by dropsondes in tropical cyclones. *Mon. Wea. Rev.*, **144**, 2177–2204, doi:10.1175/MWR-D-15-0313.1.

Stern, D. P., J. L. Vigh, and D. S. Nolan, 2015: Revisiting the relationship between eyewall contraction and intensification. *J. Atmos. Sci.*, **72**, 1283–1306, doi:10.1175/JAS-D-14-0261.1.

Stevenson, S. N., K. L. Corbosiero, and J. Molinari, 2014: The convective evolution and rapid intensification of Hurricane Earl (2010). *Mon. Wea. Rev.*, **142**, 4364–4380, doi: 10.1175/MWR-D-14-00078.1.

Torn, R. D., and G. J. Hakim, 2009: Ensemble data assimilation applied to RAINEX observations of Hurricane Katrina (2005). *Mon. Wea. Rev.*, **137**, 2817–2829, doi:10.1175/2009MWR2656.1.

U-blox, 2019: MAX-6 u-blox 6 GPS modules data sheet. U-blox, accessed: 2019-02-26, 21 pp. pp.

U-blox, 2019: MAX-8 u-blox 8 GNSS modules data sheet. U-blox, accessed: 2019-02-26, 21 pp. pp., https://www.u-blox.com/sites/default/files/MAX-8_DataSheet_%28UBX-16000093%29.pdf.

Venables, W. N., and B. D. Ripley, 2002: *Modern Applied Statistics with S*. 4th ed., Springer, 504 pp.

Vigh, J. L., and W. H. Schubert, 2009: Rapid development of the tropical cyclone warm core. *J. Atmos. Sci.*, **66**, 3335–3350, doi:10.1175/2009JAS3092.1.

Vömel, H., T. F. Hock, M. Goodstein, K. Young, and I. Suhr, 2018: The quality of observations from the updated NCAR dropsonde system in severe storms. *33rd Conference on Hurricanes and Tropical Meteorology.*

Wang, J., J. Bian, W. O. Brown, H. Cole, and V. Grubišić, 2009: Vertical air motion from T-REX radiosonde and dropsonde data. *J. Atmos. Oceanic Technol.*, **26**, 928–942, doi:10.1175/2008JTECH3.1240.1.

Wang, J., and Coauthors, 2015: A long-term, high-quality, high-vertical-resolution GPS dropsonde dataset for hurricane and other studies. *Bull. Amer. Meteor. Soc.*, **96**, 961–973, doi:10.1175/BAMS-D-13-00203.1.

Wick, G. A., T. F. Hock, P. J. Neiman, H. Vömel, M. L. Black, and J. R. Spackman, 2018: The NCAR-NOAA Global Hawk dropsonde system. *J. Atmos. Oceanic Technol.*, **35**, 1585–1604, doi:10.1175/JTECH-D-17-0225.1.

Willoughby, H. E., 1990: Gradient balance in tropical cyclones. *J. Atmos. Sci.*, **47**, 265–274.

Willoughby, H. E., and M. B. Chemlow, 1982: Objective determination of hurricane tracks from aircraft observations. *Mon. Wea. Rev.*, **110**, 1298–1305.

Wu, C., and Coauthors, 2009: Intercomparison of targeted observation guidance for tropical cyclones in the northwestern Pacific. *Mon. Wea. Rev.*, **137**, 2471–2492, doi: 10.1175/2009MWR2762.1.

Wylie, D. P., B. B. Hinton, M. R. Howland, and R. J. Lord, 1985: Autocorrelation of wind observations. *Mon. Wea. Rev.*, **113**, 849–857.

Zipser, E. J., 2003: Some views on "hot towers" after 50 years of tropical field programs and two years of TRMM data. *Cloud Systems, Hurricanes, and the Tropical Rainfall Measuring Mission (TRMM). Meteor. Monogr.*, **51**, 49–58.